Brian Brongers

Shear behaviour of tunnels subjected to fire

A numerical analysis of the Heinenoordtunnel

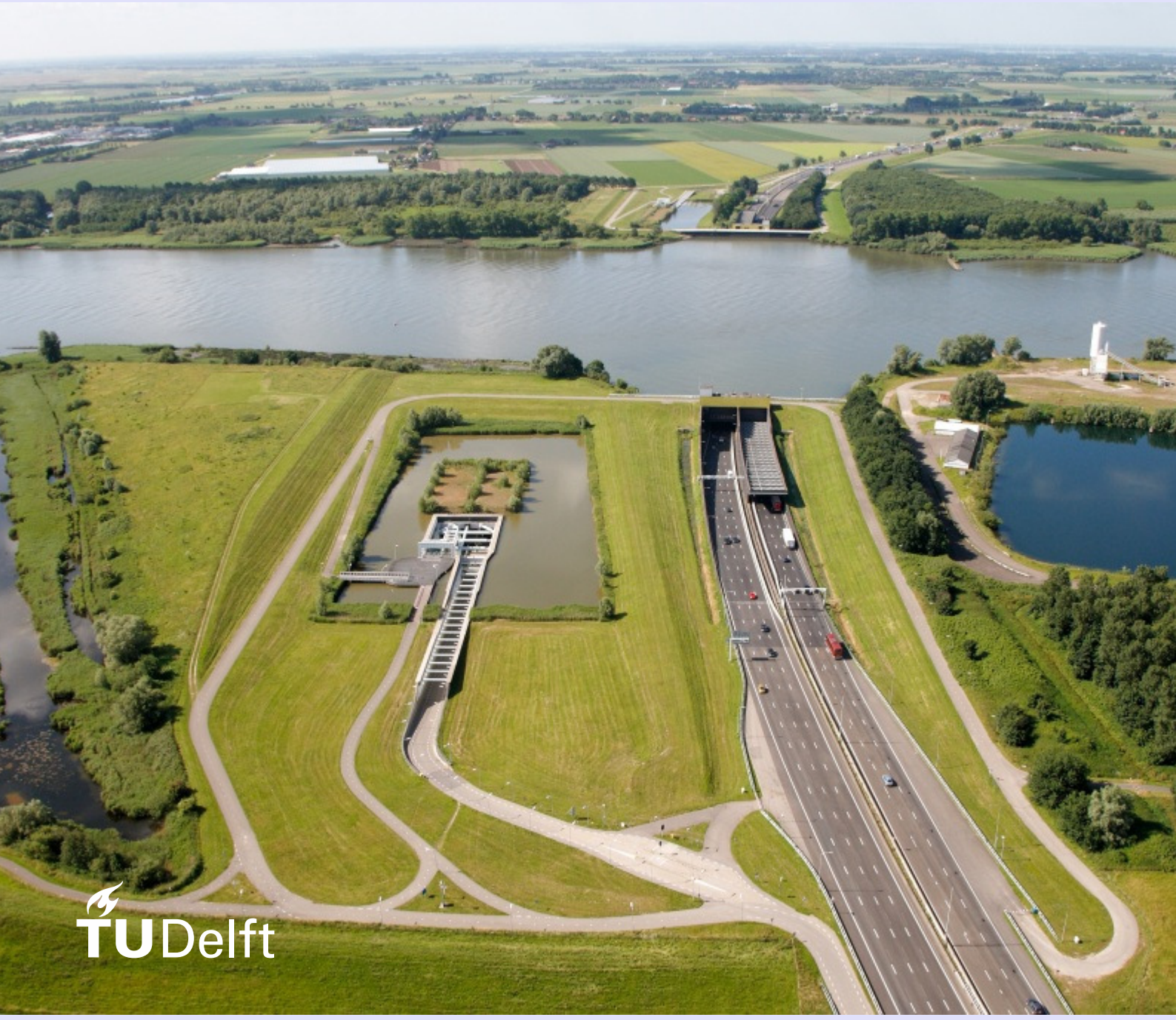

TU Delft

Shear behaviour of tunnels subjected to fire

A numerical analysis of the Heinenoordtunnel

By

B. Brongers

in partial fulfilment of the requirements for the degree of

Master of Science
in Civil Engineering

at the Delft University of Technology,
to be defended publicly on Friday January 24th, 2020 at 15:00.

Thesis committee:	Dr. ir. Y. Yang	TU Delft
	Dr. ir. C.B.M. Blom	TU Delft
	Dr. ir. M.A.N. Hendriks,	TU Delft
	Ing. H.M. Hendrix PMSE,	Rijkswaterstaat

TU Delft

Abstract

Recently experiments were conducted at the Technical University of Delft on the size effect of concrete. The size effect is a term used for the relative decrease in shear capacity with an increase in height of the structural member. The beams observed in the experiment failed much sooner than was predicted. These test results have implications for the Heinenoordtunnel, the roof of which shares many of the characteristics of the beams that were used in the experiments. The question is posed what happens to the Heinenoordtunnel in case of a fire, when also considering the recent tests on the size effect of concrete.

The Heinenoordtunnel is analysed with a numerical model. First however, in order to account for the observed size effect, the beams from the experiment are recreated. A study is performed on the effect of various parameters on the numerically obtained failure load, cracking load, crack pattern and deflection in order to find a set of parameters to approximate the observed size effect. It was found that a significant reduction in tensile strength and fracture energy is necessary to obtain a better approximation of the experimental results. However, despite these changes the numerical model still overestimates the shear capacity.

This information is used to create a model of the Heinenoordtunnel. A situation without a fire load is analysed and validated. The model is compared with the analytical IBBC-TNO method. Consequently, the model is subjected to a fire load. The fire is modelled using temperature dependent properties and by determining the temperature ingress for a 2 hour RWS fire. A significant shear crack is found present due the fire load, the location and shape of the crack suggesting onset of shear compression failure. The model however is still considered to be in equilibrium and so failure has not actually occurred in the model. A comparison with an analytical model suggests that a shift in bending moments from the increase in temperature results in a shift of shear capacity in the roof.

It is concluded that, while the numerical model does not fail, some caution is advised for the translation of these results to practical application. The change of material parameters found in modelling the size effect tests still leads to an overestimation of the shear capacity. On the other hand, the situation that was modelled was an extremity. In the model of the Heinenoordtunnel the absolute physical maximum water load was assumed in conjunction with an extreme fire. It is recommended to check the fire load with computational fluid dynamics modelling, to see if the fire load could possibly be less severe than assumed.

Acknowledgements

I would like to thank my thesis committee for their continued support and feedback throughout my entire thesis. For helping me remain objective and critical of my work. In particular I want to thank my supervisor at Rijkswaterstaat, Bart Hendrix. Bart has been an amazing support, from brainstorming thesis topics to in-depth discussions. His input and guidance helped me immensely in creating this thesis.

To my colleagues at Rijkswaterstaat, thank you for sharing your insight and experience. You have all been very accommodative and helpful during my stay. I would especially like to thank Gerrit Wolsink, I feel like I learned something from every single conversation with you. Your interest in my thesis is much appreciated.

To my friends and family, thanks for all the moral support these past few months. Thank you for helping me blow off some steam or listening to me ramble about my thesis. A special thanks to my roommates for doing so on a daily basis. It has been a long journey, but you all made it feel very bearable and rewarding.

Contents

1 Introduction

1.1. Problem description

Rijkswaterstaat (RWS), as part of the Ministry of Infrastructure and Water Management of The Netherlands, is asset owner of several large tunnels in The Netherlands. Some of these tunnels are over 50 years old, and have been designed with the GBV 1962 design codes (Gewapend-Betonvoorschriften in Dutch or Reinforced Concrete requirements in English), or even earlier versions of these codes. Most of the tunnels designed with the GBV 1962 have no shear reinforcement, because it stated that the shear capacity of concrete alone would be sufficient. Later design codes brought significant changes in the calculation of the shear capacity and prompted further research into the shear capacity of reinforced concrete [1].

According to the current design codes some of the older tunnels without shear reinforcement could be considered unsafe. Of these tunnels Rijkswaterstaat considers the Heinenoordtunnel to be the most pressing case. In 2009 TNO performed a probabilistic analysis to assess the structural safety of the Heinenoordtunnel [2]. In this calculation TNO used their own shear prediction formulas, the IBBC-TNO method, developed in cooperation with Rijkswaterstaat in 1981. From this analysis it followed that the Heinenoordtunnel is just barely meeting the safety requirements.

Recent tests at Delft University of Technology revealed deficiencies in the size effect used in the design codes. The size effect is a relative reduction in shear capacity based on the height of the concrete cross-section. In its current form the size effect is underestimated, leading to an overestimation of the shear capacity of deep beams. This put the structural reliability of the Heinenoordtunnel into question once again.

Additionally, there is a growing concern with regard to fire safety in tunnels. In May 2014 a truck crashed in the Heinenoordtunnel and a fire erupted. The fire lasted only thirty minutes and was relatively mild as far as tunnel fires go. The question is posed what happens to the Heinenoordtunnel when an extreme fire occurs.

In traffic tunnels without shear reinforcement flexural shear failure is expected. This stems from the general dimensions of traffic tunnels. The roof and floor slabs in traffic tunnels have considerable spans, compared to those of train tunnels. The author expects that in a tunnel such as the Heinenoordtunnel, where shear force is critical, a fire could lead to a different failure mechanism. The increase in temperature could change the stress situation in the roof of the tunnel and lead to shear tension failure or shear compression failure instead. The Heinenoordtunnel is due for large-scale maintenance in 2023/2024, but all these uncertainties warrant further research.

1.2. Research question

The aim of this thesis is to provide insight on the interaction between shear force and fire and how this applies to the Heinenoordtunnel in particular. Additionally, the applicability of a numerical software analysis package to determine the shear capacity is tested. From this follows the research question:

To what degree does fire influence the shear capacity of the Heinenoordtunnel based on numerical analysis?

To answer this question the following sub questions will be addressed:

- To what degree is the size effect of concrete taken into account when modelling in a non-linear finite element analysis program? How accurate is the shear capacity prediction of numerical analysis for deep beams?
- Which parameters are critical for a numerical analysis of the shear capacity?
- How does the numerical model of the Heinenoordtunnel compare to the IBBC-TNO method?

The first and second sub question follow from recent tests at Delft University of Technology (TU Delft). The concrete beams tested at TU Delft are on some levels representative of the roof of the Heinenoordtunnel. This includes concrete strength, reinforcement ratio, and more importantly, effective height. Effective height is directly related to the size effect observed in concrete. By modelling the beams tested at TU Delft valuable information can be gained for improving the numerical model of the Heinenoordtunnel.

With the knowledge obtained from modelling the beam tests, a model of the Heinenoordtunnel will be created. This model does not include a fire load, and is compared to the analysis performed by TNO. This comparison is performed as a means to validate the model. This explains the third sub question.

With the information obtained from modelling the beams in the size effect tests, and the validation of the model of the Heinenoordtunnel, a fire loaded model is analysed. And so, using the sub questions, the main research question can be answered.

The research hypothesis is posed as follows:
The Heinenoordtunnel, while barely passing the requirements in terms of shear capacity in regular loading situations, will fail in shear when subjected to a fire load.

1.3. Scope

The work in this thesis is realized based on two-dimensional analysis. More specifically, two-dimensional analyses in the finite element analyser Atena. The choice for two dimensional analysis stems from research by Sherwood et al. [54]. Where it was found that an increase in width does not provide any significant influence on the capacity per unit of width. As such, a two dimensional analysis is sufficient. While findings may be applicable to other finite element packages or three dimensional problems, these are not explicitly discussed. Spalling is excluded on the basis that spalling of concrete is prevented through the amount of heat resistant cladding applied in the Heinenoordtunnel. Post-fire behaviour is not analysed, as the Richtlijn Ontwerp Kunstwerken only requires tunnels to be able to sustain a 2 hour RWS curve fire, and no cooling trajectory is prescribed.

1.4. Research methodology

A collection of point-loaded beams from the size effect tests at TU Delft will be modelled in Atena. First three “regular size” beams to serve as a baseline, and then two deep beams. The numerical results of these beams are compared to their experimental counter parts and any differences are analysed. This helps answering the first two sub questions. The differences in loading conditions between the beams and the tunnel are considered and its consequences explained. The Heinenoordtunnel is observed in two scenarios. In the first scenario the regular loading is considered, analysing the differences of the numerical model with the IBBC-TNO method. This will help answer the third sub question. In the second model, the tunnel loaded by fire will be analysed. The results of regular loading and fire loading are compared and discussed in order to answer to what degree the fire loading influences the shear capacity of the Heinenoordtunnel.

2 Literature review

In this chapter literature with respect to fire is discussed. This includes the topics of fire development, the effects on fire on reinforced concrete and the different failure modes in fire. Literature pertaining to other topics will be handled when it is introduced. The reason for this is because fire related topics were the biggest unknown when the author started this thesis.

2.1. Fire development

At the fundamental level three elements are required for combustion: heat, fuel, and oxygen. Also known as the fire triangle, see Figure 1. Once these three are present at a sufficient high level an exothermic reaction takes place, meaning that as long as there is fuel and oxygen the fire will sustain itself. Heat is transferred in three ways: conduction, convection, and radiation. Important here is the rate of heat transfer. An average fire loses approximately 70% of its energy (heat) through convection, and 30% through radiation. Despite the fact that only 30% is through radiation, it is a significantly contributing factor, the rate of heat transfer due to radiation is proportional to T^4 [4].

Figure 1: Fire triangle [4]

A fire starts with ignition and is followed by a growth phase. The temperature gradually increases until flashover occurs, greatly accelerating the heating rate. From this point onwards the fire is fully developed which will only start to decay with lower availability of fuel for fuel bed controlled fire or lower availability of oxygen for ventilation controlled fire [5].

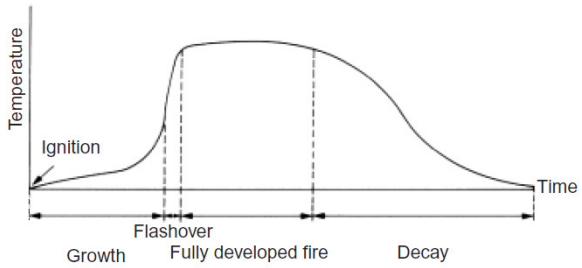

Figure 2: 'real' temperature development due to fire [5]

In the field of fire safety engineering curves have been developed to model the temperature due to a fire over time. A few of these curves will be highlighted here. One thing that all fire curves have in common is that they all start at the flashover point, neglecting the growth phase of the fire. The cellulosic time/temperature curve (ISO 834) is one of the standard fire curves defined in various national standards. Of all the fire curves this curve is considered to have the lowest exposure used in tunnelling practice in terms of rate of heat transfer and thermal stress. It is based on the burning rate of materials found in general building materials and can be described by the following equation [6]:

$$T = 20 + 345 * \log(8t + 1)$$

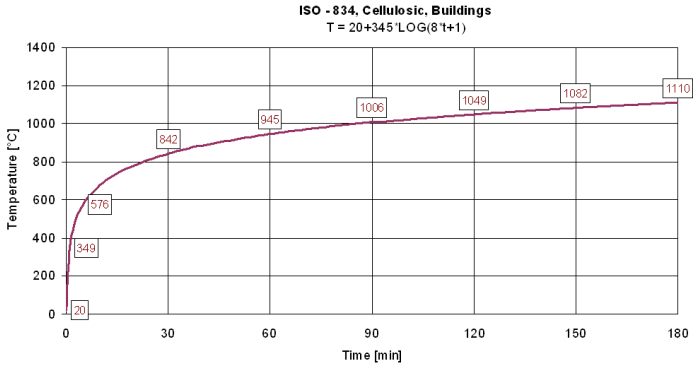

Figure 3: ISO 834 fire curve [6]

In offshore and the petrochemical industry this curve does not hold. Once it became apparent that the burning rate of petrol was much higher than that of, for example, timber, an alternative needed to be developed. From this the hydrocarbon (HC) curve was created, which can be described by the following equation [6]:

$$T = 20 + 1080 * (1 - 0.325e^{-0.167t} - 0.675e^{-2.5t})$$

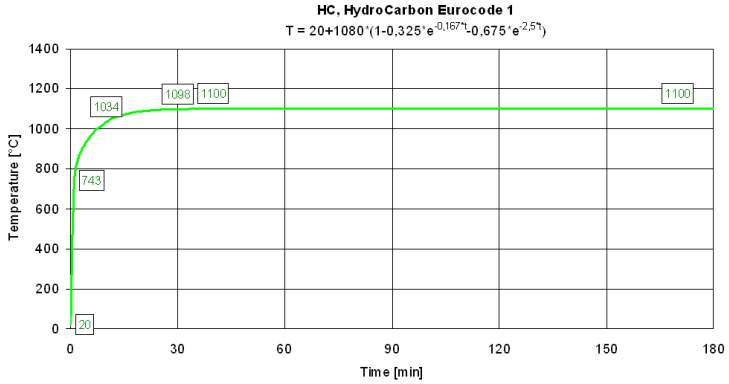

Figure 4: Hydrocarbon fire curve [6]

If Figure 3 and Figure 4 are compared, a clear difference can be observed in rate of heat transfer between the cellulosic and HC curves. Even more severe fire scenarios have been developed. The French regulators ask for a modified HC curve, with a maximum temperature of 1300°C. In the Netherland the RWS curve was developed, which reaches a maximum temperature of 1350°C as shown in Figure 5. The HC curve is based on temperatures that would be expected from a fire in a relatively open space, whereas the RWS curve is based temperatures found when a fire occurs in an enclosed space, such as a tunnel, with little to no heat dissipation into the surrounding atmosphere. The RWS curve was based on the results of tests carried out by TNO in The Netherlands in 1979 and has been reconfirmed in the full scale tests in the Runehamar tunnel in Norway [7]. Initially there was some scepticism towards the RWS curve as recent major fires did not reach RWS levels, the fire in the Mont Blanc tunnel in 1999 for example reached 1000°C. Most of this scepticism has faded however, and the RWS curve has been applied in various countries either as part of the legislation or for specific projects.

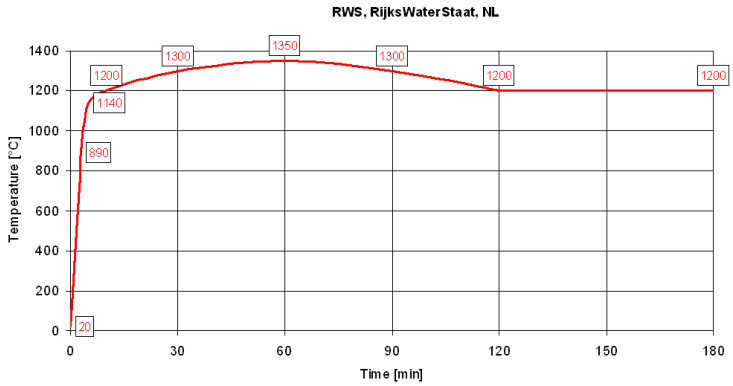

Figure 5: RWS fire curve [6]

The three curves have been combined into a single graph in Figure 6. There are more advanced models to simulate heat such as computational fluid dynamics (CFD) models. These use conservation of mass and energy equations to provide a more realistic scenario of varying temperature. This type of model is primarily used for research, studying the dispersion of smoke and heat, and are in general not used to check the impact of fire onto structural elements [8]. In this thesis the two hour RWS fire curve is used to simulate a fire load.

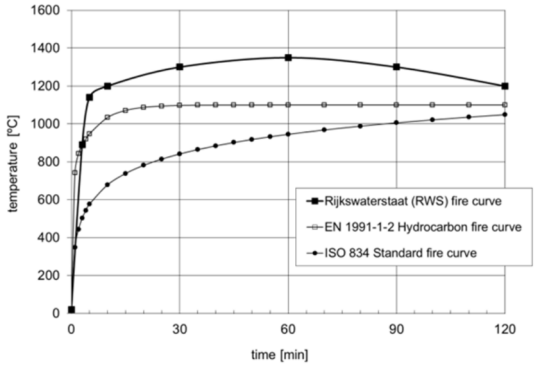

Figure 6: Collection of fire curves [4]

2.2. Effects of fire on reinforced concrete structures

Concrete has some exceptional properties making it a great material in fire. Concrete is incombustible, has low thermal conductivity, thermal diffusivity [9], and more importantly a high thermal massivity [10]. This means that concrete does not burn and the core of the concrete is relatively cool compared to the surface when heated. The interaction between concrete and fire is rather complex however [11]. From a material perspective concrete is a heterogeneous material, containing cementitious paste, aggregates, water, and steel reinforcement. Each having a different response to a thermal load, and due to the difference in temperature the response is also different throughout an entire cross-section.

Khoury [5] describes the concrete response as a steep temperature gradient within the concrete, which causes an increased pore pressure and thermal stresses. When water evaporates it produces a volume increase of 1600 times that of water. The water is confined within the concrete however, restricting the volume increase, which leads to the increased pore pressure. This increased pore pressure in combination with the thermal stresses lead to a deterioration of the mechanical properties in regions with elevated temperatures and potentially (explosive) spalling of concrete.

An increase of the temperature of concrete changes its behaviour on various levels. These changes can be traced back to physicochemical changes (reaction of physical properties on chemical processes, see Figure 7) in the cement paste and in the aggregate and are affected by factors such as the rate of heating and applied loading [9]. Additionally, the behaviour depends on the type of cement paste, the type of aggregate, the bond region, and the interaction between them. As such, there is no fixed reaction for concrete, but rather for a specific concrete type [5]. For this reason there are seemingly conflicting statements in literature with regards to at which temperatures certain reactions happen.

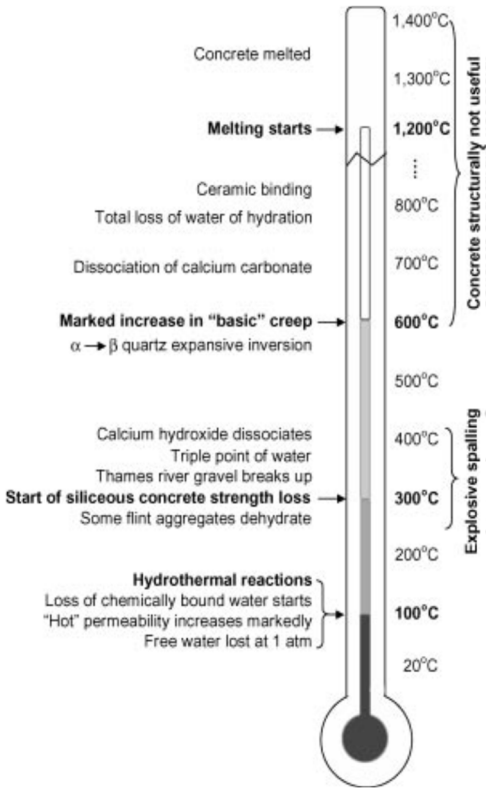

Figure 7: Simplified presentation of physicochemical processes in concrete [5]

In general concrete starts to lose strength from 80 to 140°C due to liquid water turning into a vapor and the separation of calcium silicate hydrate (CSH) layers. From around 250°C (flint) and 350°C (gravel) certain aggregates start to disintegrate, further reducing the strength and reducing the stiffness of the concrete. Alternatives for these aggregates are basalt and granite, which do not disintegrate at these lower temperatures [5]. Around 400°C the calcium hydroxide (CH) in the cement starts to dehydrate, which generates water vapor and greatly reduces the strength of the concrete [11]. This could be one of the reasons RWS prescribes a maximum concrete temperature of 380 °C in concrete tunnels [12], more on this in paragraph 2.4. Khoury [5], amongst others, provides more information with regard to concrete reactions at higher temperatures, see Figure 7, but these are not as relevant for this thesis due to the maximum concrete temperature criteria provided by RWS. With regard to steel strength as a consequence of increased temperature, the performance of steel is generally better understood and the steel strength for a specific temperature can be reasonably predicted. It is generally known that steel reinforcement needs to be protected from temperatures over 250 to 300°C, because it is known to exhibit so called 'blue brittleness' between 200 and 300°C [11], substantially decreasing the ductility of the steel. It is likely that Rijkswaterstaat prescribes a maximum reinforcement steel temperature of 250°C [12] for this reason.

Some of the changes in the material properties listed above are irreversible, meaning that after the fire has been extinguished and the concrete has cooled down there are permanent changes in the material properties. As a result the residual strength of the concrete is reduced despite the fact that there is possibly no visible damage. While post-fire behaviour is not considered in this thesis, it might potentially be a significant factor on the performance of concrete as shown by Wetzig [13] in a test where the concrete sample survived a fire load for two hours, but in the cooling phase it collapsed explosively. It should also be noted that this cooling phase does not start immediately. There is a lagging effect, causing the temperature of the construction to rise even after the fire has been extinguished [12]. However, this could be considered an exception to the rule. There is no official cooling trajectory for the RWS fire curve, and there are no official requirements set with regard to post-fire behaviour other than that the tunnel needs to remain in a repairable state.

A special note is made of spalling, this is a phenomenon where layers or pieces of concrete break off of a concrete element during heating [14]. As a result (part of) the cover of reinforcement is lost, reducing the cross-section of the concrete and exposing the reinforcement to high temperatures, quickly reducing the strength of the reinforcement and often incurring structural failure [11]. Spalling is a very complicated issue, it has been noted to occur from anywhere in the range of 200°C and up. It depends on various material properties, such as moisture content and aggregate type, and in practice empirical evidence is always needed to assure a specific concrete mix does not spall. Modelling of spalling is becoming more promising [15], it will however take a while before this becomes a common practice in fire safety design. Inclusion of polypropylene (PP) fibres in the concrete mixture is proven to have a positive effect on the spalling behaviour of concrete, severely limiting the depth of the spalled concrete layer however at the expense of the workability of the concrete [15]. PP fibres help reducing the impact of spalling but there is no way to completely eliminate it, only the likelihood of spalling occurring and its severity can be lowered [5]. One of the common practices used to help prevent spalling is the application of heat-resistant cladding.

Figure 8: Spalling without (left) and with (right) inclusion of PP fibers in the mixture [15]

Guidelines for modelling of concrete at elevated temperatures are provided in Eurocode 1992-1-2 [19] among others. These guidelines include graphs and tables list changes in concrete and steel properties at elevated temperatures. An overview of the used graphs for modelling the heated concrete is provided in paragraph 5.2. The Eurocode is less insightful when modelling failure of concrete structures at elevated temperatures. General statements are made with regard to so-called advanced calculation methods (methods for simulating

the behaviour of structural members, parts of the structure or the entire structure). These include statements such as “The method should include calculation models for the determination of the thermal response and the mechanical response” [19], stating that the temperature dependent properties and effects of thermally induced stresses and strains should be considered.

More thorough information is provided for example in fib Bulletin 38 [8] and 46 [10]. The calculation methods for thermal analysis are split in three distinct categories based on their complexity. These are the “simplified calculations based on limit state analysis”, the “thermo-mechanical finite element analysis”, and the “comprehensive thermo-hydro-mechanical finite element analysis”. The first method based on limit state analysis is an analytical method to check fire resistance, and is also covered in the Eurocode. The second method, the thermo-mechanical finite element analysis, is the type of calculation performed by most numerical programs. Here, mechanical and thermal analyses are conducted ‘separately’. Thermal analysis is performed and used as input for the mechanical analysis to produce the stresses and strains for the structure [8]. There is no interaction between the two analyses, and moisture effects are not included. The majority of performance based software packages uses this method, and is also the method used in this thesis. In the third method the analyses are integrated and moisture effects are included. This method would for example be capable of predicting spalling. This method is mostly used in research rather than the assessment of structures, as the simpler methods provide adequate results for the analysis of structures subjected to fire.

2.3. Failure modes in fire

Various types of failure need to be considered when evaluating the fire resistance of a concrete structure. Which failure mode occurs depends on several circumstances including, but not limited to, the loading situation, temperature, rate of heat transfer, and the type of structure. The types of failure are:

- Bending failure
- Buckling failure
- Anchorage/Bond failure
- Shear or torsional failure
- Spalling failure

Bending (flexural) failure is the most common failure type for beams and one-way slabs [8]. Rupture of the reinforcement can occur for the sagging bending moments due to the reduced tensile strength of the reinforcement [9]. Buckling failure usually occurs for walls and columns. Due to the increased temperature the strength of concrete decreases, as well as the modulus of elasticity leading to a reduced buckling strength. Anchorage failure is usually associated with concrete tensile failure, however it is generally not considered to be governing in structures without prestressing. This is because there is usually sufficient anchorage for reinforcement, for example by bending the reinforcement at the ends. Bond failure for reinforced concrete could occur when heating reduces the bond strength between steel and concrete. Shear or torsional failure in concrete is influenced by concrete tensile strength, but is poorly defined experimentally [11]. In fib bulletin 38 [8] it is stated that shear or torsion failure is generally not governing for the behaviour of fire exposed concrete structures, because shear forces are transferred near the centre of the cross-section, which is relatively cold. It can still occur however, especially in structures without shear reinforcement. The elevated temperature in concrete leads to a reduction of the shear capacity, because of the change in concrete tensile strength. Determining shear failure in fire is rather complex due to is due to limited experimental experience compared to bending failure and the more brittle behaviour requiring consideration of thermal deformations [8]. Spalling failure has been mentioned earlier, while not a structural failure in itself, a severe reduction in cross-sectional area can lead to other failure modes such as bending failure or bonding failure.

Of these five failure modes two are deemed most relevant for this thesis, namely bending failure and shear failure. Bending failure being the generally assumed mode of failure and shear failure being the failure mode to be proven to more relevant than generally assumed. Buckling failure is not an issue as the critical cross-section is located in the roof of the tunnel, rather than in the walls. Anchorage failure is not considered governing as the considered tunnel is not prestressed, and the anchorage length of the reinforcement is reasonably long. Bond failure is particularly plausible for smooth reinforcement bars, however only ribbed bars are used in the thesis. And spalling failure is not considered as it is assumed spalling is prevented by the use of heat-resistant cladding.

There are three types of shear failure that can be considered, namely shear tensile failure, flexural shear failure, and shear compression failure. Of these three flexural shear failure is the type of shear failure expected in tunnels, it occurs in locations with high bending stresses. Flexural shear failure follows from a critical inclined crack, originating from a flexural crack. This crack eventually develops branches in the compressive zone and along the rebar. Once both these branches are developed the concrete loses its capacity and fails. Of the two other shear failure types compression failure is most likely to occur. This failure type can be observed when the compressive force is larger than the maximum shear strength of the concrete. Shear compression failure is most likely to occur close to the supports. Shear compression failure develops similarly to flexural shear failure, however a compressive strut is formed. This allows the concrete to retain its capacity and sustain a much higher load.

When considering the shear resistance there have been various calculation methods in the past. The Eurocode currently provides normative design resistance verification procedures, however a special note is made of the TNO IBBC method. In 1976 the Institute TNO for Building materials and Building Construction started development of a calculation method specifically for shear capacity in concrete plates. The cause for starting this research was a change in normative codes in the Netherlands, the new codes (VB 1974) meant that suddenly shear reinforcement was required in tunnel cross-sections where this was previously not necessary. However these new codes did not take several factors into account, such as a scaling effect for the height or the slenderness of the construction. Additionally, the calculation methods during those years were almost exclusively based on three or four point bending tests, while information regarding uniformly distributed loads were desired.

The research of TNO provided a calculation method that takes six defining parameters into account that influence the shear capacity of concrete. These parameters are concrete strength, the percentage of longitudinal reinforcement, the ratio of moment to shear force, the normal force, the shear reinforcement, a uniformly distributed load, the static indeterminacy, and the size effect (or scale factor). Especially the last three of these parameters were rarely considered in prior calculations [1]. With these both failure by shear compression and diagonal tension are considered. The result is a calculation method that is able to provide better insight in the shear behaviour of reinforced concrete slabs. Full insight into the actual calculation process with the IBBC method will be provided in paragraph 2.5.

Besides visible damage inside a tunnel due to fire there is also damage that cannot be seen, namely outside the tunnel. The large temperature gradient created during a fire results in (restrained) deformation of the roof and walls of the tunnel. This might result in cracks at the outside of the tunnel as shown in Figure 9. These cracks are rather problematic, as observing and repairing them is practically impossible [16].

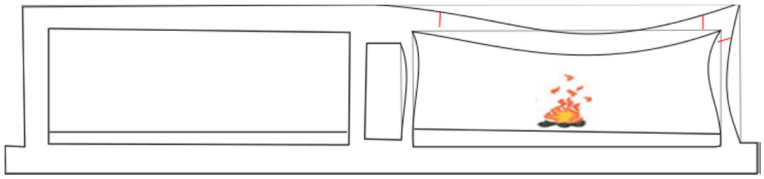

Figure 9: Deformations and outside cracks due to fire [16]

2.4. Research needs

While there has been a lot of separate research in the past decades on the topics discussed in this thesis, there are still several gaps in our knowledge. This is because the problem itself is very specific and complex. There is a significant database of experiments on shear failure in beams without shear reinforcement. However, if that data is filtered on the appropriate concrete strength, beam height, or load condition, the amount of available data quickly dwindles. In fact, there is no experimental data on beams that are comparable to the Heinenoordtunnel based on these three criteria alone. In addition, there is very minimal research addressing the shear capacity of concrete at an elevated temperature. Most of the research on the performance of structural concrete elements loaded by fire is focused on bending.

Other than the lack of referential data, there is also a gap in the understanding of the data that has been obtained. The size effect of concrete, a relative reduction in capacity as the height increases, is a characteristic that we still do not fully grasp. At this point in time there is not a single analytical or numerical method that is able to consistently provide accurate shear prediction results for beams heights over 1 meter.

While there has been some degree of research on individual aspects such as size effect and temperature, the interaction has not been researched to the authors' knowledge.

2.5. The Heinenoordtunnel

This thesis focusses specifically on the Heinenoordtunnel. The Heinenoordtunnel is an immersed tunnel under the river "Oude Maas" as part of the highway A29 near Barendrecht and was opened in 1969. Originally the tunnel consisted of two tubes with two highway lanes and a separate lane for slow traffic, but in 1991, due to capacity problems, the slow lane was transformed into a third highway lane and a second tunnel was constructed for slow traffic (2e Heinenoordtunnel). The cross-section shown in Figure 11 is from the original tunnel. The tunnel is due for large-scale maintenance in 2023/2024.

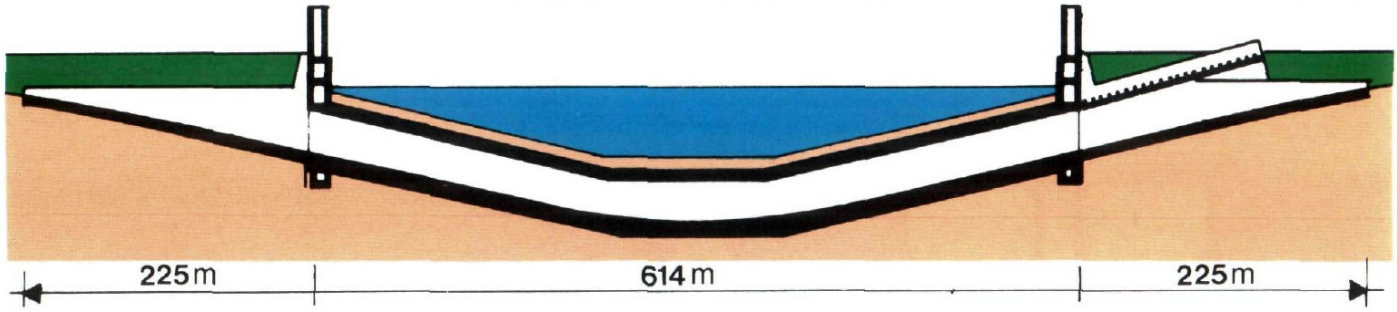

Figure 10: Longitudinal cross-section of the Heinenoordtunnel [21]

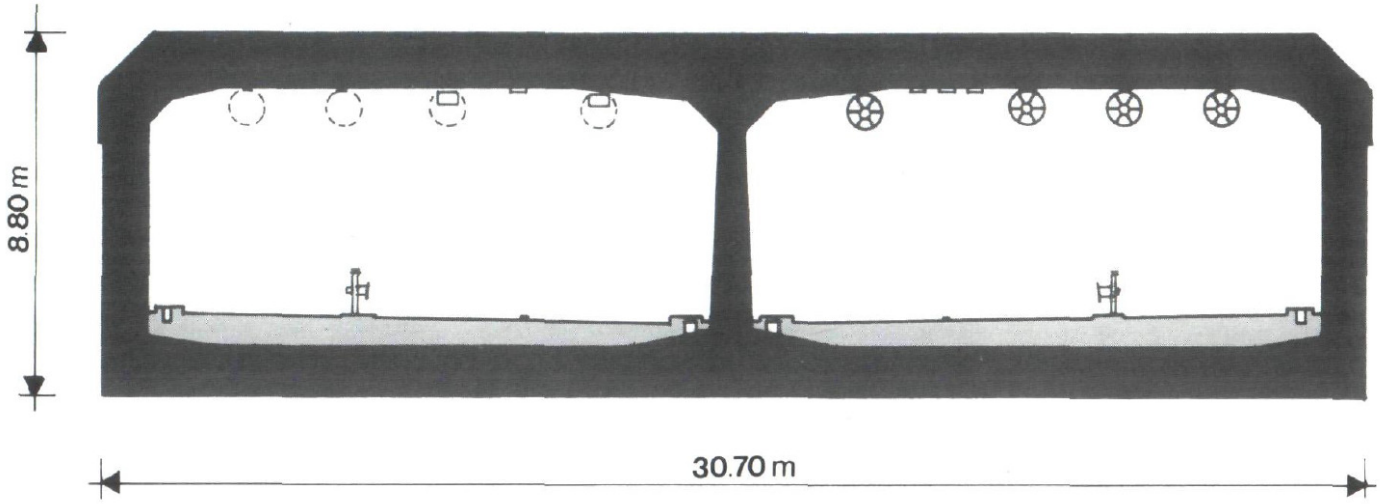

Figure 11: Cross-section of the Heinenoordtunnel before 1991 [21]

The Heinenoordtunnel was designed in accordance with GBV 1962 (Gewapend beton voorschriften), which was normative at the time it was constructed. However, the GBV differs significantly from the norms that succeeded it, especially in determining the amount of shear reinforcement required. As a result, the Heinenoordtunnel does not have any shear reinforcement. However, all the norms that followed the GBV state that the tunnel needs shear reinforcement in order to have sufficient shear capacity. This is one of the cases that eventually led to the TNO IBBC method [1].

It should not come as a surprise that the shear force check is the governing check in terms of structural safety. The question remains however, whether or not this is also the case when a fire load is applied. The Eurocode states in Annex D of Eurocode 1992-1-2 that shear failures due to fire are very uncommon [19] and by doing this study it can be checked if this holds even for a tunnel such as the Heinenoordtunnel, where no shear reinforcement is presented and shear capacity is an issue.

Figure 12: 2nd Heinenoordtunnel (left) and Heinenoordtunnel (right) [22]

2.6. IBBC-TNO method

The IBBC-TNO method has been mentioned a few times already in this thesis. As a way of reaffirming the numerical results obtained, some analytical checks will be performed using this method. The IBBC-TNO method, how it is used and some of the method's intricacies are described in this paragraph.

The IBBC-TNO method considers the following parameters to be influential on the shear capacity: the concrete quality, the longitudinal reinforcement ratio, the moment to shear force ratio, the dimensions of the concrete, and the normal force [1]. It is also possible to use the method for concrete with shear reinforcement, in which case the shear reinforcement becomes a sixth parameter, but this is not used in this thesis. For each of these parameters a short description is given as to why these are taken into account. The concrete quality is an obvious parameter, it is clear that the shear capacity is dependent on the strength of the concrete, both in compression and in tension. An increase in longitudinal reinforcement leads to an increase in shear capacity. As this causes a reduction in the crack width and an increase in the concrete compression zone. This means a greater amount of shear force can be transferred by aggregate interlock and through the uncracked concrete zone. The moment to shear force ratio reflects notion that failure occurs with a combination of moment and shear force. The distinction here is made that a situation with a point load has a shear slenderness, which is a constant value, and a situation with a uniformly distributed load has the aforementioned moment to shear force ratio, which is not a constant value. The dimensions are relevant due to the fact that an increase in height leads to a relative decrease shear capacity, also known as the size effect. Lastly, an increase normal force (compression) leads to an increase in shear capacity. Inversely, an increase in tensile normal force leads to a decrease of the shear capacity.

The IBBC-TNO method considers the two most prevalent shear failure modes, diagonal tension failure (also known as flexural shear failure) and shear compression failure [1]. Flexural shear failure is characterised by a brittle behaviour, at a certain point in loading the critically inclined shear crack propagates into the concrete compression zone and the shear capacity is reached at that location. Shear compression on the other hand is not such a brittle mechanism. Failure occurs after full development of the cracks. As the load increases so

does the crack width, reducing aggregate interlock and dowel action, forcing the uncracked concrete to transfer all the shear force. At a certain point the concrete reaches its capacity and crushing of concrete occurs at the crack tip.

There are six empirically determined formulas for the shear capacity against flexural shear failure, denoted as τ_{11}, and the shear capacity against shear compression failure, denoted as τ_{12}. Of the six formulas there are two which provide a design value and four which provide an average value of the shear capacity. The experiments on which the formulas are based contain various load- and support configurations, both point loaded and uniformly distributed loads are considered, and both simply supported and continuous beams have been tested. For every cross-section the nominal shear capacity, τ_1, is determined and checked with the shear stress. In general the nominal shear capacity is equal to τ_{11} unless shear compression failure is possible. The IBBC-TNO method assumes this is only possible when there is a compressive force in the concrete compression zone, usually coming from a (clamped) support.

The design formulas for τ_{11} and τ_{12} are as follows:

$$\tau_{11} = 0.17\left(1 + 0.01\, f_{ck,cube}\right)(1 + \omega_o)\left(1 + 1.12\left|\frac{1}{\lambda_x}\right|\right)\left(\frac{d}{d_0}\right)^{-\frac{1}{4}}\left(1 + 0.12\left|\frac{N_d}{bd}\right|\right)$$

$$\tau_{12} = 0.45\left(1 + 0.06\, f_{ck,cube}\right)(1 + \omega_o)\left(\left|\frac{1}{\lambda_x}\right|\right)\left(\frac{d}{d_0}\right)^{-\frac{1}{4}}\left(1 + 0.045\left|\frac{N_d}{bd}\right|\right)$$

With

$f_{ck,cube}$ = characteristic cubic compressive strength of concrete in N/mm²
ω_o = longitudinal reinforcement ratio in %
λ_x = $\frac{M_x}{V_x d}$ = moment to shear force ratio for a specific location
d = effective height in mm
d_0 = reference height set to 300 mm
N_d = normal force from loading in N

These two formulas are set to provide an absolute minimum shear capacity. Another set of formulas was created to represent average shear capacity values. The formulas for average shear capacity are split specified for reinforcement ratios lower than 1% and reinforcement ratios greater than or equal to 1%.

For $\omega_o < 1\%$:

$$\tau_{11} = 0.263\left(1 + 0.0125\, f_{cm,cube}\right)(1 + \omega_o)\left(1 + 1.213\left|\frac{1}{\lambda_x}\right|\right)\left(\frac{d}{d_0}\right)^{-\frac{1}{4}}\left(1 + 0.12\left|\frac{N_d}{bd}\right|\right)$$

$$\tau_{12} = 0.739\left(1 + 0.06\, f_{cm,cube}\right)(1 + \omega_o)\left(\left|\frac{1}{\lambda_x}\right|\right)\left(\frac{d}{d_0}\right)^{-\frac{1}{4}}\left(1 + 0.045\left|\frac{N_d}{bd}\right|\right)$$

For $\omega_o \geq 1\%$:

$$\tau_{11} = 0.455\left(1 + 0.0125\, f_{cm,cube}\right)(1 + 0.156\, \omega_o)\left(1 + 1.213\left|\frac{1}{\lambda_x}\right|\right)\left(\frac{d}{d_0}\right)^{-\frac{1}{4}}\left(1 + 0.12\left|\frac{N_d}{bd}\right|\right)$$

$$\tau_{12} = 1.386\left(1 + 0.06\, f_{cm,cube}\right)(1 + 0.067\, \omega_o)\left(\left|\frac{1}{\lambda_x}\right|\right)\left(\frac{d}{d_0}\right)^{-\frac{1}{4}}\left(1 + 0.045\left|\frac{N_d}{bd}\right|\right)$$

With

$f_{cm,cube}$ = mean cubic compressive strength of concrete in N/mm²

There are a few details included in the method to more accurately represent the actual shear capacity. In the case of a clamped support a part of the load close to the clamped end is directly taken by the support. This is taken into account by reducing the applied shear force over a distance x_u from the support, which depends on the moment M_s and shear force V_s at the clamped support, also see Figure 13.

$$x_u = 0.5\frac{M_s}{V_s}$$

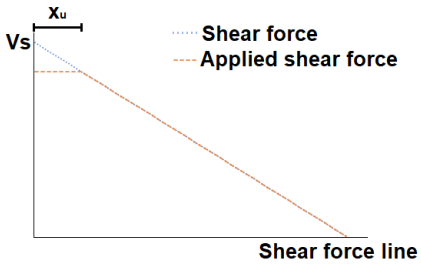

Figure 13: Normative shear force line

Experiments [1] have shown that when the moment shear ratio λ_x becomes smaller than 1, the shear capacity does not actually increase. This is implemented by limiting the shear capacity to the τ_{12} value for $\lambda_x = 1$. This is located around the moment zero points in the moment distribution, which would otherwise lead to an asymptote, suggesting infinite shear capacity. The observed failure mechanisms, flexural shear failure and shear compression failure, rely on a combination moment and shear force. Hence why the shear capacity against these two mechanisms is high for the moment zero points.

Lastly, in the case that the observed structure has a voute the shear resistance against compressive shear failure (τ_{12}) needs to be reduced depending on the angle of the voute ϕ. This does not necessarily mean that the actual resistance is reduced, as the shear stress is also reduced in this area. The τ_{12} is reduced by a factor (1-tan(ϕ)) up to a maximum of 0.67 [1].

3 Numerical analysis of size effects in reinforced concrete beams

3.1. Introduction

Throughout 2018 and the start of 2019 tests conducted in the Stevin laboratory of Delft University of Technology showed unexpected results for the shear capacity of reinforced deep concrete beams. The beams that were tested failed much sooner than anticipated by any codes, and displayed erratic failure modes. These results are considered to be relevant for the Heinenoordtunnel, as the specimen height, reinforcement ratio, concrete strength, and expected failure of some of the beams represent the situation of the roof of the tunnel, see Table 1.

	h [mm]	**d** [mm]	$\boldsymbol{\rho}$ [%]	$\boldsymbol{f_{c,cube}}$ [MPa]	**Exp. failure** [-]
Heinenoordtunnel*	1180	1094	0.8	74	Flex. shear failure
Deep beams	1200	1150-1160	0.27-1.14	78-87	Flex. shear failure

Table 1: Differences Heinenoordtunnel and deep beam tests. *: More information in chapter 4

As such, it could mean that the tunnel has a lower capacity than calculated in the past. Considering not only the accuracy of any predictions made in this thesis, but also the upcoming renovation of the Heinenoordtunnel it would be prudent to investigate size effects further. Some samples of the beams tested in the Stevin laboratory are modelled in Atena to help explain the discrepancies in the experimental results. Additionally, in doing so the material settings can be validated for the eventual implementation in the numerical model of the Heinenoordtunnel.

3.2. NLFEM models

In the upcoming paragraphs the various Atena models are described. Before the samples from the recent tests are modelled a reference needs to be set, determining the performance of Atena in relation to experimental results for beams without any size effect. This has been done by modelling some of the earlier tests carried out in 2015 by Yang et al. [23] in their research on the transition between flexural and shear failure of reinforced concrete beams without shear reinforcement. The tests carried out in 2015 are essentially a precursor to the deep beam tests.

3.2.1. Model description (h = 300 mm)

The beam series considered in this reference consists of beams with a height $h = 300\ mm$, concrete class C65, and B500 rebar. The differences between the specimen within the series are the actual height (slight variation between $h = 304.5\ to\ 311.0\ mm$), rebar configuration (from 1Ø10+2Ø16 to 3Ø20), and shear slenderness (from $a/d = 2.18\ to\ 5.57$). In total three beam specimen are considered, the dimensions of which can be found in Figure 14 and Table 2. Also listed in Table 2 is load $P_{u,exp}$ for which failure occurs. An in-depth view into the material parameters is provided in paragraph 3.2.3.

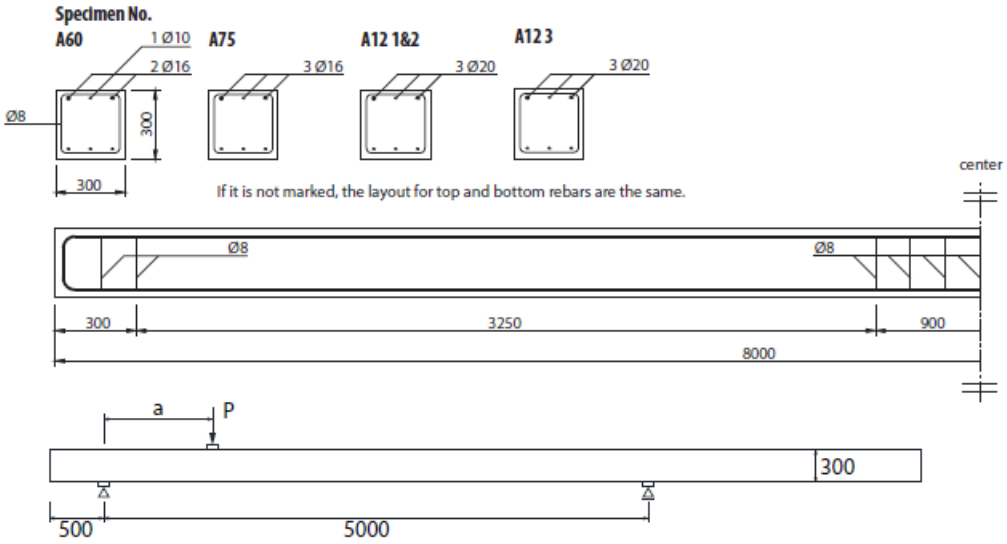

Figure 14: Reinforcement layout A-series [23]

Specimen	h [mm]	d [mm]	a [mm]	a/d [mm/mm]	ρ [%]	$f_{c,cube}$ [MPa]	$P_{u,exp}$ [kN]
A122	305.5	270.5	1000	3.7	1.16	78.5	152.3
A123	305.0	270.0	1000	3.7	1.16	79.2*	136.5
A75	307.5	274.5	800	2.9	0.73	78.5	106.7

Table 2: Specimen characteristics [23] *: no cubes were tested for this concrete batch, average strength of all other casts in used instead.

At first only two models were considered in Atena, consisting of the standard 2D plane stress material model SBeta with either a fixed smeared crack model or a rotating smeared crack model. However, after some initial results the choice was made to include a different material model and focus on a fixed smeared crack model. This second material model was added, since the model allowed is supposed to be a more realistic representation of the concrete. The second material model is the so-called “3D Non Linear Cementitious 2” model (NLCEM), which is a fracture-plastic constitutive model, combining constitutive models for tensile (fracturing) and compressive (plastic) behaviour [24]. The fixed crack model might result in higher limit failure loads (compared to a rotating crack model), due to a phenomena called stress-locking [25] [26], but provides better, more realistic crack patterns than those found with rotating crack models. This can be explained as follows: a crack in concrete forms when the maximum principal stress in a point exceeds the tensile strength of concrete. In a fixed crack model the orientation of this crack is defined by the principal stress orientation, and this crack orientation remains unchanged even if the principal stress changes direction and exceeds the tensile strength in the new direction. In reality the same is true, once a crack is formed the crack orientation is locked. The principal stress can change in orientation, due to aggregate interlock and dowel action of the reinforcement [50], if in this case the tensile strength is exceeded once more the rotating crack model would result in a rotated crack, and the fixed crack model would result in a stiffer response (which could lead to a higher failure load) [38].

In crack models there is also a distinction between discrete and smeared crack models. Discrete crack models are based on cracking along predefined mesh edges, whereas in smeared crack models cracking is spread over the area that belongs to an integration point. The advantage of the smeared crack model is that cracks can occur anywhere in the mesh. In this work only smeared crack models are considered, as the crack location is not known beforehand.

The actual model in Atena can be observed in Figure 15. The model consists of quadratic quadrilateral elements. A mesh refinement has been applied in the area where cracking occurs, as a means to greatly reduce calculation time, the mesh size is a 15th of the height at 20 mm. The purple markers in the model are so-called monitoring points, measuring the forces (upper monitoring point) and the displacement (lower

monitoring point) in order to represent the measuring setup of the actual tests. The choices made with regard to material properties are described in paragraph 3.2.3.

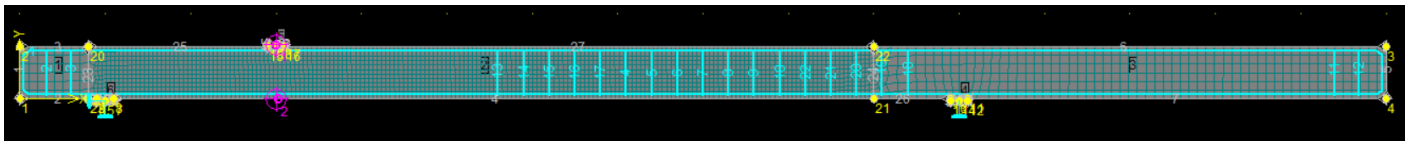

Figure 15: Atena model of A122

3.2.2. Model description (h = 1200 mm)

The latest series of tests conducted in the Stevin laboratory, which were concluded in May 2019, consists of various deep beams. This series are different from the A-series due to a beam height $h = 1200\ mm$. The researchers at the Delft University of Technology found the results interestingly enough to organize a shear prediction contest, where analytical and numerical prediction are compared with the experimental results. The beams considered in this contest are modelled and the results are presented in paragraph 3.3.2.

The contest challenges engineers to provide an analytical and numerical solution for two beams, H352 and H123. The dimensions of the two specimen can be seen in Figure 16 and Table 3, the only difference between the two being the longitudinal reinforcement. The beams are simply supported and loaded by a single point load in the middle of the span. Steel plates with the dimension 300x100x10 mm were used at the point load and at the supports. Stirrups are applied in one half of the span to ensure shear failure on the observed side.

Specimen	**h** [mm]	**d** [mm]	ρ [%]	$f_{c,cube}$ [MPa]	$f_{ct,split}$ [MPa]	a_g [mm]	f_{yk} [MPa]	f_{tk} [MPa]
H123	1200.0	1162.5	1.13	86.9	5.7	16	583.9	683.9
H352	1200.0	1165.0	0.36	86.9	5.7	16	583.9	683.9

Table 3: Specimen characteristics for H123 and H352 [27]

Of the two specimen, beam H123 is the most comparable to the beams that are observed in the reference, having a reinforcement ratio of 1.13% and a shear slenderness of 3.88. Similar to the reference two sets of models were analysed for each specimen, one model with the SBeta material and another with the NLCEM material. Choices made with regard to material properties are described in paragraph 3.2.3.

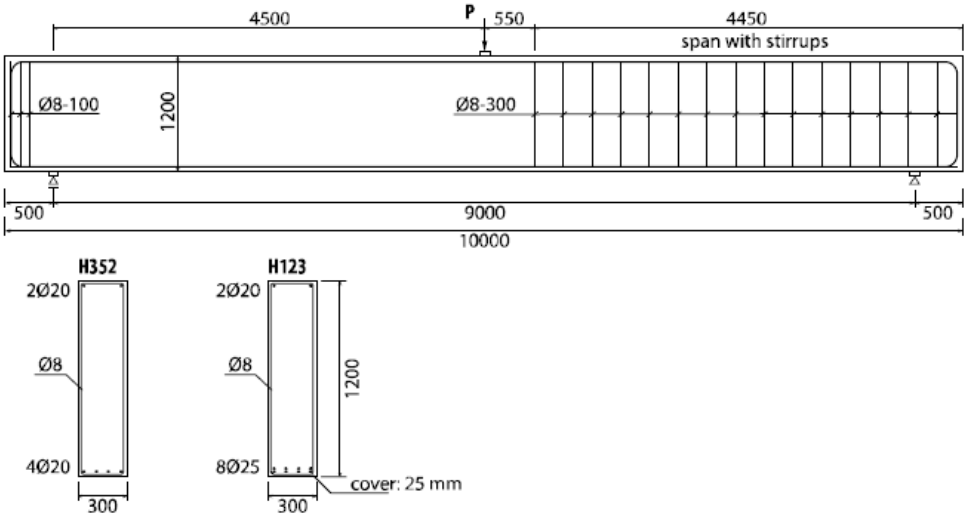

Figure 16: Configuration of test specimen H352 and H123 [43]

In Figure 17 the Atena model of H352 is shown. Once more the model uses quadratic quadrilateral elements. One of the big differences between the H352 and H123 models with the models defined in paragraph 3.2.1 is the mesh refinement. The entire beam has been modelled with a fine mesh. In early testing of the numerical model the application of a small refined area led to large flexural cracks wherever the mesh changed from fine to coarse. It has not been researched what the exact cause is for this effect. It is considered an undesirable side effect, which has been circumvented by applying the same mesh for the entire beam. The mesh size applied is 50 mm.

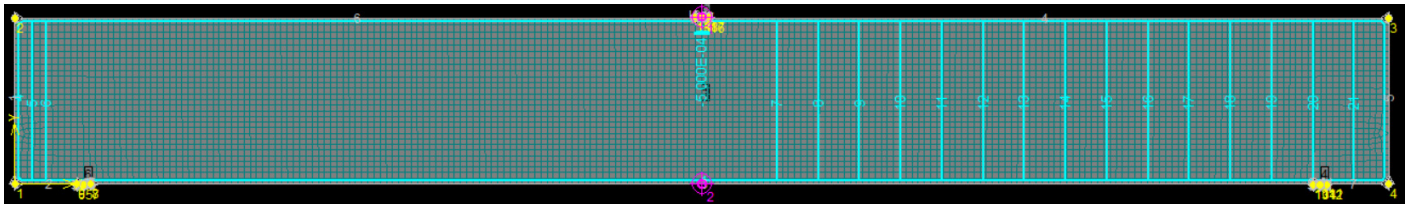

Figure 17: Atena model of H352

3.2.3. Variables in Atena

In the next few paragraphs an overview is given on how the variables in the Atena model have been determined. For each parameter a short description is provided, along with either a formula or static value for the parameter. These parameters are presented in the same order as they are filled in within Atena, divided into five categories: Basic, Tensile, Compressive, Shear, and Miscellaneous. Most of the theory presented here is based on the information as provided in the Atena Theory manual [24].

Basic variables

The Young's modulus (or elastic modulus) E is the mechanical property that defines the stiffness of the material. This property is calculated based on the mean compressive strength of the concrete (f_{cm}) through the following formula:

$$E_c = 0.85E_{ci} = 0.85E_{c0}\left(\frac{f_{cm}}{f_{cm0}}\right)^{0.3}$$

With $E_{c0} = 22000\ MPa$ and $f_{cm0} = 10\ MPa$ [25]. The Young's modulus is reduced by 0.85 to account for initial cracking due to creep, shrinkage, and such as per "Guidelines for Nonlinear Finite Element Analysis of Concrete Structures" [25].

The Poisson's ratio μ is the ratio of transverse contraction and longitudinal extension. This is assumed to be equal to 0.15, regardless of the concrete strength, as per "Guidelines for Nonlinear Finite Element Analysis of Concrete Structures" [25].

The mean tensile strength f_{ctm} of concrete can be derived in various ways. For a compressive cube strength of $60\ N/mm^2$ or higher the following formula is used to calculate the mean tensile strength:

$$f_{ctm} = 2.12 * \ln(1 + f_{cm}/10)$$

Alternatively, the tensile strength can be determined from tests. Usually splitting tests are performed, as these are more easily performed than uniaxial tensile tests. There are however some inconsistencies in the literature regarding the differences in splitting strength and uniaxial strength. The fib Model Code [28] suggests that the concrete tensile strength, as determined from splitting tests, is actually smaller than the uniaxial tensile strength in contrary with national and international codes which all state that the uniaxial tensile strength is between 67% and 95% of the splitting tensile strength. The model code bases these claims on the findings of Malárics, V. and Müller, H. S. [29]. However, considering the vast majority of publications suggest otherwise the conservative assumption is made that $f_{ctm} = 0.9f_{ctm,sp}$.

Concluding the basic material properties is the characteristic compressive strength of concrete f_{ck}. Concrete compressive strength can be calculated with cubes or cylinders, but there is a difference in compressive strength between the two. $f_{ck,cyl}$ is considered to be equal to $0.82 * f_{ck,cube}$ [30].

Tensile variables

The main variable in this category is the fracture energy G_F. The fracture energy is a toughness property and relates to the energy required to cause a crack to develop. By default Atena uses a rewritten version of the formula Vos used [31]:

$$f_t = 1.3 * 0.3 * \left(f_{cyl} - 8\right)^{2/3} \text{ and } G_F = 10 * \left(f_{cyl} - 8\right)^{2/3}$$
$$G_F = 25.64 * f_t$$

There are a few issues with this however, first and foremost Vos used results for G_F obtained by Petersson [32] and approximated those values with the formula given above. Vos then states that his approximation does not seem to give the best fit, but uses it nonetheless for sake of convenience, see Figure 18. This approximation also does not take into account the change in the tensile strength formula for concrete grades higher than C50.

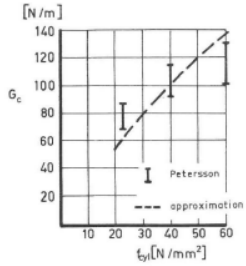

Figure 18: Fracture energy approximation by Vos [31]

The Model Code states that in the absence of experimental data, G_F for normal weight concrete the fracture energy may be estimated as follows [28]:

$$G_F = 73 f_{cm}^{0.18}$$

But this formula does not solve any of the problems mentioned about Vos's approximation. When both formulas are plotted in the same diagram it becomes obvious that if Vos's approximation does not give the best fit for the results of Petersson, then the formula of the Model Code seems even more ill-fitted, overestimating at every point. In Figure 19 both formulas are plotted, the coloured vertical lines are the ranges of fracture energy found by Petersson.

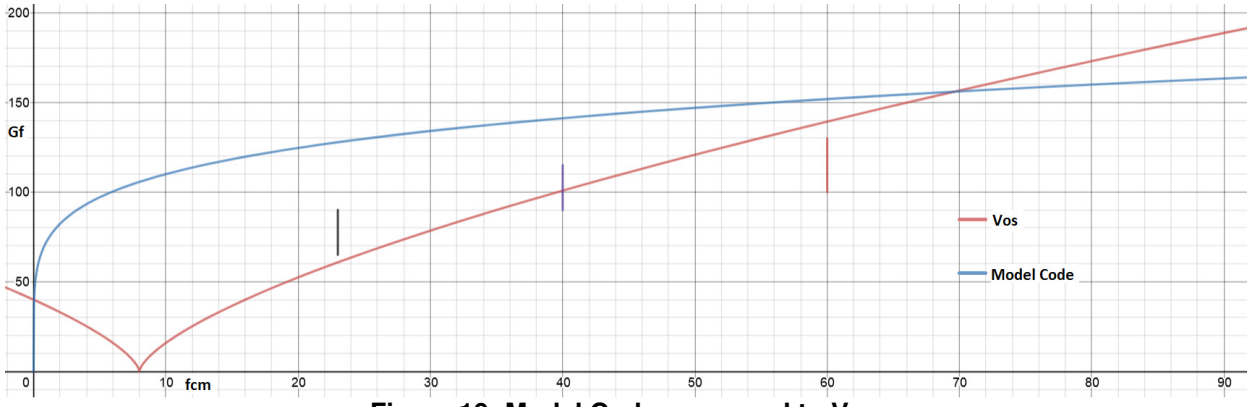

Figure 19: Model Code compared to Vos

However, when the sources of the Model Code are examined it can be observed that the formula for fracture energy is well-fitted to their respective data. In Figure 20 the relation between the compressive strength and the fracture energy is displayed, as provided in fib bulletin 42. There are various problems with fracture energy as a material parameter, most notably that the fracture energy is affected by the size of a structural member [33], meaning that it is not truly a material parameter. This is because curing conditions have a significant effect on the fracture energy and temperature in larger specimen will always be higher than that of a smaller specimen, even if cured in the same environment [32]. Other parameters that influence the fracture energy are the water-cement ratio, the maximum aggregate size, and the age of the concrete [33]. Additionally, there are multiple ways to determine the fracture energy. The best way to do so is from uniaxial tension tests on unnotched specimens, but it is much easier to perform bending tests on notched specimens. The downside of using notched specimens is that this method leads to lower values for the fracture energy [33].

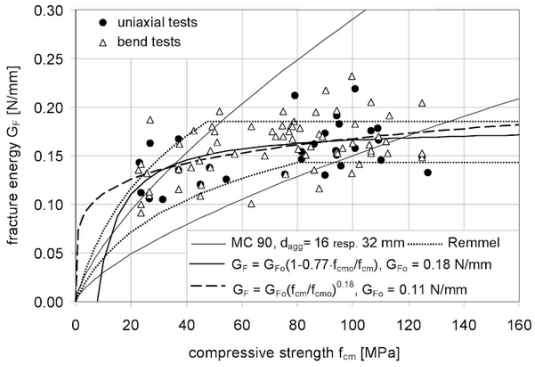

Figure 20: Relation between compressive strength and fracture energy [33]

The solution would be to just test the fracture energy, but this has not been done. The formula provided by the Model Code fits their data well, but there is considerable spread in the test results. The material in Atena will be modelled in accordance with the Model Code, however it would be prudent to check the sensitivity of the model to changes in the fracture energy.

The SBeta material then provides the opportunity to select a tension softening type, for the cementitious material type this is set to an “exponential” tension softening without any ability to change it. While it is listed and shown in Figure 21 as an exponential softening curve, in the theory it is explained that in fact the Hordijk tension softening laws are being applied. There are various other tension softening curves, however the selection in Atena is quite limited. Considering the fact that the cementitious material model uses exponential softening, the same is chosen for the SBeta material model.

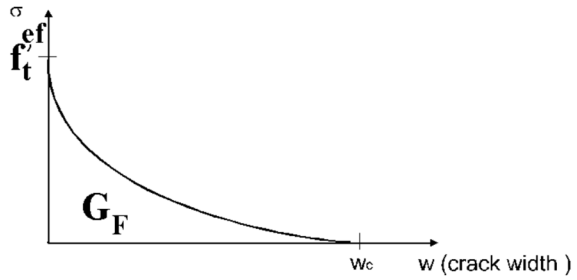

Figure 21: Exponential crack opening law [24]

Tension stiffening factor c_{ts} is a variable in the cementitious material model of Atena. It arises from the fact that in heavily reinforced concrete structures the cracks cannot fully develop and concrete starts to contribute to the steel stiffness [24]. This factor limits the tension softening effect, creating a minimum tensile strength. The fib Model Code [28] recommends a tension stiffening factor c_{ts} of 0.4, however the beams that are tested are not considered to be heavily reinforced and as such, tension stiffening is not taken into account.

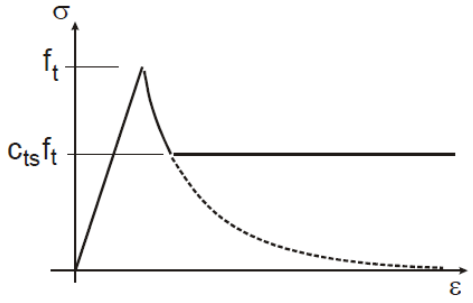

Figure 22: Tension stiffening [24]

Similarly, Atena allows the user to manually define crack spacing. In heavily reinforced concrete the crack band approach tends to lead to an overestimation of the crack width, as crack spacing may be smaller than the finite element size while the crack band approach assumes it is larger than a finite element size [24]. For these cases providing a manual crack space would be useful, however since the beams that are tested are not considered to be heavily reinforced, crack spacing is not defined.

Concluding the tensile category of the variables that can be adjusted in Atena is an unloading factor f_U. This factor determines whether unloading occurs to the origin, parallel to the initial elastic stiffness, or anything in between. As the unloading of the beam is not part of the load step that are being considered, no further explanation is required.

Compression variables

The first compressive variable is the compressive strain ε_c at effective compressive strength f_c^{ef}. Atena uses the CEB-FIP Model code 90 for the compressive stress-strain diagram. The compressive strain can be determined using the following formula:

$$\varepsilon_c = \frac{f_c^{ef}}{E_c}$$

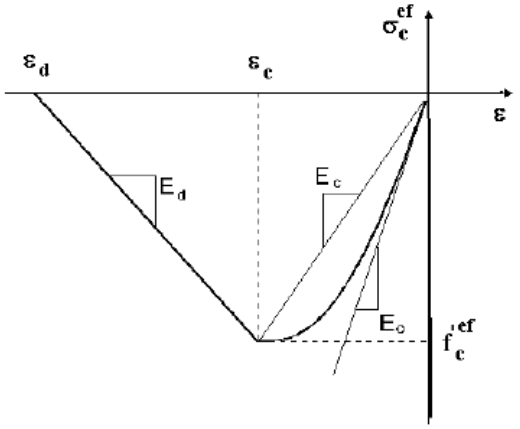

Figure 23: Compressive stress-strain diagram [24]

Next is a reduction of the compressive strength of concrete due to cracks r_C. In experiments by Vecchio and Collins in 1982 [34] a reduction in compressive strength parallel to the cracking direction was found. This reduction depends on the normal strain, with no reduction for zero strain and approaching a maximum reduction for large strains. Atena uses a default value (maximum) of $r_c = 0.8$ based on the work of Dyngeland [35].

$$f_c^{ef} = r_c f_C, r_c = c + (1-c)e^{-(128\varepsilon_u)^2}$$

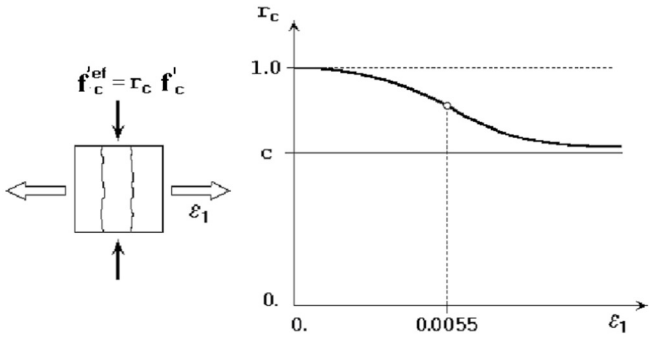

Figure 24: Compressive strength reduction of cracked concrete [24]

For the SBeta material mode two types of compression softening are available, either through a crush band or a softening modulus. The former works based on a critical compressive displacement w_d, a plastic displacement indicating the distance from the point of maximum compressive stress to the end point of the softening curve, see Figure 25. Atena uses a default value $w_d = 0.5mm$ based on the experiments of Van Mier [36]. Alternatively, a softening modulus c_d can be defined. This modulus defines the reduction of the stiffness in the tail-end of the softening diagram, E_d in Figure 23 then becomes $E_d = -c_d * E_c$. The cementitious material model only uses the crush band type of compression softening so that is also applied for SBeta.

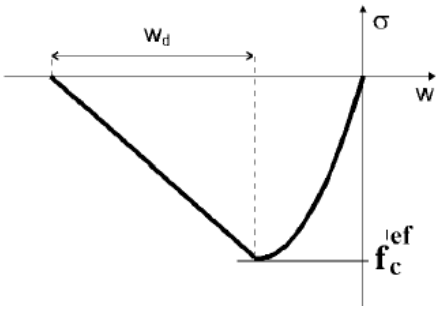

Figure 25: Compression softening, crack band [24]

Shear variables

While not truly a variable, the SBeta material model allows the user to choose between a fixed and variable shear retention factor. Kolmar derived in 1986 [24] how the shear modulus is reduced as the crack opening strain is increased. The variable factor is also dependent on reinforcing ratio but Atena does not consider this and assumes the reinforcing ratio to be 0%. Alternatively, a fixed shear retention can be used. However, as the cementitious material model only allows for a variable shear retention the same is applied for the SBeta material.

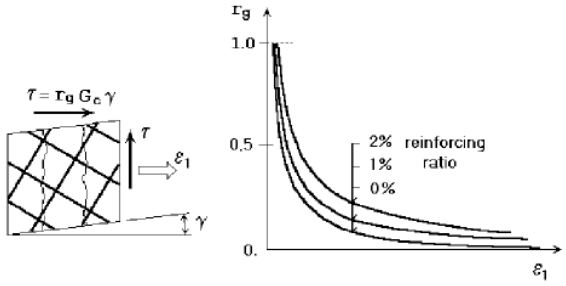

Figure 26: Variable shear retention factor [24]

Next, the SBeta material model defines three different tension-compression interaction, which can be either linear or one of two hyperbolas. In any case, the tensile strength is reduced as the compressive stress increases. This reduction is the least severe for the linear interaction and becomes worse with hyperbola A and even more so with hyperbola B. The linear tension-compression interaction is selected, default in Atena.

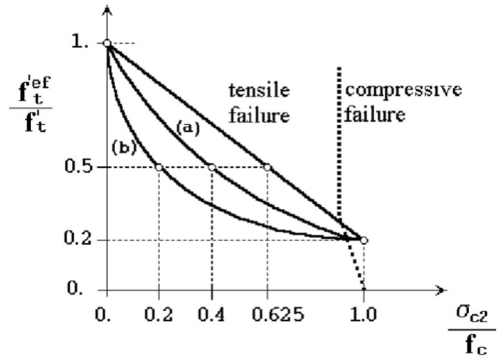

Figure 27: Tension-compression failure function of concrete [24]

The cementitious material model allows for two other variables to be defined, the shear factor s_F and the aggregate size a_g. The latter is a given parameter and is used for calculating the contribution of aggregate interlocking to the shear resisting force. The shear factor is a coefficient that defines a relationship between normal and shear crack stiffness, used in the calculation of the fracturing strains. This factor however appears to be an essential parameter, as described in a paper by Červenka et al. in 2016 [37] about a parameter study for the Toronto shear prediction competition. In the parameter study it was observed that for low shear factor values failure because of splitting cracks along the longitudinal reinforced occurred for some mesh sizes. The default value of the shear factor in Atena is 20, however a factor of 50 was used in the Toronto competition and a factor of 200 was used in the parameter study to ensure splitting cracks along the longitudinal reinforcement did not occur. A shear factor of 50 is used for the models in this work.

Miscellaneous variables

This last category of variables allows the user to define the specific material weight ρ, the coefficient of thermal expansion α, and define the crack model. In the SBeta material model this can be either fixed or rotating, while the cementitious material model asks for a coefficient. This coefficient can be a fully rotated crack model for 0.0, a fixed crack model for 1.0, and any value in between determines the crack direction locking level. This means that the crack direction becomes fixed as soon as the softening law drops, in the case of a coefficient of 0.7, 0.7 times the tensile strength.

The cementitious material model allows for two more variables to be defined, namely the direction of the plastic flow β and the shape of the failure surface. The plastic flow can either be negative, if the material is being compacted during crushing, zero, if the material volume is preserved, or positive, if the material is dilating. The Atena theory states that generally this is set to zero as the plastic flow is not perpendicular to the failure surface. The failure surface in the cementitious material model is based on the Menétrey-Willam failure surface [24], by adjusting the shape of the failure surface it is possible to deviate from the Menétrey-Willam failure surface.

3.3. Results

In the next few paragraphs the results of both the reference and the deep beam series are evaluated. For both series an analytical approach is presented and compared to the experimental results, before the results of the numerical model are discussed.

3.3.1. Evaluation of beam models (h = 300 mm)

First an analytical prediction is presented using the IBBC-TNO method, this gives the option to check the numerical results with more than just the experimental results. The beam is simply supported, as such τ_{11}, the shear capacity for flexural shear failure, needs to be determined, see paragraph 2.5. There are two different types of formulas provided, one for design values and one for average values. The average value should provide a shear capacity more comparable to the experimentally obtained results, both are presented here. These values are then recalculated to point load needed to reach that shear capacity which is presented in Table 4. V_{ud} and $V_{u,avg}$ represent the design and average values for the allowable shear force, which are recalculated to point loads P_{ud} and $P_{u,avg}$ which would cause that shear force. $P_{u,test}$ is the observed failure load in the experiment.

$$V_{ud} = \tau_{11,d} * bh$$

$$\tau_{11,d} = 0.17(1 + 0.01 f_{ck})(1 + \omega_0)\left(1 + 1.2\left|\frac{1}{\lambda_x}\right|\right)\left(\frac{d}{d_0}\right)^{-0.25}$$

$$V_{u,avg} = \tau_{11,avg} * bh$$

$$\tau_{11,avg} = 0.455(1 + 0.0125 f_{cm})(1 + 0.156\omega_0)\left(1 + 1.213\left|\frac{1}{\lambda_x}\right|\right)\left(\frac{d}{d_0}\right)^{-0.25}$$

Specimen	V_{ud} [kN]	$V_{u,avg}$ [kN]	P_{ud} [kN]	$P_{u,avg}$ [kN]	$P_{u,test}$ [kN]
A122	69.5	127.7	86.9	159.6	152.3
A123	69.7	128.1	87.1	160.1	136.5
A75	64.4	129.0	76.7	153.6	106.7

Table 4: Analytical failure load solution

The following things are notable from the analytical solution provided in Table 4. First of all, the average shear capacity of the A75 beam is higher than that of the A122 and A123 beams, despite having less longitudinal reinforcement than the A122 and A123 beams. This can be attributed to the fact that the influence of the reinforcement is rather low in the equation for average shear stress capacity, meanwhile the A75 beam has a lower shear slenderness ratio (a/d = 2.91, rather than a/d = 3.70). Secondly, the scatter does not seem to be insignificant. Both A12* beams are essentially the same, however the difference in the experimentally obtained failure loads, and therefor shear capacity, is notable. An explanation for this could be that the assumed strength of specimen A123, an average of all other tests, is incorrect. While the average values for the shear capacity should provide more comparable results, they seem to overestimate in all three cases. Considering they are average values some variance is to be expected, but this variance seems to be significant. All experimentally obtained results are however greater than the calculated design values. This corroborates that the analytical solution for the design value can be considered a conservative assumption, at least for the observed beam models with a height of h = 300 mm.

The numerical results are presented in Table 5 and Table 6, which are split up in several model variants. Every specimen has a base model, with parameters as described in 3.2.3, denoted as P_{base}. In almost every case this base model has the tendency that the tensile strength, calculated as a part of the tensile splitting strength, is too high. This can be observed in the cracking load for the beams with the base model parameter settings in Figure 28. In order to negate this a second set of models is created with a reduced tensile strength, denoted as $P_{ft,red}$. In general the reduction in tensile strength necessary to match the cracking load observed in the experiments is 45%. A third set of models, $P_{ft,red\&shrinkage}$, is created where in addition to the reduced tensile strength the effects of shrinkage are taken into account. This is done as per Atena theory [24] by reducing the fracture energy in combination with the reduction in tensile strength. This represents the part of the tensile capacity that is exhausted due to the reinforcement restraining the volume change. It is suggested to reduce the fracture energy to 50 to 10% of the original value. In modelling these effects are limited to their

minimum reduction (50%), as a greater reduction leads to unrealistic crack patterns or different failure mechanics in some cases.

Specimen	P_{base} [kN]	$P_{ft,red}$ [kN]	$P_{ft,red\&shrinkage}$ [kN]	$P_{u,test}$ [kN]
A122	161.4	158.2	139.6	152.3
A123	162.2	159.6	136.0	136.5
A75	125.0	126.1	115.7	106.7

Table 5: Numerical failure load solution with SBeta material

Specimen	P_{base} [kN]	$P_{ft,red}$ [kN]	$P_{ft,red\&shrinkage}$ [kN]	$P_{u,test}$ [kN]
A122	160.5	160.8	156.2	152.3
A123	159.8	161.4	155.9	136.5
A75	126.0	127.8	122.4	106.7

Table 6: Numerical failure load solution with NLCEM material

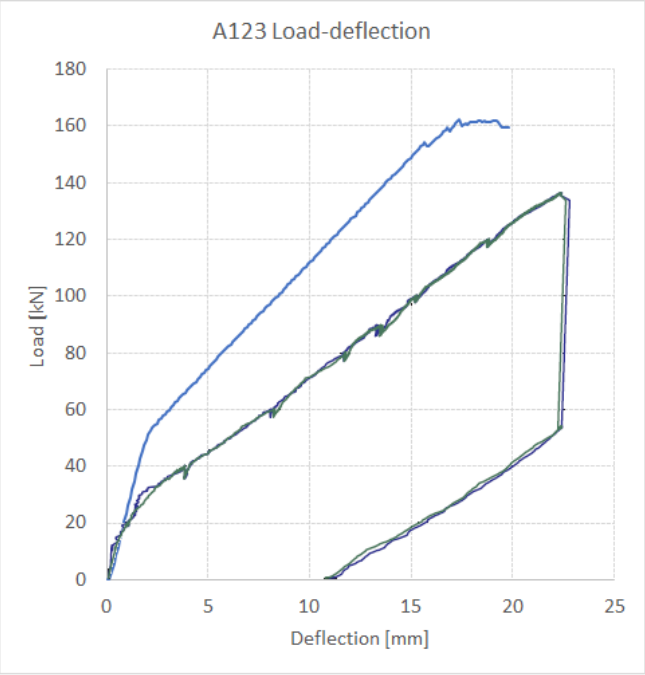

Figure 28: Load deflection of A123 of the SBeta model with base material parameters (top, blue) versus the experimentally obtained load deflection (bottom, green/black)

From Table 5 and Table 6 it can be observed that a reduction of the tensile strength does not seem to correspond with a tangible, consistent, difference in maximum applied load. When comparing the failure loads for P_{base} and $P_{ft,red}$ the change in maximum load is minimal, despite a severe decrease in tensile strength (40% reduction). The addition of shrinkage consistently leads to a reduction in the maximum load, upwards to 14%. The failure load obtained through Atena is all but one case a slight overestimation of the experimentally obtained failure load, all results are within 15% of the experiments. The inclusion of shrinkage seems to produce a smaller impact in the NLCEM material than it does with the SBeta material, and overall the NLCEM models seem to provide more inaccurate results than the SBeta models for the currently observed specimen. Some of the material properties that are only available in NLCEM, such as aggregate size, were unknown and as such, default parameters were used. This could potentially be a reason for higher inaccuracy, but a small parameter study could not find any significant change in failure load by differentiating in NLCEM-specific parameters.

Please note that not all eighteen models are presented and discussed in full detail here, for a full overview of all models see Appendix A. When comparing the load-deflection curves of the experiment and Atena (Figure 29) it can be concluded that some Atena models are stiffer than the actual beams after the concrete becomes

cracked. As a result the maximum deflection is lower in the Atena models than in the experiments. Several attempts have been made to try and replicate the load-deflection curve of the experiment with a reduction of the Young's modulus, however these efforts were fruitless. As the Young's modulus represents the stiffness prior to cracking, or the linear elastic part of the analysis, and the stiffness post-cracking is too high. The reason for these differences could be attributed to the way the experiments were executed. Every specimen was tested multiple times, strengthened in between. However, as concrete cracks its stiffness reduces. This is backed up by some experiments where the load-deflection curve is a straight diagonal line without any notable bends or drops indicating that the tensile strength has been reached and actual cracking occurs, see Figure 30. Alternatively, one could argue that this is purely a result of the chosen crack model. A fixed smeared crack concept is used in the analysis, in these models fracture occurs when the principal stress in a point exceeds the tensile strength. The orientation of the crack remains fixed throughout the loading process. The principal stress can change direction however, due to aggregate interlock and dowel action of the reinforcement. In this new direction the principal stress can exceed the tensile strength again, in which case the numerical response will be stiffer than the experimental response [38].

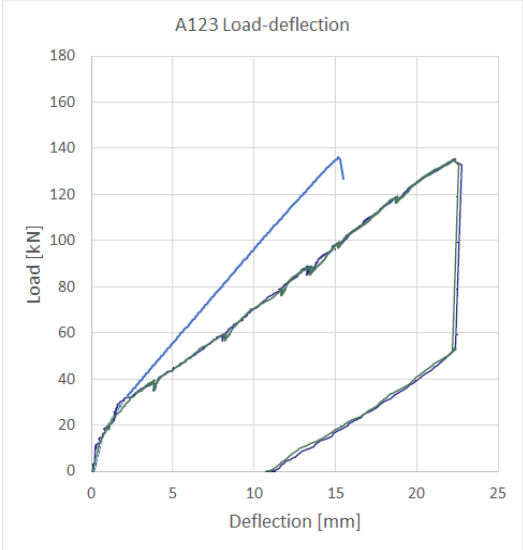

Figure 29: Load-deflection curves. Experimental (bottom, green/black) Atena SBeta model with reduced tensile strength and accounting for shrinkage (top, blue)

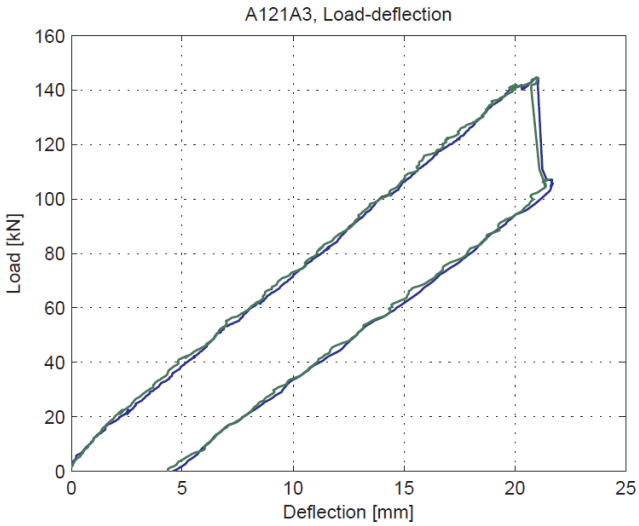

Figure 30: Experimentally obtained load-deflection curve of a "pre-cracked beam" without observable cracking load

Next, the crack pattern and failure mechanism is observed. All three experiments failed in shear, not all Atena models did however. Flexural shear cracks developed in all models, but did not always develop as much as the flexural cracks close to the load point. When this happens there is a dominant flexural shear crack present as shown in Figure 31, up until the model reaches a sort of loading plateau as can be seen in Figure 32. At this point the maximum load no longer increases but the maximum deflection keeps increasing as the reinforcement starts yielding and a flexural crack near the loading point keeps widening. This type of failure was observed for example in the base SBeta model of beam A75, shown in Figure 32.

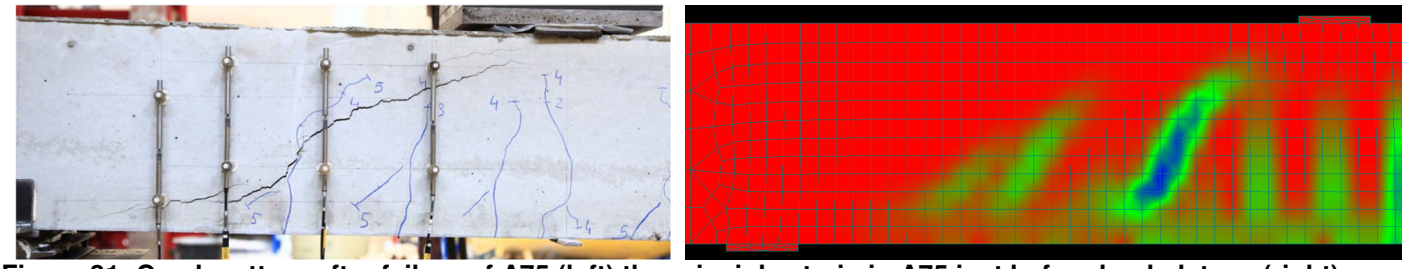

Figure 31: Crack pattern after failure of A75 (left) the principle strain in A75 just before load plateau (right)

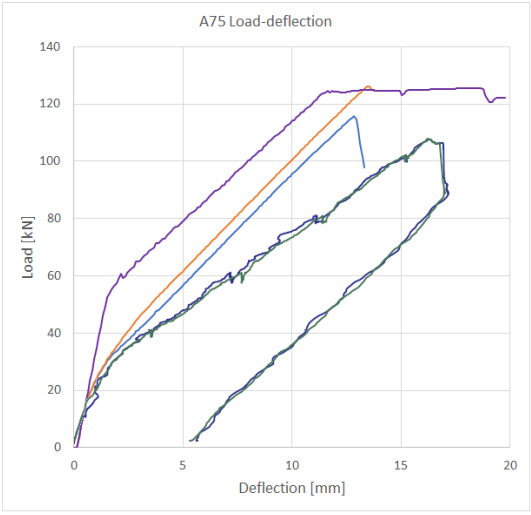

Figure 32: Load-deflection curve of A75 showing a loading plateau for P_{base} (purple) with $P_{ft,red}$ (orange), $P_{ft,red\&shrinkage}$ (blue), and P_{test} (green/black)

The final A122 and A123 models displayed crack patterns comparable to the experiments. Figure 33 shows the actual crack pattern of beam A123 and the start of the horizontal cracks in the model, just before failure. This is the case for both the SBeta and NLCEM models.

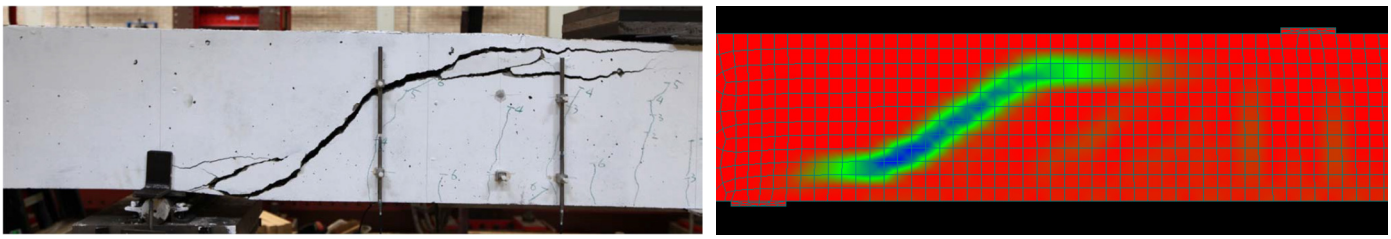

Figure 33: Crack pattern after failure of A123 (left) and principal strain on the load step before failure (right)

3.3.2. Evaluation of deep beam models (h = 1200 mm)

First an analytical prediction is presented using the IBBC-TNO method. The beam is simply supported, as such τ_{11} needs to be determined. There are two different types of formulas provided, one for design value of the shear force capacity V_{ud}, and one for average value for the shear force capacity $V_{u,avg}$. The average value should provide a shear capacity more comparable to the experimentally obtained results ($V_{u,test}$), both are presented here. For the sake of clarity, the values presented in Table 7 are

$$V_{ud} = \tau_{11,d} * bh$$

$$\tau_{11,d} = 0.17(1 + 0.01f_{ck})(1 + \omega_0)\left(1 + 1.2\left|\frac{1}{\lambda_x}\right|\right)\left(\frac{d}{d_0}\right)^{-0.25}$$

$$V_{u,avg} = \tau_{11,avg} * bh$$

$$\tau_{11,avg} = 0.455(1 + 0.0125f_{cm})(1 + 0.156\omega_0)\left(1 + 1.213\left|\frac{1}{\lambda_x}\right|\right)\left(\frac{d}{d_0}\right)^{-0.25}$$

Specimen	V_{ud} [kN]	$V_{u,avg}$ [kN]	$V_{u,test}$ [kN]
H123	208.1	340.9	245.7
H352	133.0	306.2	116.9

Table 7 Analytical solution

The analytical solution presented in Table 7 is the cause of concern that eventually led to the shear prediction workshop in Trondheim, Norway in May 2019. Almost all of the 18 beams in the deep beam series failed at a much lower load level than predicted by the Eurocode, the new Eurocode proposal, and the critical shear displacement model. Even the average shear capacity formula of the IBBC-TNO greatly overestimate the actual shear capacity, and in case of specimen H352 even the design value obtained through the IBBC-TNO method overestimates the actual capacity.

The numerical results are presented in Table 8 and Table 9, as with the reference baseline tests presented in paragraph 3.3.1 a couple of additional models have been created in order to adhere to the load-deflection curve obtained from the experiment and to take into account shrinkage as per the Atena Theory [24]. The models are compared with the experimental results based on peak load, failure mode, and cracking behaviour.

Specimen	P_{base} [kN]	$P_{ft,red}$ [kN]	$P_{ft,red\&shrinkage}$ [kN]	$P_{u,test}$ [kN]
H123	724.3	688.9	524.3	445.0
H352	369.9	364.4	363.0	211.0

Table 8: Numerical solutions with SBeta

Specimen	P_{base} [kN]	$P_{ft,red}$ [kN]	$P_{ft,red\&shrinkage}$ [kN]	$P_{u,test}$ [kN]
H123	520.3	775.4	524.1	445.0
H352	203.5	168.6	125.0	211.0

Table 9: Numerical solutions with NLCEM

There are a couple of things that stand out in the failure load tables. Where the differences between all the SBeta and NLCEM models for the “normal” beams were fairly minimal, for these deep beams the difference seems rather significant. Starting with the SBeta models: The base models grossly overestimate the beam capacity, with a failure load over 60% higher than observed in the experiment for the H123 beam and over 75% higher failure load for the H352 beam. The reduction of the tensile strength has some more noticeable effect for the deep beams, but does not come anywhere close to acceptable. The effects of shrinkage have a mixed effect on the failure load, it brings down the H123 model to within 18% of the failure load but the H352 model stays relatively the same. While the results for beam H352 are still rather poor, the result of H123 being within the 20% confidence interval is decent. The NLCEM models showed some unexpected behaviour. The base model of beam H123 showed potential, providing a much better estimation of the failure load than the SBeta base model. However, purely reducing the tensile strength has some interesting effects. Where other models experience a drop in the cracking load while adhering to the general load-deflection curve of

the experiment, this model did not. Instead of a jump in the simulated response, caused by the sudden propagation of a vertical crack, there is more of a bend with three very small jumps. After this bend the simulated response goes in a fairly smooth line all the way to 775.4 kN after which the simulation shows failure by shear. This type of failure is what is known as compression shear failure. A compressive strut is formed after the critical shear crack develops, allowing a much higher load level. When this exact model is changed to also include shrinkage it becomes more representative of the experiment. The first jump in simulated response indicating crack propagation, while less pronounced than in other models, coincides with the experimental results, see Figure 34. This is also the first model that includes shrinkage which ends up with a higher failure load than the base model, albeit the difference is minimal.

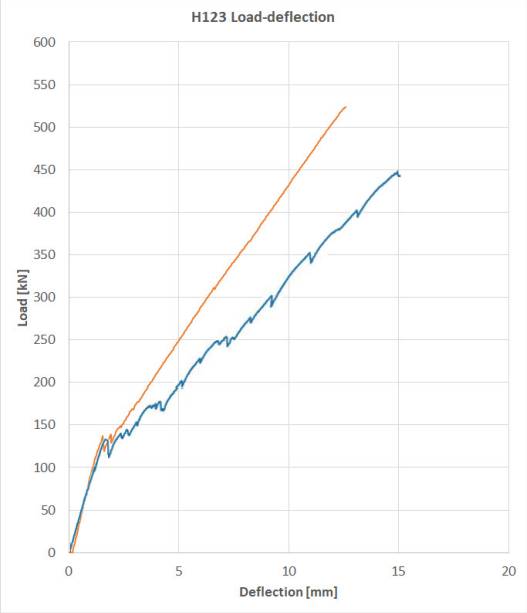

Figure 34: Load-deflection curve H123 experiment (blue) Atena NLCEM model with shrinkage (orange)

An interesting point to consider is that a very fine mesh was used in these models. In a recent paper by Cervenka et al. [37] it was concluded from a parametric study that the use of extremely fine meshes provided excellent crack patterns, but leads to an overestimation of the failure load result. Extremely coarse meshes lead to safe and conservative strength. This is thought to be caused by a difference in strain localizations in the different meshes. Further research and testing with different mesh sizes and probabilistic distribution of material properties has not been conducted but could be a way to make more accurate predictions of the shear capacity of concrete without shear reinforcement.

Despite the poor SBeta results of H352, the NLCEM results seem to be a good estimation. The failure load of the base model (P_{base}) is lower than that of the experiment, suggesting that it is a safe predictor of the shear capacity. This is not the case however, as the model simply diverges without showing any suggestions of actual failure. The model shows flexural cracks, but the reinforcement is not even close to yielding. There is a single simulated shear cracks that could suggest a sudden failure, but the model fails much sooner in terms of deflection than the actual experiment. Continuing with the other NLCEM models for H352 similar results are found. The model with a reduced tensile strength ($P_{ft,red}$) provides an even lower failure load and a single flexural shear crack forming in the last load step. The experiment itself and every other Atena model showed propagation of multiple flexural shear cracks before actual failure. The model that includes both a tensile strength reduction and shrinkage ($P_{ft,red\&shrinkage}$) is even worse, reaching the cracking load but subsequently failing even before recovering from the jump in load induced by the crack propagation. Figure 35 and Figure 36 show both SBeta and NLCEM models do not represent what has occurred in the experiment. The SBeta models all fail due to yielding of the reinforcement, rather than due to shear, but the NLCEM models do not even show any sign of failure. As there were no other changes to this model besides switching from the SBeta material model to the NLCEM material model these results suggest that the fracture-plastic constitutive model of Atena is unable to provide workable results for deep beams with a very low reinforcement ratio such as H352 ($\rho = 0.36\%$).

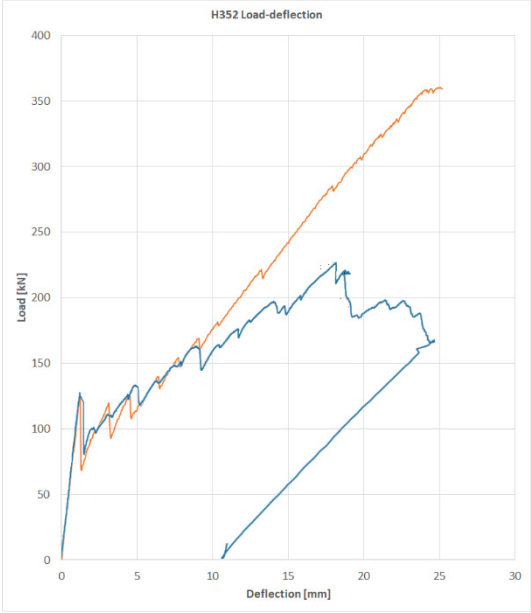

Figure 35: Load-deflection curve for H352. Experimental (blue) and SBeta with shrinkage (orange)

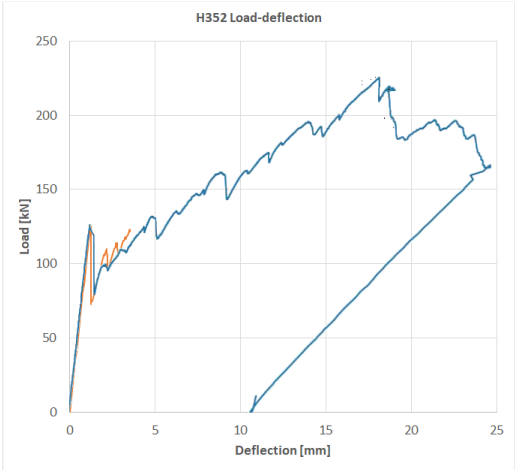

Figure 36: Load-deflection curve for H352. Experimental (blue) and NLCEM model with shrinkage (orange)

Similarly to what was mentioned in paragraph 3.3.1 the stiffness of the H123 beam models post-cracking is higher than the beams in the experiment (Figure 34). As a result the maximum deflection in all the models is lower than those obtained in the experiments. Drastically changing the Young's modulus would lead to a greater discrepancies in the linear elastic part of the load-deflection curve and were not pursued any further. There are two likely causes for this increased stiffness: the fine mesh size, as was also concluded in [37] that mesh refinement led to a systematic increase in stiffness, and the fixed smeared crack model. A fixed smeared crack concept is used in the analysis, in these models fracture occurs when the principal stress in a point exceeds the tensile strength. The orientation of the crack remains fixed throughout the loading process. The principal stress can change direction however, due to aggregate interlock and dowel action of the reinforcement. In this new direction the principal stress can exceed the tensile strength again, in which case the numerical response will be stiffer than the experimental response [38].

Next, the crack pattern and failure mechanism are observed. In beam H123 various flexural shear cracks propagated before secondary shear cracks developed for the critical shear crack around the height of the bottom and top longitudinal reinforcement bars, see Figure 37. Which makes sense as the concrete area around this zone is smaller. This is roughly what happens in both the SBeta models and the NLCEM models, however the secondary cracks rarely align so clearly with the reinforcement as in Figure 37. This can partly be explained by the cracking model. All the Atena models used in this research used a fixed crack model with smeared cracking. As a result in Atena a nearly uniform field of smeared cracks is formed as the load is increased. Consequently, horizontal cracks cannot be formed in the nodes that already have cracks.

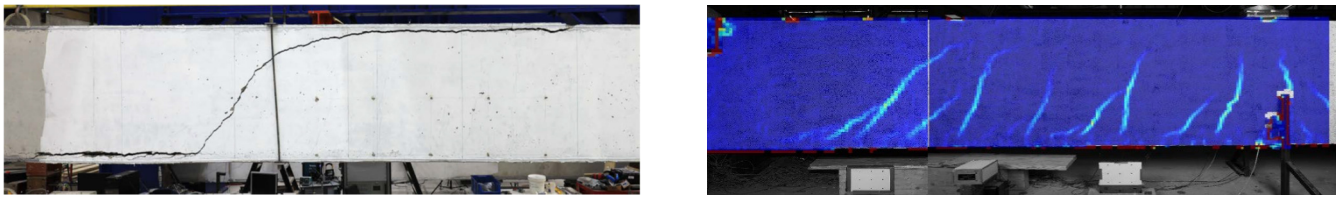

Figure 37: Critical shear crack (left) and flexural shear crack formation (right) of H123

The principle strain of both models with reduced tensile strength and inclusion of shrinkage effects are compared to the actual beam. In Figure 38 it is clear that the SBeta model has a large shear crack developing which eventually caused it to fail. While it is not clear from the NLCEM model before the last load step, this model also fails in shear, as seen in the same figure. In terms of critical shear crack location the NLCEM model seems to be more accurate, the critical shear crack in the SBeta model starts in a closer proximation to the loading point than found in the experiment.

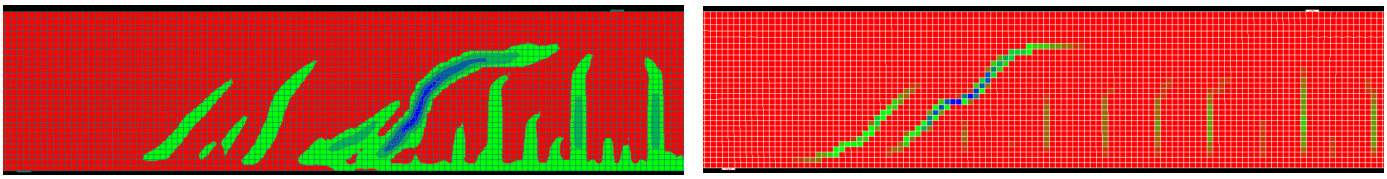

Figure 38: Principal strain of H123 just before failure in SBeta (left) and NLCEM (right) as it is failing

In the experiment beam H352 some erratic behaviour was observed. Two identical beams were tested and in one of the two tests the concrete near the reinforcement spalled off, while in the other experiment it did not (Figure 39). Of course concrete is not a homogeneous material, and as such some minor deviations are to be expected despite running tests on two otherwise identical beams, but not to this extend. The failure mode observed in H352 is now called dowel failure [51]. There was some hope that this failure mode could be reproduced in Atena, but as was mentioned earlier the only failure that Atena obtained for beam H352 was flexural. Perhaps this failure could be reproduced by means of forcibly applying weak layers in Atena, but this was not tested. Even if the application of weak layers could lead to dowel failure its application would be impractical for standard engineering work and is not considered to be applicable for the evaluation of the Heinenoordtunnel. It should be noted that in some models, not presented here, did display severe cracking in the compressed zone around the top reinforcement, however this cracking would only occur after failure was induced rather than being the cause of failure as was observed in the experiment.

Figure 39: Spalling on concrete on test specimen H351 (left) and failure on test specimen H352 (right)

3.4. Influence of load conditions

Most shear tests such as the ones performed in the Stevin laboratory of Delft University of Technology are beams subjected to point loads. For submerged tunnels such as the Heinenoordtunnel these load conditions do not apply. Tunnels are subjected to uniformly distributed loads and changing from a point load to a distributed load leads to a different shear force distribution. For point loads the shear force is constant between the support and the load. For distributed loads the shear force is not constant, there is a linear reduction in shear force along the element axis.

Research into the shear resistance of concrete without stirrups loaded by distributed loads is limited compared to the research with point loads. As a result there is no data available of beams that would be directly comparable to the situation of the Heinenoordtunnel. The closest research is by Iguro et al. [39] where the shear strength of beams with heights up to 3m were tested under uniformly distributed loads. By far the biggest difference with the beams in previous paragraphs is the concrete class (roughly C25/30), but despite that there are still valuable information in the paper that can be taken into account.

Iguro et al. showed that, as is now known, the size effect does not stop increasing past an effective height of 600 mm. The increased size effect observed by Iguro et al. was not a significantly greater reduction in shear capacity compared to the maximum reduction of the shear capacity found in the codes of 1978 (Figure 40). This suggests that there is more to the results found in the Stevin laboratory than simply the size effect, another factor that has considerable effect on the shear resistance. In their conclusions Iguro et al. state that they consider the size effect of the shear strength as part of the size effect of concrete strength itself.

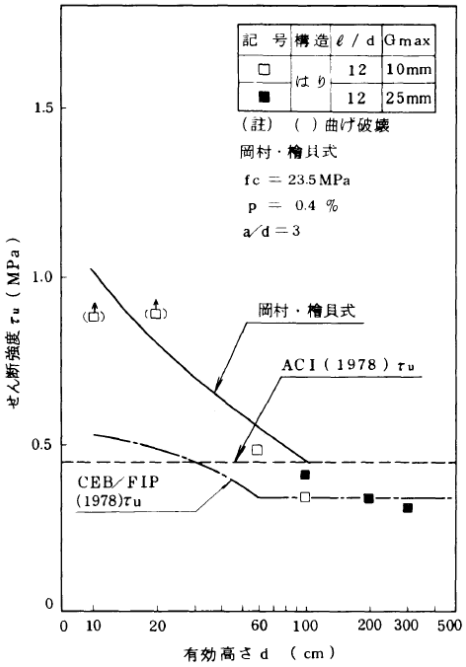

Figure 40: Relation between shear strength and effective height [39]

Interestingly enough the critical shear crack occurred at the same location for all tests that were conducted. For all seven tests the critical shear crack originated from a distance roughly 1.5 times the effective height away from the support location, see Figure 41. It is very likely that this distance for the critical shear crack won't be found in tunnels due to the voute that often is applied. A voute is a thickening of the slab to locally increase the bending strength and shear capacity of a section. The consistency in critical shear crack location was not found in the point load tests.

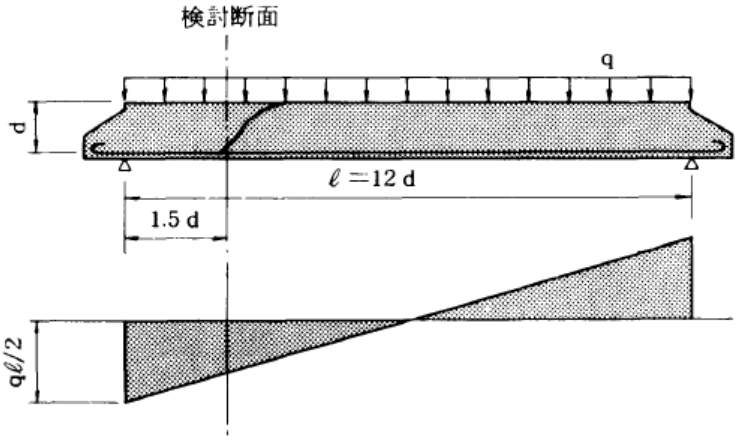

Figure 41: Critical shear crack location [39]

Modelling of a uniformly distributed load using displacement control is somewhat tricky. A uniform displacement over the entire length of the beam does not represent the actual consequence of a uniformly distributed load. Even applying several displacements in a specific pattern is likely to result in a situation that does not represent a uniformly distributed load. Ghahremannejad et al. [53] suggest modelling with a series of infinitely stiff plates, see Figure 42, in order to get a representative load under displacement control. Alternatively, force displacement can be used, but this results in the loss of some information.

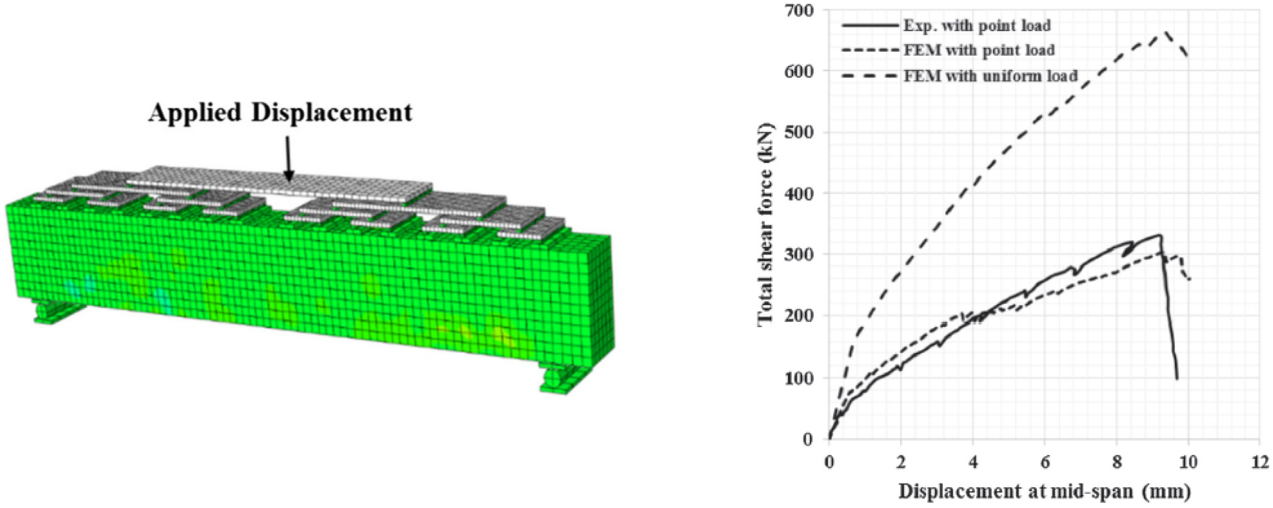

Figure 42: Framework to apply displacement control of uniformly distributed load (left) and an example of the load-deflection Ghahremannejad et al. obtained with this framework [53]

This framework was used to check several beams that failed in shear for a point load, to see if this was also the case for a uniformly distributed load. This was the case for all the observed beams [53], but resulted in a higher shear force required to initiate failure. These beams had significant longitudinal reinforcement to prevent flexural failure ($\rho = 1.72\%$ to $\rho = 2.72\%$).

The Heinenoordtunnel does not have this much reinforcement, so it could be possible that the tunnel fails in bending, rather than shear. However, there is another factor to consider. Due to the horizontal water pressure on the tunnel there is a significant normal force present. This acts as a sort of prestressing in the roof of the tunnel. As a result, both the bending moment capacity and the shear capacity will be increased.

3.5. Discussion

Five different beams were modelled with in total thirty numerical models, testing different constitutive models and various material parameter settings. For regular beams (h=300mm) there are no notable differences between the two constitutive models and the impact of changing material parameters, such as tensile strength and fracture energy, seemed minimal. Based on the experimental data used in this research, the models in Atena seem to slightly overestimate the shear capacity of concrete. The following reasons are considered as a possibility for this overestimation in the shear capacity: increased failure load as a result of using a fixed crack model, increased failure load as a result of using mesh that is too fine, and a mismatch in actual material parameters and modelled material parameters.

First, the influence is of the fixed crack model is discussed. As stated by Rots [26], the use of a fixed crack model may lead to an overestimation of the strength and stiffness in the numerical model during the fracturing process. This would explain the differences observed in the load-deflection diagrams such as Figure 29. In order to check the influence of this choice a single model is created with a rotating crack model for comparison. Figure 43 depicts the load-deflection curve for the A123 beam. The exact same model is run with a rotating crack model instead of a fixed crack model. While the stiffness post-cracking is more representative of that observed in the experiment, the modelled failure load is in fact slightly higher than that of the fixed crack model. In terms of cracks observed in the models the fixed crack model is more representative of the experimentally observed cracks, see Figure 44. The choice for a fixed crack model makes sense from a physical point of view, in reality a crack cannot change in direction, which was the reason

for choosing a fixed crack model in the first place. The effect of changing to a rotating crack model does not appear to be significant enough to warrant further modelling.

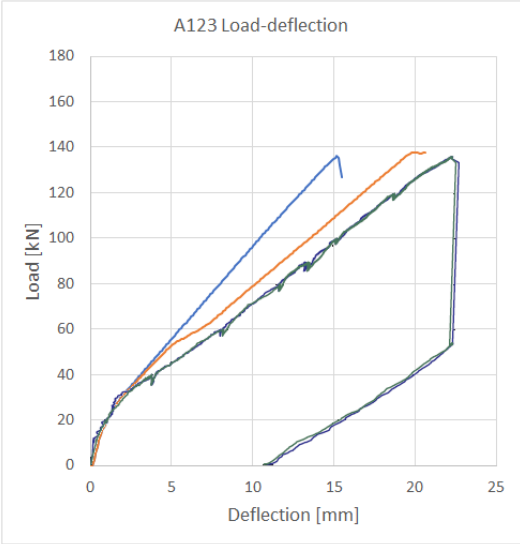

Figure 43: Load-deflection of the A123 beam (bottom, green/black), fixed crack SBeta model (top, blue), rotating crack SBeta model (middle, orange)

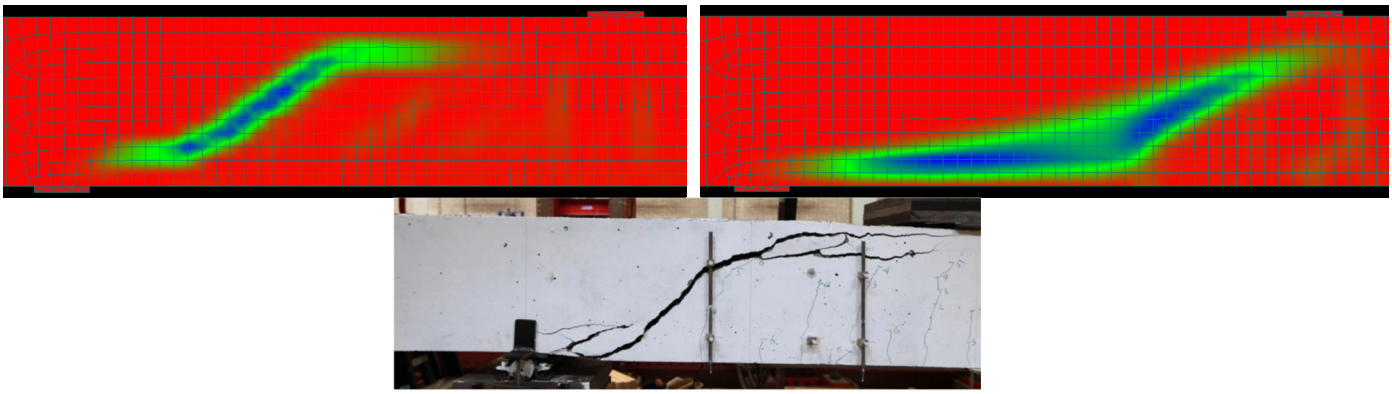

Figure 44: Crack pattern observed in the fixed crack model (top left), in the rotating crack model (top right), and experimentally obtained (bottom)

Secondly, the influence of the mesh size is discussed. Similar to the choice for crack model, the choice for a specific mesh size brings various pros and cons. Cervenka et al. [37] showed the effects of differentiating in mesh size for a very large beam. For a model with quadratic elements, differentiating between a very fine mesh and a very coarse mesh caused an uncertainty in the strength in range of +/- 13%. For a very fine mesh excellent crack patterns were found, but so was an overestimation of the shear capacity. For a very coarse mesh the opposite is true, providing a conservative estimation of the shear capacity.

Thirdly, a mismatch in material parameters is discussed. There are some distinct differences between the way the beams are modelled and how the actual beams are created and tested. The numerical models that were used assume that concrete is a homogeneous material. In reality however, concrete is a heterogeneous material. Some parts are relatively stronger, others are relatively weaker. Cervenka et al. [37] tested the effects of this variability by probabilistic modelling, testing the shear capacity for random field distributions of the tensile strength and fracture energy (see Figure 45). The effects of this variability on the strength was in the range of +/- 26% [37]. The actual range of this effect likely depends on the standard deviation of the randomised material properties. The size of which requires various tests to determine with some sense of accuracy.

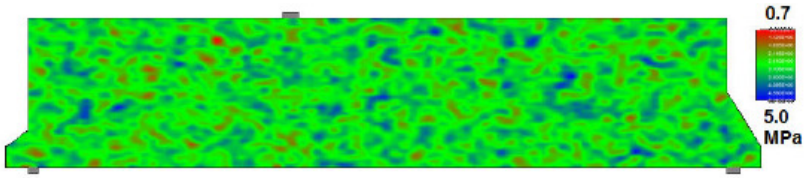

Figure 45: Example of a random field of tensile strength [37]

Reconsidering these three influential factors the first factor, use of the fixed crack model, seems to be an unlikely cause. An overestimation of the shear capacity due to the mesh size is possible, considering its relatively small impact falls in line with the deviation observed in some of the models, see Table 5 and Table 6. The overestimation as a result of inhomogeneous material parameters is hard to quantify without additional research into the material.

In terms of the modelled failure load compared to the experimentally obtained failure load the SBeta models seem a little bit better, providing better estimation of the shear capacity. For deep beams this changes considerably, the SBeta models struggle with a low reinforcement ratio, consistently failing to provide shear failure and satisfying failure loads, and for a normal reinforcement ratio the models are rather sensitive in terms of parameter settings. This makes the SBeta constitutive model rather poor for accurate shear capacity prediction, being at best roughly 17% off, but possibly up to 75% off. This was somewhat expected, as Červenka Consulting themselves seem to prefer their own NLCEM model over the SBeta model for their shear predictions [37]. While the NLCEM constitutive model is better off, it failed to produce satisfactory results for the low reinforcement beam, but unlike the SBeta model it did not provide a false sense of security with regards to the capacity of the beam.

The results of beam H352 are worth reiterating. This beam did not fail in flexural shear or shear compression, but with a mechanism now called dowel failure. None of the models showed this behaviour despite the initial load-deflection relation being similar. This is not necessarily a fault in the constitutive models of Atena, when the shear predictions from other users with different finite element packages are considered, almost every single prediction is off, see Figure 46. In orange the results of the three SBeta models are shown, number 1 represents P_{base}, 2 represents $P_{ft,red}$, and 3 represented $P_{ft,red\&shrinkage}$. These fall in line with the majority of the predictions. In purple the three NLCEM models are shown. While these three seem to be conservative predictions, the actual correct failure mechanism was not found. It appears that the observed failure mechanism can only occur for very low reinforcement ratios [51]. Considering the reinforcement applied in the Heinenoordtunnel, the model results for this failure mode are not consequential for the modelling of the tunnel as discussed in chapters 4 and 5.

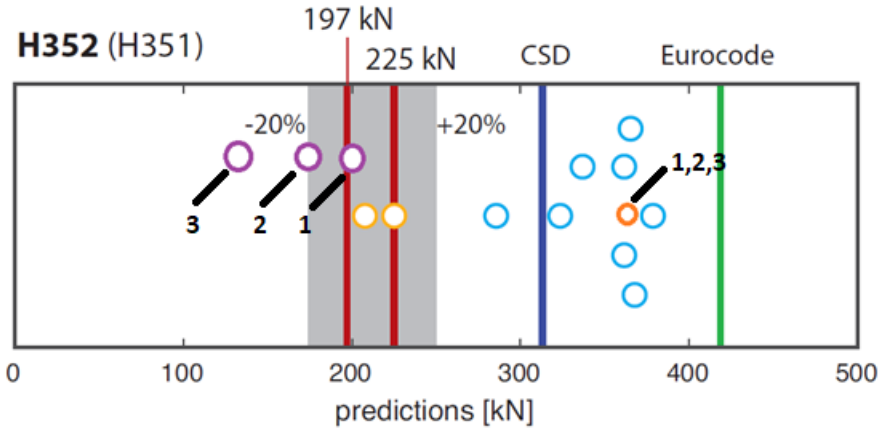

Figure 46: Shear predictions and postdictions for H352

Focussing back on beam H123, with a normal reinforcement ratio, the NLCEM model stays within a 20% confidence margin of the shear capacity, which is reasonably accurate. The sample size is a bit small for heavy statistics but based on the data used it can be stated that the SBeta material model can be rather inaccurate, providing results anywhere in the range over 15 to 75% over the actual failure load. The NLCEM model is based on the Modified Compression Field Theory, which essentially takes the size effect into account through the increased crack width for an increase in height. As the crack width increases, the aggregate

interlock decreases, effectively reducing the shear capacity. This poses the question of how accurately this reflects the experimentally observed size effect. Is the overestimation of the shear capacity in the model a result of an inaccurate representation of the size effect or are the earlier mentioned influential factors the cause?

Figure 47 shows the shear predictions for beam H123 and the results obtained from the models described in this chapter. While in general the mean overestimation is lower for this beam, the standard deviation from the mean is significantly higher. In other words, there is a significant scatter in the predictions. From this it should become clear that user choices in modelling have an enormous impact on the shear prediction results. All users modelled with the exact same set of (minimal) data, yet there is such a great difference in results. Choices made by the user such as load step sizes, material parameters based off of the compressive concrete strength, and the aforementioned mesh size are apparently very impactful.

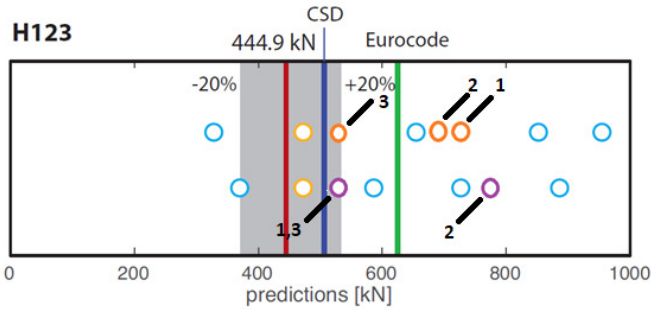

Figure 47: Shear predictions and postdictions for H123

In order to get a better grasp of the impact of the mesh size on the results, a single model is tested of beam H123 with a coarse mesh. For this model the mesh size has been increased from 50 mm to 150 mm. In Figure 48 the load-deflection diagram is shown for the NLCEM model comparing $P_{ft,red\&shrinkage}$ with the two mesh sizes and the experiment. The coarse mesh presents a failure load of 456.6 kN, only a 2% overestimation of the experiment, however the cracking load is no longer representative of the experimentally obtained cracking load.

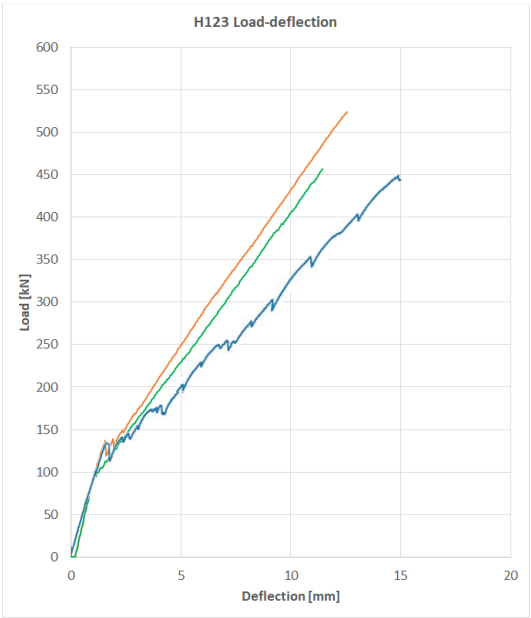

Figure 48: Effect of mesh size on the failure load. Mesh of 50 mm (top/orange), mesh of 150 mm (middle/green), experimental results (bottom/blue)

3.6. Conclusions

With the information gathered in this chapter two of the sub-questions can be answered:

- How accurate is the shear capacity prediction of Atena for deep beams? To what degree is the size effect of concrete taken into account in Atena?
- Which parameters are critical for a 2D Atena analysis of the shear capacity?

In general the shear capacity of the deep beams models analysed in this chapter was an overestimation of the experimentally obtained results. Even when ignoring the H352 beam with its problematic dowel failure that was not obtained in the models, all results of the H123 beam overestimated the shear capacity. For the SBeta material model significant improvements can be made to the model by applying a reduction of the tensile strength and taking into account shrinkage. In doing so the overestimation changes from roughly 75% to roughly 17%. The NLCEM material model performs better without knowledge of the experimental results, with both the basic model and the model with reduced tensile strength and shrinkage effect providing also a roughly 17% overestimation of the shear capacity. This brings these models within the 20% confidence interval for the H123 beam.

It is known how the size effect is taken into account for the material models of Atena. In the Modified Compression Field Theory, upon which the material models are based, there is a relation between the crack width and the shear stress at the crack. As the crack width increases, there is a decrease in the amount of shear that can be transferred by aggregate interlock. This results in a lower shear capacity for beams with a greater height. However, does this sufficiently represent the size effect as it is observed in the experiments? It would be easy to dismiss the overestimation in the models as merely an error in the representation of the size effect. But there are other factors that have a considerable impact on the shear capacity as is shown in paragraph 3.5. It was shown that a coarse mesh leads to more conservative shear capacity estimation and brings the model very much in line with the experimentally observed failure load. In the paper by Cervenka et al. [37] it was shown that the actual failure load was found somewhere in between the very fine mesh and the very coarse mesh. This suggests that for the beams observed using a very coarse mesh, the shear capacity should be underestimated, rather than representing the shear capacity. From this it can be concluded that there is another factor which causes an overestimation of the shear capacity. However, without additional data from the material used in the experiment it cannot be determined whether this is the result of a misrepresentation in the homogeneity of the material parameters, or a misrepresentation of the size effect.

It has become apparent that there are several parameters which are critical for an analysis of the shear capacity in Atena. First of which is the concrete compressive strength. In most codes the determination of any material parameter is related back to the concrete compressive strength. While this is also the case for the tensile strength, it was found that the tensile strength as calculated based on the compressive strength leads to a higher cracking load than observed experimentally. For the deep beams that were observed a reduction to 55% of the calculated tensile strength was necessary to accurately represent the experimental cracking load. It was found that the mesh size can have a significant impact on the shear capacity. In general a coarser mesh leads to a more conservative estimation, but a realistic representation of the shear capacity is found somewhere in between a fine and coarse mesh. Additionally, there are likely differences between the actual beams and the way they are modelled. While concrete is modelled as a homogeneous material, in reality its properties are heterogenous. As discussed in paragraph 3.5 this can significantly impact the shear capacity.

Despite various experimentation with the abovementioned parameters, none the deep beam models were able to accurately replicate the laboratory results obtained at TU Delft. This leads to believe that there could be some other unforeseen factor, a piece of the puzzle, that we are missing at this point in time. The obtained information is used for modelling the Heinenoordtunnel, with the knowledge that it provided a slight overestimation of the deep beam results.

4 Evaluation of the shear capacity of the Heinenoordtunnel under regular loading conditions

4.1. Introduction

The Heinenoordtunnel is an immersed tunnel in the A29 highway in the Netherlands, crossing the Oude Maas river and connecting Barendrecht and the town Heinenoord, where the tunnel got its name from. The tunnel was constructed in the construction dock of Barendrecht, directly next to where the tunnel was immersed. The Heinenoordtunnel opened in the summer of 1969, with three lanes in both direction. One lane for slow traffic and two lanes for fast traffic. As it became apparent that the tunnel did not have enough capacity for fast traffic a second tunnel was constructed in 1991 for slow traffic and the Heinenoordtunnel switched to having three lanes for fast traffic.

The Heinenoordtunnel was designed using the GBV 1962 (Gewapend-Beton Voorschriften) design codes. These contain concepts of shear design that assume a much greater contribution of concrete to the shear resistance, especially compared to today's design codes. As a result the Heinenoordtunnel was constructed without any shear reinforcement. The last decade there were some concerns with regards to structural safety of the Heinenoordtunnel, if the tunnel as designed is tested with current design codes it would not be considered safe. However, the current state of the tunnel is not as it was designed. Initially the tunnel was constructed with K300 concrete (roughly C18/25 concrete), but years of continuous hydration allowed the concrete to attain a much higher strength class.

Figure 49 shows a cross-section of the tunnel, this is the situation after 1991, only half of the tunnel is depicted because of its symmetric nature. On top of the tunnel is a non-constructive concrete protection layer on top of which rests 3 m of soil. This brings the top of the soil layer to -10 m N.A.P. The Oude Maas is a tidal river, meaning the water level is not constant. The mean high water level is located at +1.2 m N.A.P. and the higher high water level is located at +3.8 m N.A.P. This last water level is considered to be the physical limit due to the height of the surrounding dikes. The load due to this water is by far the most prevalent load, considering it is up to roughly 17 meters of water on the structure. This is also shown in Figure 50.

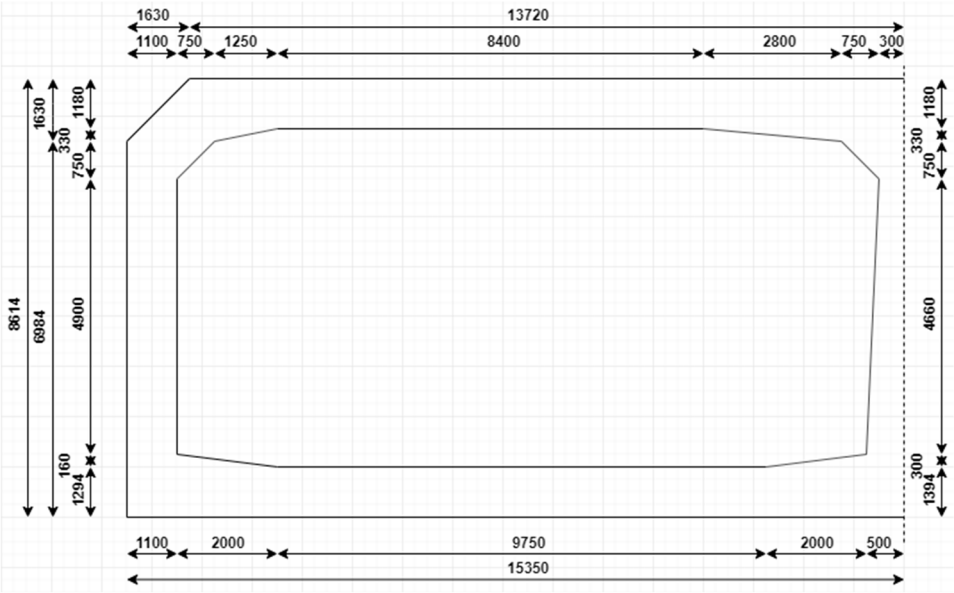

Figure 49: Cross-section of the left tunnel half

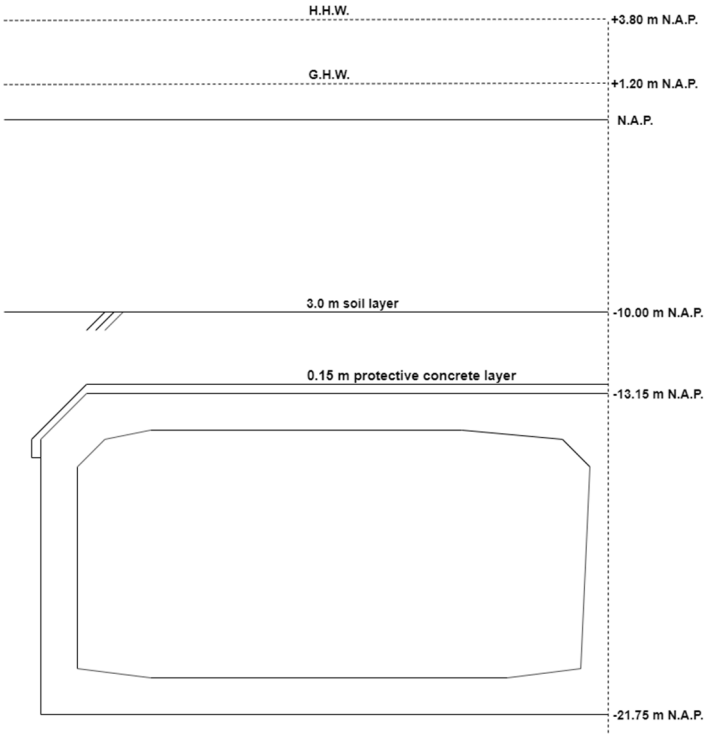

Figure 50: Water level Heinenoordtunnel

In 2009 the independent research organisation TNO performed a shear capacity check for the Heinenoordtunnel. In their research TNO used the IBBC-TNO method to assess the shear capacity for various water levels. As a way to check the model created in Atena the forces and moments will be compared with TNO's results to see if they are in the correct order of magnitude. Slight differences in modelling are likely to lead to small differences, so an exact match is not expected.

4.2. Structural model description

This paragraph discusses the various choices made in creating the model used for analysing the Heinenoordtunnel. This introduction for the chapter briefly mentioned some details regarding the tunnel. The tunnel is 8.6 m by 30.7 m and has a length of 614 m, the model observes only a 1 m cross-section of the tunnel. For the sake of consistency with the model of the tunnel loaded by fire symmetry is not applied in this model, despite the fact that the tunnel is symmetrical.

The tunnel models are not created in Atena 2D like the beams discussed in Chapter 3, but by using a combination of Atena Studio and GiD. The reason for this is because the Atena 2D package does not allow for the use of temperature dependent properties in the used materials but Atena Studio does. The Atena Studio package performs the actual analysis and allows post-processing of a model, but requires input data from a pre-processor. This data input can be created in Atena 3D and then exported to Atena Studio, but Červenka Consulting recommends using GiD. GiD is a universal pre- and post-processor, and by applying a set of scripts specifically created for Atena it is relatively simple to create the required input files for Atena Studio. In GiD a 2D plane strain model is created of the tunnel. The actual material model used for concrete is still the same as for the beams observed in Chapter 3 (nonlinear cementitious), but Atena Studio allows for some extra parameter sets to be adjusted such as fatigue and temperature dependence.

In the introduction of this chapter the concrete class was briefly discussed. The tunnel was constructed using K300 concrete, which is roughly comparable to C18/25 as described in the Eurocode. Due to continuous hydration of the concrete over time, the actual strength far surpasses that of a C18/25. In 2009 the engineering firm Witteveen+Bos was tasked by RWS to research the concrete strength of various structures, including the 1e Heinenoordtunnel. In total six concrete cores were drilled over the length of the tunnel to determine the concrete compressive strength, the results of which are presented in Table 10 [40]. The most important statistic of this table is the mean compressive cylinder strength of 69.1 N/mm^2, which equates to a characteristic compressive cylinder strength of 61.1 N/mm^2, bringing the concrete class to C60/75. This is a

considerable increase from the concrete class with which the tunnel was originally designed. There are two likely reasons for this increase: First of all because the tunnel is submerged it has been in the perfect condition for continuous hydration, the Dutch guidelines for the evaluation of existing structures (Richtlijn Beoordeling Bestaande Kunstwerken, RBBK) states that the strengthening of concrete structures over time is more notable with older structures due to the use of coarser aggregates and/or different use of binder [41]. Second of all it is likely that the actual concrete delivered on site was stronger than the K300 that the tunnel was designed with.

Specimen	Diameter [mm]	Height [mm]	Vol. weight [kg/m^3]	Fmax [kN]	Comp. stress [N/mm^2]
301	99.6	101.2	2365	541.88	69.5
302	99.6	101.4	2352	491.15	63.0
303	99.6	101.6	2329	516.51	66.3
304-2	99.6	101.2	2359	586.28	75.2
305-2	99.6	101.6	2371	561.95	72.1
306-2	99.6	101.1	2331	532.82	68.4
Mean	**99.6**	**101.4**	**2351**	**538.43**	**69.1**

Table 10: Overview of drilled concrete cores [40]

The RBBK advises not to calculate the tensile strength based on the measured concrete compressive cylinder strength, as the tensile strength often does not grow as much over time as the compressive strength does. In addition to the six cores mentioned in Table 10, two more cores were drilled which were tested on splitting strength. These are presented in Table 11. The tensile splitting strength determined from these tests is used to calculate the tensile strength as described in 3.2.3. As described in [30] the concrete splitting strength relation for existing structures does not necessarily follow the same relation with the concrete compressive strength as assumed for new structures. In some cases the concrete splitting strength does not have the same strengthening trajectory that the compressive strength does. The two tested cores show that the measured splitting strength is not less than 75% of the calculated splitting strength based on the mean compressive strength ($f_{ctm,sp} = 2.36 * \ln(1 + f_{cm}/10) = 4.88\ N/mm^2$). While the measured splitting strength is slightly lower than the calculated splitting strength, these results do not warrant additional investigation, in accordance with [46].

Specimen	Diameter [mm]	Height [mm]	Vol. weight [kg/m^3]	F_{max} [kN]	$F_{ct,split}$ [N/mm^2]
304-1	99.6	105.9	2351	75.9	4.6
306-1	99.6	104.6	2350	65.0	4.0
Average	**99.6**	**105.3**	**2351**	**70.5**	**4.3**

Table 11: Overview of drilled cores for concrete splitting strength [40]

All the other concrete material properties are calculated as described in paragraph 3.2.3., based on the compressive strength derived from the cores. An overview of the changed material properties is provided in Table 12, parameters not mentioned are defined according to default settings as described earlier.

Parameter	Value	Unit
Young's modulus E	34808	[MPa]
Poisson's ratio ν	0.15	[-]
Tensile strength f_t	1.94	[MPa]
Compressive strength f_{ck}	-61.1	[MPa]
Fracture energy G_f	78.23	[N/m]
Aggregate size a_g	32	[mm]

Table 12: Overview applied concrete properties

The reinforcement steel used in the Heinenoordtunnel is QR40, also known as FeB400 [41]. This means that the yield stress of the bars used for the Heinenoordtunnel is lower than that of steel commonly used nowadays. The amount of reinforcement applied is based on the deepest tunnel section, drawings for which

are presented in Figure 51. These are scans of old drawings and are rather unintelligible at any presentable scale in this report, a clearer view of the applied reinforcement is presented in Figure 52.

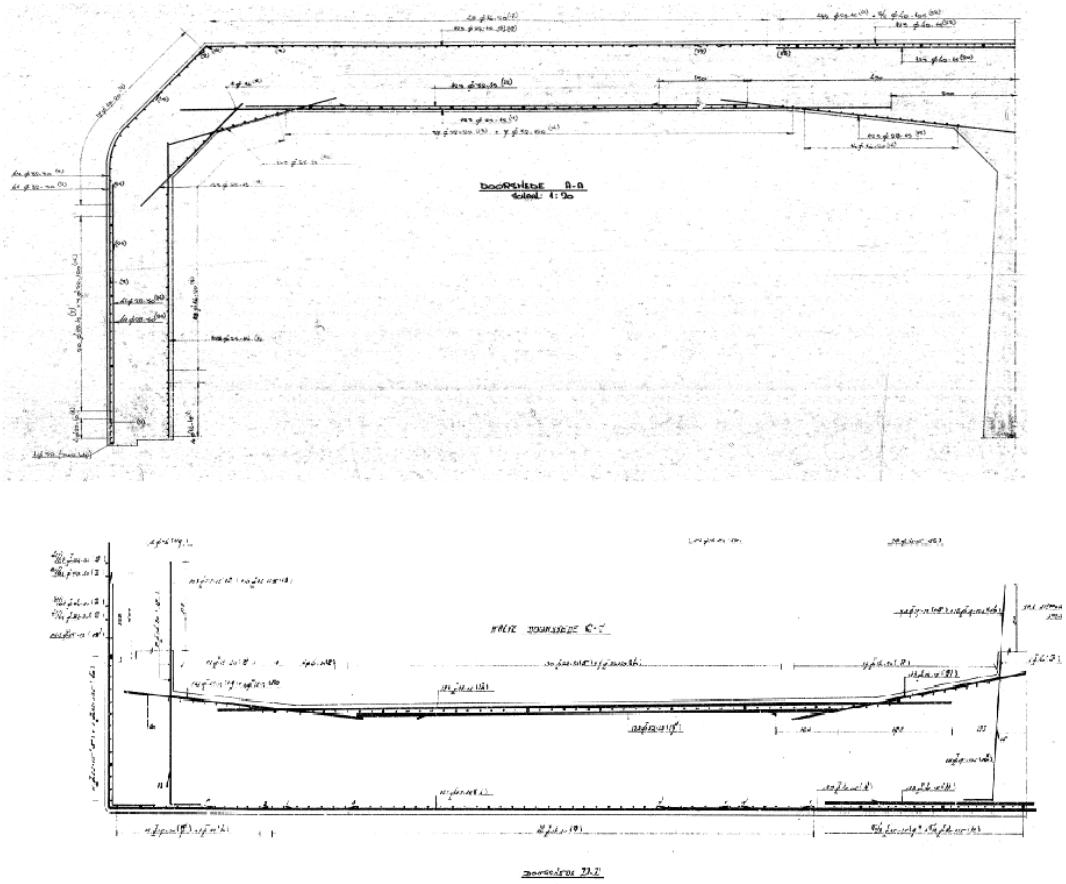

Figure 51: Reinforcement drawings 1e Heinenoordtunnel

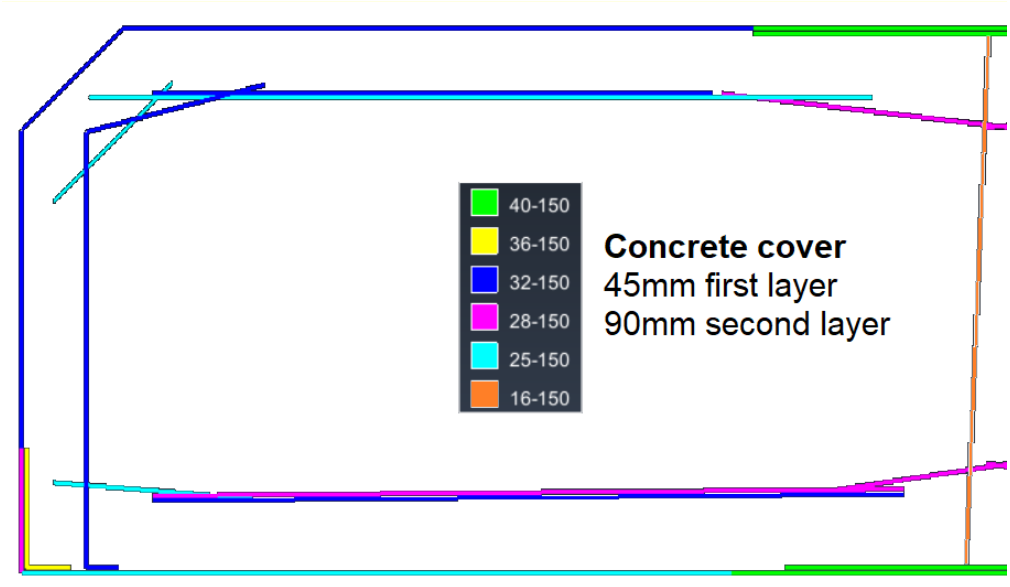

Figure 52: Reinforcement as applied in Atena

The following loads are considered in the analysis: dead load of the structure, load of the soil, and the load of the water. Traffic loading inside the tunnel is not considered as it provides a positive effect, in other words the tunnel is more heavily loaded when it is empty. The loads are applied on the model in different intervals, as it is called in GiD. These are essentially load steps as described in Atena theory. In the first load step dead load and support conditions are applied, the dead load is based on a specific weight of reinforce concrete of 25 kg/m^3. In addition to the concrete of the tunnel, some ballast concrete and asphalt is present in the two

tunnel tubes, this is approximately 0.1 m of asphalt at 23 kg/m^3 and 0.58 m of ballast concrete at 25 kg/m^3. The soil supports the floor of the tunnel, but only in compression. The modulus of subgrade reaction c is set to 0.15 N/mm^3 which is very stiff. The Atena theory suggests not to set the stiffness of the inactive side to zero, but rather to very low value between a hundredth and a thousandth of the stiffness in the active direction. In order to block all rigid-body motion modes and ensure the equation system does not become singular a horizontal support has been applied in the middle of the tunnel cross-section at the bottom of the floor and vertical supports in both lower left and lower right corner of the cross-section. This interval can be seen in Figure 53.

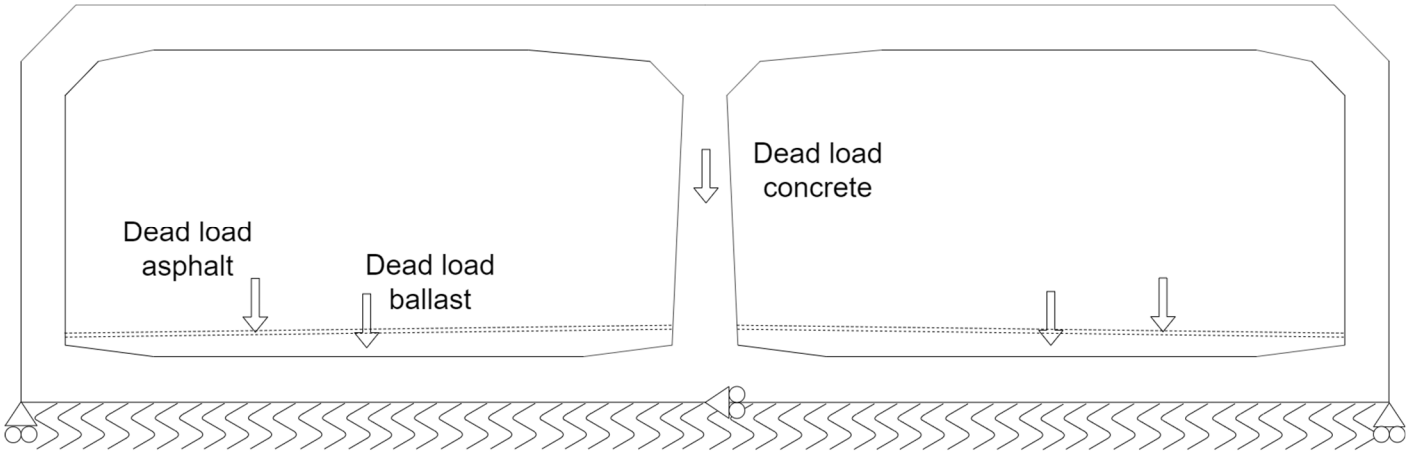

Figure 53: Overview of interval 1

The second interval (see Figure 54) considers the load of the soil on the tunnel, the load of the concrete protection layer, and the load of the water up to -13.15 m N.A.P. (roof of the tunnel). The soil has a volumetric weight of 20 kN/m^3, reduced by water pressure. The soil is assumed to be neutral in vertical direction (K_o=0.5). The concrete protection layer is a 0.15 m sheet of concrete over the roof of the tunnel, the weight of which is also assumed to be 25 kg/m^3. Lastly, the water load up to -13.15 m N.A.P. is applied in this interval. The reason for applying this specific load is for simplifying the remaining load in the third and last interval.

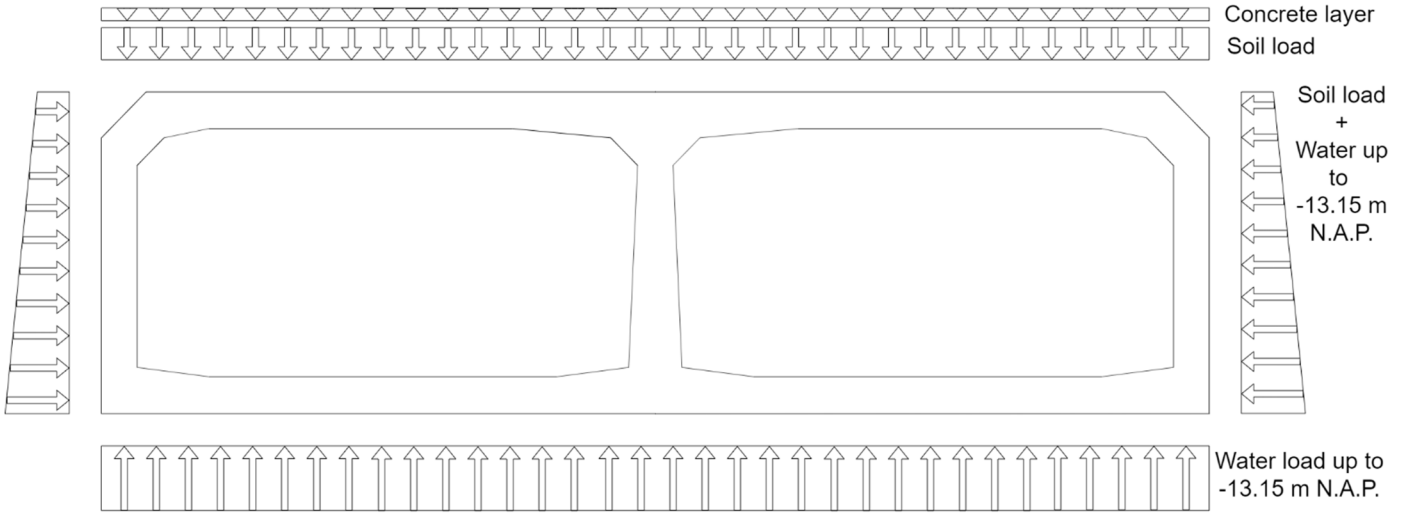

Figure 54: Overview of interval 2

The third interval considers the water load from -13.15 m N.A.P., in doing so the load increases uniformly on the tunnel for this interval, and the same load can be applied to every surface of the tunnel. This also allows for a more easily recognizable way of checking the water depth applied, as each load step in this interval corresponds with a static increase of the water depth. This essentially means that each load step represents a rise in the water load on top of tunnel, on the walls of the tunnel, and on the floor of the tunnel. The ultimate limit state is observed, but considering the water level is at its physical limit, it is only increased by 1.05.

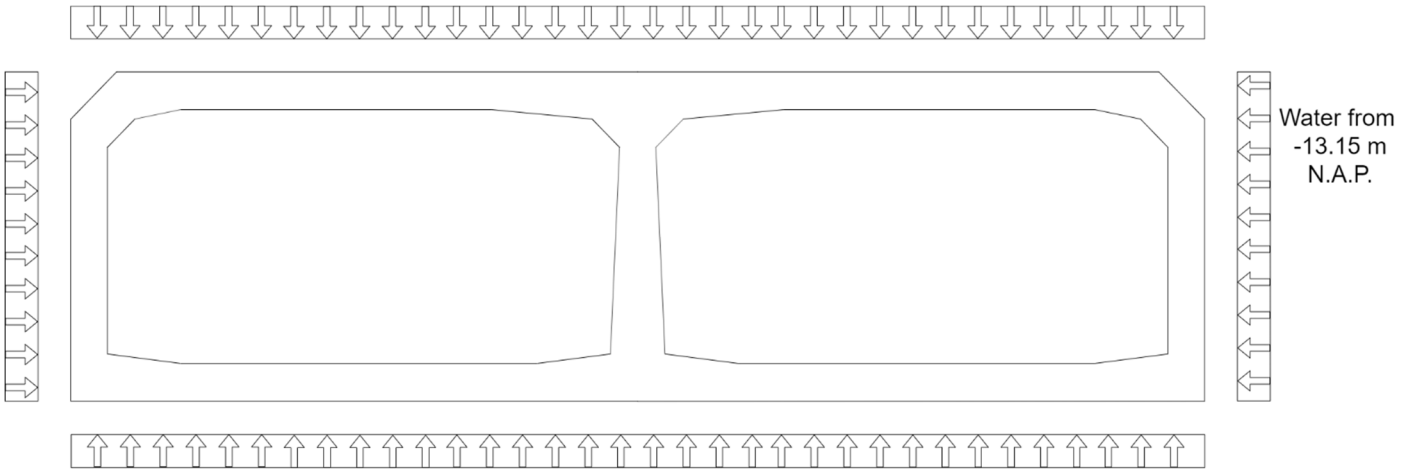

Figure 55: Overview of interval 3

The default equation solver for Atena Studio is called Pardiso, however instead the solver LU is used. This solver is slower and more memory intensive, but more robust [42]. For the first two intervals a regular Newton-Raphson method is applied, but for the last interval a modified Newton-Raphson method is used instead for stability reasons. The elements that are solved is a mesh of quadratic quadrilateral elements with a size of 0.1 m. This mesh size is slightly coarser than the mesh size used for the deep beams, resulting in a slightly lower overestimation of the shear capacity. Additionally, the computation time for the model is severely reduced.

4.3. Results

In the next few paragraphs the results of the Heinenoordtunnel model in Atena will be discussed. As a means of validation of the model, the results are compared to those obtained by the Diana model of TNO in their report where possible. In the rest of this chapter the tunnel model in Atena is referred to as the “Model” and the TNO report as the “Reference”. The Model is loaded with a water load of 17 m on the roof of the structure. In the Reference the tunnel is loaded with five different water loads, starting at 14.2 m of water and increasing with a 1 m interval up to 18.2 m. For the sake of comparison the results at 17 m is assumed by interpolating between the 16.2 m and 17.2 m values.

The force distribution is considered first. The main point of interest here is the force distribution in the roof of the structure, because this is the most critical section of the tunnel. Because of the symmetric nature of the tunnel only the force distribution in one of the roofs is observed. In the Reference the force distribution is observed in the roof, from the start of the voute closest the sidewall up to the middle wall, the same area is observed in the Model. In Figure 56 the moment distribution is presented, in Figure 57 the shear force distribution, and in Figure 58 the normal force distribution. The figure suggests that an earlier point in the shear force distribution provides a higher shear force value, however this is not the case. The height of the line in the force distribution is based on both the numerical value of the force but also on the position of the plane where the force distribution is obtained from. Additionally, the question could be asked as to why the edges of the observed roof are rather jagged. This is a by-product of the way force distribution is obtained in Atena Studio. In order to get an accurate display of the force evolution cuts need to made based on a node selection, as the mesh at the edge is not perfectly orthogonal there is a jagged appearance.

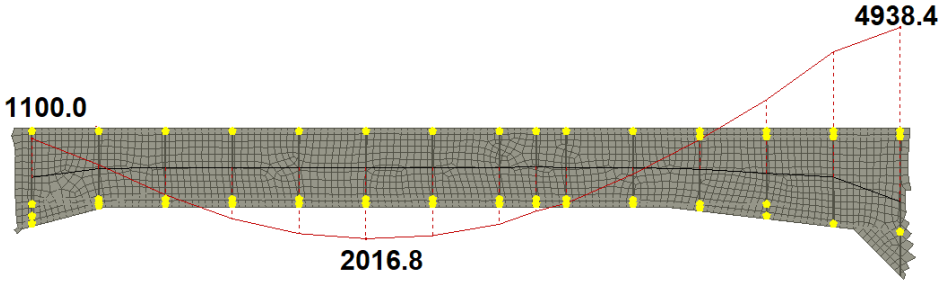

Figure 56: Moment distribution in the roof of the Heinenoordtunnel with water at +3.8 m N.A.P. (ULS)

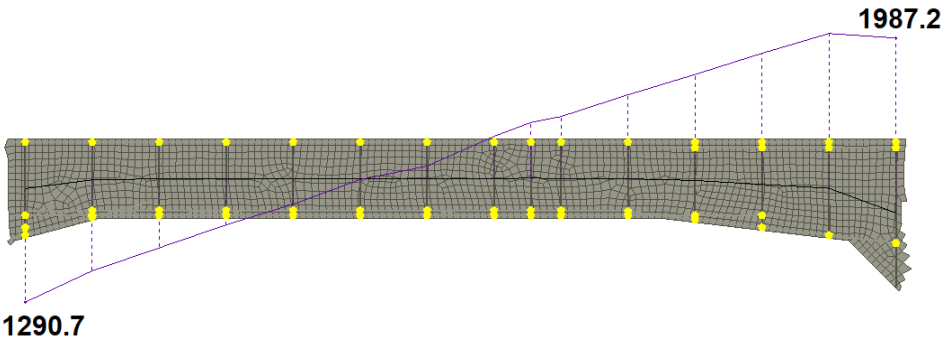

Figure 57: Shear force distribution in the roof of the Heinenoordtunnel with water at +3.8 m N.A.P. (ULS)

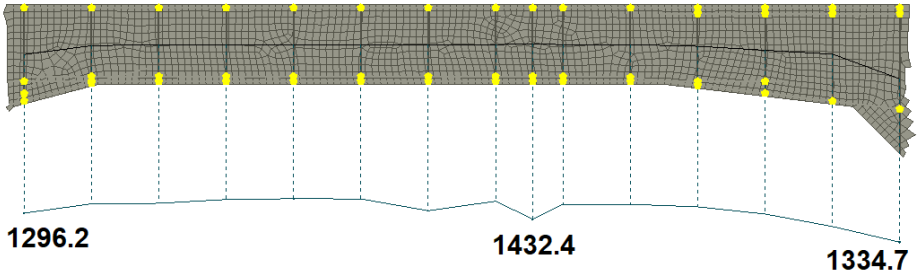

Figure 58: Normal force distribution in the roof of the Heinenoordtunnel with water at +3.8 m N.A.P. (ULS)

The various force distributions have been collected into a single table where the results are compared to those obtained in the Reference, see Table 13. For the normal force an average of the normal force readings is compared with the Reference. Overall the Model and the Reference are quite close to one another, with a maximum deviation of 6%.

Specimen	**$M_{sup,d}$**	**$M_{field,d}$**	**$M_{mid,d}$**	**$V_{sup,d}$**	**$V_{mid,d}$**	**N_d**
Model	1100	-2017	4938	1291	1987	-1364
Reference	1090	-2054	5238	1323	1897	-1453
Model/Reference	**1.01**	**0.98**	**0.95**	**0.98**	**1.05**	**0.94**

Table 13: Force distribution in the roof of the tunnel

Next, the cracks in the Model are observed. Figure 59 depicts the cracks that are formed at a water load of 17 m. Cracking is present in all the expected locations: flexural cracks from the inside of the tunnel around the midspan of the roof and floor of the tunnel, flexural cracks from the outside of the tunnel around the mid support, and some flexural cracks from the outside of the tunnel at the top of the side walls. These are all locations where high bending moments are expected. There are no shear cracks present in the Model for this load. An analysis has been made with regards to where shear cracks would occur by increasing the load even further, which is presented in paragraph 4.4.

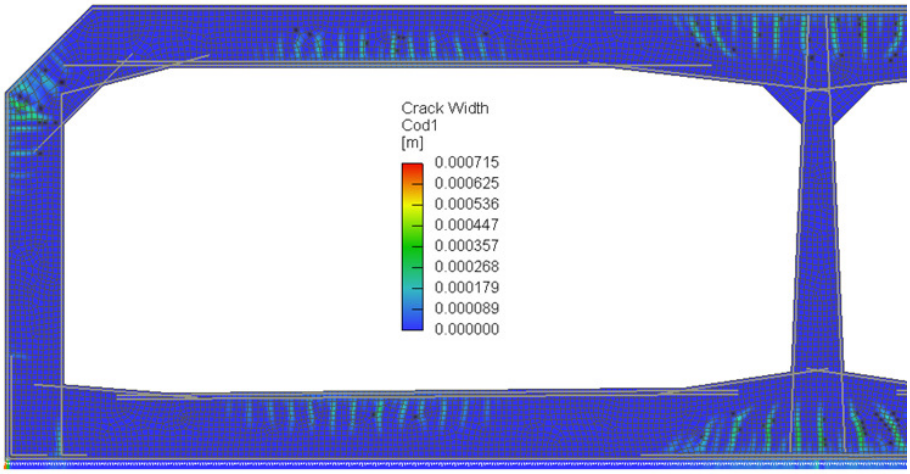

Figure 59: Crack distribution in the Heinenoordtunnel with a H.H.W. load

4.4. Failure mechanism(s)

The Model as presented in paragraph 4.3 does not fail, it shows a state of equilibrium. While the Model has mostly flexural cracks, the tunnel is expected to failure in shear. As a means of testing this, the Model is loaded further beyond the physical limit load. Presented in Figure 60 is the tunnel with a water load of 20 m (+6.8 m N.A.P., 3 m higher than the H.H.W.). This is an absolutely unobtainable water load under current circumstances, the water would be pouring over the dikes and flood the tunnel. The probability of the water level reaching even a 17 m water load in the next thirty years are already rather unlikely (P(30yr)=0.000064786) [43], but as was shown in Figure 46 and Figure 47 numerical predictors have a tendency to overestimate the shear capacity. When loading up to 20 m of water load shear crack start to develop, see Figure 60. The Model is still in equilibrium, failure does not occur, but flexural shear cracks have started to develop. This is an interesting fact however, as the IBBC-TNO method states that near the supports shear-compression failure is to be expected, not flexural shear failure.

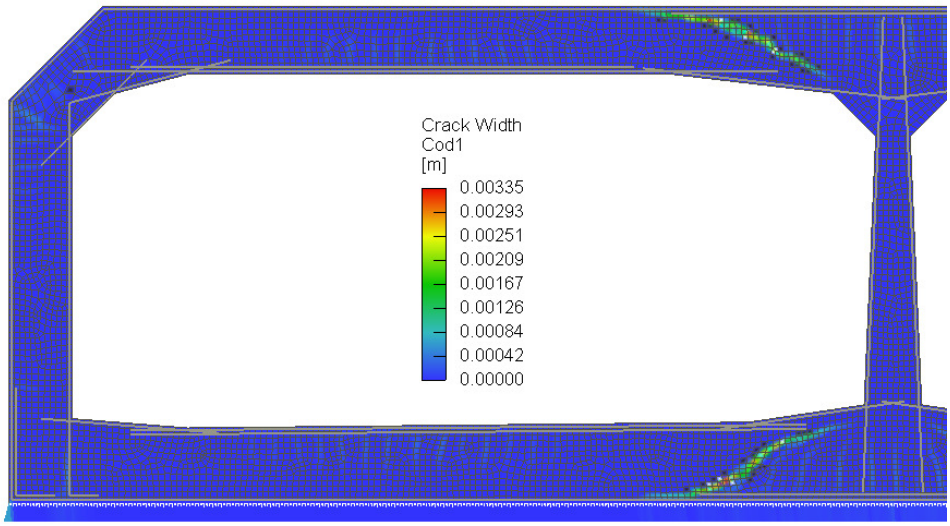

Figure 60: Crack distribution in the Heinenoordtunnel when overloaded up to +6.8 m N.A.P.

In Figure 61 the load-deflection curve of the Heinenoordtunnel is presented, based on the external force applied on the tunnel. For this reason there is an initial deflection without any load, due to self weight being an internal force. In this diagram several points are marked. The green marker in the graph represents the physical water limit, or rather, the model presented in paragraph 4.3 with a 17 m water load. The yellow marker in the graph represents the point where the model stops adhering to the convergence criteria, which occurs at a 19.25 m water load (+6.05 m N.A.P.). The model continues up to the red marker, where the divergence criteria is surpassed, which occurs at a 25 m water load. The tunnel is considered to be failing from the yellow marker onward.

Figure 61: Load-deflection curve of the Heinenoordtunnel loaded until failure

In the Reference model the tunnel did not fail either, however in the report for the probabilistic analysis the IBBC-TNO method was applied with the force distribution obtained from their Diana model to check the shear capacity. Which in itself could be argued as biased or distorted analysis. The numerical model should be able to show whether or not the shear capacity has been reached. The formulas in the IBBC-TNO method are based on empirical results for an analytical solution, yet are now used with input from a numerical model. Their reasoning for this is that due to computation time it is not reasonable to perform a 100,000 checks such as in a Monte Carlo simulation with stochastic parameters in a numerical model. With the analytical results, based on the numerical model, it is possible to perform such a vast amount of checks. Figure 62 shows the results for the shear stress and shear capacity, for C40/50 and a water load of 17.2 m in the ultimate limit state. The IBBC-TNO method states that τ_1 (as used here) represents the shear capacity against diagonal tension failure (described now as flexural shear failure [44]), and τ_2 (as used here) represents the shear capacity against shear-compression failure. τ_2 is governing close to the supports while τ_1 is governing in the field. τ_d (as used here) represents the shear stress, and if this surpasses the shear capacity a given location, such as at x = 7.7 m in Figure 62, the structure would fail.

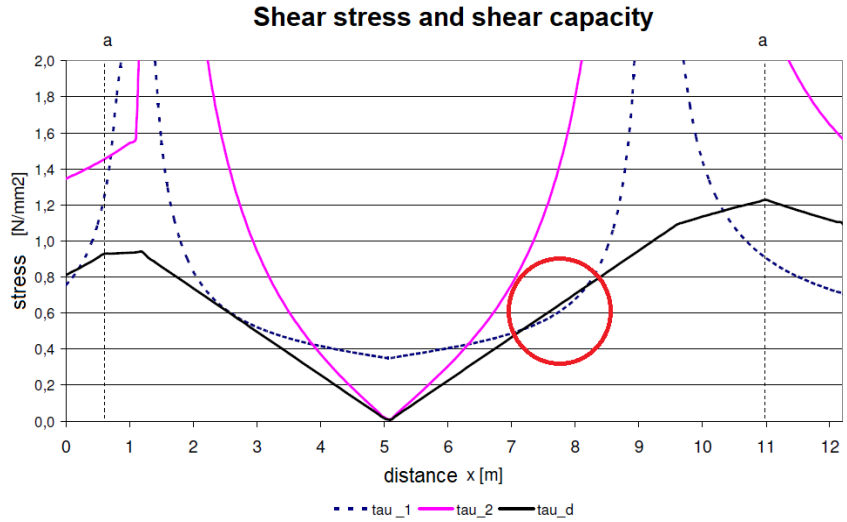

Figure 62: Shear stress and shear capacity with the IBBC-TNO method [2]

Granted, the report states that $f_{ck,cube}$ = 60 N/mm^2 would suffice for the tunnel [2], which is the case based on the concrete cores that were tested [40]. In fact, for comparison, both with the reference and with the fire loaded model, which will be discussed in Chapter 5, the Model results have been used to check the shear capacity with the IBBC-TNO method in Figure 63. In this figure the notations have been used as described in the IBBC-TNO documentation [1]. The shear stress remains lower than the nominal shear capacity for the entire roof, which does correspond with the results from the numerical model.

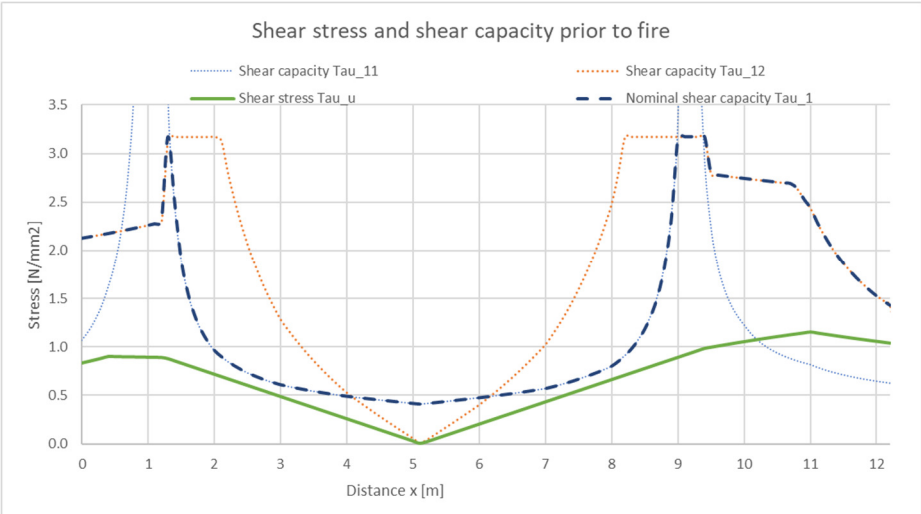

Figure 63: Shear stress and shear capacity of the Heinenoordtunnel

4.5. Discussion

The numerical model created in Atena is compared with the Diana model created by TNO in their assessment of the Heinenoordtunnel in 2009. The two models show a strong correspondence with one another. As was shown in Table 13 the deviation between the two models is minimal. This comparison was made as a means to validate the model of the Heinenoordtunnel in Atena. In validating the regularly loaded model, an extension of the tunnel model can be created upon which a fire load can be applied to check if the shear capacity of the tunnel is sufficient in case of a fire. The fire-loaded model is presented in chapter 5.

In order to say something about the safety of the Heinenoordtunnel it is worth discussing the results of the probabilistic analysis conducted by TNO, and the implications of the results found in this report on this analysis. Safety is a rather vague definition however. The Dutch Building Decree and the Guidelines for Existing Structures (RBK in Dutch) state that a reliability index β of at least 3.3 is required for existing structures in order to be deemed safe enough. However for renovation the NEN 8700 states that a minimum reliability index of β = 3.6 is required [45]. This reliability index is a measure directly correlated to the chance of failure. A higher reliability index indicates a lower chance of failure.

TNO determined a reliability index for the Heinenoordtunnel with a Monte Carlo simulation of the shear capacity at the most critical location in the roof. This location is shown in Figure 64 by combining Figure 49 and Figure 62. At this location (x = 7.7 m) the shear stress surpasses the nominal shear capacity.

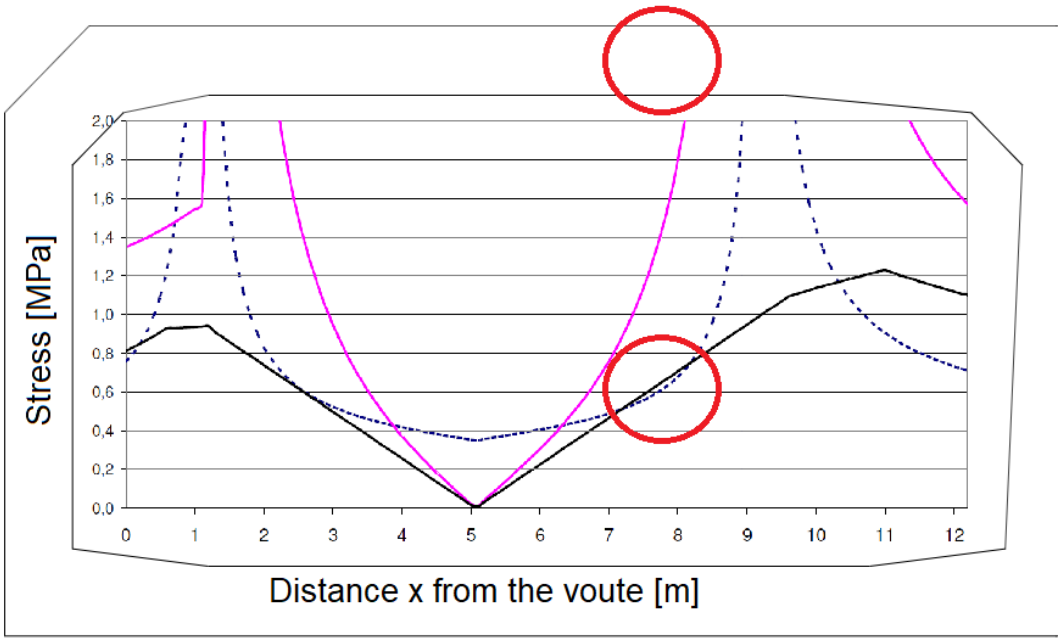

Figure 64: Most critical location in the roof of the Heinenoordtunnel according to IBBC-TNO method [2]

Various stochastic parameters are introduced for this simulation, such as the water level, the average concrete strength, but also factors to model the uncertainty of the shear capacity formula and the uncertainty of the actual shear stress. Monte Carlo simulation performs risk analysis by building models of possible results by substituting for any variable factor. A 100,000 samples are simulated to determine the chance of failure for the tunnel, and with that the reliability index β. In Table 14 an overview is provided of the reliability index for various mean compressive cubic strength grades. From this it can be seen that for a concrete class of C40/50 the Heinenoordtunnel has a reliability index of 3.42, at which point it meets the requirement of the Dutch Building Decree.

$F_{cm,cube}$ [N/mm^2]	β [-]	P_f
35	2.86	2.1 10^{-3}
40	3.06	1.1 10^{-3}
45	3.25	5.8 10^{-4}
50	3.42	3.1 10^{-4}
55	3.59	1.7 10^{-4}
60	3.74	9.2 10^{-5}
65	3.88	5.2 10^{-5}

Table 14: Reliability index β and chance of failure P_f based on compressive concrete strength [2]

Considering the compressive strength of the six *cylinder* cores taken from the Heinenoordtunnel averages to 69.1 N/mm^2 (see Table 10), it is arguable that the reliability index ought to be higher than the 3.42 derived by TNO. In their probabilistic model some rather conservative assumptions were made. The assumption was made that the average concrete cylinder core strength that was measured was in fact the expected value of the concrete cubic core strength. Additionally, the standard deviation of these cores was set to 10 N/mm^2. The validity of these choices is debatable, the sample size of tunnels studied for this standard deviation was very low (N=2), and in those two samples the standard deviation of the mean and characteristic concrete cylinder strength was 0.8 N/mm^2 and 0.7 N/mm^2 respectively [46]. These conservative assumptions lead to a significant reduction in the shear capacity. The characteristic cubic compressive strength $f_{ck,cube}$ is taken into account in the equation of the shear capacity against flexural shear failure (τ_{11}) with a factor of ($1+0.01f_{ck,cube}$). For the equation of the shear capacity against shear compression failure (τ_{12}) it is with a factor of ($1+0.06f_{ck,cube}$). The result is a reduction in shear capacity τ_{11} of 12% and a reduction of the shear capacity τ_{12} of 22%.

Interestingly enough, from numerical model in Figure 60 it can be observed that without the conservative assumption for the concrete strength, and a change in load to an extreme (and impossible) water load, the critical location in the roof appears to shift towards the partition wall. Rather than flexural shear failure, the start of compressive shear failure is seen. This is interesting because despite the increased load the IBBC-TNO method still suggests τ_{11} at x = 7.7 m should be the governing shear capacity. Granted, the structure has not failed. The numerical model is still considered to be in equilibrium, and it is known that in the case of shear compression there is still significant capacity remaining after cracking occurs. In the case of both flexural shear failure and shear compression failure, failure is initiated from pre-existing critically inclined flexural cracks. When the existing cracks in the structure at a 17 m water load are observed (Figure 59) it can be seen that there are substantially more flexural cracks, some already inclined, near the partition wall rather than at mid span. In fact, there are no flexural cracks present in the 'critical' location as determined in Figure 64. From this it makes sense why shear compression is observed near the partition wall in the numerical model.

A possible explanation for the observed discrepancies is that there is a difference between the tunnel roof and the clamped beams that were tested for the development of the IBBC-TNO method. The tunnel roof is essentially part of a continuous beam. The experiments upon which the shear capacity in the IBBC-TNO method are based do not consider continuous beams. Due to the increased bending moment at the partition wall a greater amount of flexural cracks are present at this location. Their presence could allow flexural shear cracks to develop sooner.

Both the results of the numerical model in Atena and the probabilistic analysis conducted by TNO suggest that the Heinenoordtunnel is just barely safe, but in the very least in accordance with the Dutch Building Decree and the RBK. A caveat to this is the so-called α^2 space, or the influence of the stochastic parameters on the chance of failure as shown in Table 15. In this table, based on the Monte Carlo simulations, an α^2 value is given to each stochastic parameter. These values represent how impactful the parameter is, and the sum of all these values equals to 1. It is shown that the model uncertainty factor for the shear capacity is by far the most impactful parameter, contributing for 87% to the α^2 space. In other words, the uncertainty in the shear capacity equation is convincingly the largest unknown in the probabilistic analysis. This notion is exemplified by the differences between the numerical model and the IBBC-TNO method the impossible water load as discussed earlier in this paragraph. The tunnel did not fail at this load in the numerical model though.

Table 15 shows a relatively low impact of the water level on the chance of failure of the tunnel. This could stem from the low chance of extremely high water occurring, however this result confirms that the water level is significantly less impactful than, say, the concrete compressive strength.

Stochastic parameter	α^2	X_d
Normal force component dependent on permanent loads	0.000064	0.274 [MPa]
Model uncertainty factor shear stress	0.044521	1.041 [-]
Mean cubic compressive strength	0.074529	54.87 [MPa]
Water level	0.000841	15.41 [m]
Shear stress component dependent on permanent loads	0.007225	0.174 [MPa]
Model uncertainty factor shear capacity	0.872356	-0.435 [-]

Table 15: Stochastic parameter influence α^2 and design value X_d [2]

4.6. Conclusions

With the information gathered in this chapter the following sub-question can be answered:

- How does the numerical model of the Heinenoordtunnel compare to the IBBC-TNO method?

The probabilistic analysis conducted by TNO considers various factors that make the calculation more conservative, some in ways that could not be considered in the numerical model. Model uncertainty factors are introduced for the normal force, shear stress, and shear capacity. These factors are used to account for scatter similar to the scatter found in the tests that were used to formulate the IBBC-TNO method. Additionally, a decrease in the factor representing the size effect is applied, lowering the shear capacity even further. Next, conservative assumptions were made with regard to the concrete cylinders obtained from the tunnel. On the other hand the water load was linked to the probability of the specific water level occurring, rather than assuming the physical water limit as was done in the numerical model in Atena.

Because of these factors a direct comparison between the end result of the probabilistic analysis and the numerical model does not make sense. The goal of this chapter was to validate the model of the Heinenoordtunnel under regular loading, in order to be able to confidently use the model to analyse a fire-loaded scenario. In terms of force distribution there is a strong correspondence between the numerical model in Atena and the numerical used to set up the probabilistic analysis. With deviations up to only 6% between the two models, as can been seen in Table 13. The probabilistic analysis suggests that no shear failure occurs for a 17 meter water load and the numerical model in Atena with a higher shear capacity corroborates this notion. Depending on the observed failure mode in the fire-loaded model (if any) it could be worthwhile to model with the conservative concrete strength assumption asserted in the probabilistic model, as the 11% decrease in shear capacity for τ_{11} roughly equals the overestimation found in the deep beam models in chapter 3.

5 Shear capacity of the Heinenoordtunnel under fire loading conditions

5.1. Introduction

The Atena model of the Heinenoordtunnel as described in 4.2 Model description has been validated with the results obtained by TNO and is used as a basis for the evaluation of the shear capacity under fire loading conditions. The hypothesis is that the introduction of a 2 hour RWS fire curve will cause shear failure in the roof of the tunnel. In this chapter a description will be provided of the changes made to model to incorporate the fire load, and the results of the model will be thoroughly discussed.

5.2. Model description

The fire-loaded model in Atena is created by the inclusion of a new load interval on the model as described in paragraph 4.2. The only difference for the load intervals as described is the change from ultimate limit state. Fire is considered as an accidental load, and with that characteristic loads are assumed. Other than that no changes were made to the first three load intervals.

In order to determine the temperature of the concrete as a result of the fire the temperature ingress is calculated. Assumed is a one dimensional temperature flow, which can be calculated using a partial differential equation of Fourier's law:

$$\rho * c(T) * \frac{\mathrm{dT}}{\mathrm{dt}} = \frac{d\lambda(T)}{dx} * \frac{dT}{dx} + \lambda(T) * \frac{d^2T}{dx^2}$$

Where:

ρ = density
c(T) = specific heat
λ(T) = thermal conductivity coefficient
T = temperature
t = time
x = location coordinate

PCTempFlow has been used to calculate and display the temperature ingress for the Heinenoordtunnel. The roof of the Heinenoordtunnel and the top meter of the walls are protected with heat resistant cladding, 27.5 mm thick plates that protect the concrete surface from the brunt of the temperature load. The application of such cladding is almost a necessity, as the maximum concrete temperature of 380 °C would otherwise be reached very quickly. These plates have a density of 870 kg/m^3 and a thermal conductivity coefficient and specific heat as specified by the manufacturer, see Figure 65.

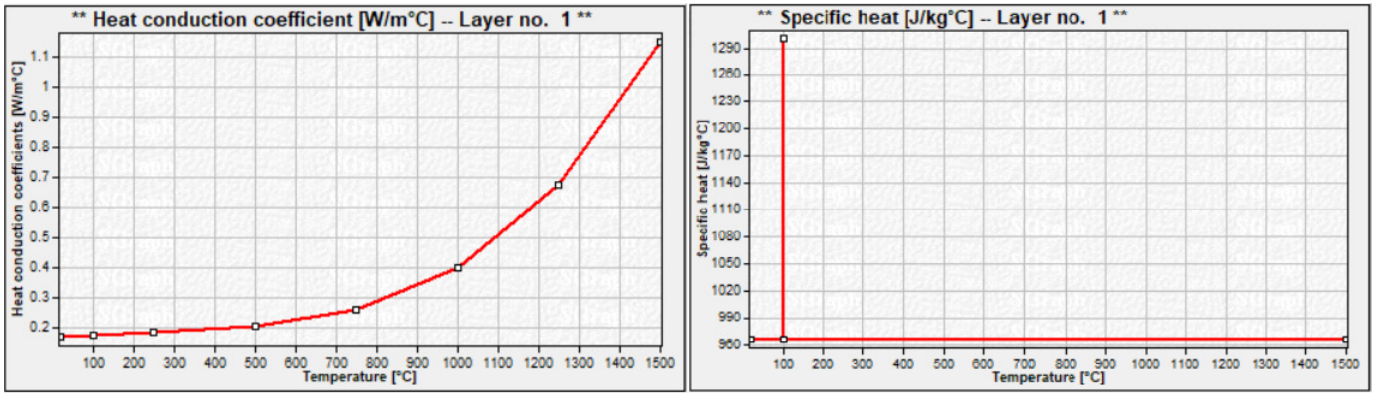

Figure 65: Thermal conductivity coefficient (left) and specific heat (right) for the applied heat resistant cladding

For concrete the parameters have been applied as per Eurocode 1992-1-2 chapters 3.3.2 and 3.3.3, see Figure 66.

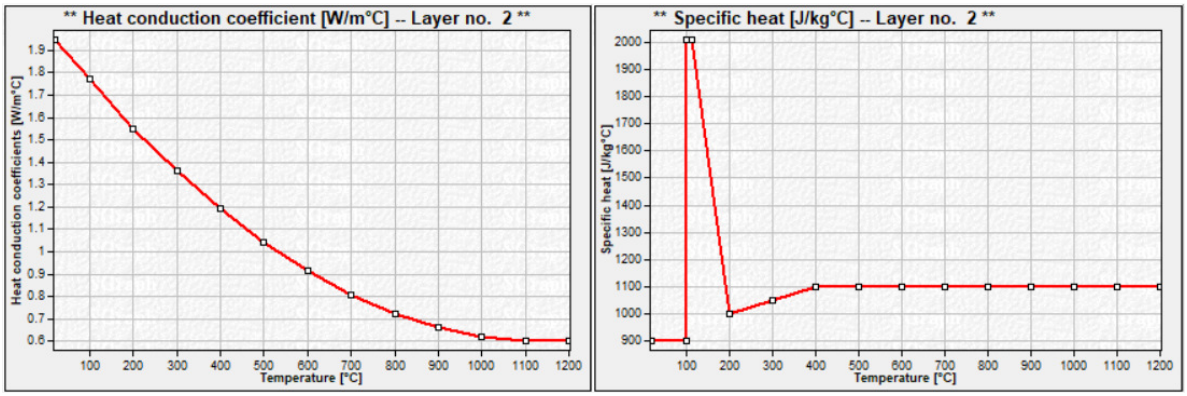

Figure 66: Thermal conductivity coefficient (left) and specific heat (right) for the concrete

Figure 67 shows the temperature ingress for roof of the tunnel. Due to the way a temperature load is modelled, the focus is placed upon the ingress after a two hour fire. The load itself is split up in load steps as with any load, which then directly acts as a way to linearly load up to the maximum temperature. However, there is another limitation in the way temperature loads can be implemented in GiD. The input only allows for constant and linear temperature loads. In order to cope with this the temperature load has been split up in two linear loads, see Figure 68. The first load is a linear load the encompasses the first 50 mm of the concrete, the second load is a linear load to represent the temperature from 50 mm to 200 mm depth. After 200 mm of depth the concrete temperature is roughly 20 °C, at which point there are no noticeable effects of the increased temperature. This way of presenting the temperature load is slightly more negative for the structure than it actually is, but the effect should be relatively small.

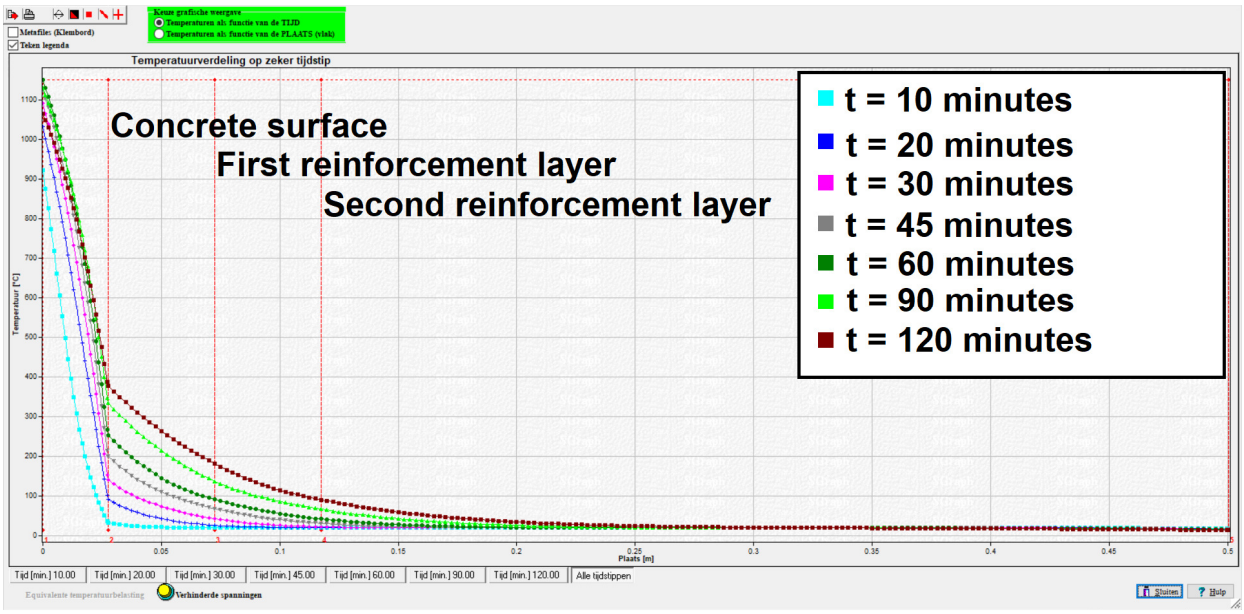

Figure 67: Temperature ingress at various times for the roof of the tunnel

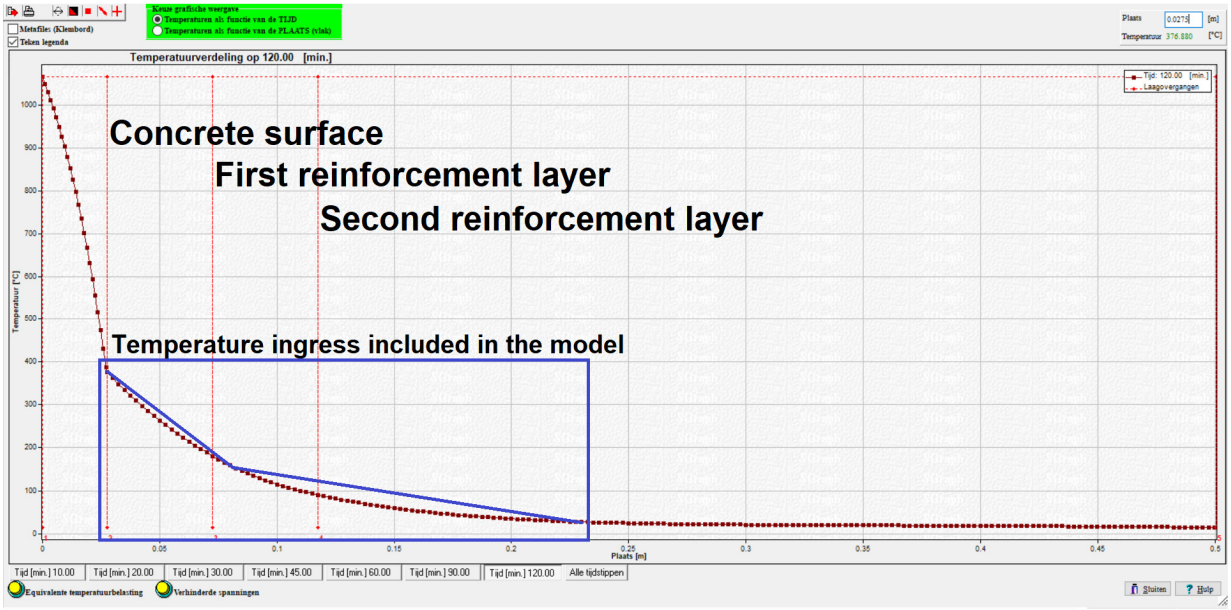

Figure 68: Temperature ingress as modelled for the roof of the tunnel

The temperature ingress is determined similarly for the rest of the tunnel. Naturally, there is a difference due to the lack of the heat resistant cladding. As a consequence, the concrete surface reaches a temperature of over 380 °C and the reinforcement reaches a temperature of over 250 °C, however these ROK rules don't have to be applied to for the walls as the outer reinforcement bars carry the bending moment. The temperature ingress is shown in Figure 69. The temperature ingress in the floor of the tunnels is modelled as inconsequential. Due to the presence of a thick layer of ballast concrete the temperature in the floor does not reach levels where the performance is impacted.

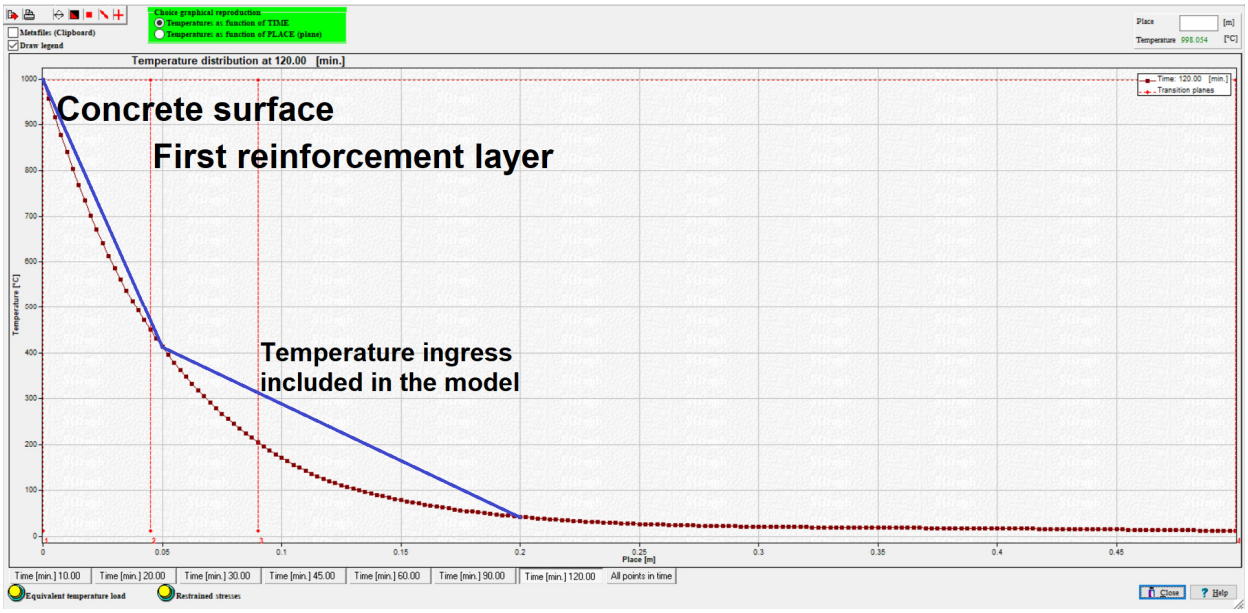

Figure 69: Temperature ingress as modelled for walls without heat resistant cladding

In Table 16 and Figure 70 an overview is given of the start and end values of the linear temperature distribution as applied in the model. For the application in the model an extra step needed to be performed. In order to apply a linear temperature load in GiD a set of equations needs to be solved for every single surface which have a temperature load, this is a surface as applied in GiD, not actual surfaces. In order to model the temperature loads the concrete surfaces in GiD were split up in three parts, two with the linear temperature loads (surface to 50 mm depth and 50 mm depth to 200 mm depth), and one without a temperature load (rest of the concrete). The temperature load is then defined as the sum of a constant, the x coordinate times a coefficient, and the y coordinate times a coefficient. So for every surface there is a system of four equations and three unknowns that need to be solved. An example is given for an inner surface with cladding:

$$ax_1 + by_1 + c = 376.88$$
$$ax_2 + by_2 + c = 376.88$$
$$ax_3 + by_3 + c = 165.76$$
$$ax_4 + by_4 + c = 165.76$$

Here $x_1..x_4$ and $y_1..y_4$ represent the corners of the surface observed. Solving these for a, b, and c provides the constant and coefficients needed to implement the temperature load.

Location	Temperature w. cladding	Temperature w/o cladding
Surface	376.88	998.05
50 mm depth	165.76	413.42
200 mm depth	27.81	42.88

Table 16: Linear temperature distribution over depth

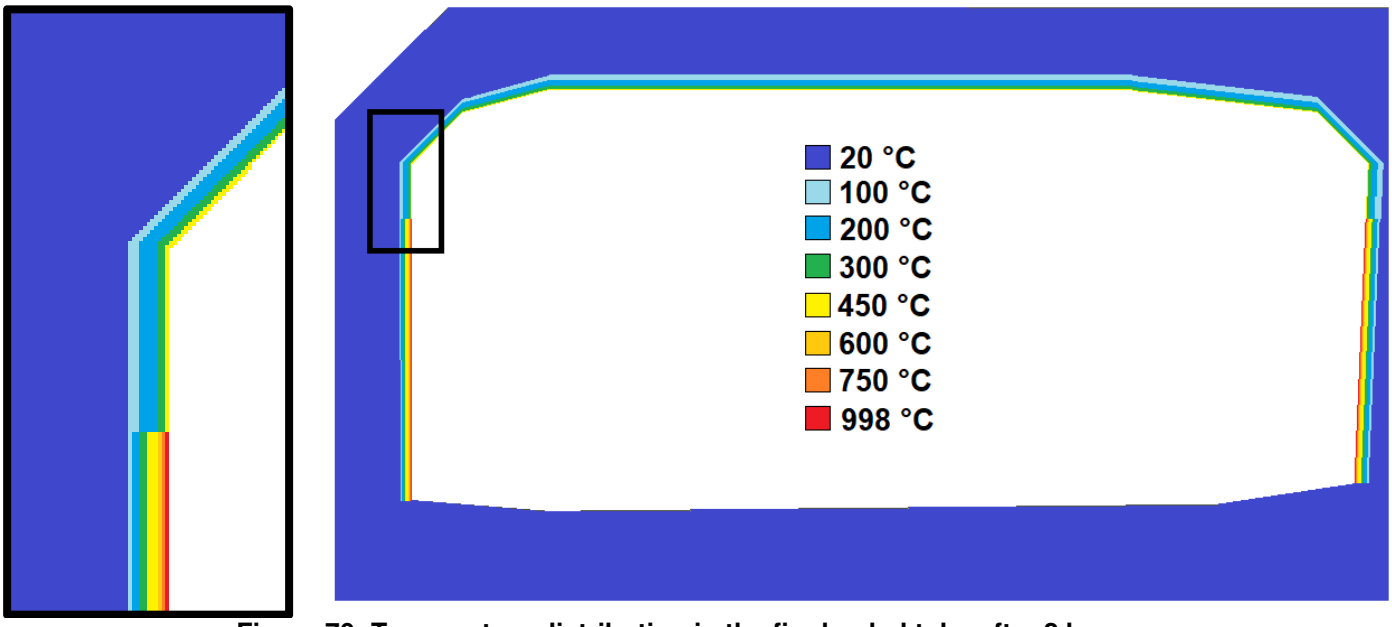

Figure 70: Temperature distribution in the fire loaded tube after 2 hours

The temperature in the structure has been determined, next is the actual effect this has on the material. One of the additional options in GiD is the material specification “CementitiousWithTempDepProperties” which, as the name implies, is the default non-linear cementitious material, but with temperature dependent properties available. By using this material specification the user gets the option to define functions for the reduction of various parameter due to the increase in temperature. The following parameters are able to be defined as a function of the temperature: Young’s modulus, tensile strength, compressive strength, onset of crushing, critical crushing displacement, plastic strain, fracture energy, and thermal strain. Similarly, the reinforcement has options to change the yield stress and thermal strain based on the temperature.

For concrete the effect of temperature on several of the listed parameters is provided in Eurocode 1992-1-2 [19]. In Figure 71 the effects on compressive strength and tensile strength is listed, from table 3.1 and figure 3.2 in [19]. In order to prevent any possible singularity issues the maximum reduction is limited to 0.01. Onset of crushing is directly linked to the reduction of the compressive strength. Figure 72 contains the thermal strain in both concrete and steel as a result of an increase in temperature, from figure 3.5 and 3.8 in [19].

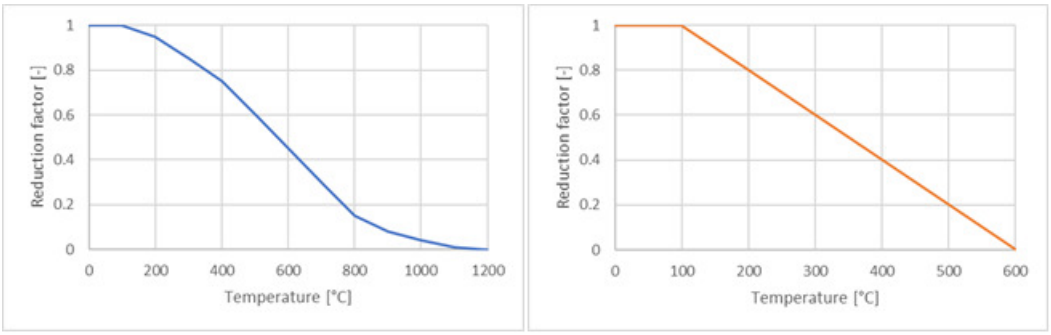

Figure 71: Reduction of compressive strength (left) and tensile strength (right) at elevated temperatures [19]

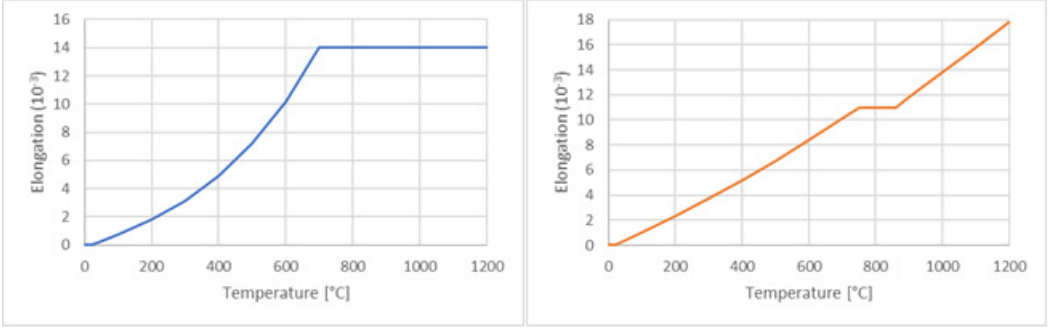

Figure 72: Thermal strain of concrete (left) and steel (right) at elevated temperatures [19]

The reduction of the yield stress of the reinforcement is presented in Figure 73, from table 3.2a in [19]. From this it can be concluded that the yield stress is unaffected for the roof with its heat resistant cladding, as there is no reduction until a temperature of 300 °C.

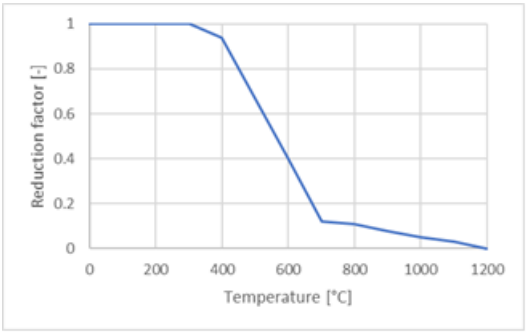

Figure 73: Reduction of the yield stress of reinforcement bars at elevated temperatures [19]

The other parameters that can be defined as a function of the temperature are not specifically listed in the Eurocode, these functions have been set based on experimental results of Castillo and Durani [47] which have been validated numerically by Červenka et al. [48]. The changes in these parameters as a consequence of a change in temperature are shown in Figure 74, Figure 75, and Figure 76.

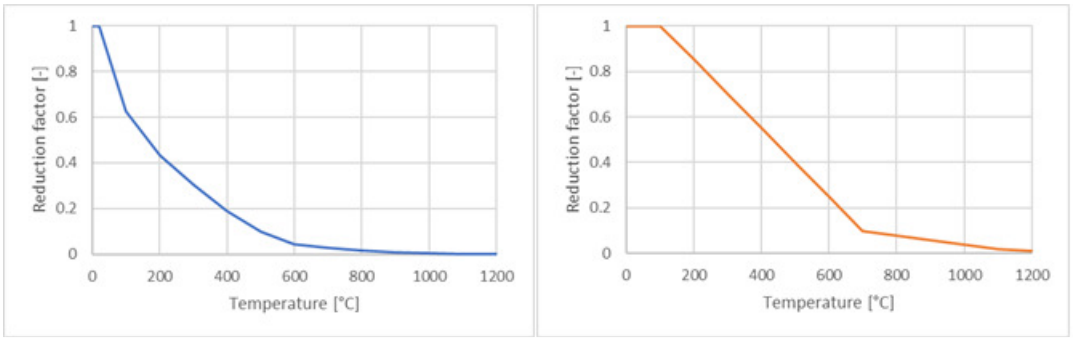

Figure 74: Reduction of the Young's modulus of concrete (left) and steel (right) at elevated temperatures [48]

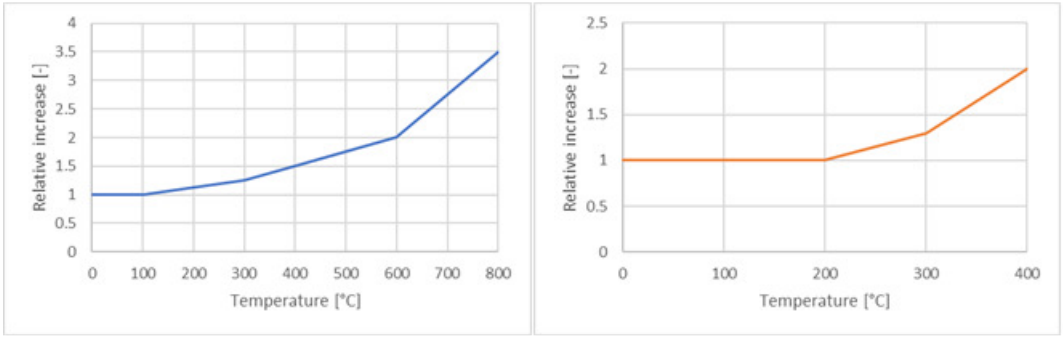

Figure 75: Relative increase in critical crushing displacement (left) and fracture energy (right) at elevated temperatures [48]

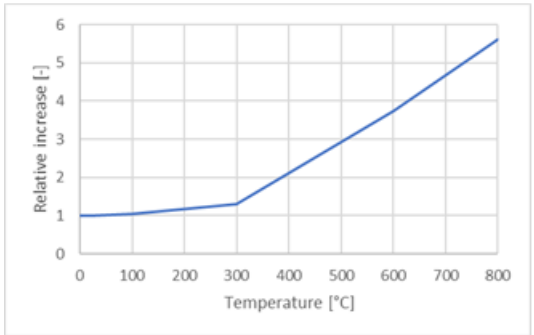

Figure 76: Relative increase in plastic strain at elevated temperatures [48]

5.3. Results

In this chapter the results of the model in Atena will be discussed and a comparison is made with the results without a fire load from paragraph 4.3. First, the force distribution is considered, it is expected that the moment distribution shifts, the moment-zero points will move inward and the maximum field moment will be reduced. This also means that the clamping moments will increase. Shear failure is an interaction between moment and shear force, and this shift will lead to greater moments with roughly the same shear force.

Starting with the moment distribution, Figure 77 shows the moment distribution in the roof and for easy comparison the moment distribution obtained in chapter 4 is also included. The moment is shifted as was anticipated, the shape is roughly retained but the clamping moments are increased by nearly 1400 kNm and the field moment is reduced by nearly 1400 kNm. This also corroborates the expectation that the shear force will remain roughly the same with the increase of temperature.

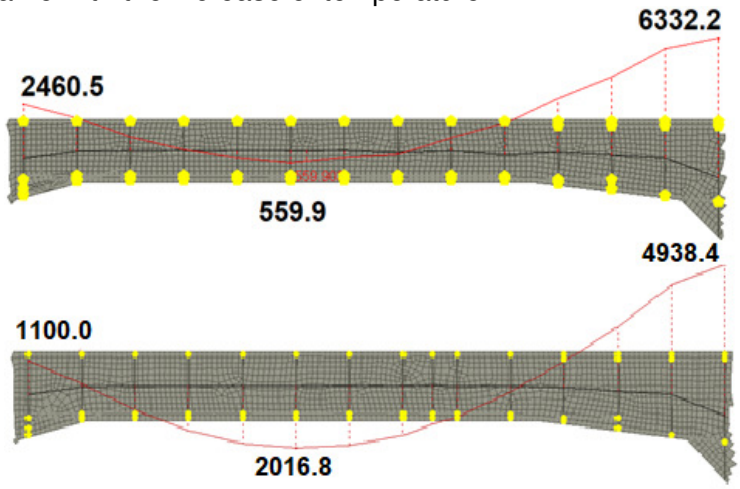

Figure 77: Moment distribution after a 2 hour fire (top) and before fire in ULS (bottom)

Next is the shear force distribution, shown in Figure 78, along with the shear force distribution obtained in chapter 4 again for comparison. The shear force is actually slightly lower in the situation after fire, a reduction of 100 kN on both ends. This can be attributed to two factors: the fire loaded model has loads an accidental load combination, while the situation before fire is in ULS, which slightly reduces the load on the structure. The other factor is related to the reduction in stiffness as a result of the increased temperature. Notable is the slight deviation in the shear force line for the fire scenario around the middle of the roof. There is more of a sudden jump visible rather than a smooth line. It is expected that is merely is visualisation error, similarly to how it appears that there is a slightly higher peak in shear force before the rightmost point is reached. The fire loaded beam has an increased deformation and the point of the shift corresponds with the largest deformation and the roofs bending point. In short, the shear force distribution slightly differs from the expectation, but this difference has been explained.

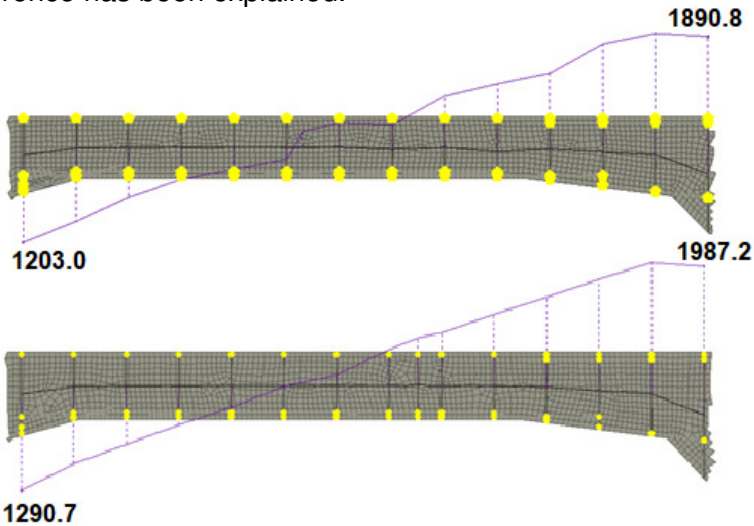

Figure 78: Shear force distribution after a 2 hour fire (top) and before fire in ULS (bottom)

The normal force distribution is now considered, see Figure 79. Overall an increase in normal force is observed, with the exception of one dip in normal force to -1075.8 kN. The average normal force increases however from -1364 kN to -1467 kN. There is an additional compressive force in the roof coming from the heated walls. As the walls want to deflect following the temperature increase, the clamping moments increase. The increase in normal force follows from the increased clamping moments.

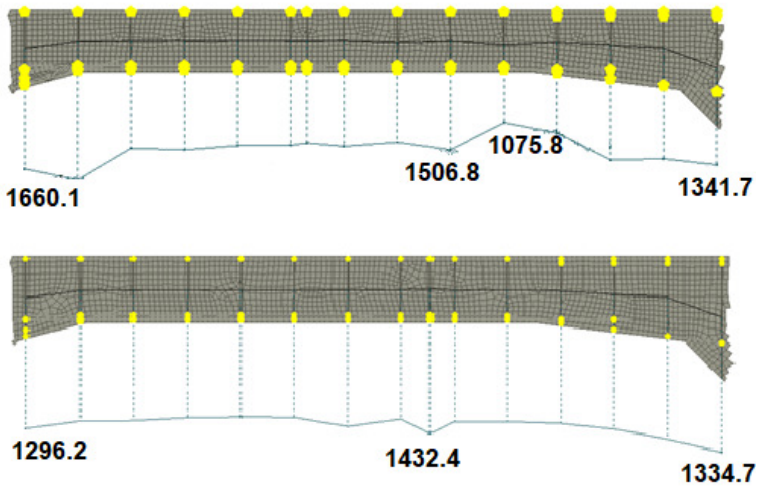

Figure 79: Normal force distribution after a 2 hour fire (top) and before fire in ULS (bottom)

Next, the deformation and cracks are observed. In Figure 80 the (exaggerated) deformed model is presented. Cracks would look distorted due to the deformation of the tunnel and will be presented in another figure. There is a clear difference in displacement between the tunnel tube with fire and without fire, loaded by fire the middle of the roof deflects by 20 to 25 mm, up from 10 to 12 mm in the situation where there is no fire in the entire tunnel. The non-fire loaded tube experiences a reduction in deflection as would be expected, deflecting only 4 to 8 mm.

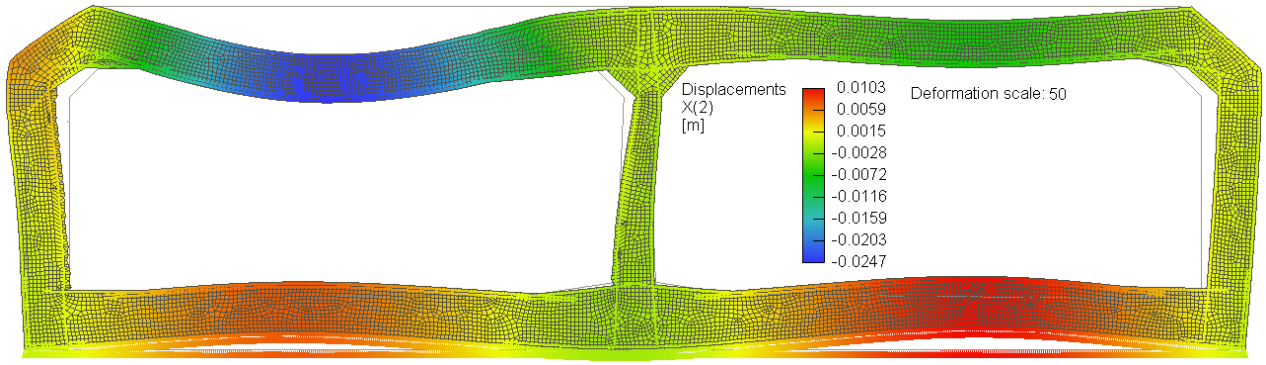

Figure 80: Deformed tunnel with vertical displacement for a fire in the left tunnel tube

In Figure 81 the cracks present in the Heinenoordtunnel after a 2 hour fire load are presented. Three cracks in particular are noted. It should be noted at this point that the tunnel is still considered to be in equilibrium by Atena, although crack #1 in particular seems to be far along in its development. The other cracks will be discussed first though. Crack #3 was already one the larger cracks visible in the non-fire loaded model, however the increased deformation of the tunnel has caused the crack to grow in width from 0.4 mm to roughly 1 mm. This type of crack could become problematic after a fire as it exposes the outer reinforcement, and cannot easily be observed or treated in situ. Crack #2 is a clear example of the start of a flexural shear crack or “diagonal shear” crack as noted in the IBBC-TNO method. The location of this crack also coincides with the location that TNO dubbed in their report as the second most likely location for shear failure to occur. Crack #1 as shown in Figure 81 actually contains two cracks worth discussing. First on the left side of the marked area is another flexural shear crack that has started developing, similar to crack #2 starting just after the voute in the roof. Much more interesting however is the other flexural shear crack that has a propagated along the roof. This crack is similar to the one observed in Figure 60, for the overloaded tunnel without a fire load. The propagation of the crack can be explained by a number of effects occurring. First, flexural cracks were already

present prior to the application of the fire load. Second, the increased temperature causes expansion (compressive forces) for the inner surface of the tunnel which leads to an increase in tensile forces for the outer surface of the tunnel, this would explain the horizontal crack propagation. The horizontal crack propagation starts about an hour into the fire and slowly but steadily starts to crack further and further along the top surface of the tunnel. The shape of the crack is similar to those observed in shear compression failure. Since the concrete does not lose its capacity as soon as the crack is formed this can be categorised as the initiation of shear compression failure. This can also be corroborated by the location of the crack, close to the partition wall.

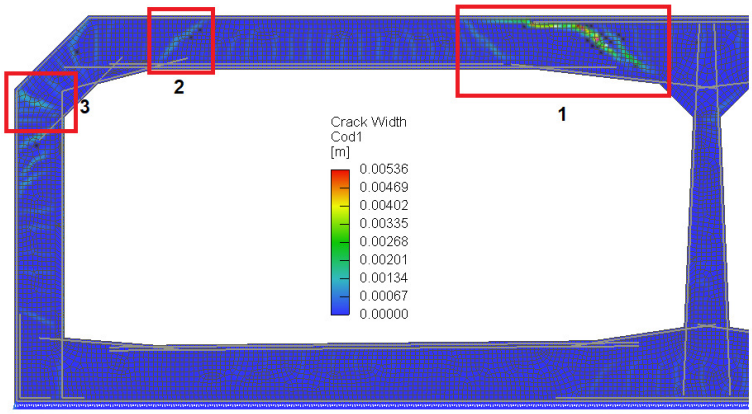

Figure 81: Crack width in the tunnel after 2 hours of fire

In term of the actual crack width, the crack seems to have fully developed and started widening. The crack has a width of 2.5 to 3.5 mm, increasing up to 5 mm at some points. One the key components in the transfer of shear forces is the aggregate interlock. Opening and slipping between two edges of cracked surfaces allows for the transfer of shear stress. As the crack width increases, the transfer of shear stress decreases. This is also one of the base principles of how the Modified Compression Field Theory (and therefor Atena) handles size effect. As the height increases, so does the crack width, decreasing the aggregate interlock contribution of shear transfer.

5.4. Failure mechanism(s)

The Atena model of the Heinenoordtunnel subjected to a fire load is still in equilibrium at the end of a two hour fire. The tunnel has not failed according to the numerical analysis. However, when the cracks in the structure are observed it suggests that the structure is very close to its limits. A massive flexural shear crack has formed, the width of which has been increasing steadily. The crack can be explained by the flexural cracks that were already present, and the effect of the increased temperature. As a result of the increased temperature on the inside layer of the roof, this part wants to expand, creating a compressive force. The outside layer of the roof is consequently loaded in tension, which would explain the horizontal crack propagation.

As was shortly discussed in paragraph 4.4, the use of the numerically obtained force distribution in the empirically obtained formulas of the IBBC-TNO method seems counter-intuitive. The numerical analysis program could have a redistribution of forces in place, remaining in a state of equilibrium. The case of a fire loaded tunnel does not necessarily fit within the scope of the formulas. A prime example of this is the fact that flexural shear cracks are observed close to the support, while the IBBC-TNO method states that there are exclusively shear compression cracks near the supports. Nonetheless, to get a sense of the performance of the tunnel the shear capacity is checked with the IBBC-TNO method based on the results in paragraph 5.3.

In Figure 82 the shear stress and shear capacity both before and after fire are presented. Just as with the shift in the moment distribution observed in Figure 77 there is a supposed shift of the shear capacity peaks. This can be explained by the change in the "shear slenderness" λ_x. For uniformly distributed loads shear slenderness is not the correct term. Shear slenderness refers to a static ratio of maximum bending moment to maximum shear force. For a point load the shear force is constant and thus there is a single point with a maximum bending moment to shear force ratio. For uniformly distributed loads this ratio is a variable, every point with its own defined bending moment to shear force ratio. This ratio is defined as:

$$\lambda_x = M/Vd$$

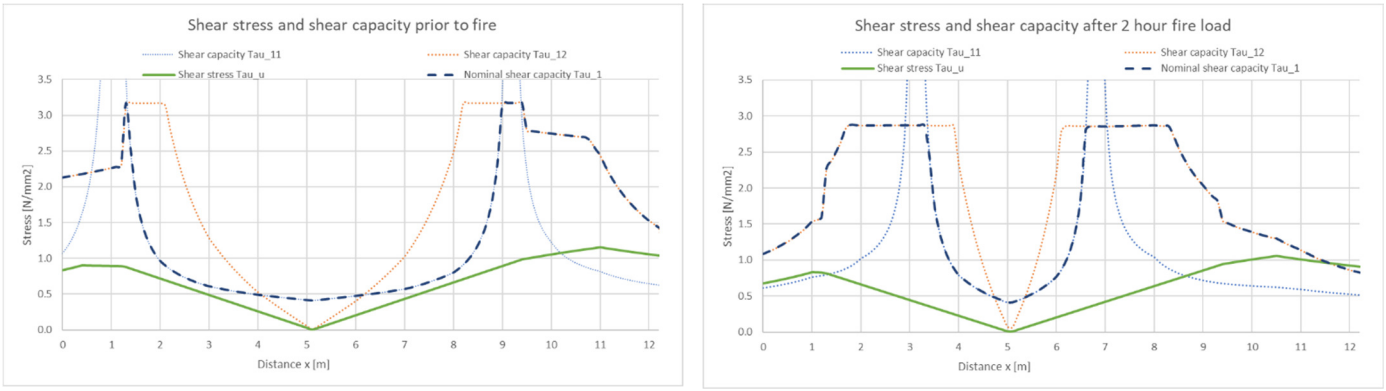

Figure 82: Shear stress and shear capacity following IBBC-TNO prior to fire (left) and post fire (right)

The shift in shear capacity is interesting, the locations that were once considered the weak points at x = 2.7 m and x = 7.7 m are now thoroughly covered by the nominal shear capacity following the shift from the increased temperature. However, the sections close to the walls which were considered to be safe, are experiencing a reduced capacity. It can be observed in Figure 82 for the fire loaded tunnel that around x = 11.7 m the shear stress starts exceeding the nominal shear capacity. This actually coincides with one of the tail ends of the flexural shear crack observed in Figure 81 at crack #1. While the structure has not failed yet, shear compression failure has initiated. This is also the type of failure that the IBBC-TNO method claims to occur.

On the other hand, it might not be realistic to use the IBBC-TNO method to determine the shear capacity in this situation. The equations for τ_{11} and τ_{12} are based on a set of experiments. While the accuracy of these equations for comparable conditions has been confirmed, the observed situation clearly lies outside the scope of the experiments. While the IBBC-TNO method does suggest shear compression failure at the same location as the critically inclined shear crack present in the numerical model, it does not mean that the IBBC-TNO method can correctly assess the shear capacity over the entire span of the roof. This can be exemplified

by considering the stress distribution in the heated concrete. In general, any temperature load can be split into three components: mean temperature, temperature difference, and eigen temperature. Since the tunnel is only heated from one side there is a significant eigen temperature, which equates to a significant eigenstress. This changes the stress distribution considerably, yet does not affect the IBBC-TNO formula in any way.

5.5. Discussion

While the tunnel has not failed according to the numerical analysis, it is clear that the fire load has had a severe impact on the tunnel. The flexural shear crack that was formed during the fire has propagated into a larger crack than the crack that was observed for the severely overloaded tunnel. The critically inclined shear crack has developed, but from other tests [51] it is known that for shear compression failure the failure load is significantly higher than the cracking load. This suggests the there is still some capacity left in the tunnel. This was tested by increasing the water level in a final load interval by 1 meter, after which the numerical model still appeared to be in equilibrium.

When the overestimation of the shear capacity from chapter 3 is considered, it could very well mean that the capacity will be reached. On the other hand, the observed situation is a world of extremes. The model considers an extreme water load in combination with an extreme fire load. The probability of either occurring is very low, the probability of both occurring at the same time is miniscule. There is no correlation between the height of the water and the likelihood of a fire occurring.

In the past 50 years there has been a fire in the Heinenoordtunnel once (May 2014), and in general the number of tunnel fires is rather small. Additionally, even when a fire occurs, the temperature load does not always reach the extremities of the RWS fire curve [52]. As such it is hard to reflect the effect the fire load in terms of a reliability index. However, considering the fact the reliability index for the Heinenoordtunnel is just barely meeting the minimum requirements, it would be prudent to take measures.

There are renovation plans for the Heinenoordtunnel for 2023/2024. Among these plans is the application of partition walls, creating an escape tunnel in the middle of Heinenoordtunnel. It is currently being considered whether or not these new partition walls should have any load bearing capacity. Doing so seems mildly effective for the tunnel in the regularly loaded scenario. The span of the roof is slightly reduced, and the shear force would be considerably reduced near the original partition wall. As a result the clamping moment is also reduced. These effects are barely noticeable for the critical locations determined in chapter 4, however they seem particularly interesting when considering the results presented for the fire loaded tunnel. Figure 83 shows a sketch of the additional partition walls in the Heinenoordtunnel and Figure 84 provides an indication of the possible reduction in shear force and bearing moment by making the walls load bearing.

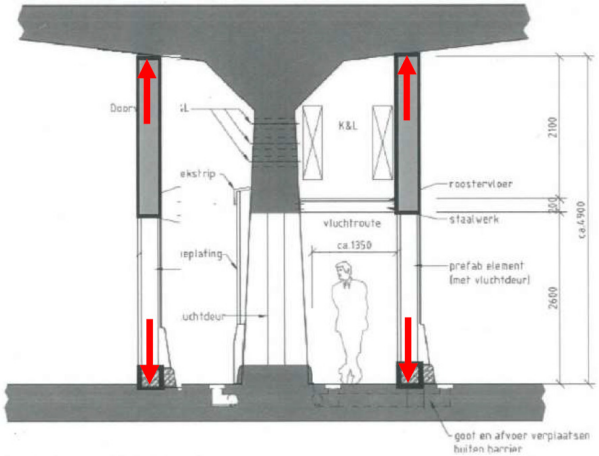

Figure 83: Application of additional load bearing partition walls [49]

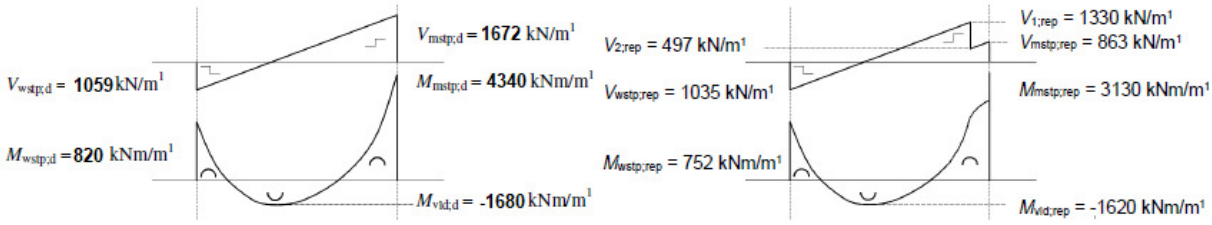

Figure 84: Indication of the reduction in shear force and bending moment from additional load bearing partition walls. Situation before (left) [2], situation after (right) [43]

5.6. Conclusions

The analysis of the Heinenoordtunnel loaded by fire was conducted in order to answer the question “To what degree does fire influence the shear capacity of the Heinenoordtunnel based on numerical analysis?”. However this is not a question with a simple to-the-point answer. The hypothesis was that that the fire load would either increase the shear stress or lower the shear capacity to the point of where shear failure would occur. The numerical analysis conducted shows that the Heinenoordtunnel does not necessarily fail, but the fire leaves the tunnel in a rather undesirable state.

Fire impacts a structure in more than one way. Temperature causes deterioration of material, depending on the magnitude this can be a permanent deterioration. The latter is not necessarily an issue, the main priority for structures such as the Heinenoordtunnel is that the structure does not collapse. Temperature causes imposed deformation, bringing additional stresses in the structure, an increased deformation, and a shift in bending moments. This shift in bending moments changes the entire system, locations that were once vulnerable can gain extra capacity, and locations that were safe initially may suddenly lose capacity. It creates a totally new situation that needs to be considered.

Numerical analysis shows that for the Heinenoordtunnel a fire can cause a weakness in the roof close to the partition wall, locally reducing the shear capacity, and causing a large flexural shear crack to form. When the results from the size effect beams discussed in chapter 3 are taken in consideration, suggesting an overestimation of the shear capacity by 17%, it seems possible that the tunnel would not be able to handle it. On the other hand, this assumes a case of an extreme high tide in combination with an extremely intense fire. The odds of either occurring in the next 3 to 4 years until renovation are very low, the odds of both occurring at the same time are miniscule at best.

This leads to believe that no direct action is necessary. It is prudent however to thoroughly consider the various protective measures that could be applied during the renovation of the Heinenoordtunnel and all the consequences that come with these options. Not only that, but it should have become clear that the way shear capacity is analysed needs to be re-evaluated. This is not limited to the IBBC-TNO method, many experiments over the past couple of years have shown how we as engineers struggle to make correct shear predictions.

To get a better sense of the direct impact of fire or more insight into the safety of the Heinenoordtunnel additional analyses could be run. An analysis with a more average water load can be considered, greatly reducing the maximum load on the system could significantly reduce the impact of the fire. Another option to consider is creating a more thorough analysis of the fire load itself. A computational fluid dynamics (CFD) analysis could show that maximal obtainable fire load is less than the RWS curve, limiting the impact of the fire. A third option is to expand the current range of experiments to a more realistic representation of the tunnel. Rather than testing a point loaded beam consider testing with a uniformly distributed load, better representing the actual load on the system. Or rebuilding a part of the tunnel for testing, rather than testing a beam. This is an expensive option but this will not only help with the evaluation of the Heinenoordtunnel, but also similar tunnels such as the Velsertunnel and the understand of shear behaviour in concrete without shear reinforcement in general.

6 Conclusions and recommendations

6.1. Conclusions

In this work the shear capacity of the 1st Heinenoordtunnel has been investigated. The tunnel is analysed with the use of numerical models in the nonlinear finite element analysis program Atena. The primary interest is the shear behaviour of the tunnel when subjected to fire. Before modelling the tunnel a series of beams were analysed in order to validate material settings. This leads to the first sub-question:

- To what degree is the size effect of concrete taken into account when modelling with in Atena? How accurate is the shear capacity prediction of Atena for deep beams?

Size effect in Atena is not a variable that can be tweaked like a model parameter, it is accounted for in the constitutive relation between the crack width and shear stress. An increase in concrete height leads to an increase in crack width. As the crack widens, aggregate interlock is reduced and so is the ability to transfer shear force.

Various beam models have been considered, with varying material models and parameter settings. In the case of deep beams (h=1200mm) all models overestimated the shear capacity in their prediction. The best prediction still overestimated the shear capacity by 17%. Several possible reasons for this overestimation have been discussed and where possible tested. It was found that a very fine mesh size has a significant impact on the shear capacity, however not significant enough to account for the 17% overestimation.

The following sub-question is directly related to the beam models that were tested:

- Which parameters are critical for a 2D Atena analysis of the shear capacity?

In order to find cracking loads comparable to those observed in experiments, the tensile strength of concrete needed to be significantly reduced. For deep beams a 45% reduction in tensile strength was necessary in order to do so. Additionally, it was found that shrinkage has a considerable impact on the obtained failure load. A special emphasis is put on the compressive strength of concrete, considering several material parameters, including the aforementioned tensile strength, are usually calculated based on their relation to this material property. Another parameters that was concluded to be critical for a 2D analysis of the shear capacity in Atena is the mesh size as discussed in the previous sub-question.

It should be noted that, while applying the material changes such as tensile strength reduction leads to a better representation of the observed experiments in Atena, there are still discrepancies between the numerical and experimental results. The numerical model still overestimates the shear capacity, albeit to a lesser extent than a numerical model without these changes. With the knowledge obtained from the beam models a model has been created of the Heinenoordtunnel. First, a regularly loaded model was considered, meaning without a fire load. As a means of validating this tunnel model it was compared to a model created by TNO for their assessment of the Heinenoordtunnel in 2009. This prompts the following sub-question:

- How does the numerical model of the Heinenoordtunnel compare to the IBBC-TNO?

The probabilistic analysis of the Heinenoordtunnel was performed with the analytical results of the IBBC-TNO method using a numerical model as input for the force distribution. This force distribution showed a strong correspondence with the force distribution obtained in Heinenoordtunnel model in created in Atena. A maximum deviation of 6% was found, with an average deviation of 3.5% in the force distribution. Both analyses suggest that shear failure does not occur in the tunnel for the compressive strength obtained from cylinder tests in tunnel. However, for the probabilistic analysis several conservative assumptions were made that are not included in the numerical model.

The model of the Heinenoordtunnel is subsequently analysed with a fire load, which leads to the governing research question:

To what degree does fire influence the shear capacity of the Heinenoordtunnel based on numerical analysis?

Temperature increase has a debilitating function on concrete material parameters. In addition, heated concrete wants to expand and causes stress build-up when it cannot expand. The temperature ingress from a two hour Rijkswaterstaat fire curve has been determined and gradually applied in the numerical model. The most critical part of the structure is the roof. For the roof of the tunnel it is observed that the increase in temperature causes a shift in the moment distribution. This shift causes an increase in the clamping moments near the walls of the tunnel and a decrease in the field moment. With the help of the IBBC-TNO method an explanation is provided for how this affects the shear capacity in the roof of the tunnel. A critical factor in the determination of the shear capacity is the ratio of bending moment to shear force. The shift in moment distribution consequently causes a change in the bending moment to shear force ratio, shifting the shear capacity. It is shown that this results in strengthening of low shear capacity locations at the cost of shear capacity near the walls of the tunnel.

This change in shear capacity is observed in the numerical model where a flexural shear crack has developed near the partition wall. Considering the location of the crack, and the fact that capacity was not lost after the crack formation this can be the initiating of shear compression failure. The model indicates that the tunnel has not failed, the model is still considered to be in equilibrium. In the case of shear compression failure there is usually considerable capacity remaining after crack formation from a compressive strut to the support. However considering the overestimation in shear capacity observed for the deep beams some caution is advised.

At the start of this thesis the hypothesis was that the Heinenoordtunnel would fail in shear when exposed to fire.

6.2. Recommendations

The situation observed in this thesis is rather extreme in nature. Assumed is an absolute maximum water load on the tunnel with an extremely intense fire load. In terms of further research it could be interesting to use computational fluid dynamics to model the fire. In doing so the impact of a fire could more accurately be represented, possibly reducing the intensity of the load. In order better estimate the impact of the fire on the structural reliability of the Heinenoordtunnel an analysis with an averaged water load should be considered. This would dramatically reduce the load on the tunnel, although it would also reduce the normal force which acts as a sort of prestressing for the roof of the tunnel.

For the renovation of the Heinenoordtunnel additional partition walls are planned. These are positioned close to the location where the shear capacity is critical in the fire loaded model. If these walls are made to be load bearing, it could significantly reduce the bending moment and shear force. Additionally, these partition walls will cause a change in temperature distribution as the original partition wall will no longer be directly exposed to the fire. This could in turn impact the shift in shear capacity.

There are still some uncertainties with regard to shear beam test results and their translation to representative results for tunnels. Not only in size effect, but also in terms of a slab effect (a possible increase in capacity with increasing width). Experiments on this subject provide conflicting results. It would be interesting to see if this slab effect can be reproduced in a numerical model and to what degree it impacts the shear capacity.

The IBBC-TNO method turned out to be a somewhat ill-fitting method of assessing the shear capacity of concrete at elevated temperatures. While the method suggested the same location of the critical shear crack as observed in the numerical model, it is lacking in a specific aspect. An increase in temperature can lead to a significant thermal stress in the concrete. The IBBC-TNO method was not created with this change in the stress distribution in mind. If method is ever re-evaluated, this could be interesting to incorporate.

Bibliography

[1] Van den Beukel, A., Monnier, T., 1985. Dwarskracht. Insituut TNO voor bouwmaterialen en bouwconstructies. https://www.cob.nl/wp-content/uploads/2018/01/GWO-408.CT_.14.A.pdf

[2] Zwarthoed, J., Gijsbers, F., Vrouwenvelder, A., Courage, W., and van der Veen, C. 2009. TNO-rapport TNO-034-DTM-2009-01448/B Controle dwarskrachtcapaciteit Heinenoordtunnel. TNO Bouw en Ondergrond.

[3] Beton nieuwe tunnels minder brandwerend dan gedacht (2017, Aug 9th), *NOS*. Obtained from https://nos.nl/artikel/2187153-beton-nieuwe-tunnels-minder-brandwerend-dan-gedacht.html

[4] Tromp, A. J., van Mierlo, R.J.M., 2013. Fire Safety Engineering – Handboek voor de bouw. 2nd ed. Delft: Eburon Uitgeverij B.V. ISBN: 9789059727342. pp. 45-51

[5] Khoury, G.A., 2008. Passive fire protection of concrete structures. Structures and Buildings 161(3). pp. 135-145 https://doi.org/10.1680/stbu.2008.161.3.135

[6] Promat, 2015. Fire curves. Obtained from https://www.promat-tunnel.com/en/advices/fire-protection/fire%20curves. Accessed 25th of February 2019.

[7] Ingason, H., Lönnermark, A., Zhen Li, Y., (2003). SP Technical Research Institute of Sweden. Runehamar Tunnel Fire Tests. Obtained from http://www.diva-portal.org/smash/get/diva2:962640/FULLTEXT01.pdf

[8] fib Bulletin 38, 2007. Fire design of concrete structures – materials, structures and modelling. International Federation for Structural Concrete (fib), Lausanne, Switzerland.

[9] Khoury, G.A., 2000. Effect of fire on concrete and concrete structures. Progress in Structural Engineering and Materials, volume 2, issue 4. pp. 429-447 https://doi.org/10.1002/pse.51

[10] fib Bulletin 46, 2008. Fire design of concrete structures – structural behaviour and assessment. International Federation for Structural Concrete (fib), Lausanne, Switzerland.

[11] Fletcher, I.A., Welch, S., Toredo, J.L., Carvel, R.O., Usmani, A., 2007. The behaviour of concrete structures in fire. Thermal Science, volume 11, no. 2. pp. 37-52

[12] RWS, 2017. Richtlijn Ontwerp Kunstwerken - ROK versie 1.4 (in Dutch). Utrecht, the Netherlands: Rijkswaterstaat Dienst Infrastructuur.

[13] Wetzig, V., 2001. Destruction mechanisms in concrete material in case of fire, and protection systems, 4th international conference on safety in road & rail tunnels. ISBN: 1901808173. pp. 281-290.

[14] Khoury, G.A., Anderberg, Y., 2000. Fire Safety Design – concrete spalling review. Sweden: Report submitted to the Swedish National Road Administration.

[15] Lottman, B.B.G., 2017. The spalling mechanism of fire exposed concrete. https://doi.org/10.4233/uuid:5b78d71b-708f-405f-b3b3-ca664b141ce0

[16] Van Aken, S., 2012. Cracking at the unheated side of a tunnel during the heating and cooling phase of a fire. http://resolver.tudelft.nl/uuid:55380aa5-5ead-43cd-b6ca-60de122d9158

[17] Ellingwood, B., Lin, T. (1991). ASCE. Flexure and shear behavior of concrete beams during fires. Obtained from https://ascelibrary.org/doi/10.1061/(ASCE)0733-9445(1991)117%3A2(440)

[18] Diab, M., 2014. Shear capacity of reinforced concrete beams at elevated temperatures. https://ir.lib.uwo.ca/etd/1884/

[19] Eurocode 2, 2011. Design of concrete structures - part 1-2: General rules - structural fire design – NEN-EN 1992-1-2+C1:2011. Brussels, Belgium: European Committee for Standardization.

[20] Robert, F. 2012. Fire resistance assessment of concrete structures. Workshop 'Structural Fire Design of Buildings according to the Eurocodes' – Brussels, 27-28 November 2012.

[21] Stiksma, K., 1987. Tunnels in the Netherlands: Underground transport connections. Utrecht: Ministerie van Verkeer en Waterstaat. ISBN 9066185368

[22] Beeldbank Rijkswaterstaat, 2008. Photo of the Heinenoordtunnel in 2008. Courtesy of Rijkswaterstaat / Joop van Houdt. https://beeldbank.rws.nl

[23] Yang, Y., van der Veen, C., de Boer, A., Hordijk, D., 2017. An experimental study on the transition of failure between flexural and shear for reinforced concrete beams. Maastricht, The Netherlands: Proceedings of fib symposium 2017, June 12-14, 2017.

[24] Červenka, V., Jendele, L., and Červenka, J., 2016. Atena Program Documentation Part 1, Theory. Červenka Consulting. Obtained from https://www.cervenka.cz/products/atena/documentation/

[25] Hendriks, M.A.N., de Boer, A., Belletti, B., 2017. "Guidelines for Nonlinear Finite Element Analysis of Concrete Structures", Rijkswaterstaat Centre for Infrastructure, Report RTD:1016-1:2017. Obtained from http://homepage.tudelft.nl/v5p05/

[26] Rots, J.G., 1988. Computational modeling of concrete fracture, Ph.D. thesis Delft University of Technology, Delft, The Netherlands. http://resolver.tudelft.nl/uuid:06985d0d-1230-4a08-924a-2553a171f08f

[27] Yang, Y., van der Veen, C., Hendriks, M.A.N., de Boer, A., 2019. Shear capacity of two simple poorly reinforced deep concrete beams. Diana ontwikkelingsvereniging. Obtained from https://www.dianausers.nl/pub/Users_Meeting_2019_Trondheim/Simulation%20Contest%20of%20two%20beam%20tests%20-%20%20final.pdf

[28] fib Bulletin 65, 2010. Model Code 2010 – Final draft, Volume 1. International Federation for Structural Concrete (fib), Lausanne, Switzerland.

[29] Malárics, V. and Müller, H.S., 2010. Evaluation of the splitting tension test for concrete from a fracture mechanical point of view. Jeju, South Korea: Proceedings of FraMCoS-7, May 23-28, 2010.

[30] Vervuurt, A.H.J.M., Steenbergen, R.D.J.M., 2012. TNO rapport TNO-060-DTM-2011-01450 Analyse van de materiaaleigenschappen voor de bepaling van het afschuifdraagvermogen van bestaande betonnen kunstwerken (eindrapportage oktober 2012).

[31] Vos, E., 1983. Influence of loading rate and radial pressure on bond in reinforced concrete: A numerical and experimental approach. http://resolver.tudelft.nl/uuid:29419e9e-9b56-41a5-94cb-d363b1c8c15e

[32] Petersson, P.E., 1981. Crack growth and development of fracture zones in plain concrete and similar materials. https://inis.iaea.org/search/search.aspx?orig_q=RN:13668228

[33] fib Bulletin 42, 2008. Constitutive modelling for high strength/high performance concrete. International Federation for Structural Concrete (fib), Lausanne, Switzerland.

[34] Vecchio, F.J., Collins, M.P., 1982. Compression response of cracked reinforced concrete. https://ascelibrary.org/doi/10.1061/%28ASCE%290733-9445%281993%29119%3A12%283590%29

[35] Dyngeland, T., 1989. Behaviour of reinforced concrete panels. Ph.D. thesis Norwegian University of Science and Technology, Trondheim, Norway

[36] Van Mier, J.G.M., 1986. Multi-axial strain-softening of concrete, part I: fracture. Materials and Structures, RILEM.

[37] Červenka, V., Červenka, J., Pukl, R., Sajdlova, T., 2016. Prediction of shear failure of large beam based on fracture mechanics. Berkley, United States of America: Proceedings of FraMCoS-9, May 29 – June 1, 2016. https://framcos.org/FraMCoS-9/Full-Papers/29.pdf

[38] Cruz, J., Barros, J., Azevedo, A., 2004. Elasto-plastic multi-fixed smeared crack model for concrete. Obtained from: http://hdl.handle.net/1822/13004

[39] Iguro, M., Shioya, T., Nojiri, Y., Akiyama, H., 1984. Experimental studies on the shear strength of large reinforced concrete beams under uniformly distributed load. DOI: 10.2208/jscej.1984.348_175 Obtained from: https://www.jstage.jst.go.jp/article/jscej1984/1984/348/1984_348_175/_article/-char/ja/

[40] Witteveen+Bos, 2009. Materiaalonderzoek kunstwerk 37H-312-02 '1e Heinenoordtunnel'.

[41] Weertman, D., de Rijke, W., 2004. Richtlijn beoordelen bestaande kunstwerken (RBBK). Utrecht, the Netherlands: Rijkswaterstaat Dienst Infrastructuur.

[42] Pryl, D., Červenka, J., 2019. Atena program documentation part 11, Troubleshooting manual. Červenka Consulting. Obtained from https://www.cervenka.cz/products/atena/documentation/

[43] Burggraaf, H.G., Gijsbers, F.B.J., 2018. Dwarskrachtonderzoek Heinenoordtunnel. Delft, the Netherlands. TNO-rapport R10209.

[44] Yang, Y., 2014. Shear Behaviour of Reinforced Concrete Members without Shear Reinforcement. ISBN 978-94-6169-516-1

[45] NEN 8700, 2011. Assessment of existing structures in case of reconstruction and disapproval. Nederlands Normalisatie-instituut

[46] Vervuurt, A., Courage, W., Steenbergen, R., 2012. Betonsterkte bestaande constructies. Cement 2012/4. Obtained from https://www.cementonline.nl/artikel/betonsterkte-bestaande-constructies

[47] Castillo, C. & Durani, A.J. 1990. Effect of transient high tem-perature on high-strength concrete, ACI Materials Journal, v 87 n 1, p 47-53.

[48] Cervenka, J., Surovec, J., Kabele, P., Zimmerman, T., Strauss, A., Bergmeister, K., 2007, Numerical simulation of fracture and damage in RC structures due to fire., Fracture Mechanics of Concrete and Concrete Structures, ISBN 978-0-415-44616-7, pp. 727-736.

[49] Wolsink, G.M. (21 maart 2017). Versterking dwarskrachtcapaciteit 1e Heinenoordtunnel; enige oriënterende gedachten. Rijkswaterstaat.

[50] Chen, W.F., 1982. Plasticity in Reinforced Concrete. ISBN 978-1932159745

[51] Zarate, G. I., 2018. Analysis of shear transfer mechanisms in concrete members without shear reinforcement based on kinematic measurements. http://resolver.tudelft.nl/uuid:9b40b743-73b3-4698-9e9b-c6ac05f5f99c

[52] de Feijter, M.P., van Mierlo, R.J.M., 2015. Investigation into the fire in the Heinenoordtunnel on 21 May 2014. Efectis report 2015-Efectis-R000143. Obtained from https://www.ifv.nl/kennisplein/Documents/20150201efectis-investigation-into-the-fire-in-the-heinenoordtunnel-on-21-may-2014.pdf

[53] Ghahremannejad, M., Abolmaali, A., 2018. Prediction of shear strength of reinforced concrete beams using displacement control finite element analysis. DOI: 10.1016/j.engstruct.2018.05.048

[54] Sherwood, E.G., Lubell, A.S., Bentz, E., Collins, M.P., 2006. One-Way Shear Strength of Thick Slabs and Wide Beams. DOI: 10.14359/18229

Appendix

A122: SBeta base model

The reinforcement described in Figure 90 and Figure 91 are used for all A122, A123, and A75 models.

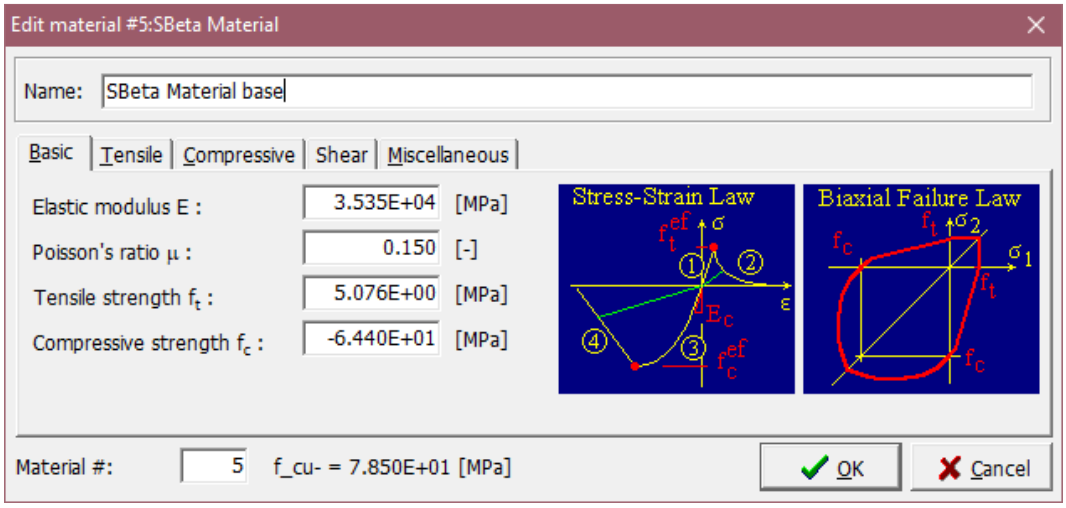

Figure 85: Finite element material specifications SBeta base model

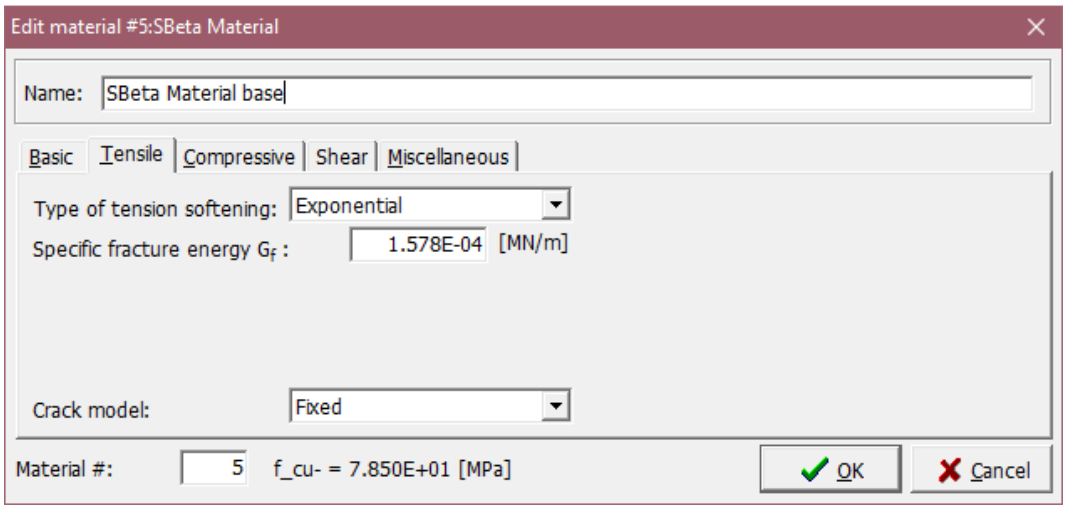

Figure 86: Finite element material specifications SBeta base model

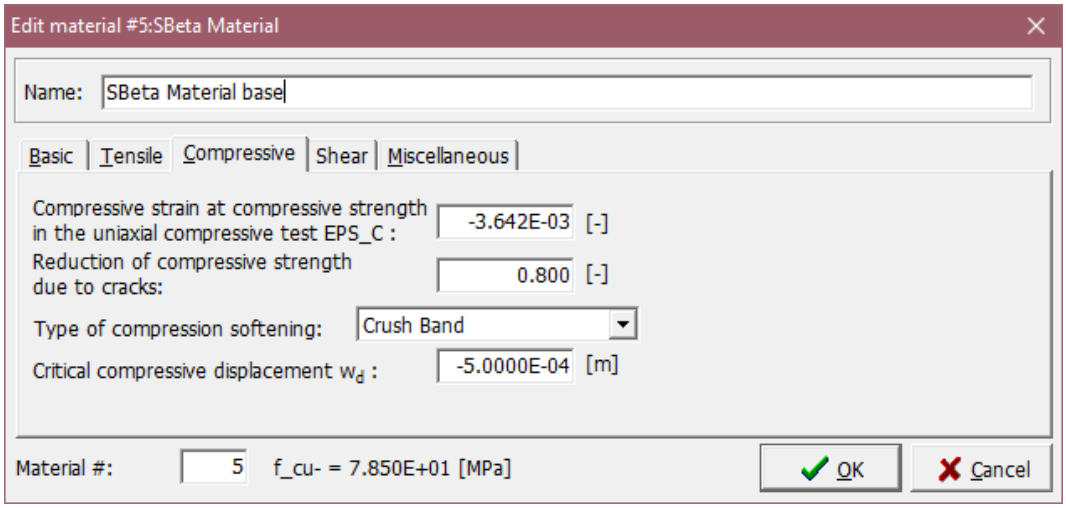

Figure 87: Finite element material specifications SBeta base model

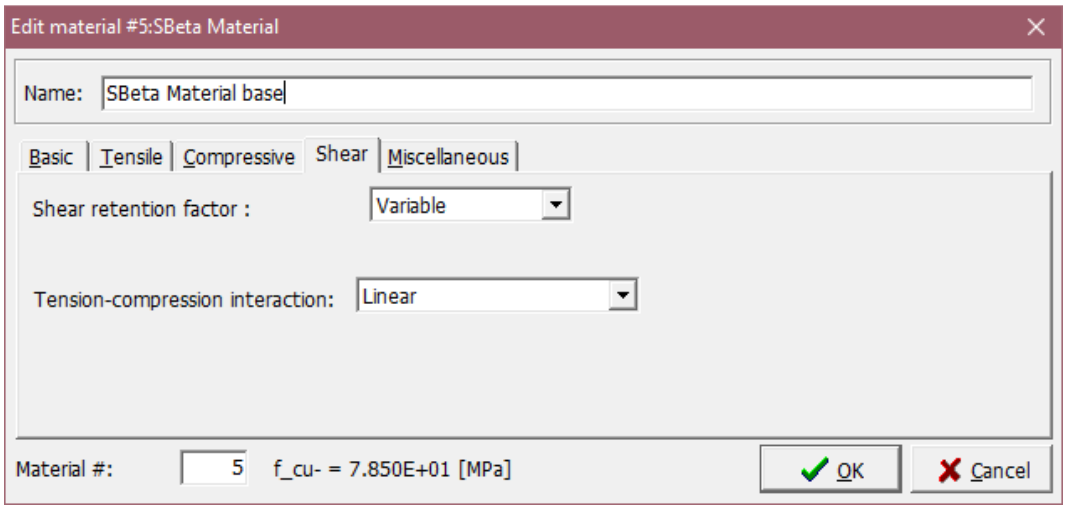

Figure 88: Finite element material specifications SBeta base model

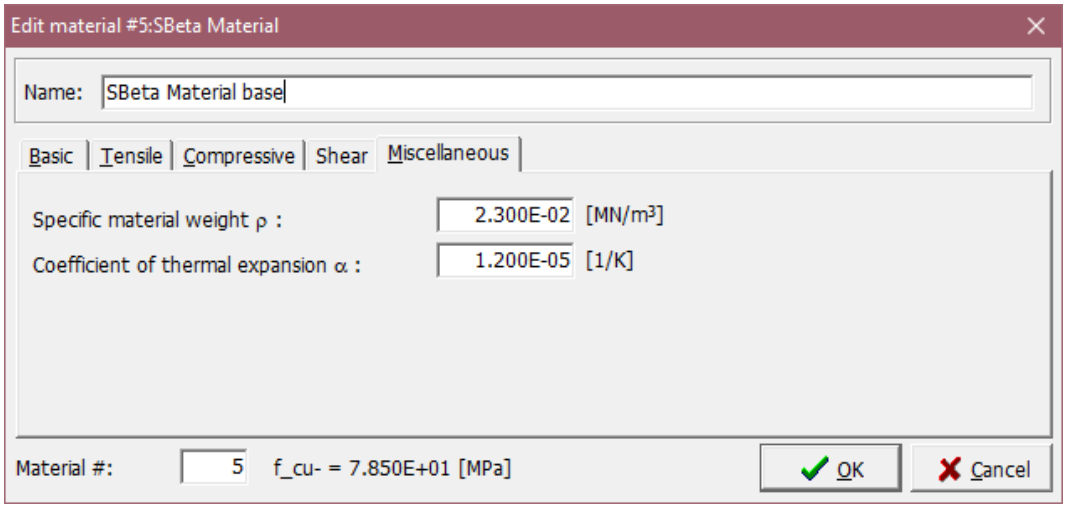

Figure 89: Finite element material specifications SBeta base model

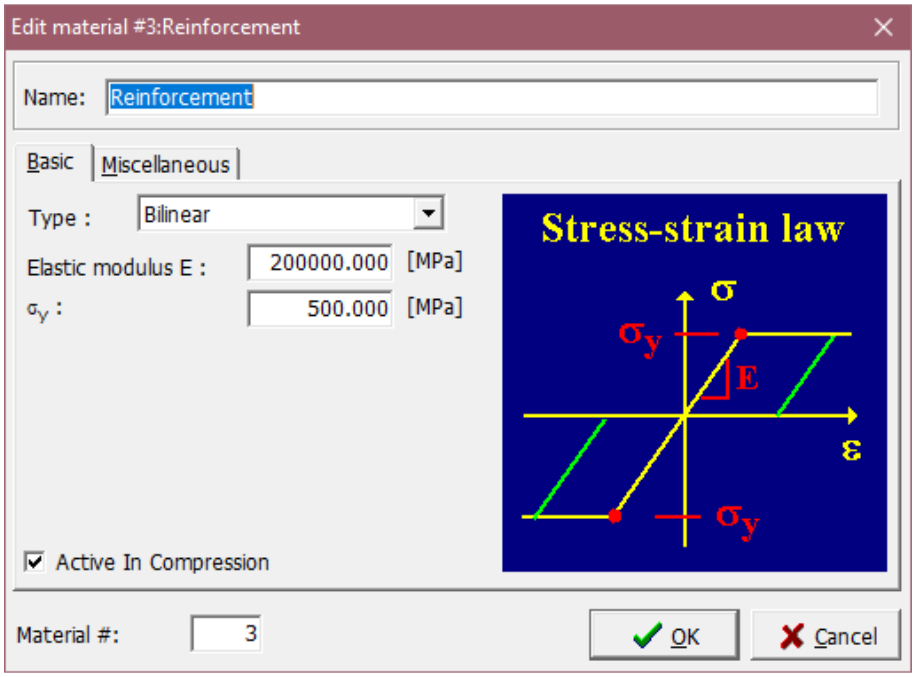

Figure 90: Finite element material specifications SBeta base model

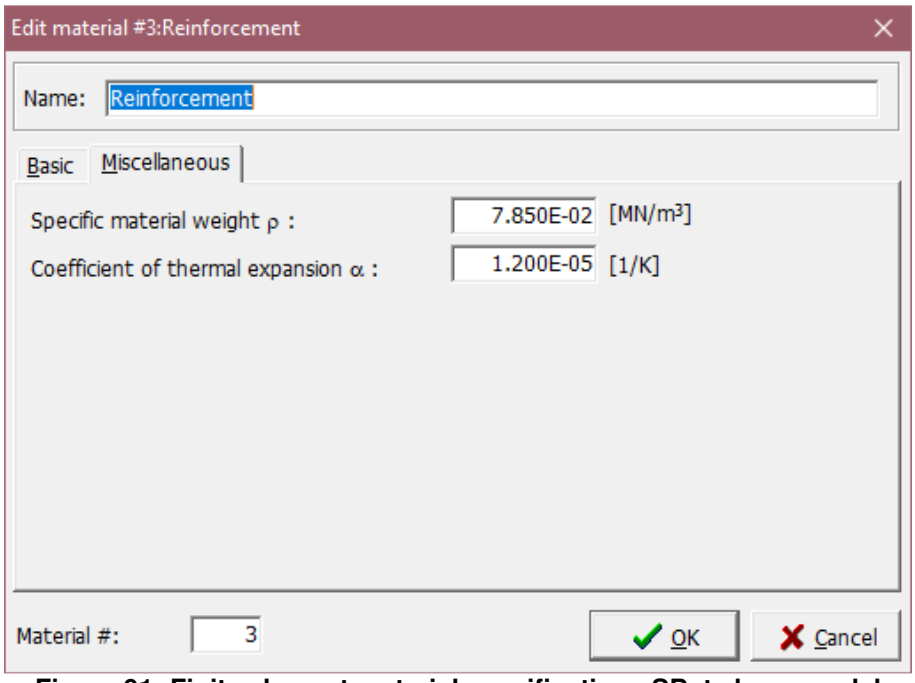

Figure 91: Finite element material specifications SBeta base model

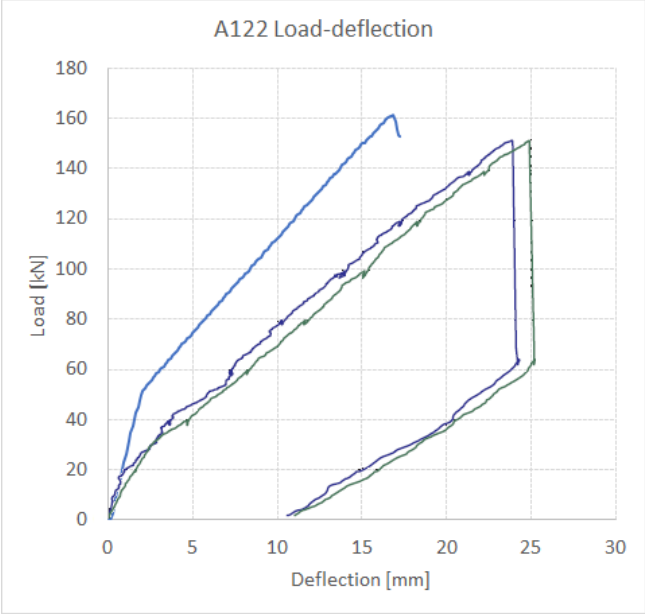

Figure 92: Load-deflection of beam A122 SBeta base model

A122: SBeta reduced tensile strength model

Only the changed parameters in comparison with the base model are presented, for the other parameters refer to Figure 86 through Figure 91.

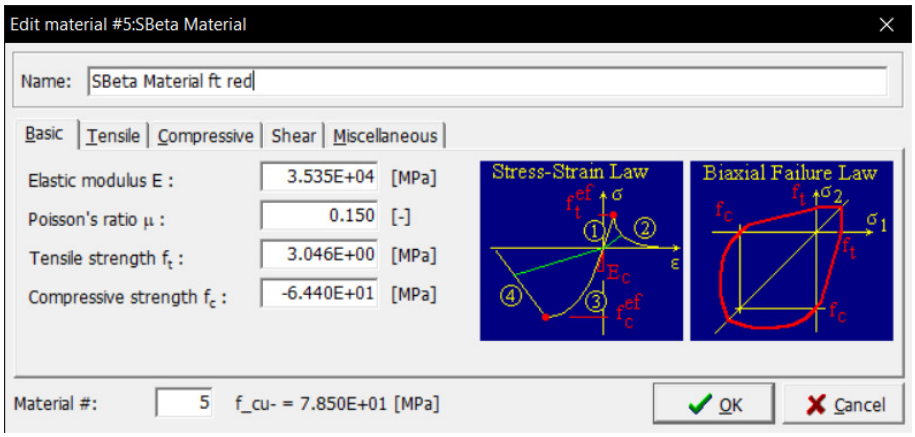

Figure 93: Finite element material specifications SBeta reduced tensile strength model

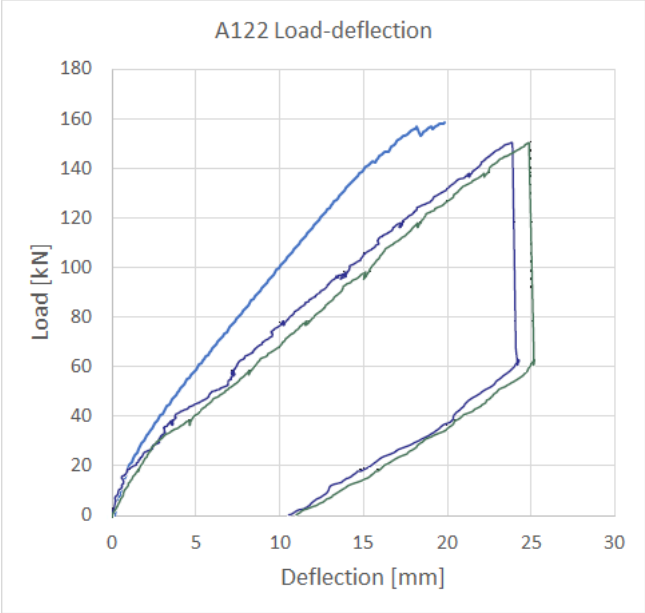

Figure 94: Load-deflection of beam A122 SBeta reduced tensile strength model

A122: SBeta reduced tensile strength and fracture energy model

Only the changed parameters in comparison with the base model are presented, for the other parameters refer to Figure 86 through Figure 91.

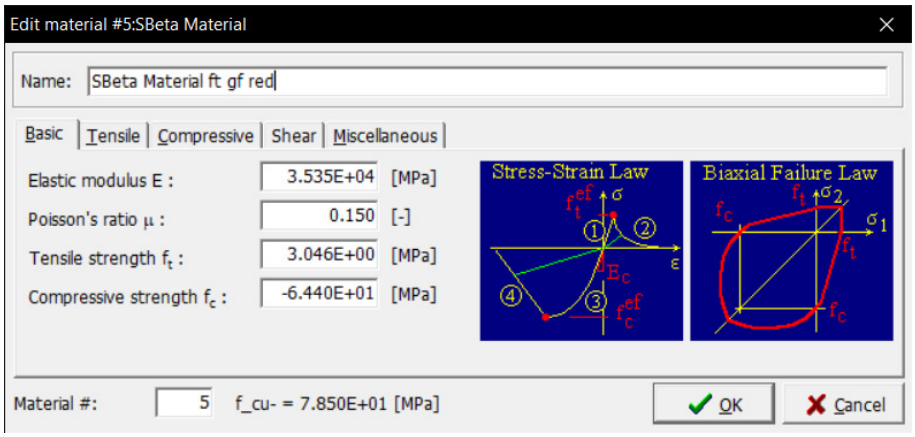

Figure 95: Finite element material specifications SBeta reduced tensile strength and fracture energy model

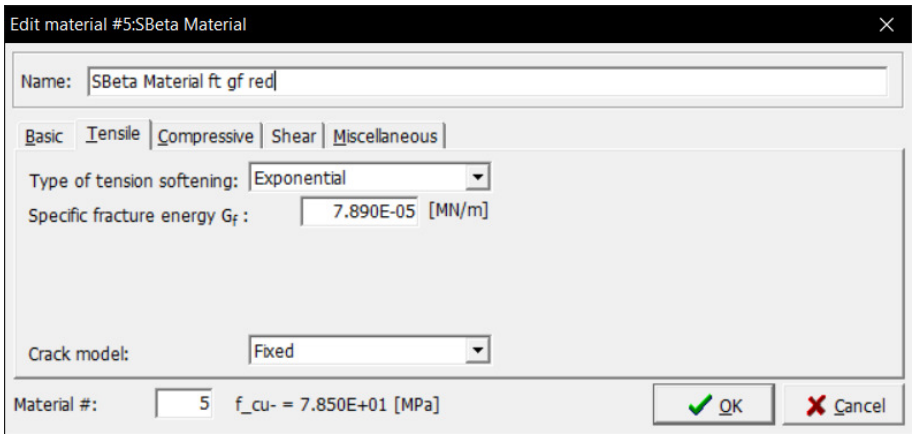

Figure 96: Finite element material specifications SBeta reduced tensile strength and fracture energy model

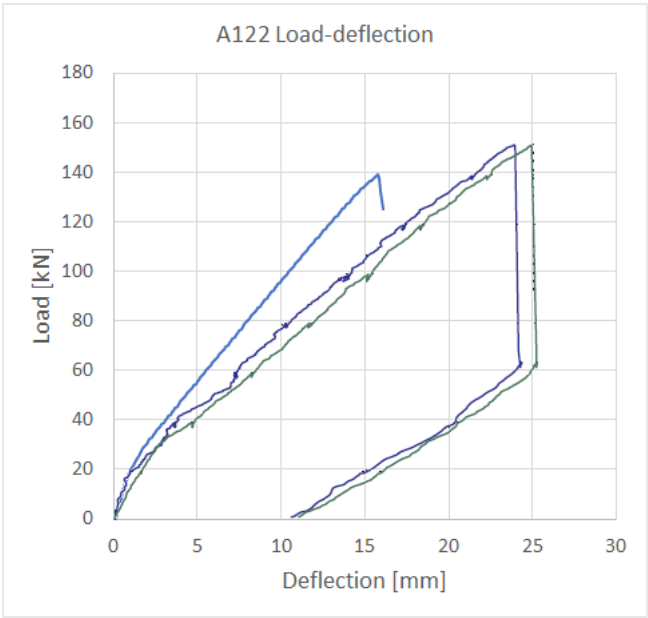

Figure 97: Load-deflection of beam A122 SBeta reduced tensile strength and fracture energy model

A122: NLCEM base model

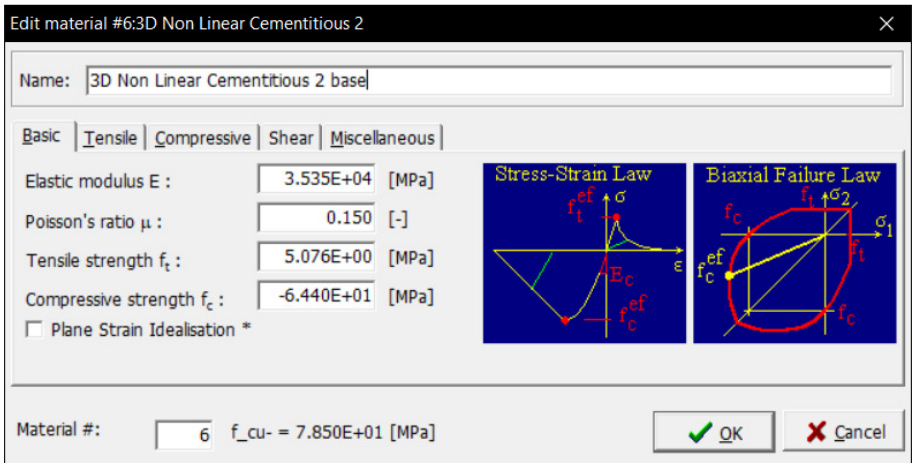

Figure 98: Finite element material specifications NLCEM base model

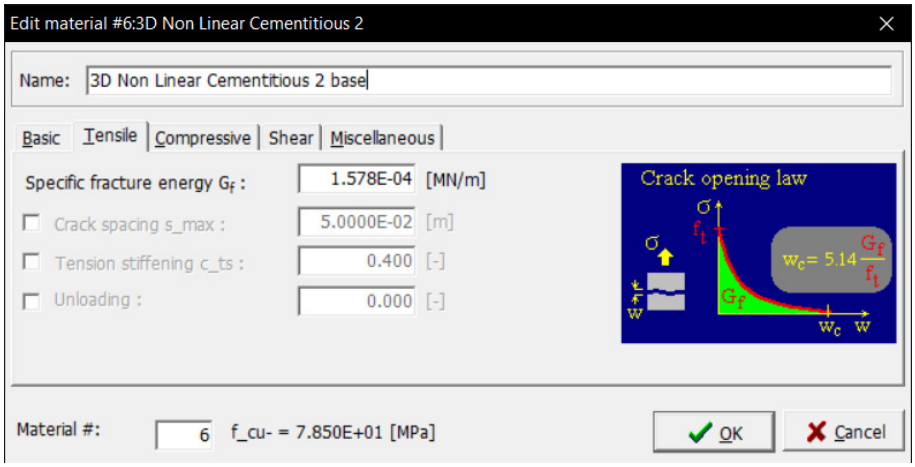

Figure 99: Finite element material specifications NLCEM base model

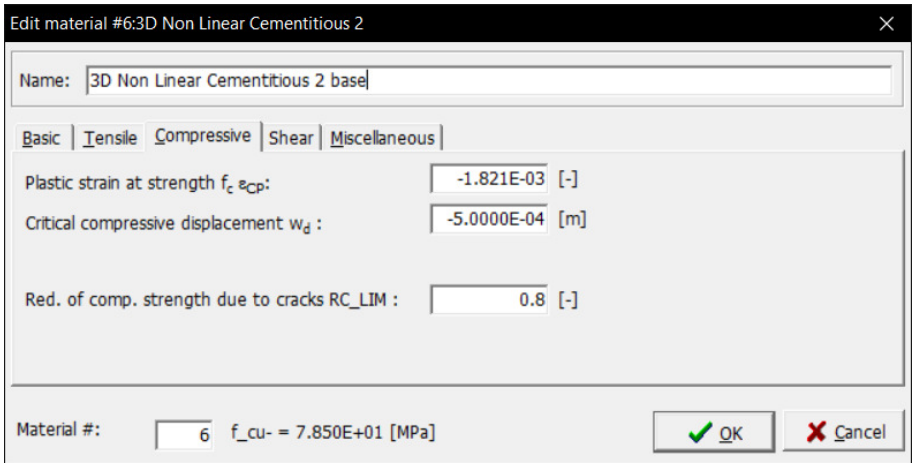

Figure 100: Finite element material specifications NLCEM base model

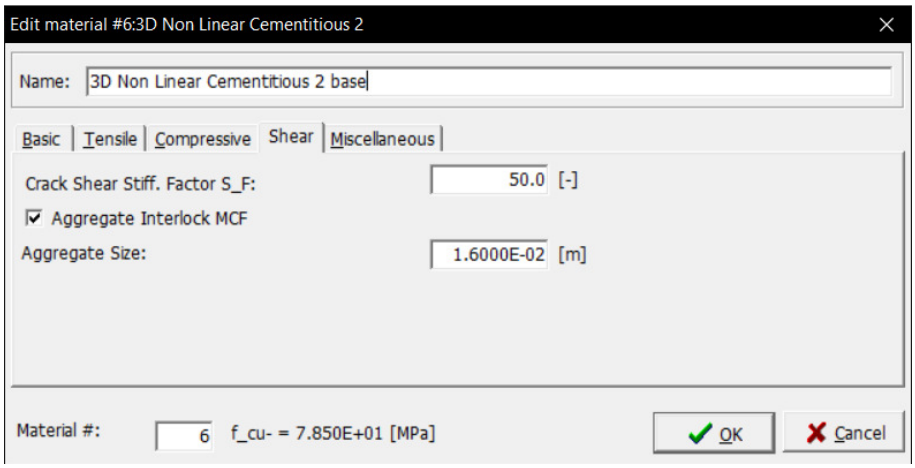

Figure 101: Finite element material specifications NLCEM base model

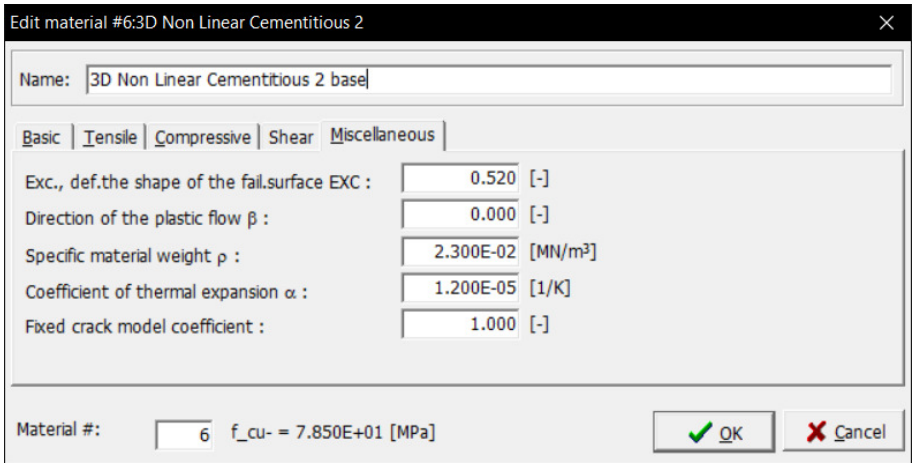

Figure 102: Finite element material specifications NLCEM base model

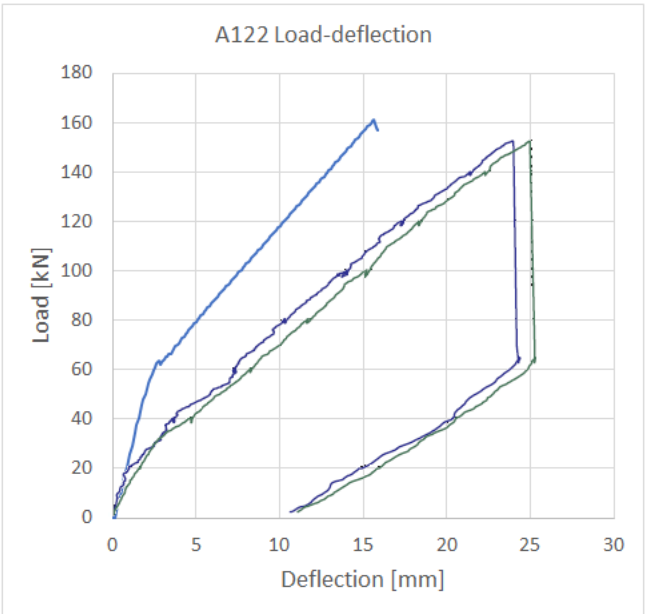

Figure 103: Load-deflection of beam A122 NLCEM base model

A122: NLCEM reduced tensile strength model

Only the changed parameters in comparison with the base model are presented, for the other parameters refer to Figure 99 through Figure 102.

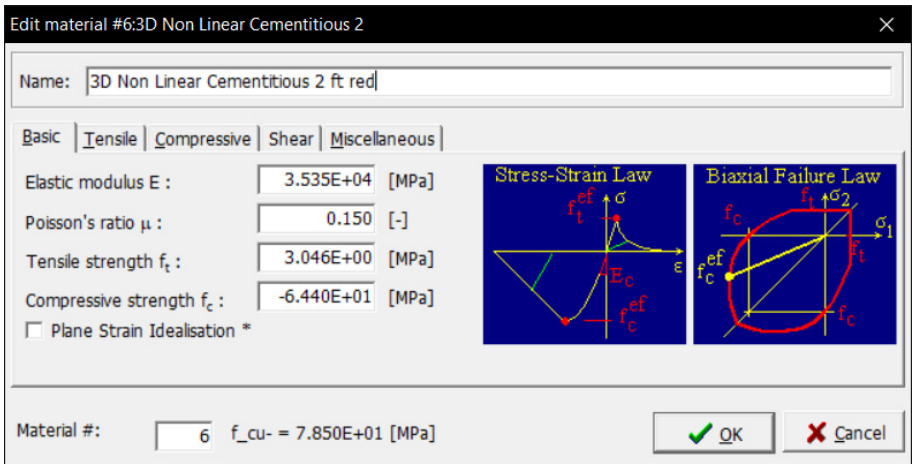

Figure 104: Finite element material specifications NLCEM reduced tensile strength model

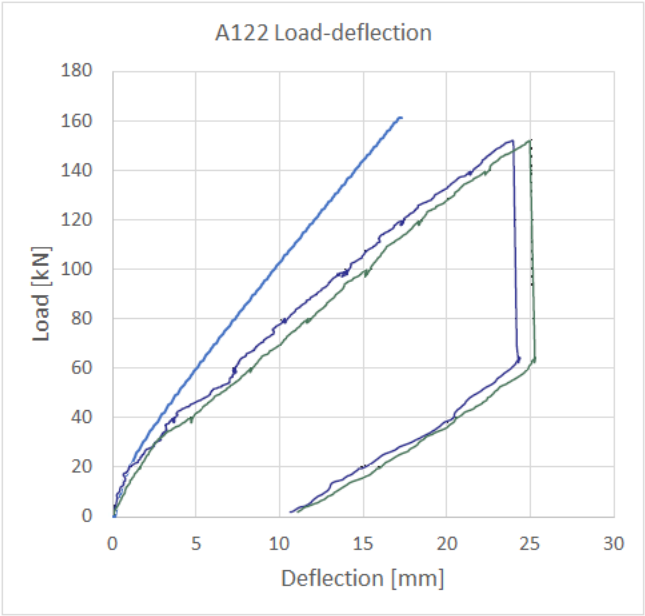

Figure 105: Load-deflection of beam A122 NLCEM reduced tensile strength model

A122: NLCEM reduced tensile strength and fracture energy model

Only the changed parameters in comparison with the base model are presented, for the other parameters refer to Figure 100 through Figure 102.

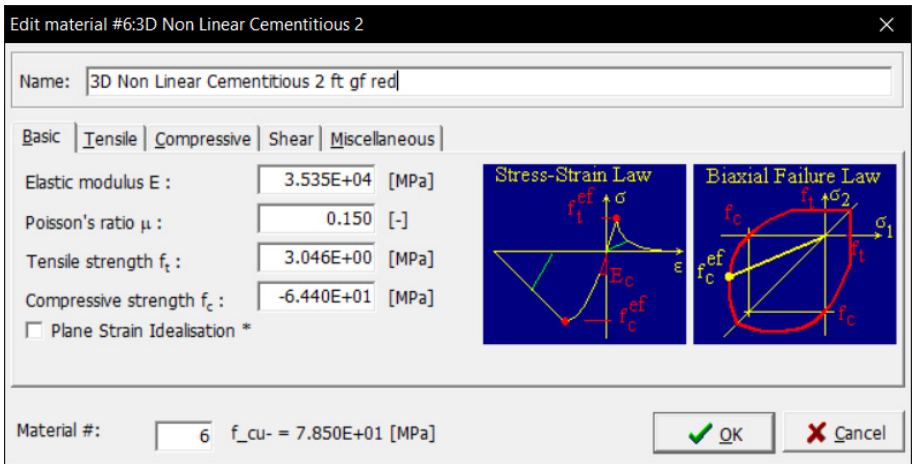

Figure 106: Finite element material specifications NLCEM reduced tensile strength and fracture energy model

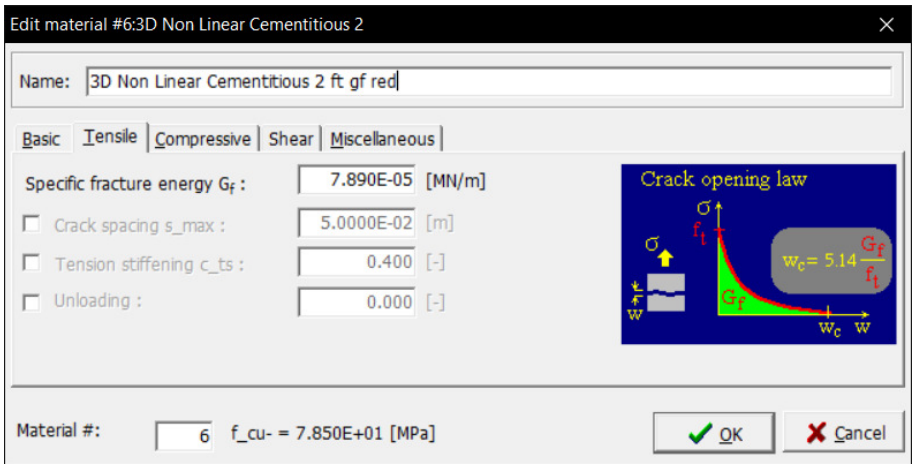

Figure 107: Finite element material specifications NLCEM reduced tensile strength and fracture energy model

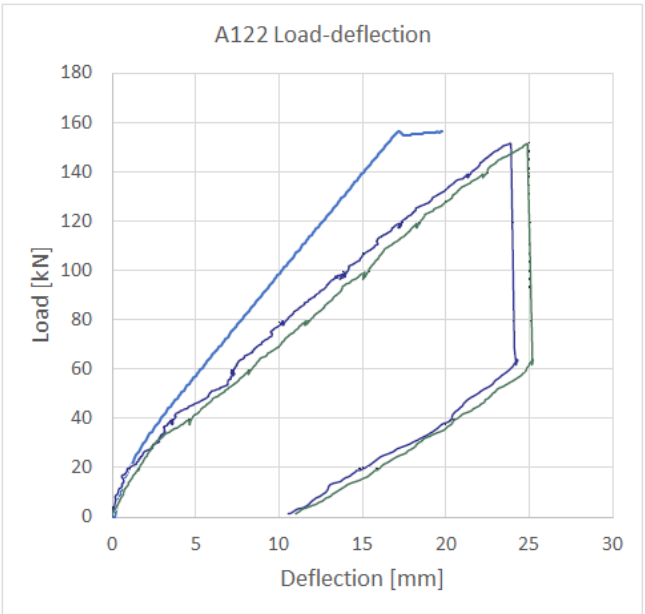

Figure 108: Load-deflection for beam A122 NLCEM reduced tensile strength and fracture energy model

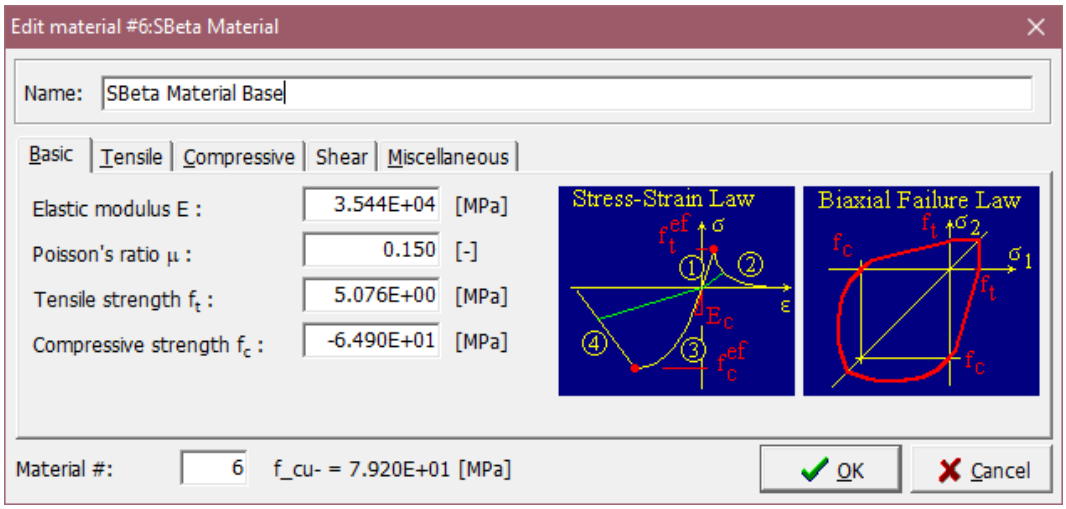

Figure 109: Finite element material specifications SBeta base model

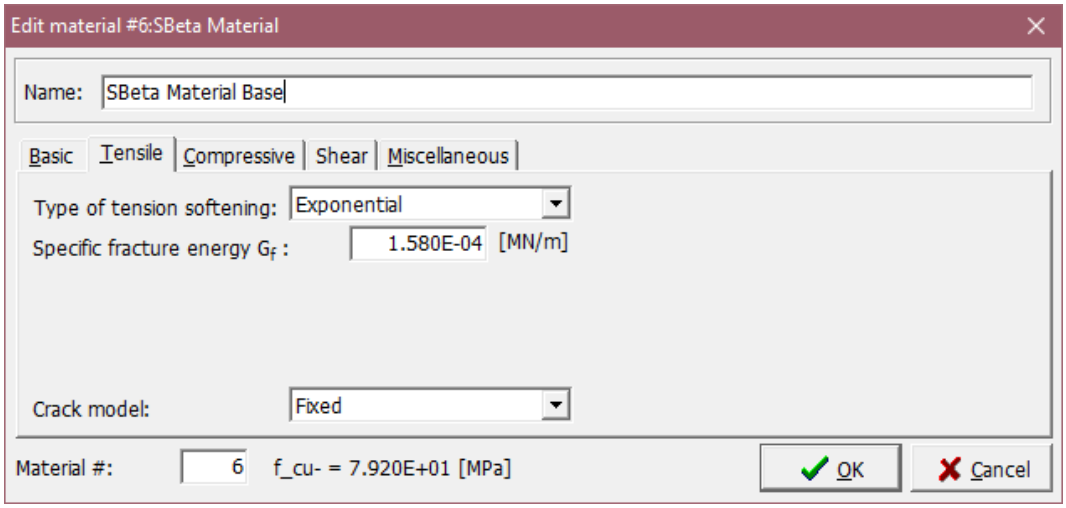

Figure 110: Finite element material specifications SBeta base model

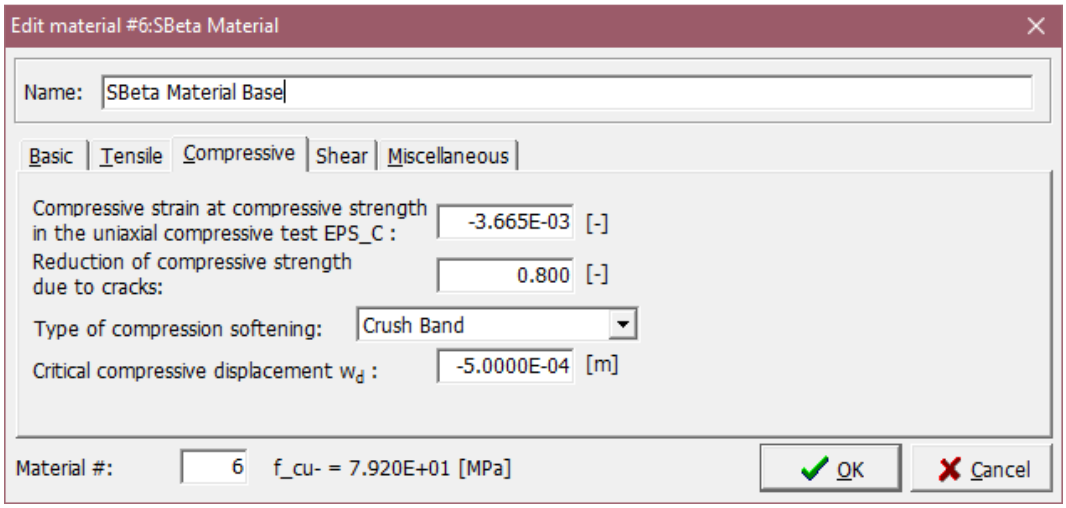

Figure 111: Finite element material specifications SBeta base model

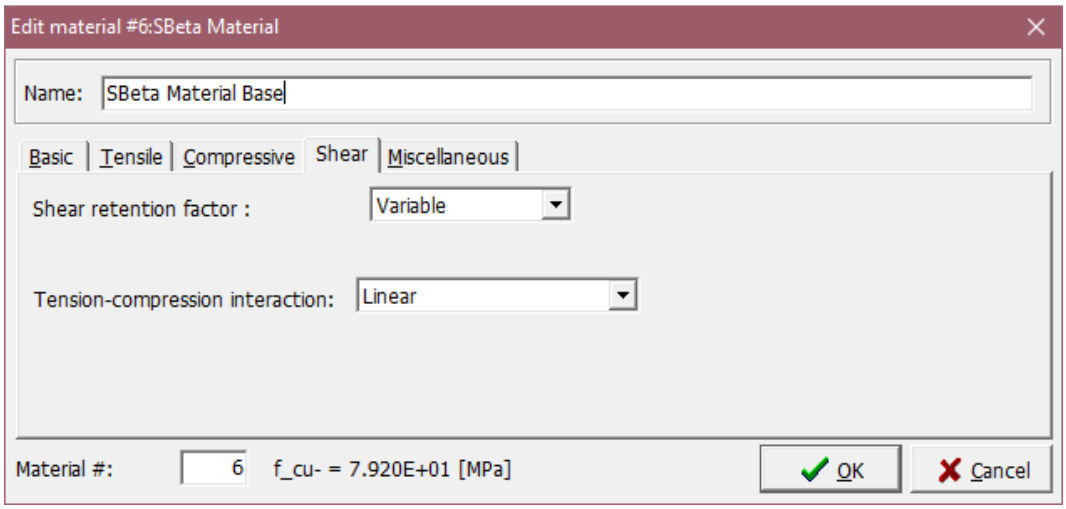

Figure 112: Finite element material specifications SBeta base model

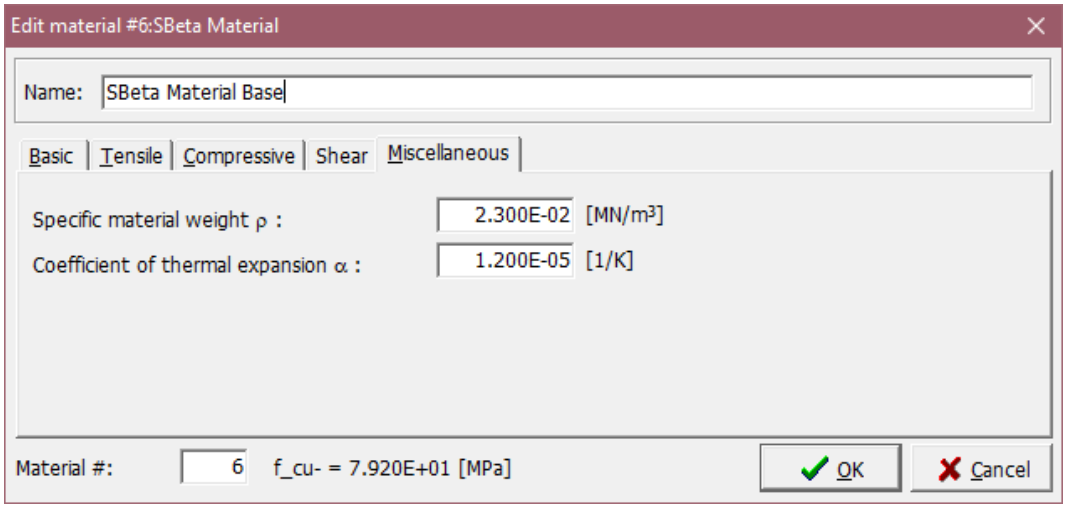

Figure 113: Finite element material specifications SBeta base model

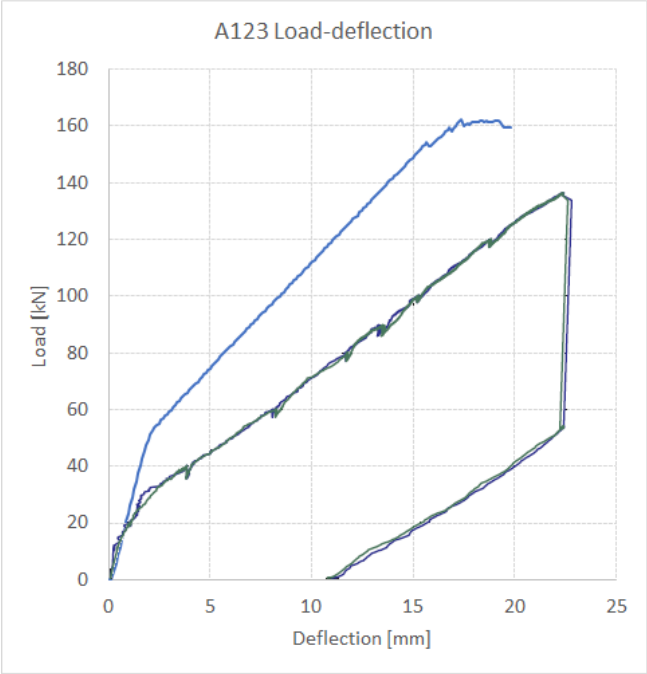

Figure 114: Load-deflection of beam A123 SBeta base model

A123: SBeta reduced tensile strength model

Only the changed parameters in comparison with the base model are presented, for the other parameters refer to Figure 110 through Figure 113.

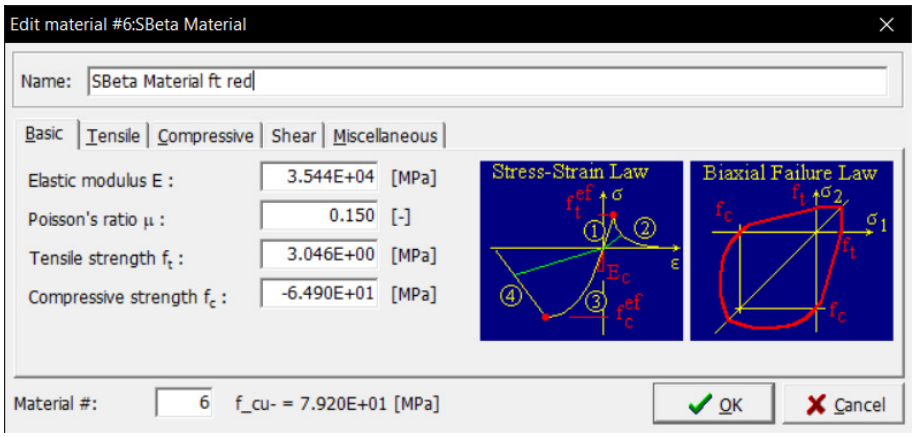

Figure 115: Finite element material specifications SBeta reduced tensile strength model

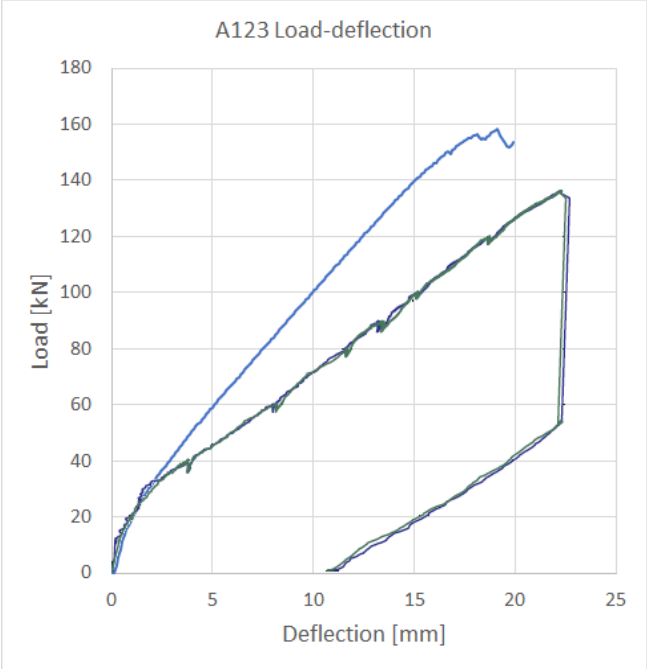

Figure 116: Load-deflection of beam A123 SBeta reduced tensile strength model

A123: SBeta reduced tensile strength and fracture energy model

Only the changed parameters in comparison with the base model are presented, for the other parameters refer to Figure 111 through Figure 113.

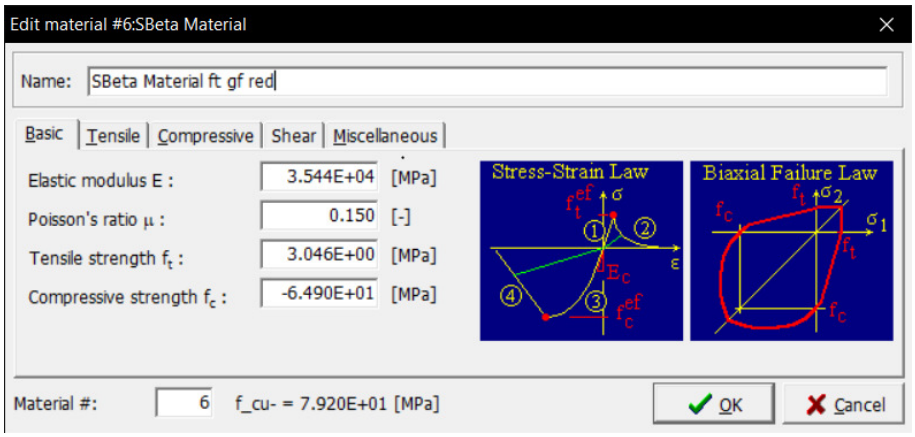

Figure 117: Finite element material specifications SBeta reduced tensile strength and fracture energy model

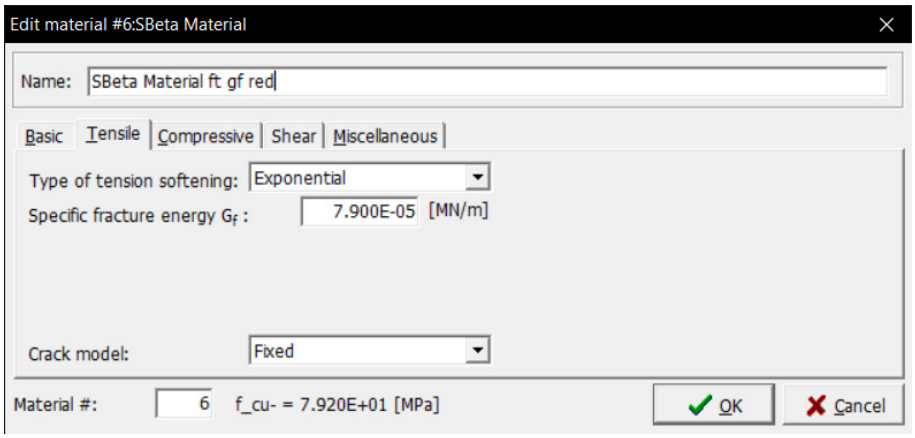

Figure 118: Finite element material specifications SBeta reduced tensile strength and fracture energy model

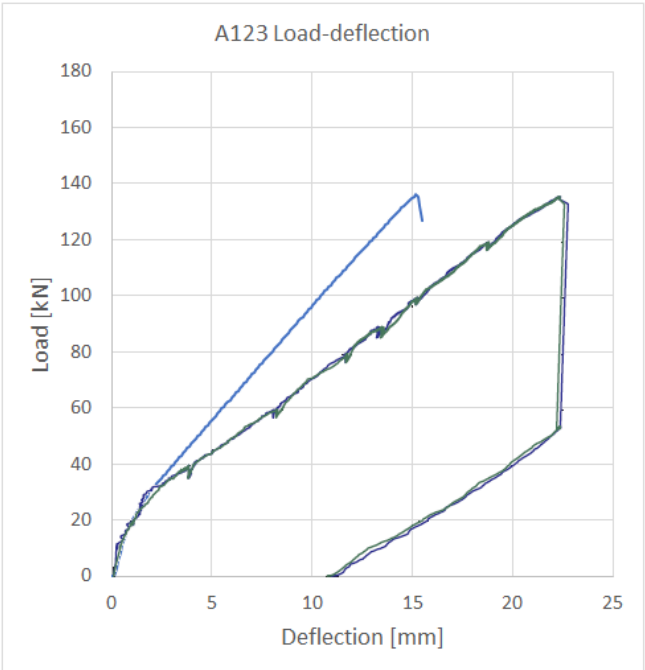

Figure 119: Load-deflection of beam A123 SBeta reduced tensile strength and fracture energy model

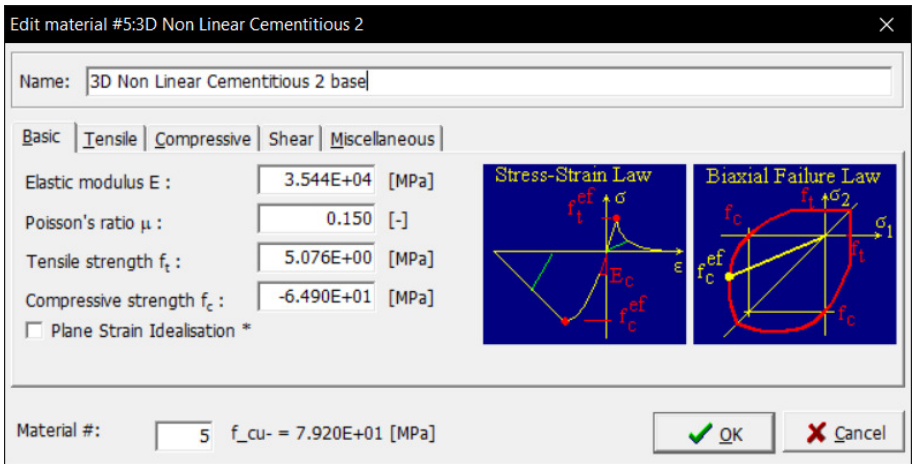

Figure 120: Finite element material specifications NLCEM base model

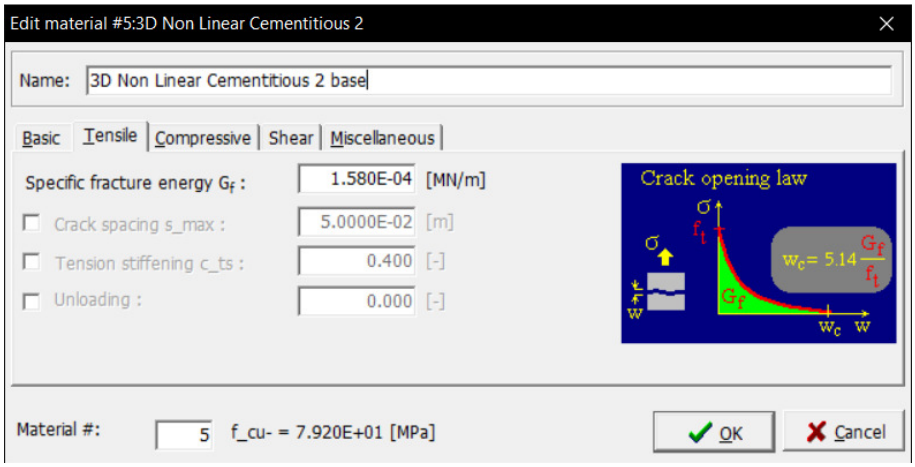

Figure 121: Finite element material specifications NLCEM base model

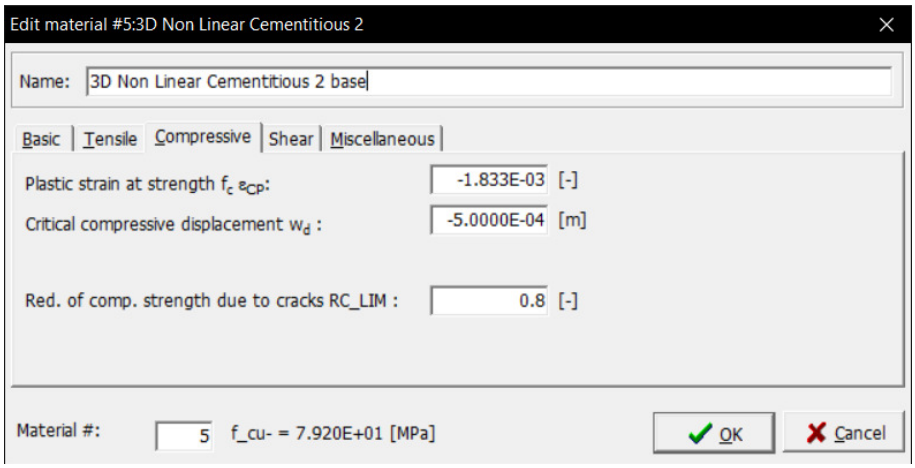

Figure 122: Finite element material specifications NLCEM base model

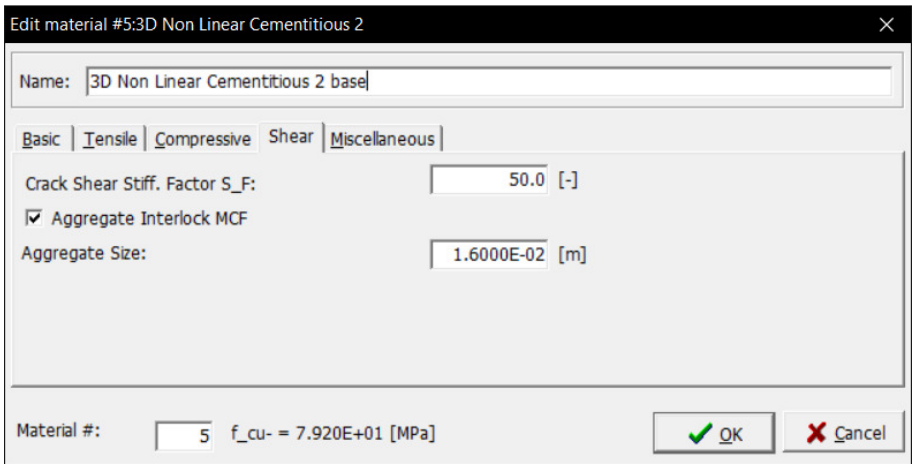

Figure 123: Finite element material specifications NLCEM base model

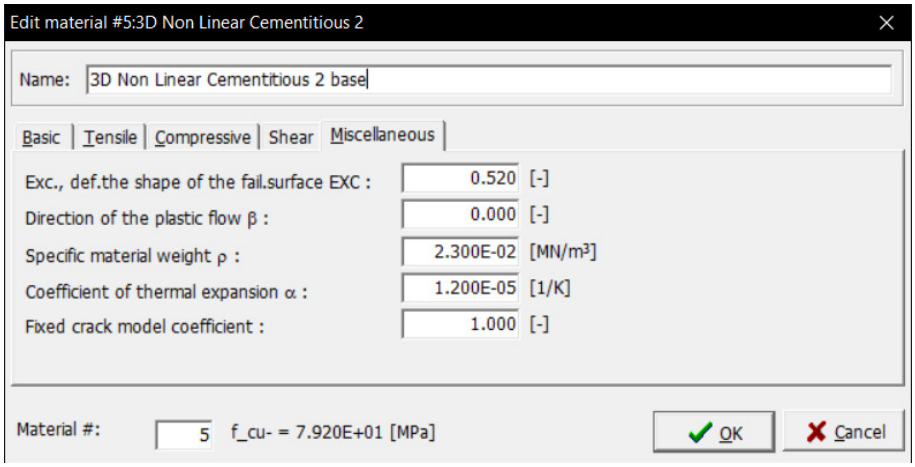

Figure 124: Finite element material specifications NLCEM base model

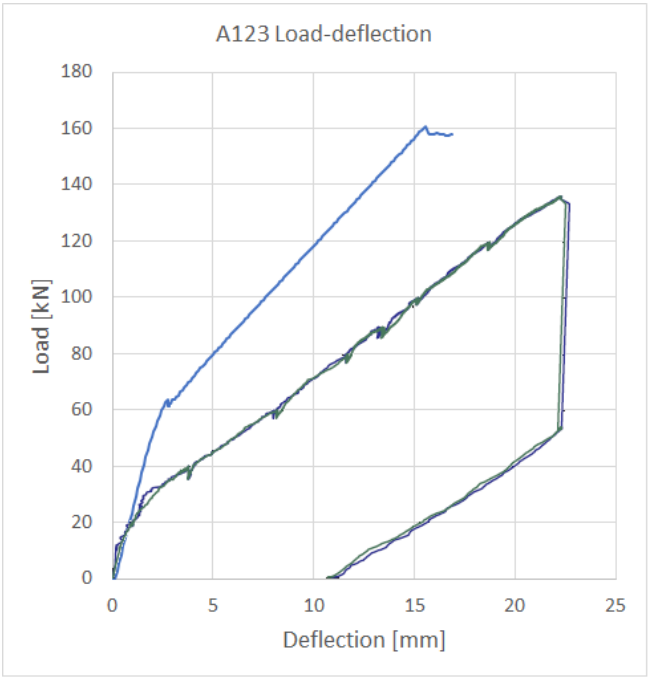

Figure 125: Load-deflection for beam A123 NLCEM base model

A123: NLCEM reduced tensile strength model

Only the changed parameters in comparison with the base model are presented, for the other parameters refer to Figure 121 through Figure 124.

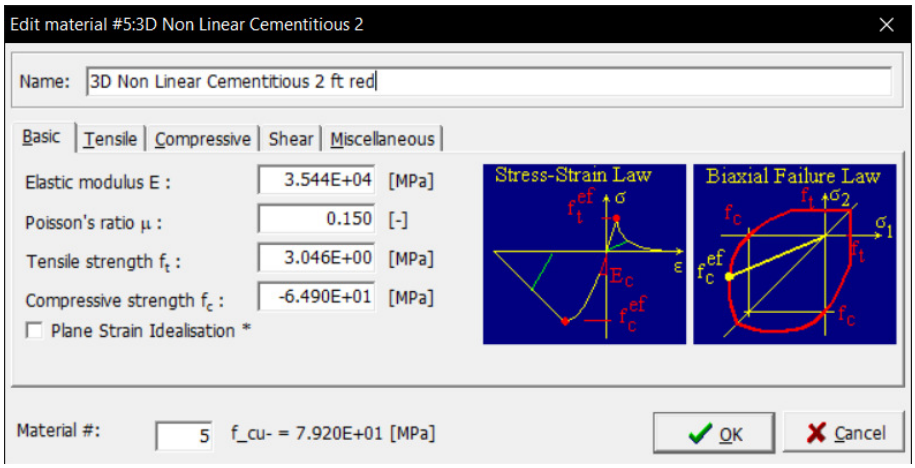

Figure 126: Finite element material specifications NLCEM reduced tensile strength model

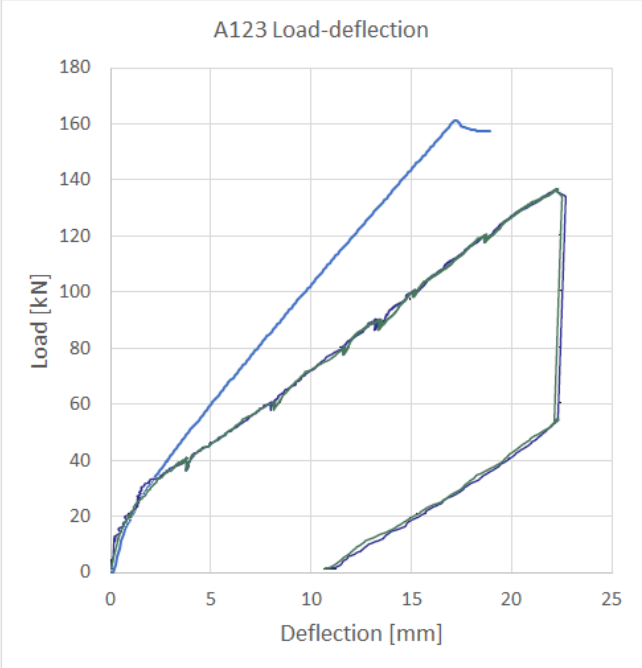

Figure 127: Load-deflection of beam A123 NLCEM reduced tensile strength model

A123: NLCEM reduced tensile strength and fracture energy model

Only the changed parameters in comparison with the base model are presented, for the other parameters refer to Figure 122 through Figure 124.

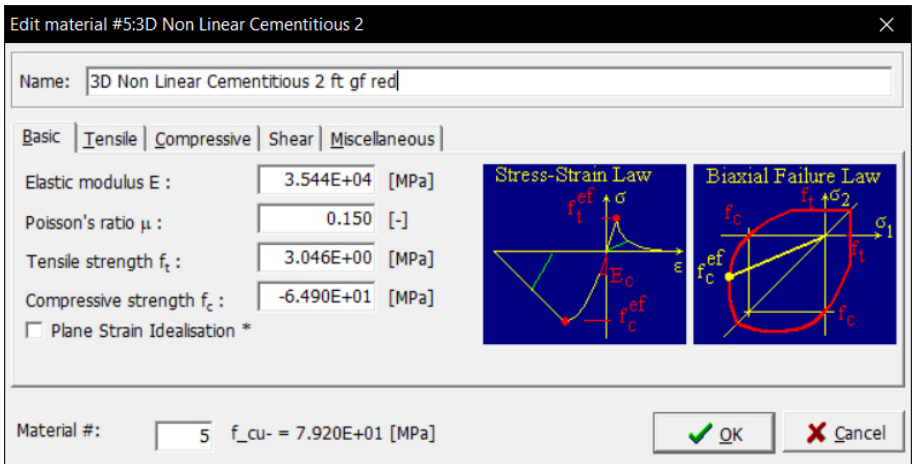

Figure 128: Finite element material specifications NLCEM reduced tensile strength and fracture energy model

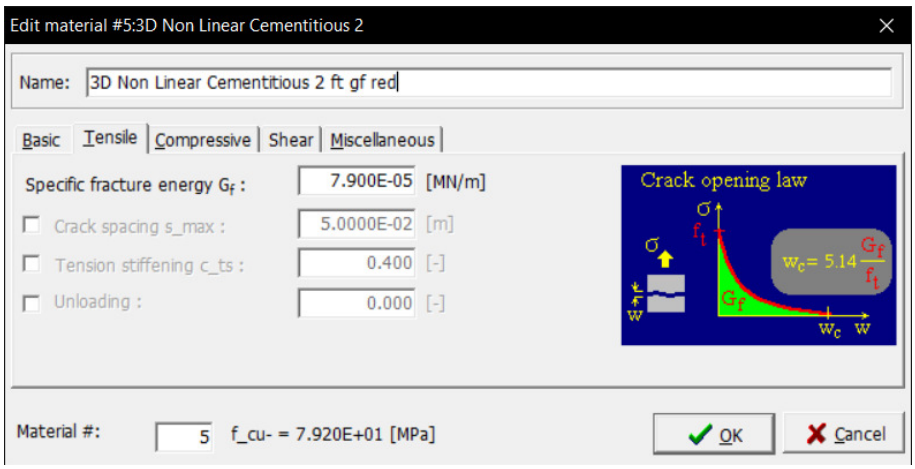

Figure 129: Finite element material specifications NLCEM reduced tensile strength and fracture energy model

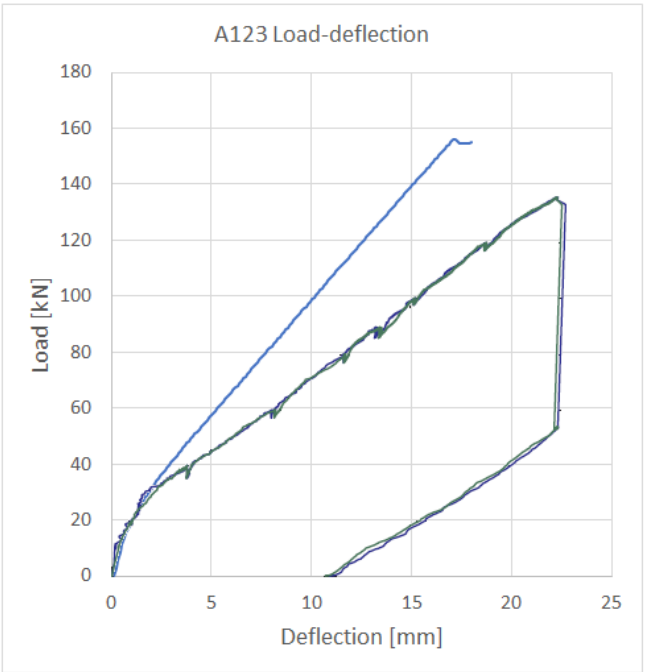

Figure 130: Load-deflection of beam A123 NLCEM reduced tensile strength and fracture energy model

A75: SBeta base model

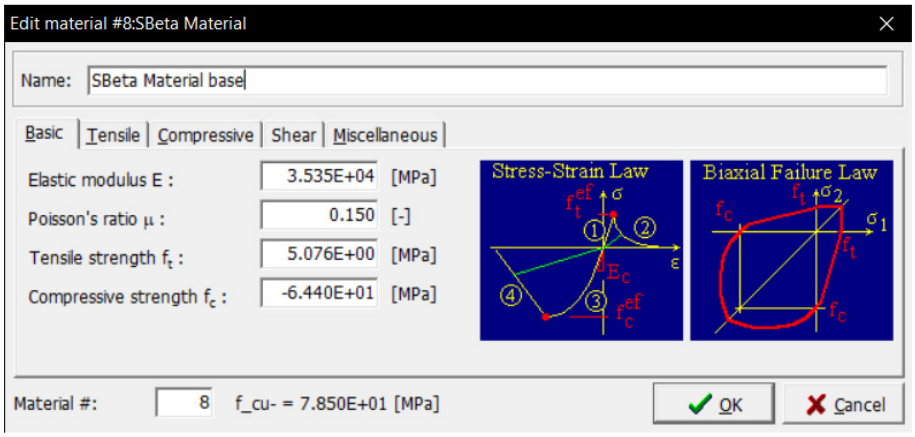

Figure 131: Finite element material specifications SBeta base model

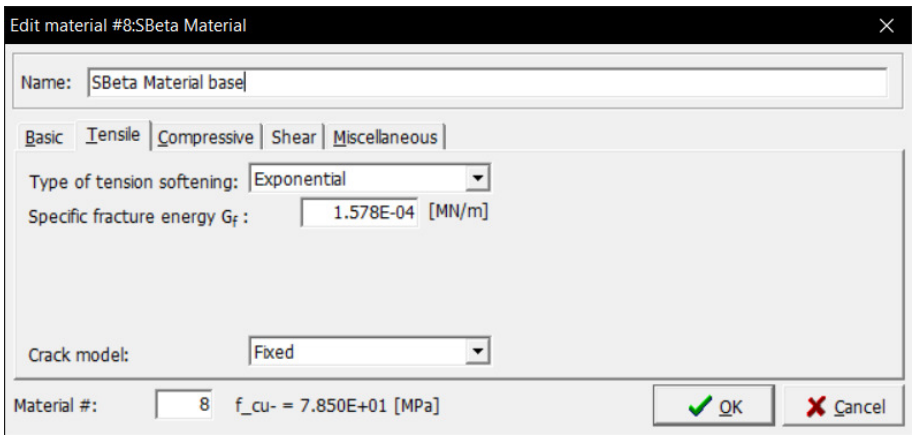

Figure 132: Finite element material specifications SBeta base model

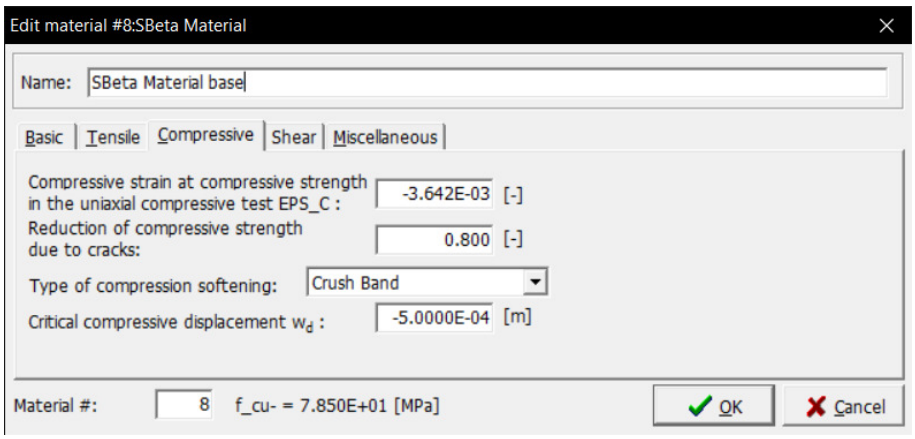

Figure 133: Finite element material specifications SBeta base model

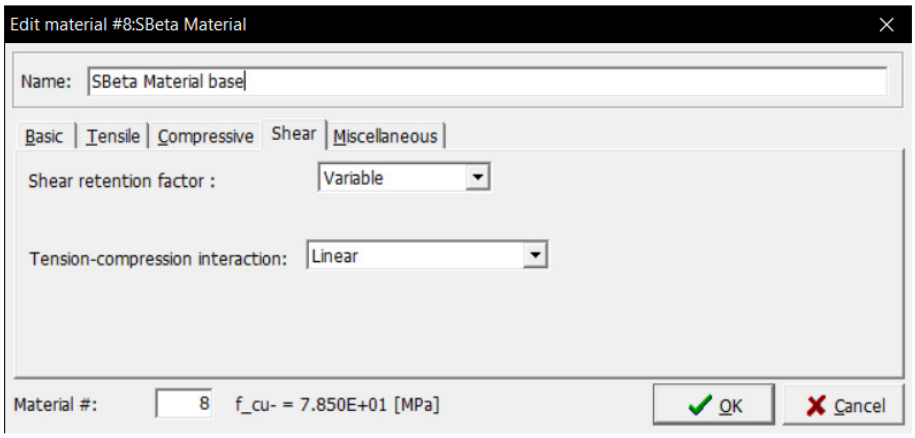

Figure 134: Finite element material specifications SBeta base model

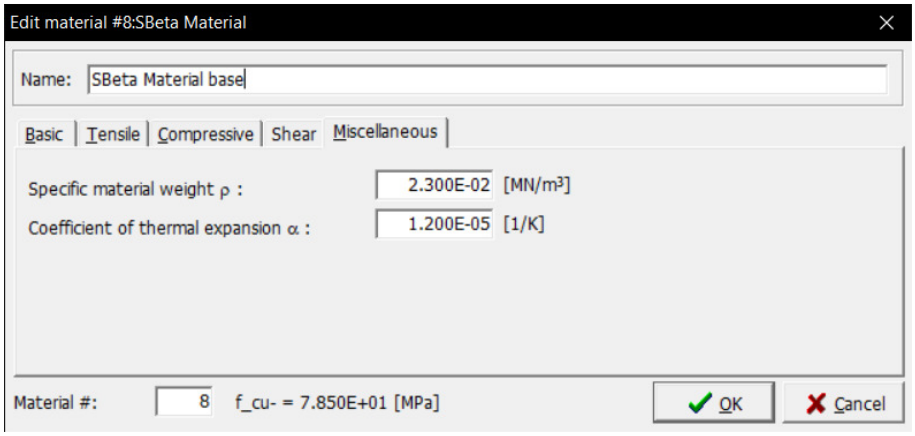

Figure 135: Finite element material specifications SBeta base model

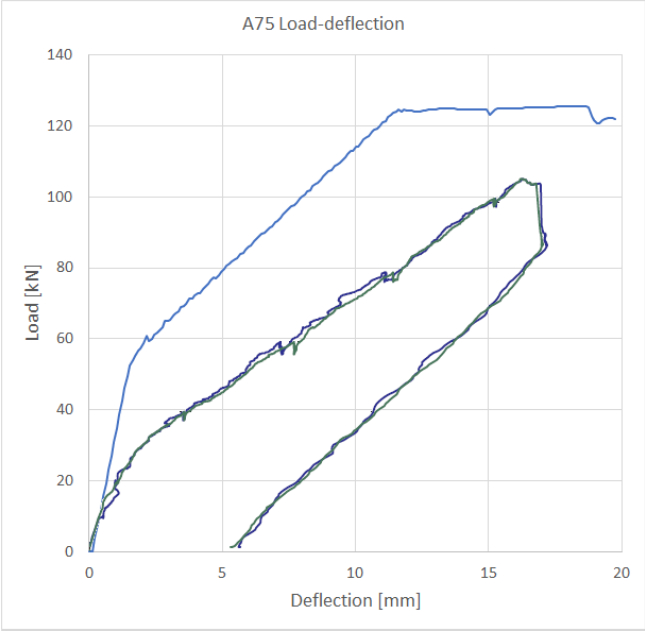

Figure 136: Load-deflection of beam A75 SBeta base model

A75: SBeta reduced tensile strength model

Only the changed parameters in comparison with the base model are presented, for the other parameters refer to Figure 132 through Figure 135.

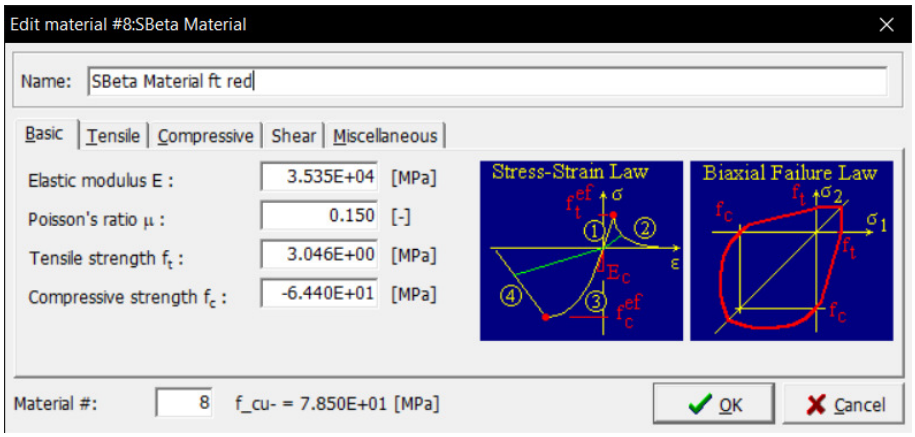

Figure 137: Finite element material specifications SBeta reduced tensile strength model

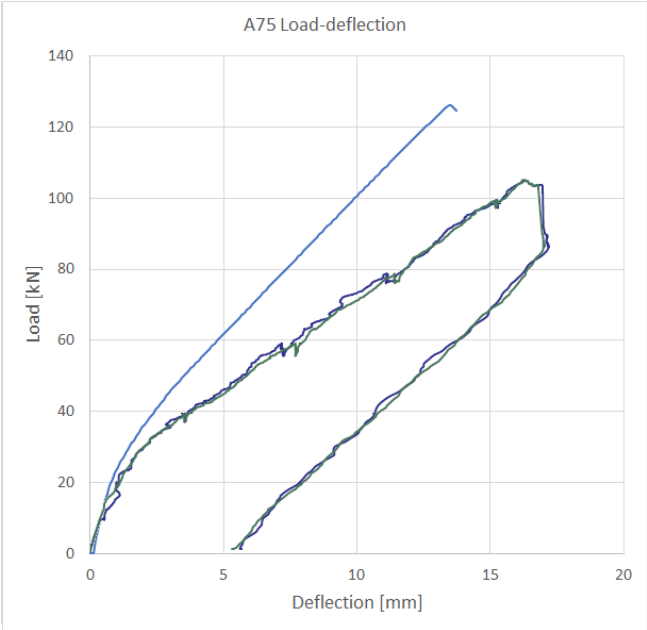

Figure 138: Load-deflection of beam A75 SBeta reduced tensile strength model

A75: Sbeta reduced tensile strength and fracture energy model

Only the changed parameters in comparison with the base model are presented, for the other parameters refer to Figure 133 through Figure 135.

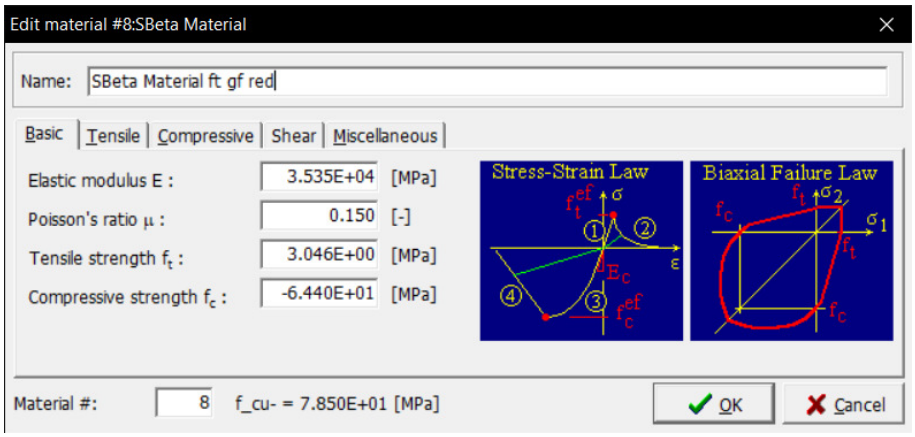

Figure 139: Finite element material specifications SBeta reduced tensile strength and fracture energy model

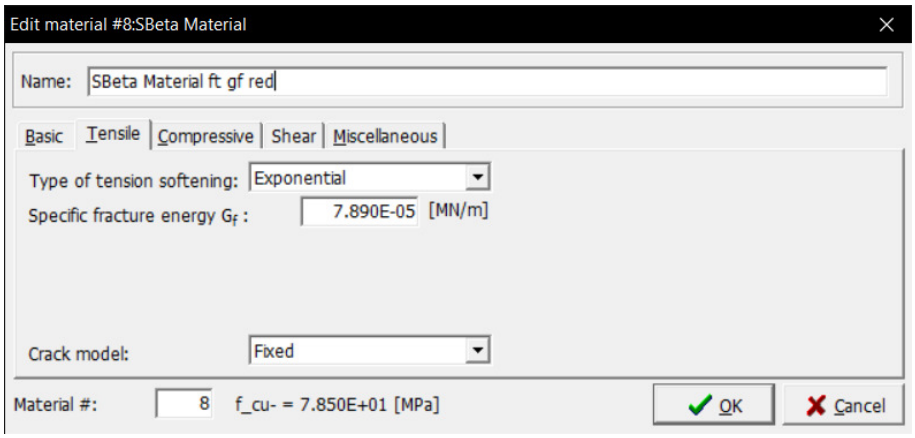

Figure 140: Finite element material specifications SBeta reduced tensile strength and fracture energy model

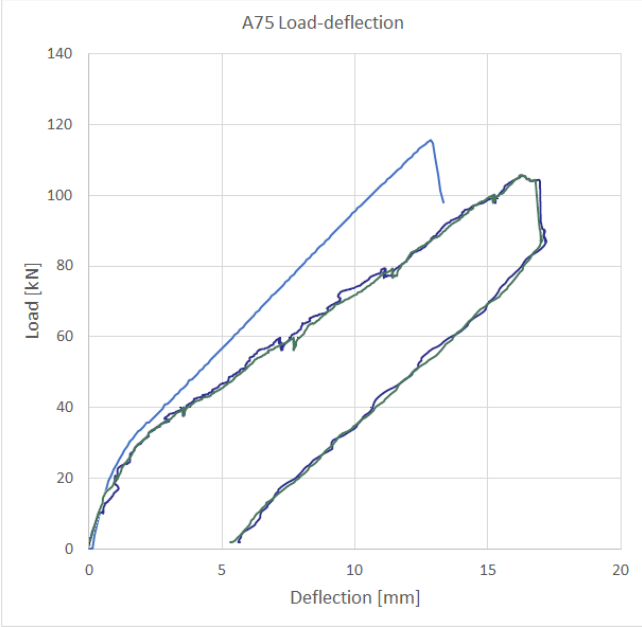

Figure 141: Load-deflection of beam A75 SBeta reduced tensile strength and fracture energy model

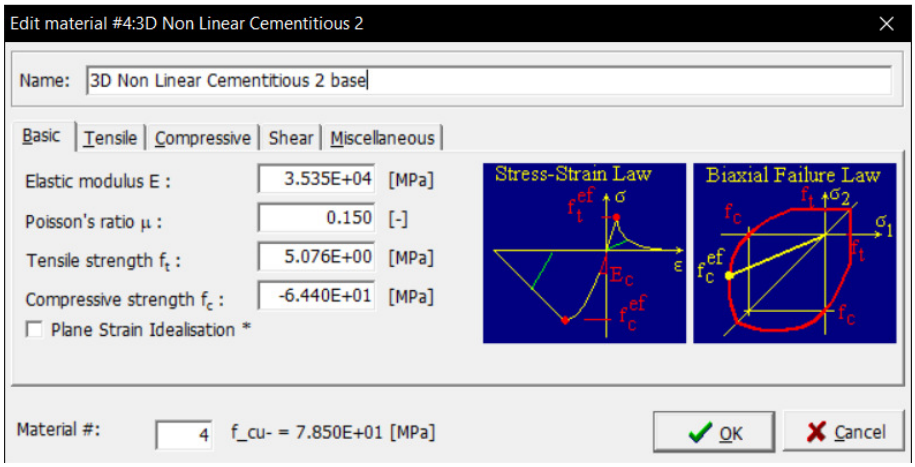

Figure 142: Finite element material specifications NLCEM base model

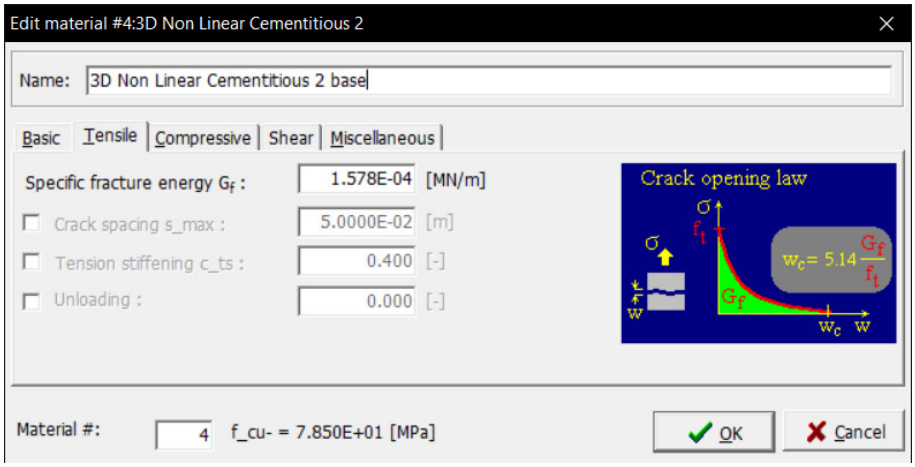

Figure 143: Finite element material specifications NLCEM base model

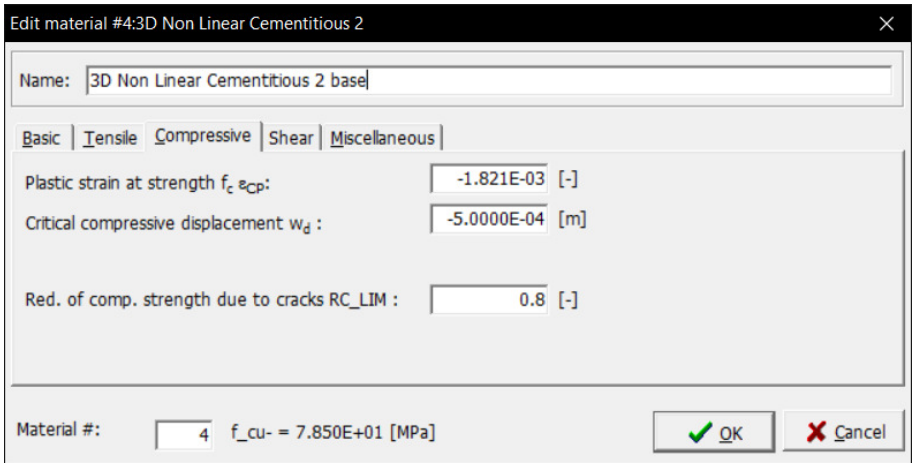

Figure 144: Finite element material specifications NLCEM base model

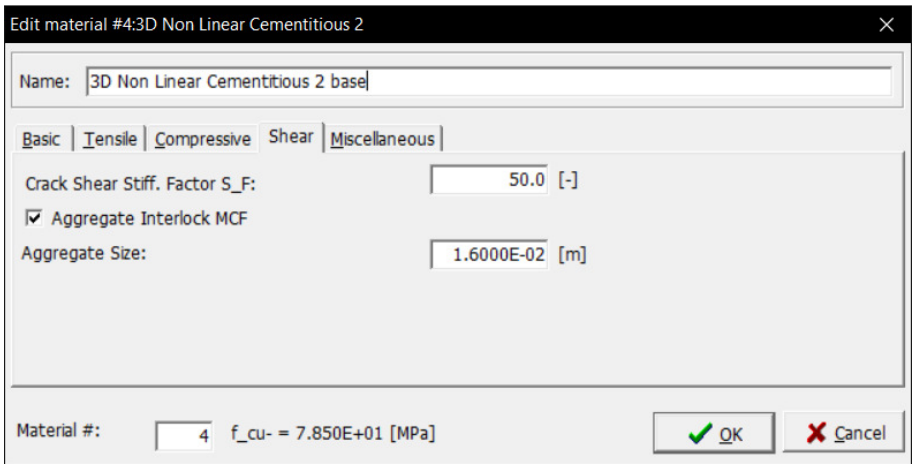

Figure 145: Finite element material specifications NLCEM base model

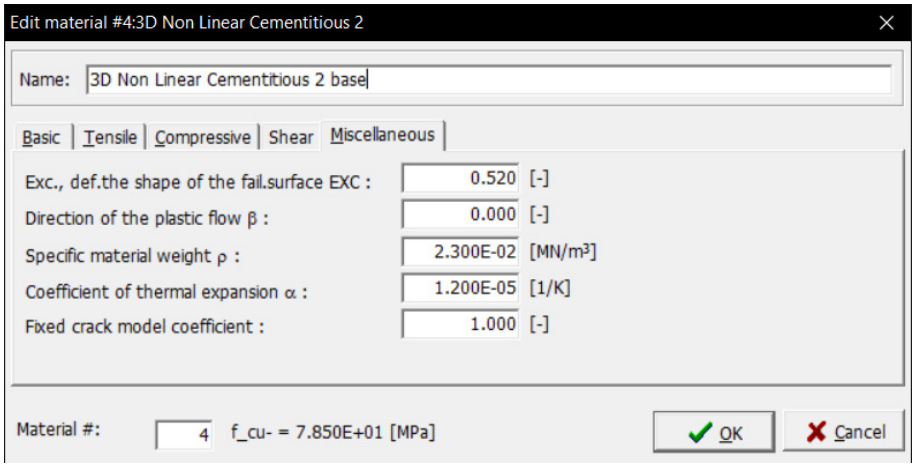

Figure 146: Finite element material specifications NLCEM base model

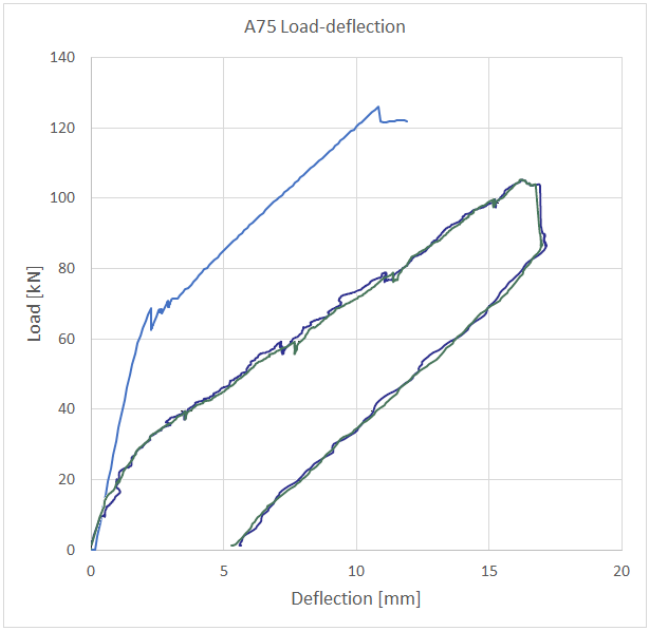

Figure 147: Load-deflection of beam A75 NLCEM base model

A75: NLCEM reduced tensile strength model

Only the changed parameters in comparison with the base model are presented, for the other parameters refer to Figure 143Figure 132 through Figure 146.

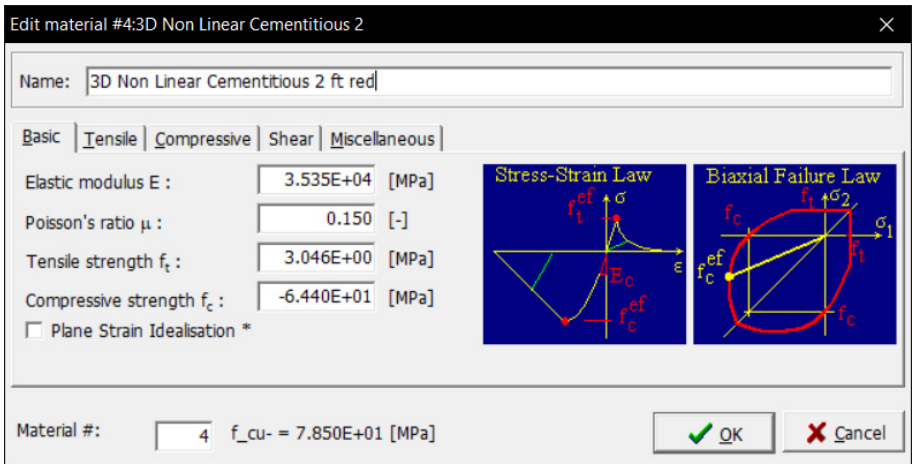

Figure 148: Finite element material specifications NLCEM reduced tensile strength model

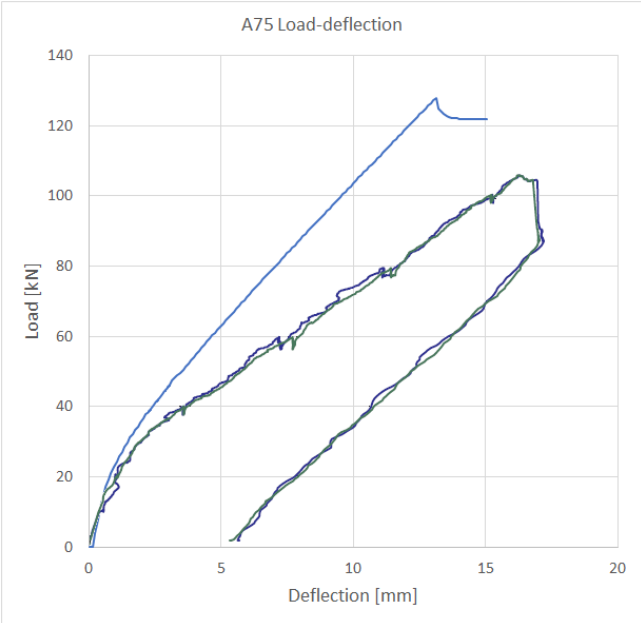

Figure 149: Load-deflection of beam A75 NLCEM reduced tensile strength model

A75: NLCEM reduced tensile strength and fracture energy model

Only the changed parameters in comparison with the base model are presented, for the other parameters refer to Figure 144Figure 132 through Figure 146.

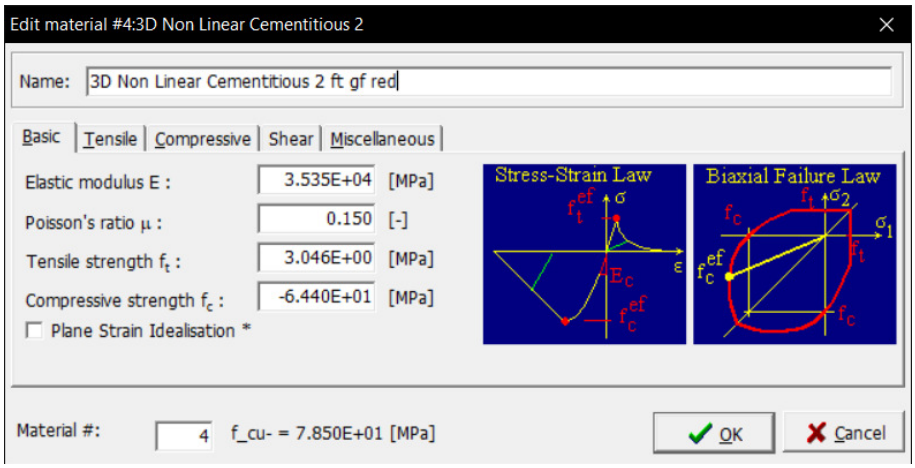

Figure 150: Finite element material specifications NLCEM reduced tensile strength and fracture energy model

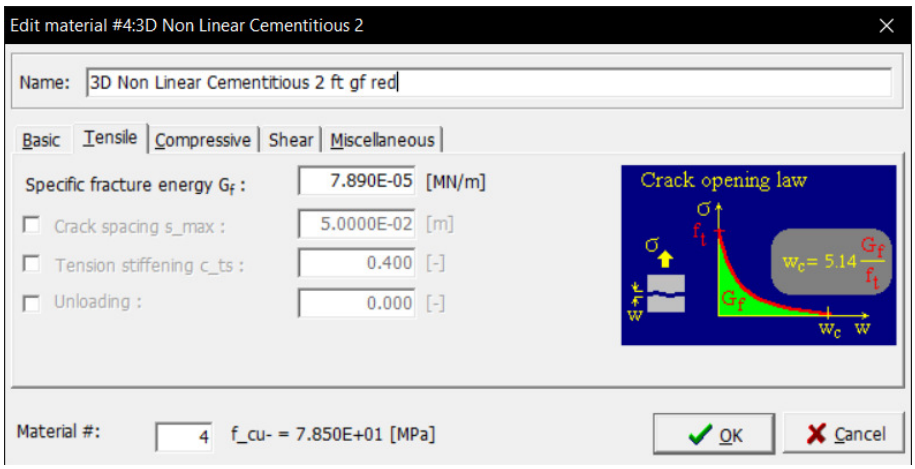

Figure 151: Finite element material specifications NLCEM reduced tensile strength and fracture energy model

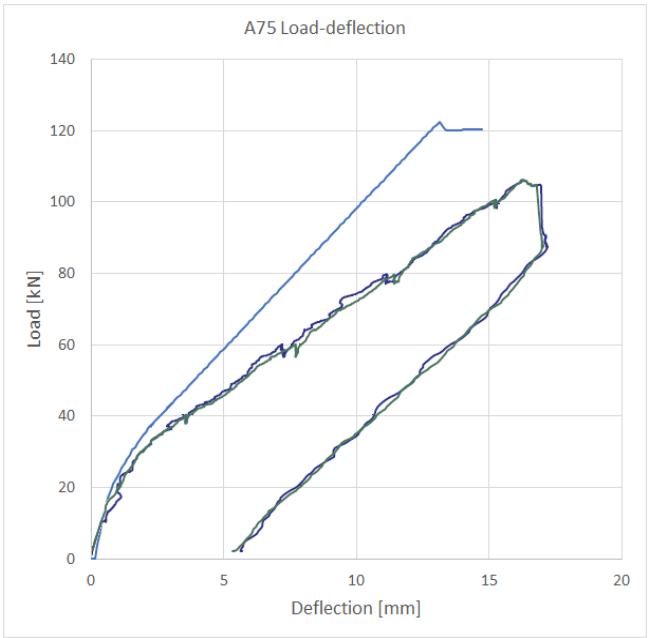

Figure 152: Load-deflection of beam A75 NLCEM reduced tensile strength and fracture energy model

H123: SBeta base model

The reinforcement described in Figure 158 and Figure 159 are used for all H123 and H352 models.

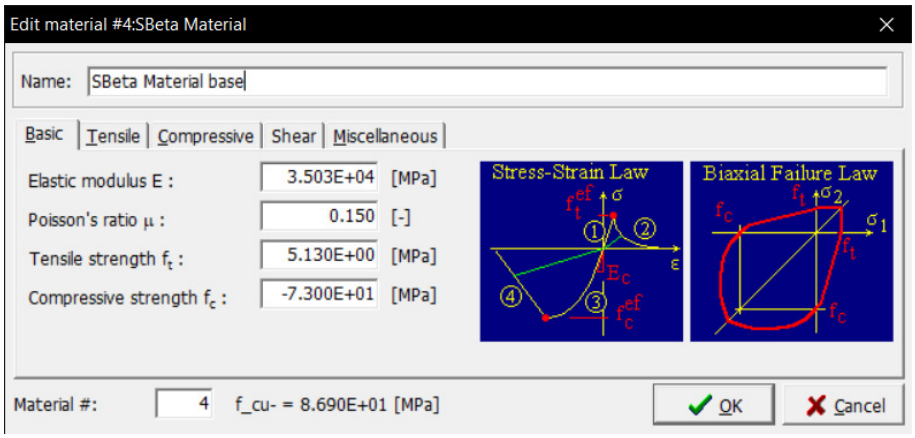

Figure 153: Finite element material specifications SBeta base model

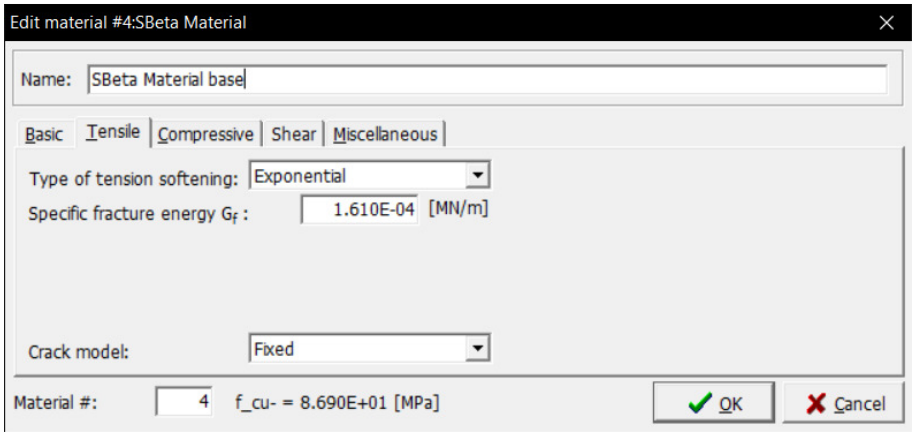

Figure 154: Finite element material specifications SBeta base model

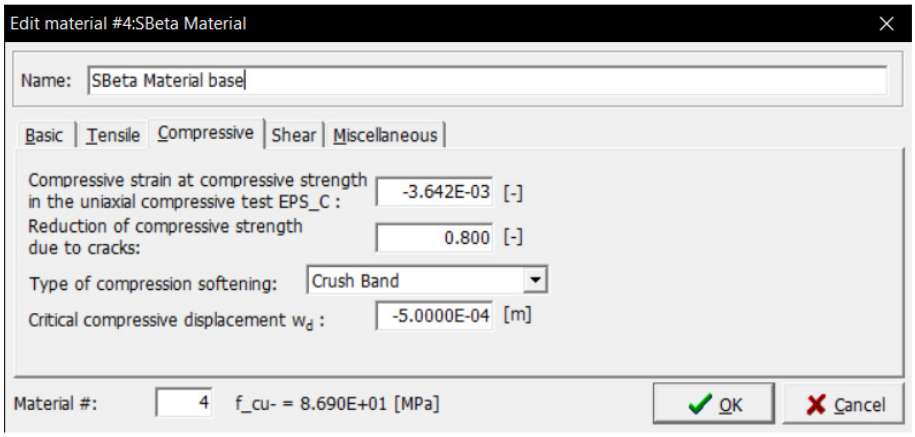

Figure 155: Finite element material specifications SBeta base model

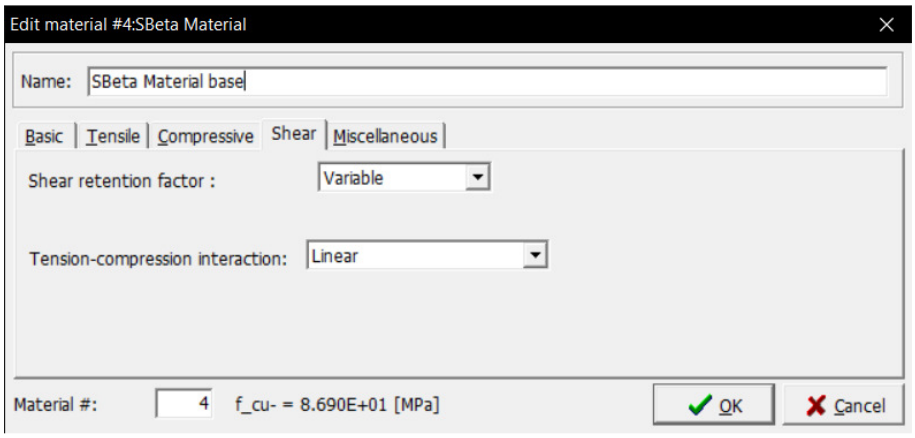

Figure 156: Finite element material specifications SBeta base model

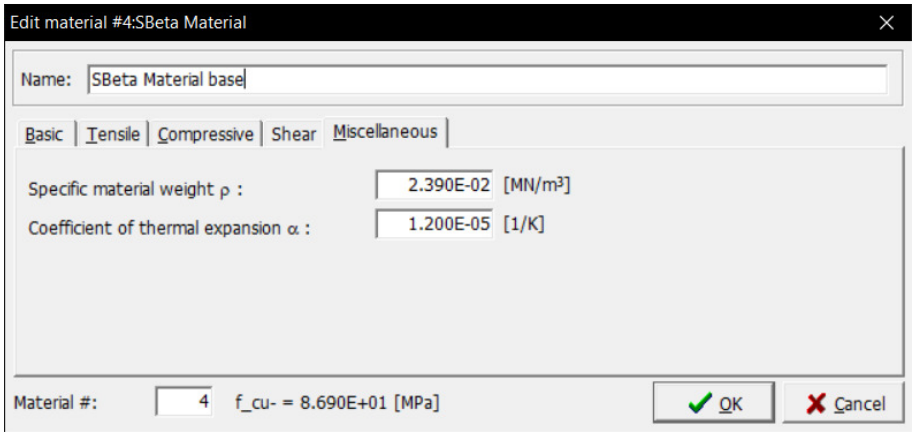

Figure 157: Finite element material specifications SBeta base model

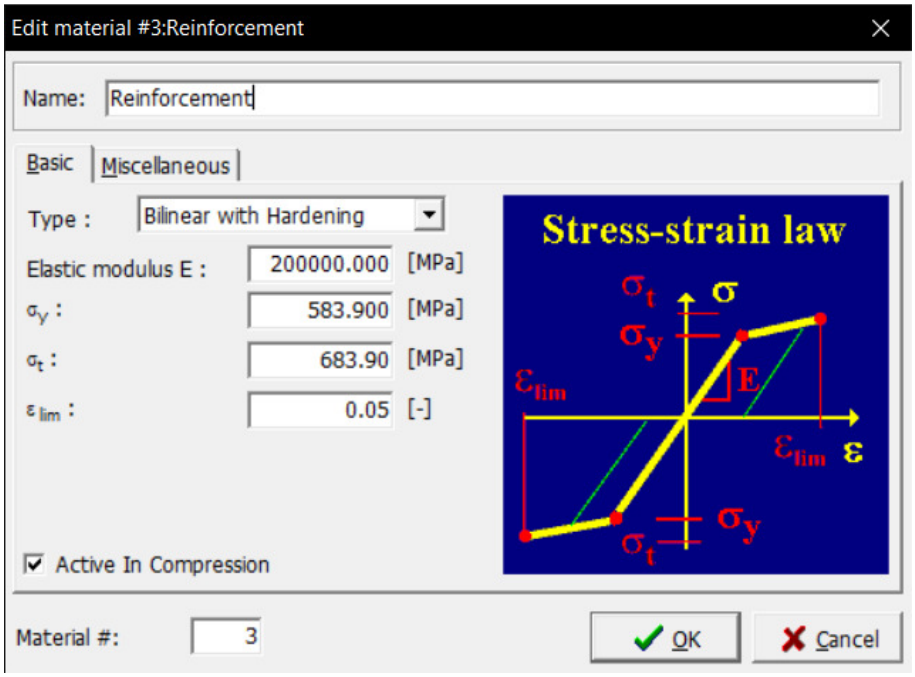

Figure 158: Finite element material specifications SBeta base model

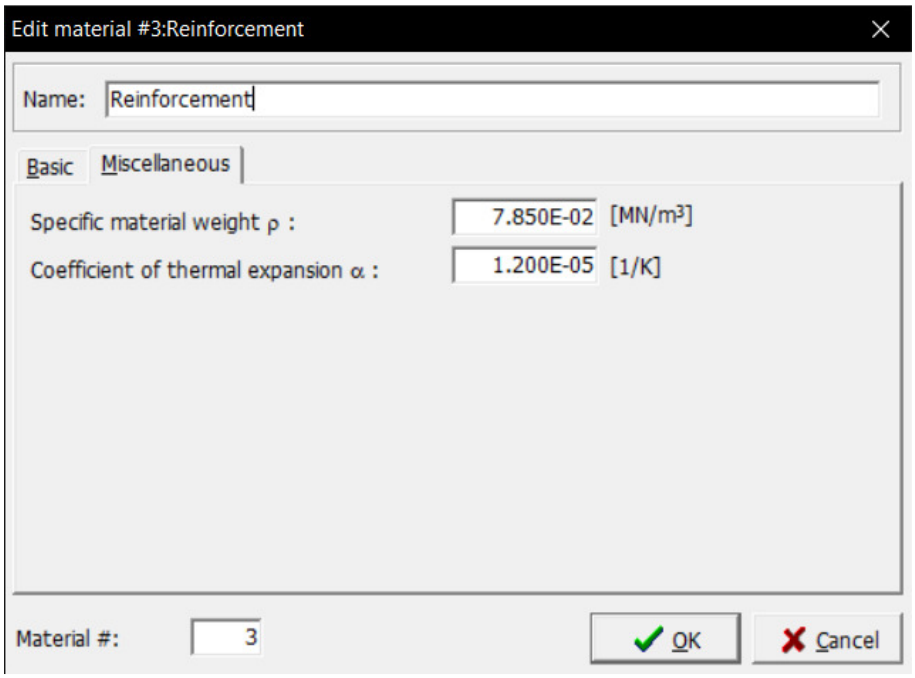

Figure 159: Finite element material specifications SBeta base model

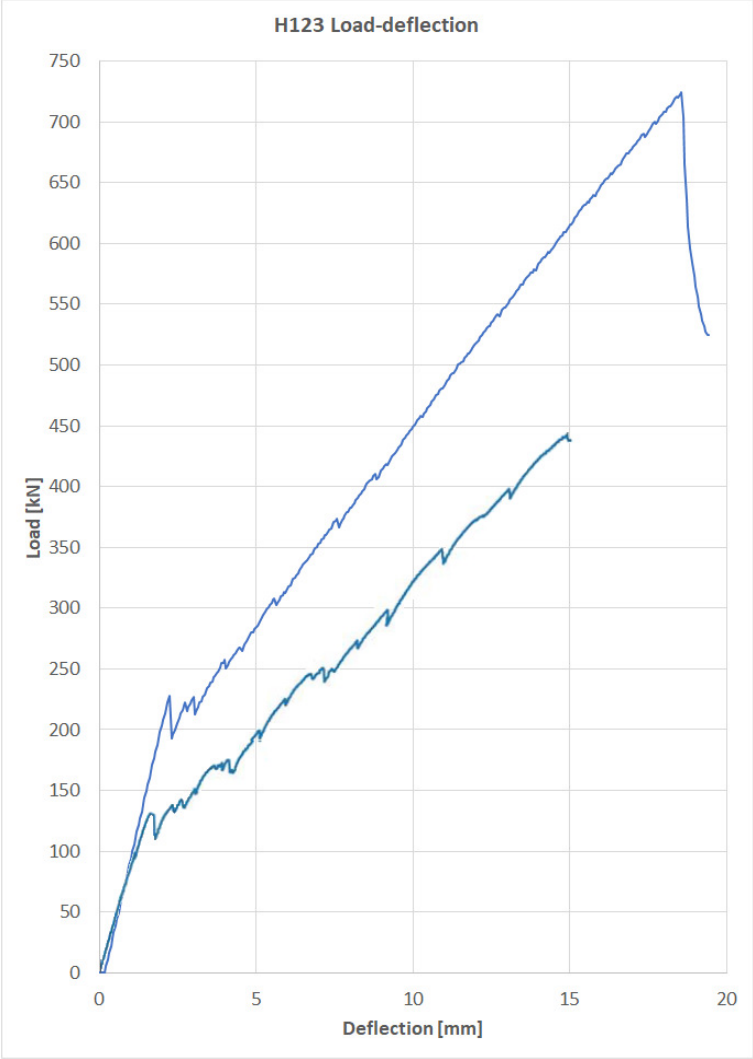

Figure 160: Load-deflection for beam H123 SBeta base model

H123: SBeta reduced tensile strength model

Only the changed parameters in comparison with the base model are presented, for the other parameters refer to Figure 154Figure 132 through Figure 157.

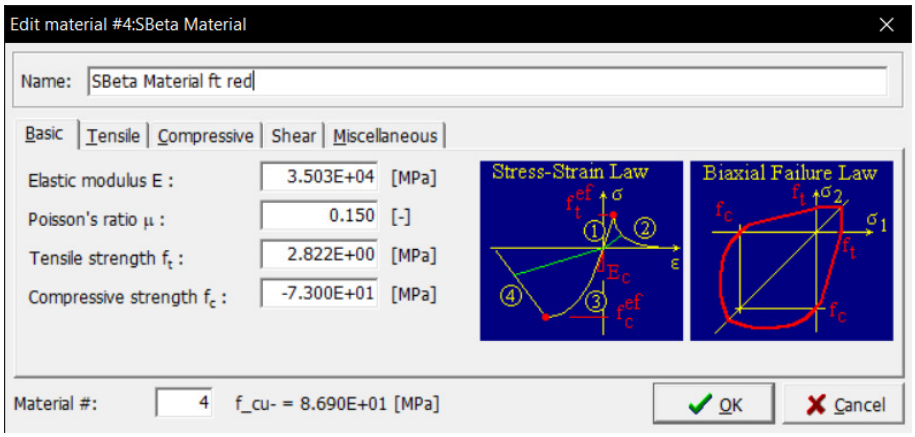

Figure 161: Finite element material specifications SBeta reduced tensile strength model

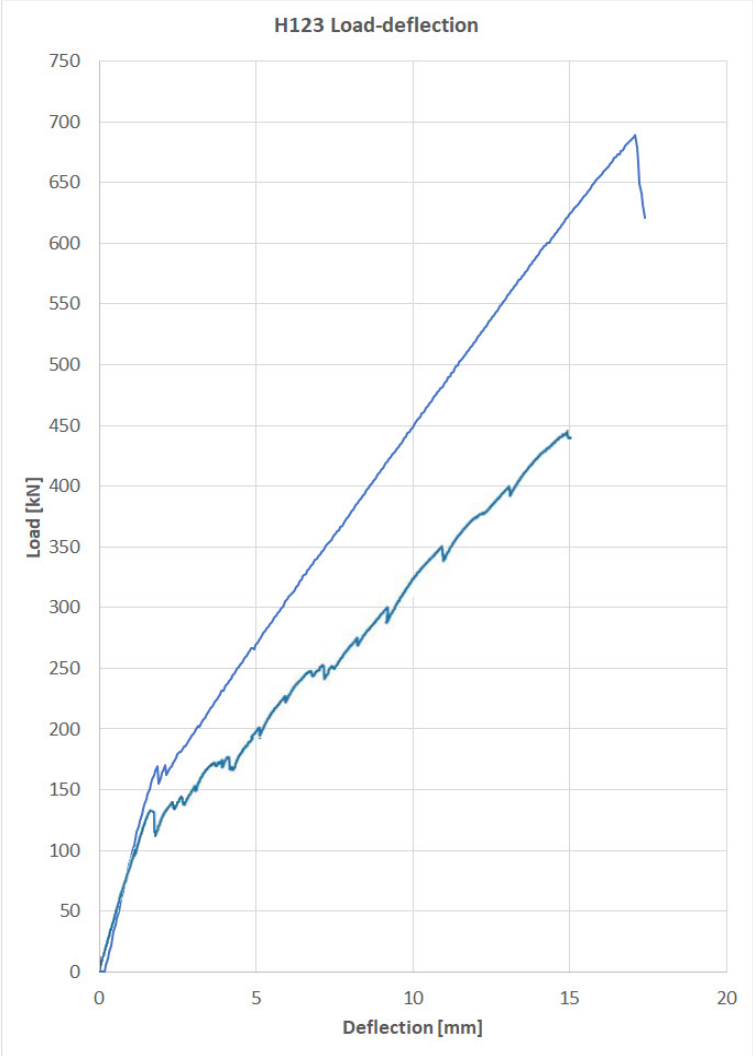

Figure 162: Load-deflection of beam H123 SBeta reduced tensile strength model

H123: SBeta reduced tensile strength and fracture energy model

Only the changed parameters in comparison with the base model are presented, for the other parameters refer to Figure 155Figure 132 through Figure 157.

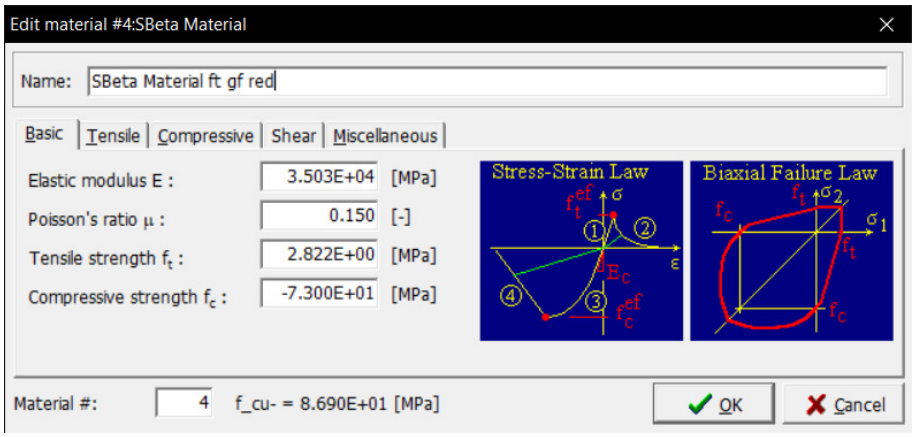

Figure 163: Finite element material specifications SBeta reduced tensile strength and fracture energy model

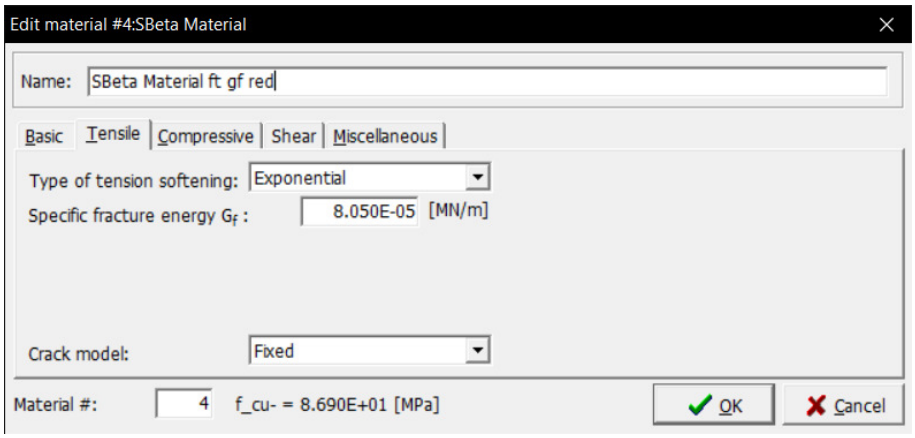

Figure 164: Finite element material specifications SBeta reduced tensile strength and fracture energy model

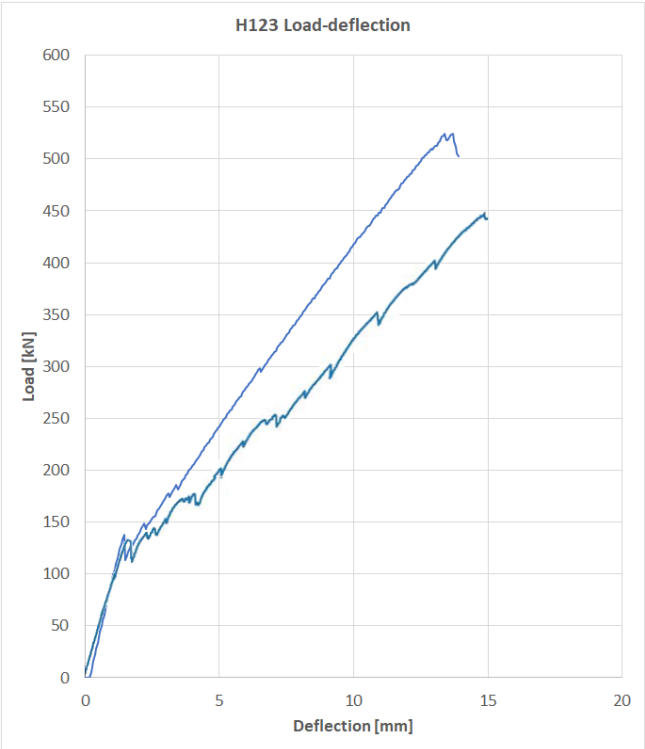

Figure 165: Load-deflection of beam H123 SBeta reduced tensile strength and fracture energy model

H123: NLCEM base model

The reinforcement described in Figure 158 and Figure 159 are used for all H123 and H352 models.

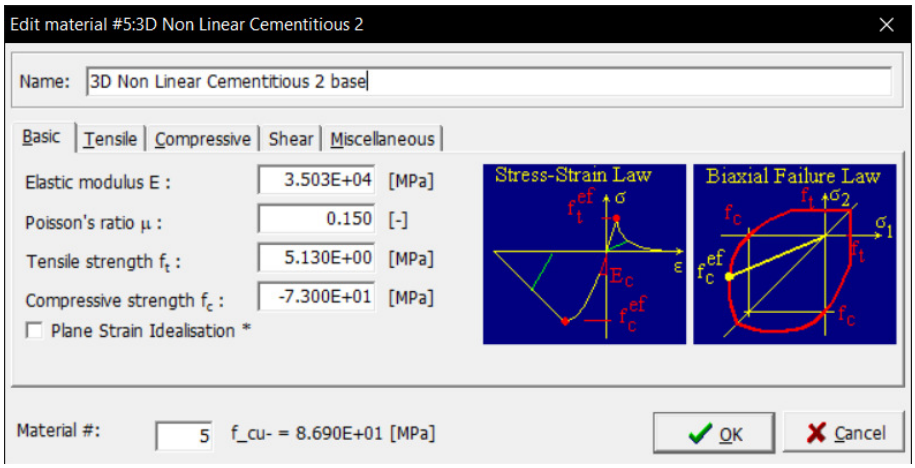

Figure 166: Finite element material specifications NLCEM base model

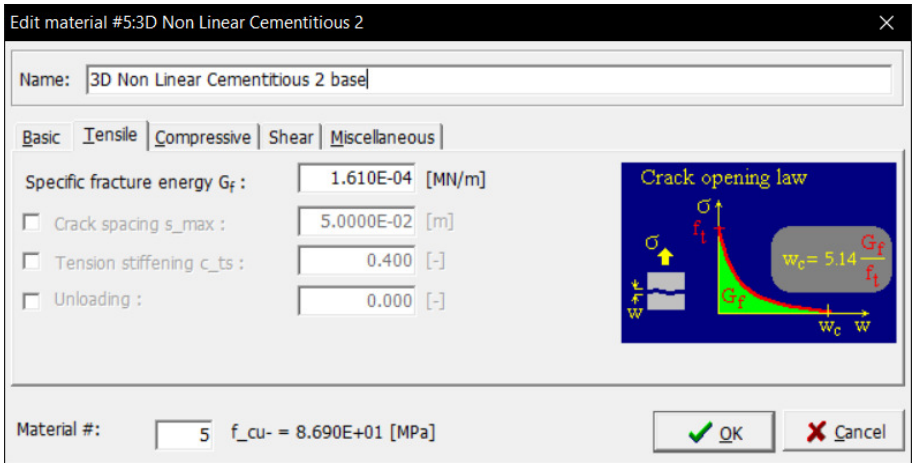

Figure 167: Finite element material specifications NLCEM base model

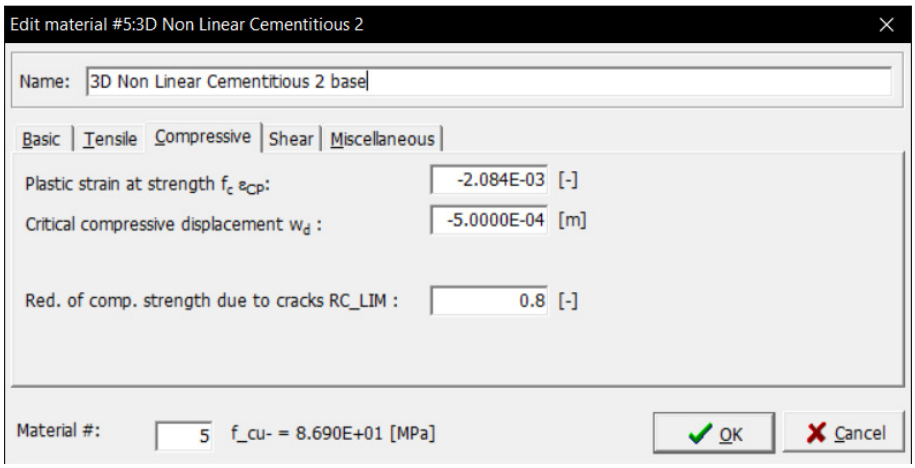

Figure 168: Finite element material specifications NLCEM base model

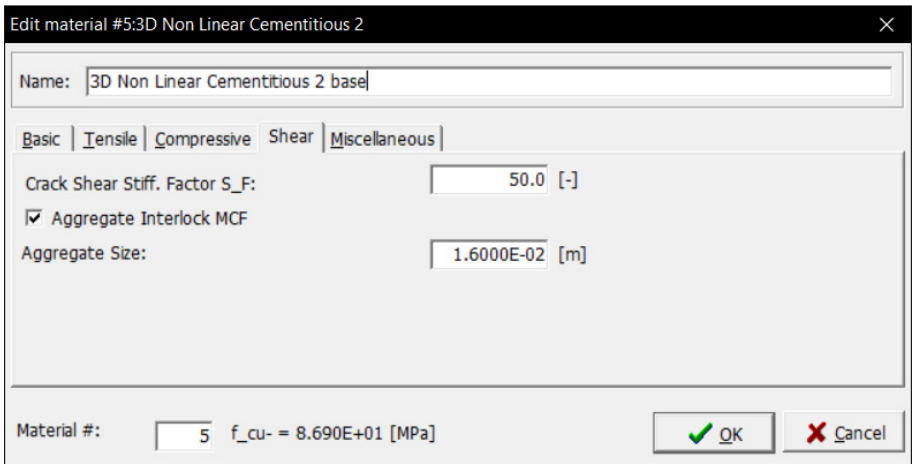

Figure 169: Finite element material specifications NLCEM base model

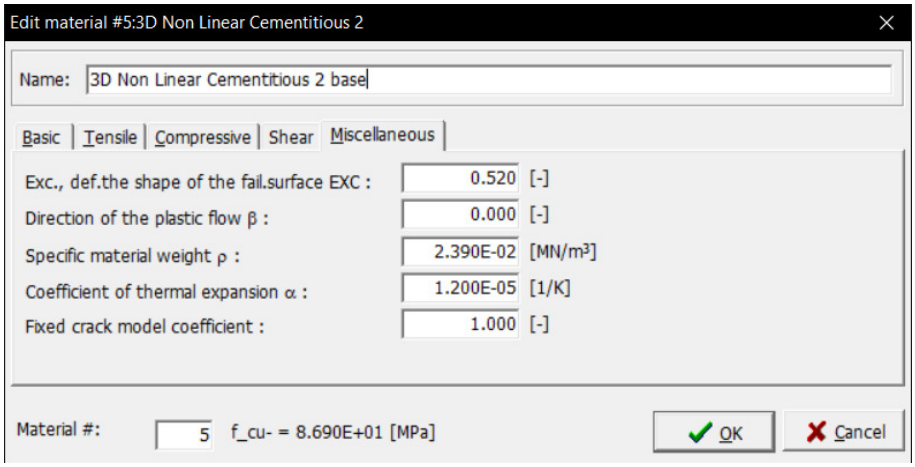

Figure 170: Finite element material specifications NLCEM base model

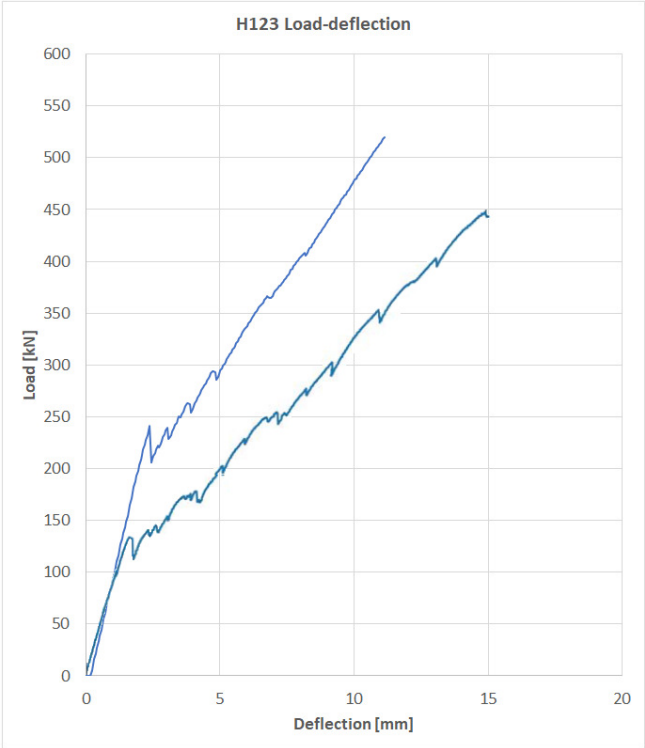

Figure 171: Load-deflection of beam H123 NLCEM base model

H123: NLCEM reduced tensile strength model

Only the changed parameters in comparison with the base model are presented, for the other parameters refer to Figure 167Figure 132 through Figure 170.

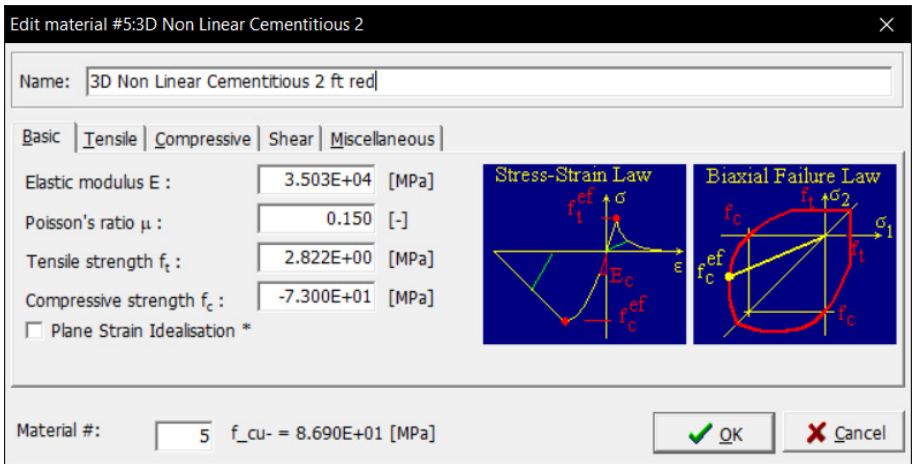

Figure 172: Finite element material specifications NLCEM reduced tensile strength model

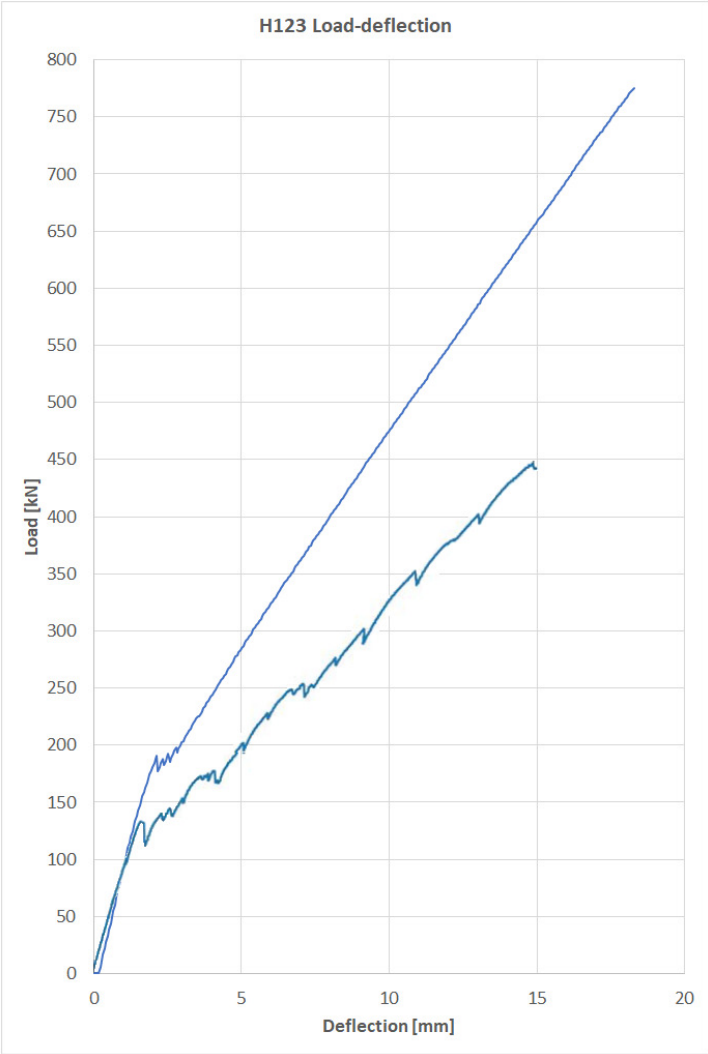

Figure 173: Load-deflection of beam H123 NLCEM reduced tensile strength model

H123: NLCEM reduced tensile strength and fracture energy model

Only the changed parameters in comparison with the base model are presented, for the other parameters refer to Figure 168Figure 132 through Figure 170.

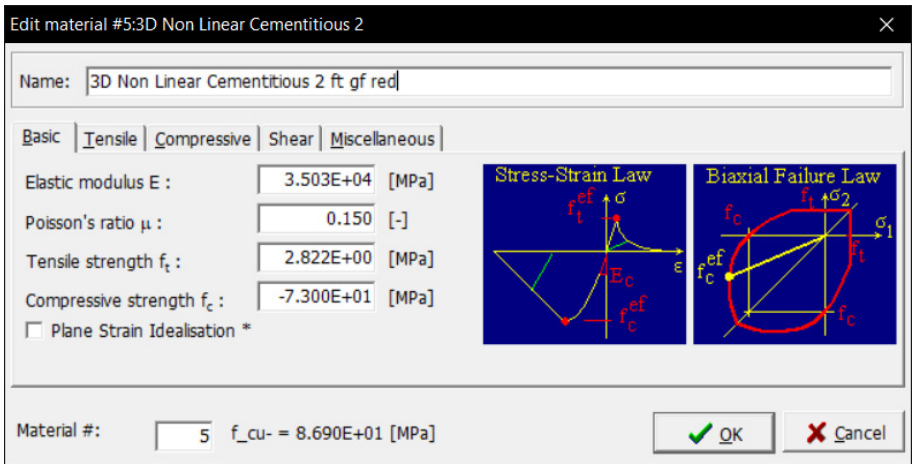

Figure 174: Finite element material specifications NLCEM reduced tensile strength and fracture energy model

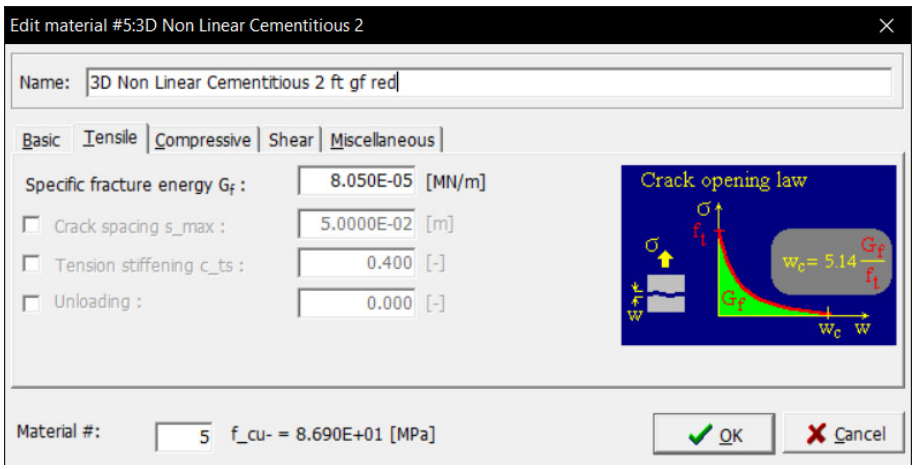

Figure 175: Finite element material specifications NLCEM reduced tensile strength and fracture energy model

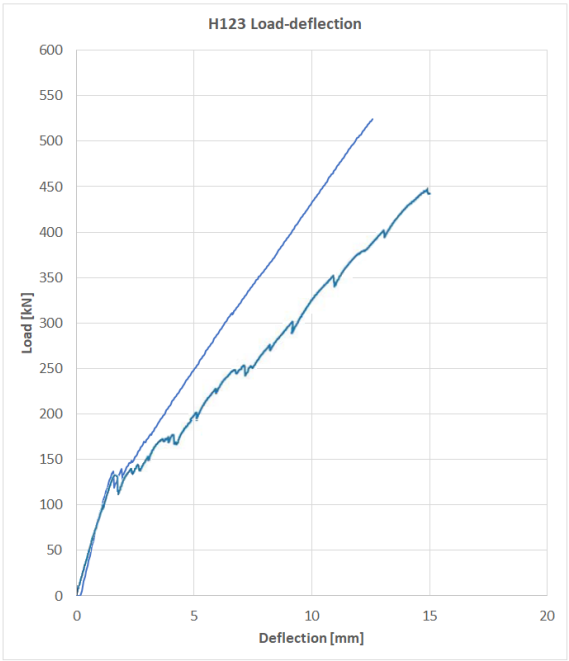

Figure 176: Load-deflection of beam H123 NLCEM reduced tensile strength and fracture energy model

H352: SBeta base model

The reinforcement described in Figure 158 and Figure 159 are used for all H123 and H352 models.

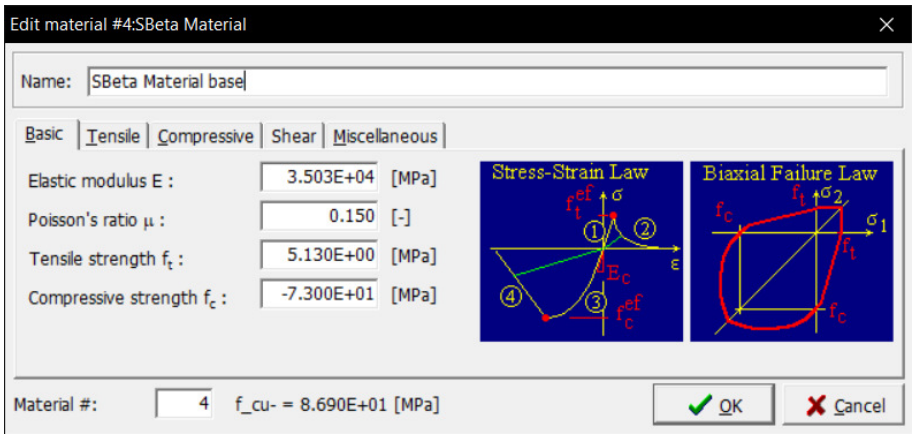

Figure 177: Finite element material specifications SBeta base model

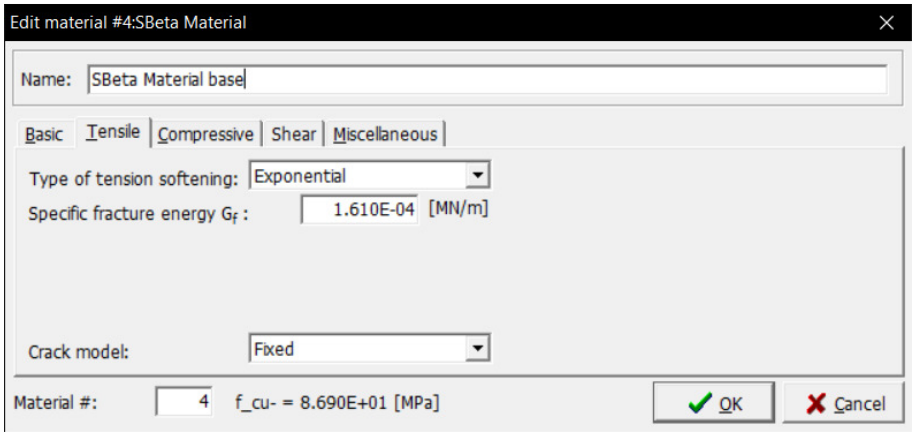

Figure 178: Finite element material specifications SBeta base model

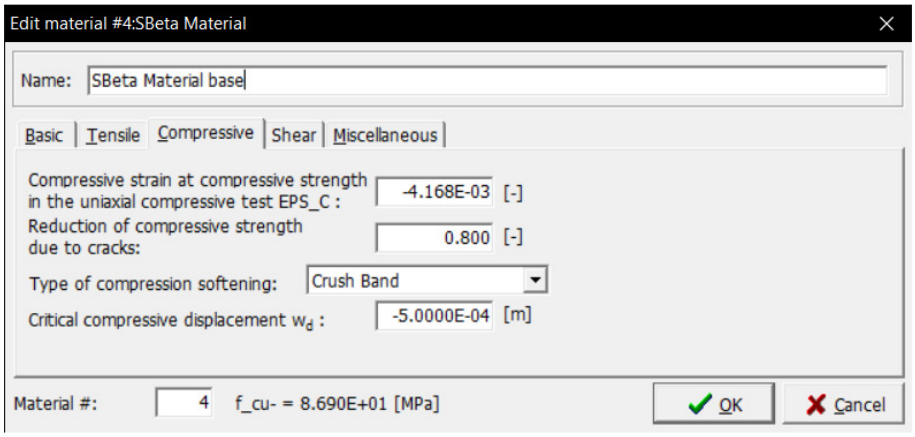

Figure 179: Finite element material specifications SBeta base model

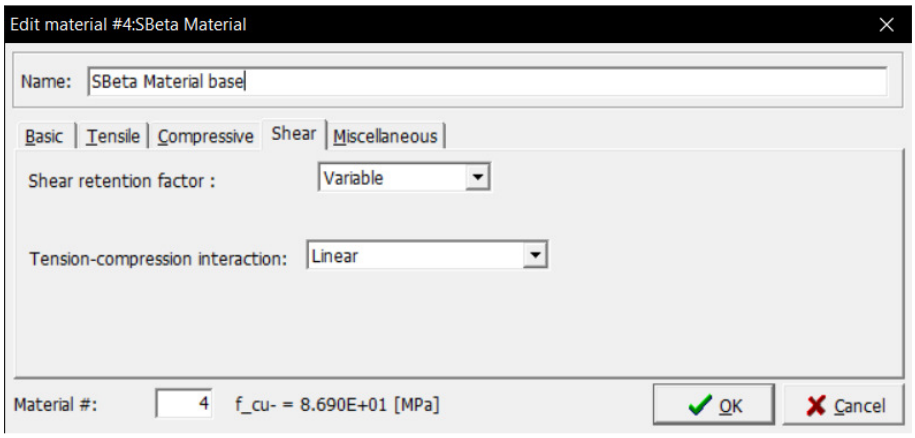

Figure 180: Finite element material specifications SBeta base model

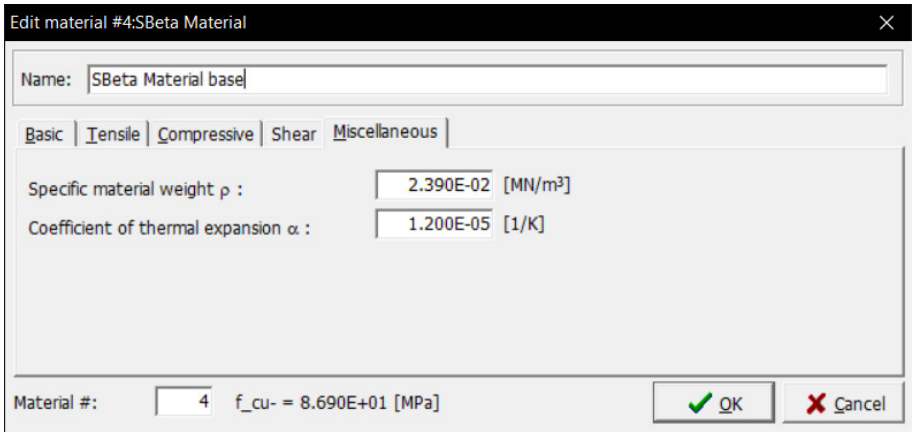

Figure 181: Finite element material specifications SBeta base model

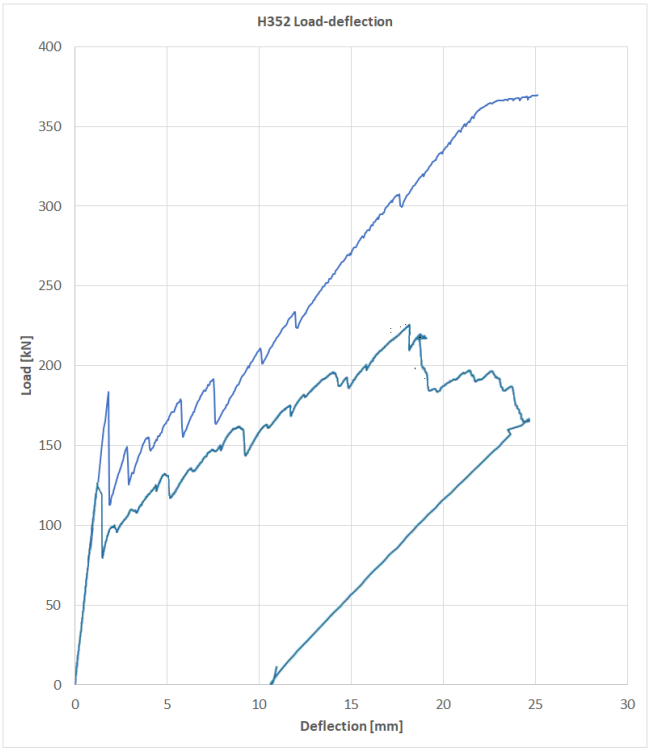

Figure 182: Load-deflection of beam H352 in SBeta base model

H352: SBeta reduced tensile strength model

Only the changed parameters in comparison with the base model are presented, for the other parameters refer to Figure 178Figure 132 through Figure 181.

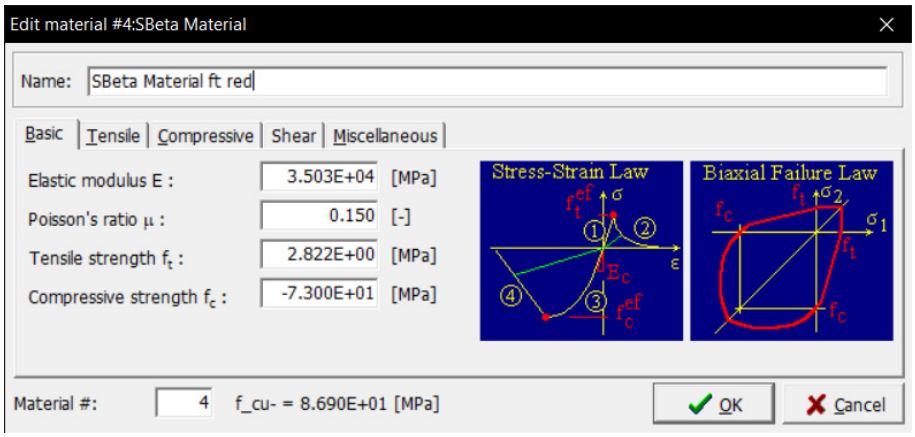

Figure 183: Finite element material specifications SBeta reduced tensile strength model

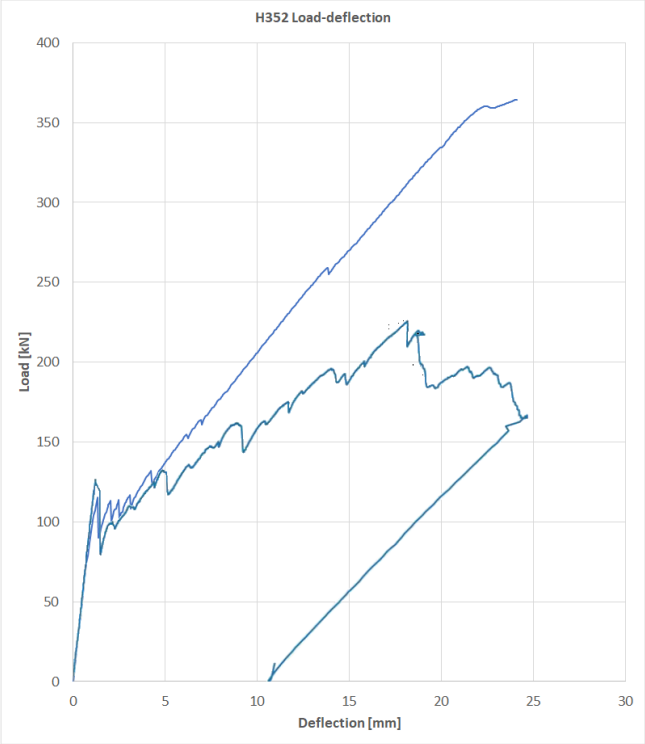

Figure 184: Load-deflection for beam H352 SBeta reduced tensile strength model

H352: SBeta reduced tensile strength and fracture energy model

Only the changed parameters in comparison with the base model are presented, for the other parameters refer to Figure 179Figure 132 through Figure 181.

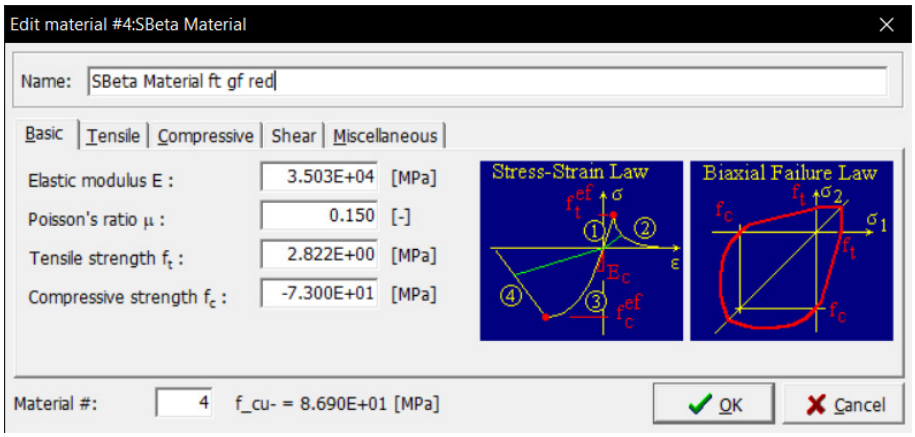

Figure 185: Finite element material specifications SBeta reduced tensile strength and fracture energy model

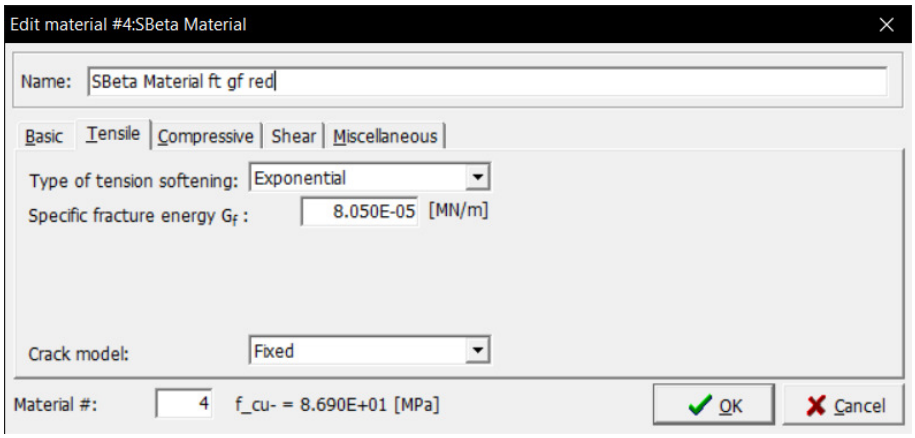

Figure 186: Finite element material specifications SBeta reduced tensile strength and fracture energy model

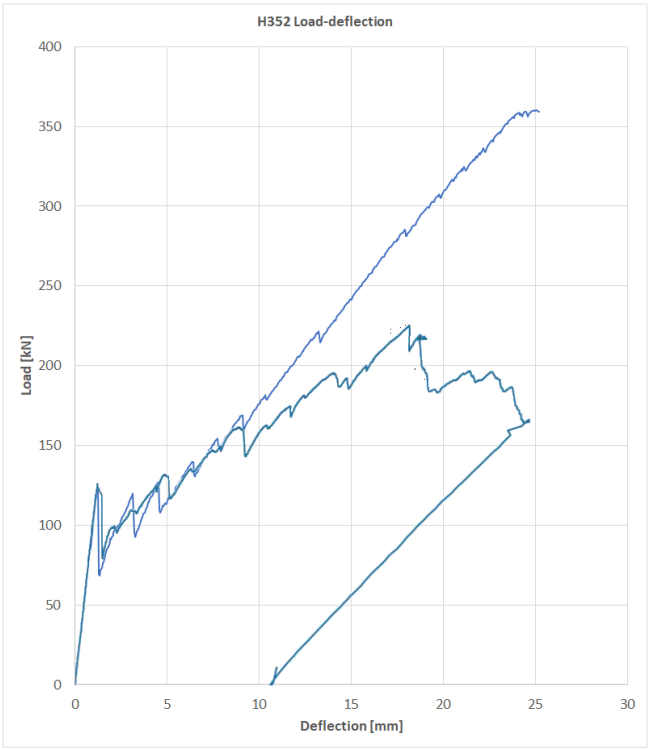

Figure 187: Load-deflection of beam H352 SBeta reduced tensile strength and fracture energy model

H352: NLCEM base model

The reinforcement described in Figure 158 and Figure 159 are used for all H123 and H352 models.

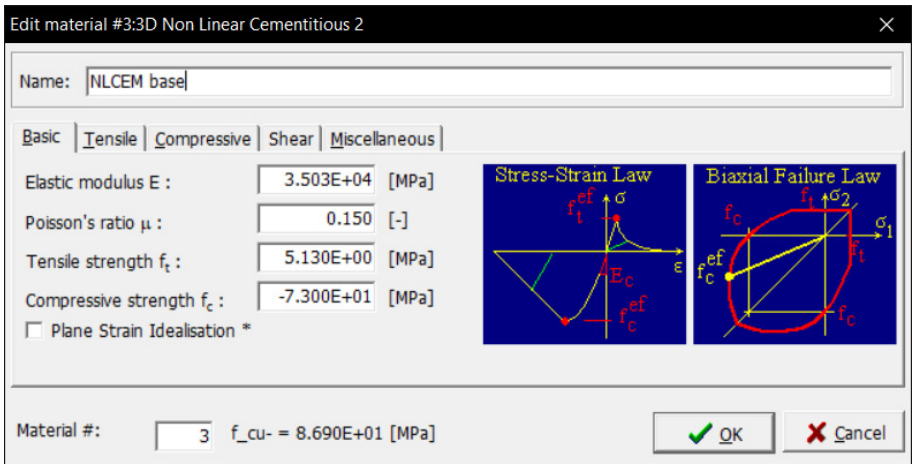

Figure 188: Finite element material specifications NLCEM base model

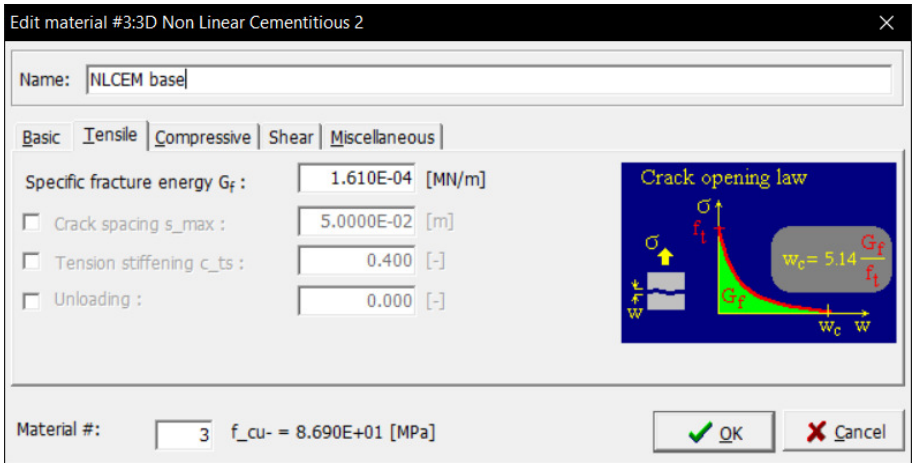

Figure 189: Finite element material specifications NLCEM base model

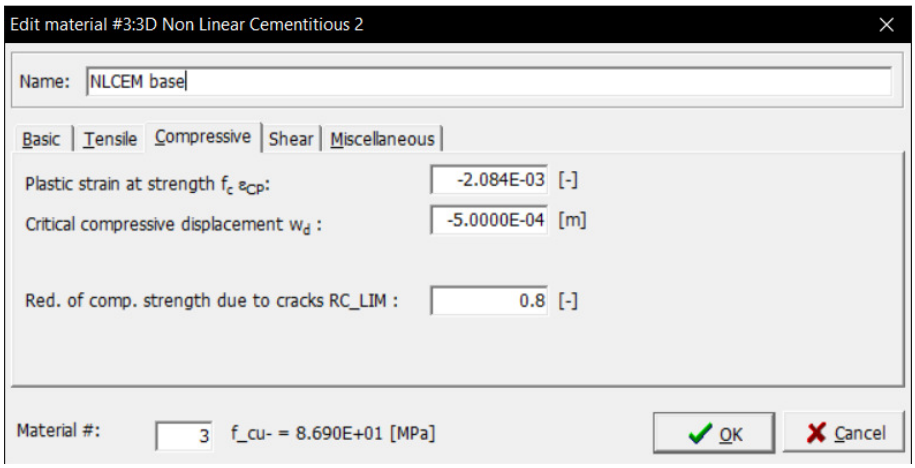

Figure 190: Finite element material specifications NLCEM base model

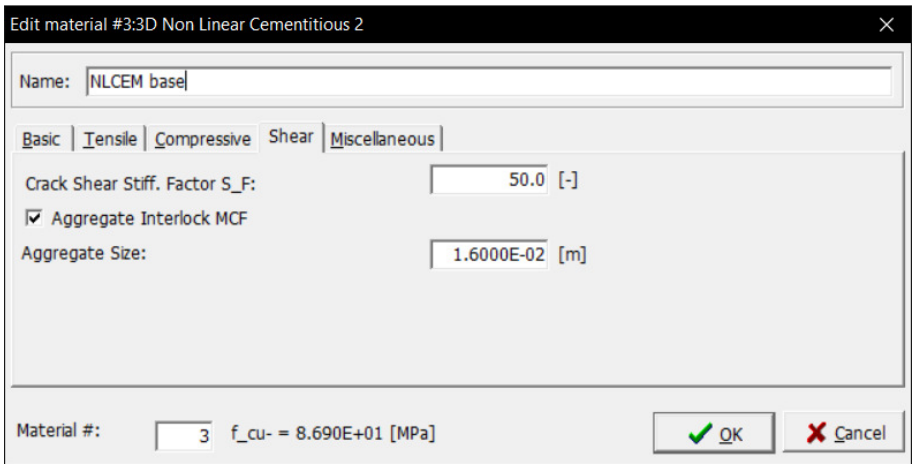

Figure 191: Finite element material specifications NLCEM base model

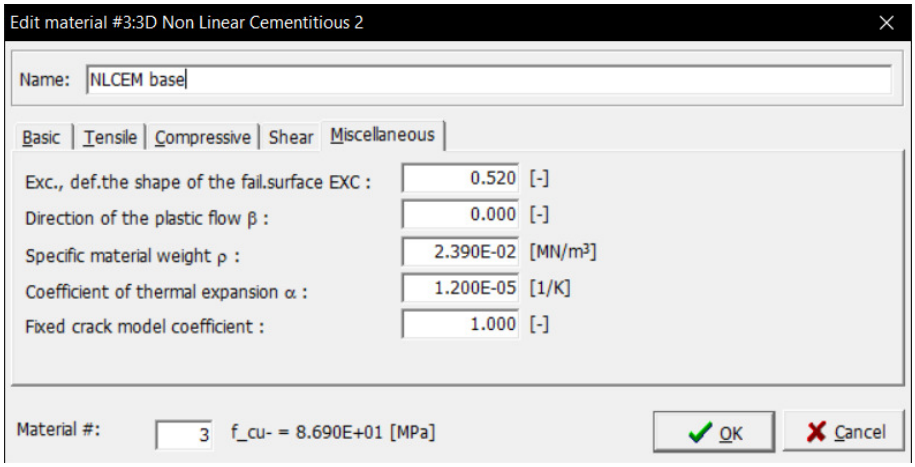

Figure 192: Finite element material specifications NLCEM base model

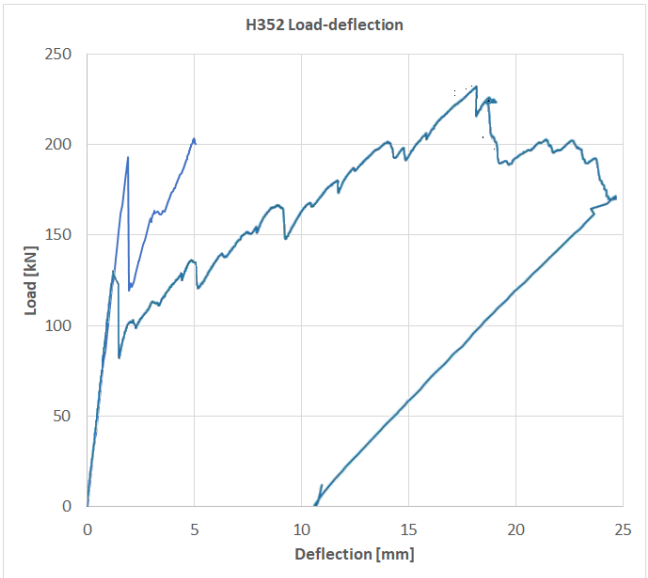

Figure 193: Load-deflection of beam H352 NLCEM base model

H352: NLCEM reduced tensile strength model

Only the changed parameters in comparison with the base model are presented, for the other parameters refer to Figure 189Figure 132 through Figure 192.

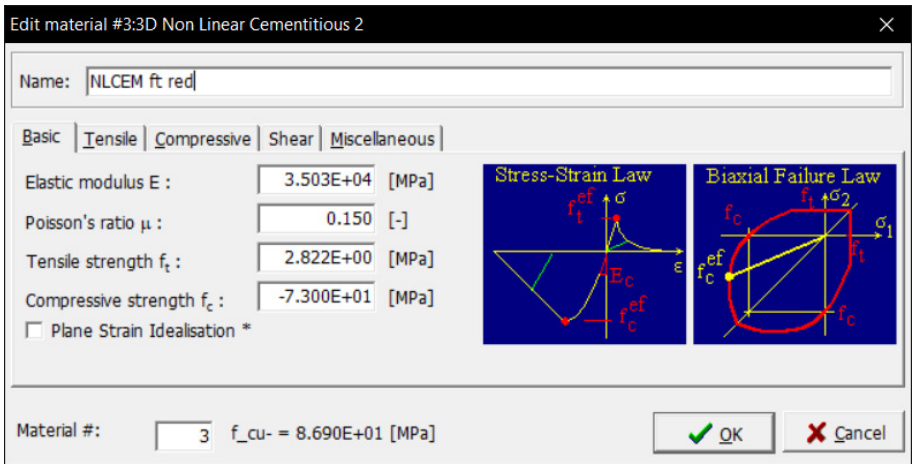

Figure 194: Finite element material specifications NLCEM reduced tensile strength model

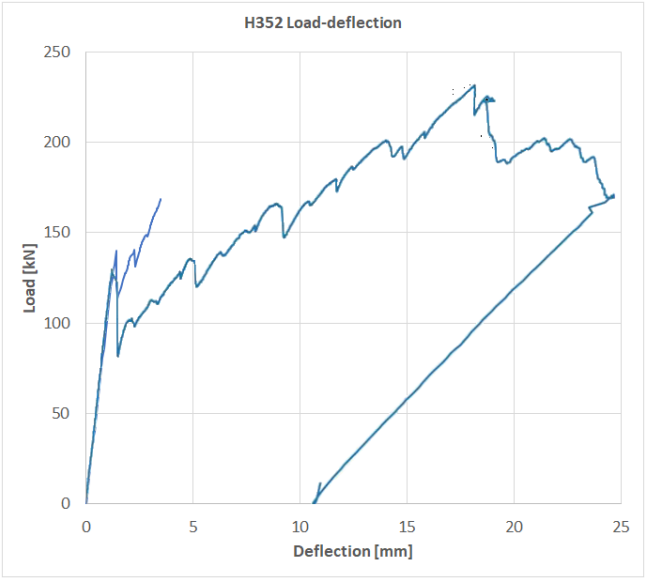

Figure 195: Load-deflection of beam H352 NLCEM reduced tensile strength model

H352: NLCEM reduced tensile strength and fracture energy model

Only the changed parameters in comparison with the base model are presented, for the other parameters refer to Figure 190Figure 132 through Figure 192.

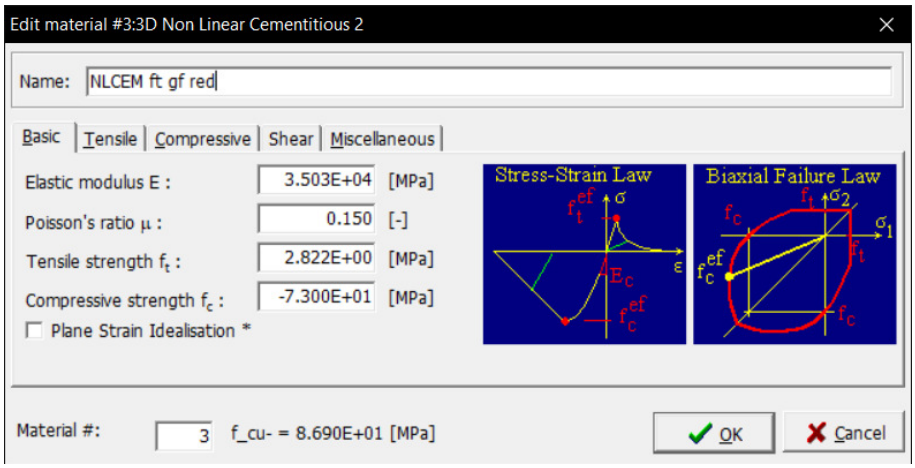

Figure 196: Finite element material specifications NLCEM reduced tensile strength and fracture energy model

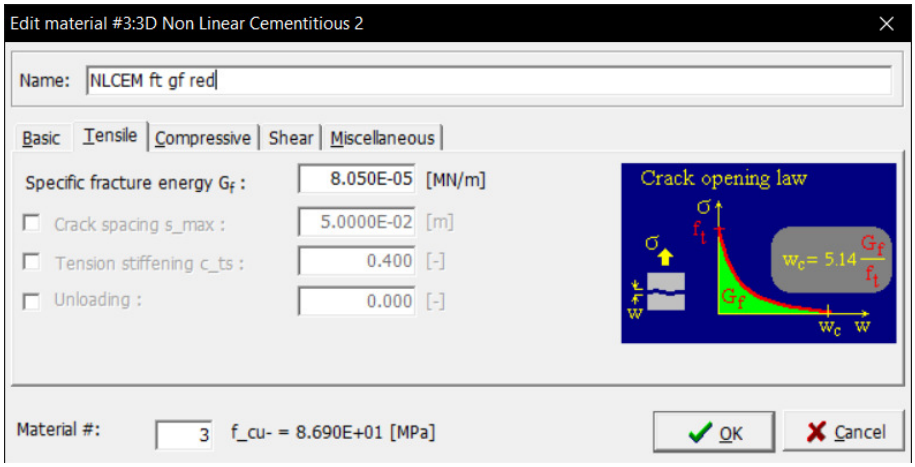

Figure 197: Finite element material specifications NLCEM reduced tensile strength and fracture energy model

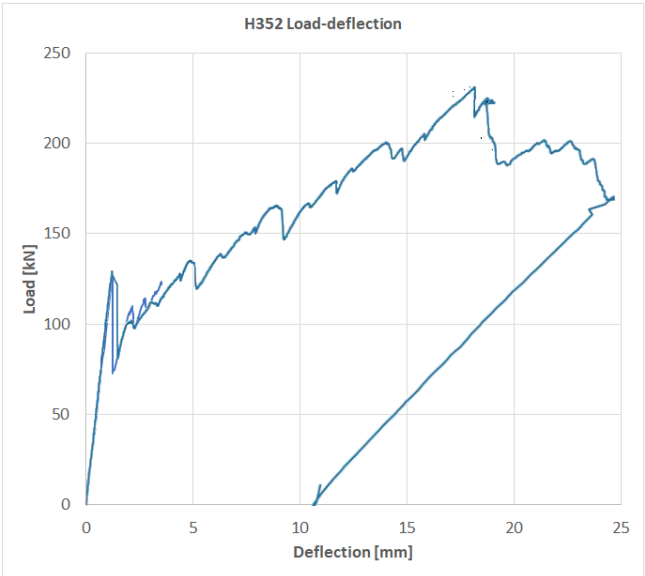

Figure 198: Load-deflection of beam H352 NLCEM reduced tensile strength and fracture energy model

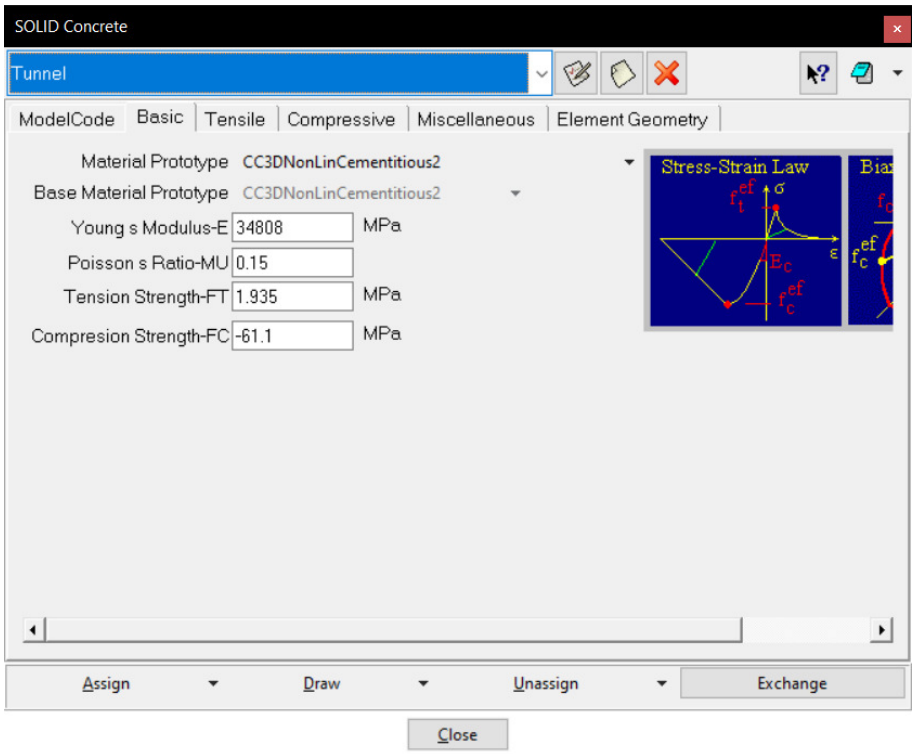

Figure 199: Finite element material specifications concrete (no fire)

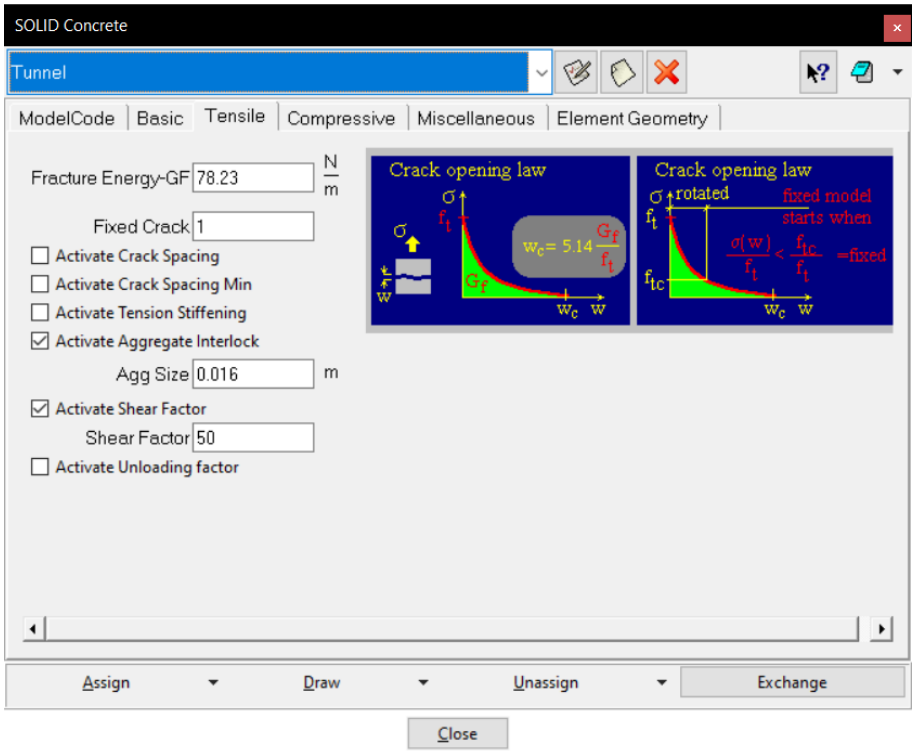

Figure 200: Finite element material specifications concrete (no fire)

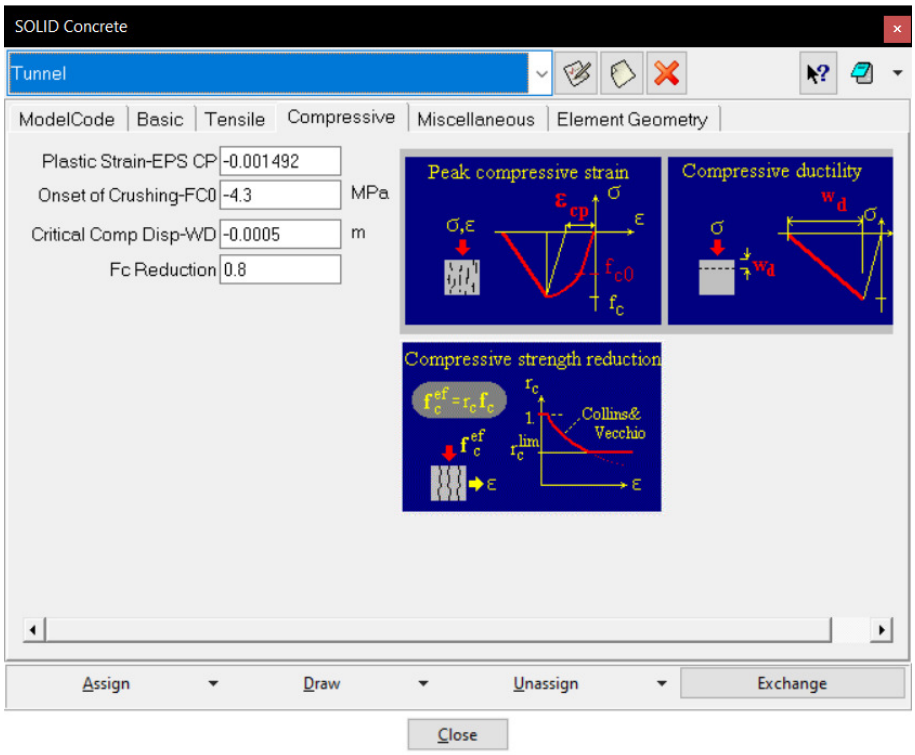

Figure 201: Finite element material specifications concrete (no fire)

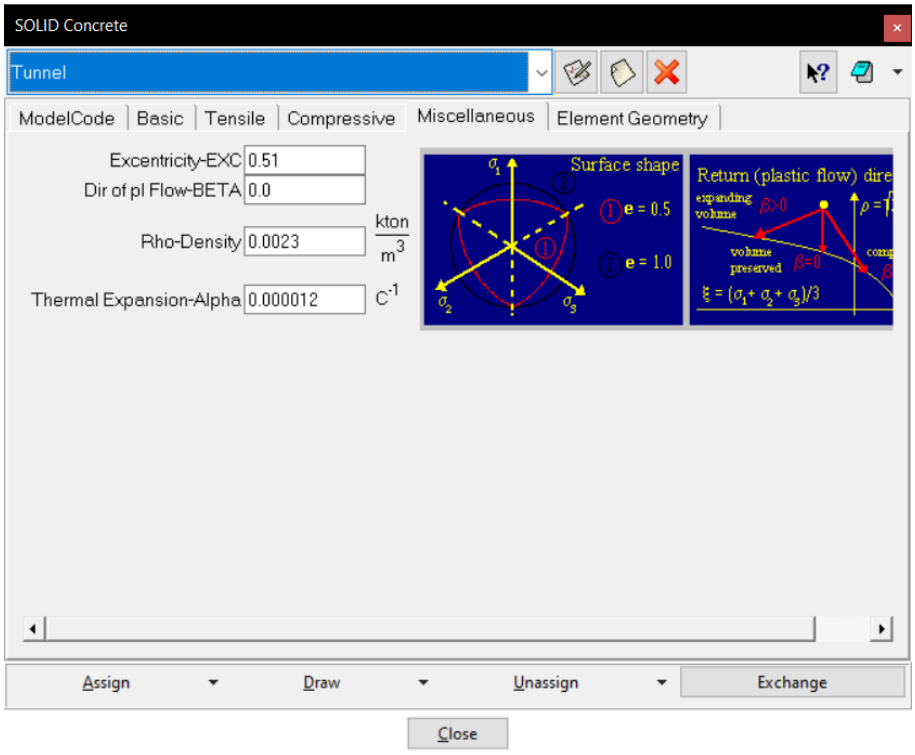

Figure 202: Finite element material specifications concrete (no fire)

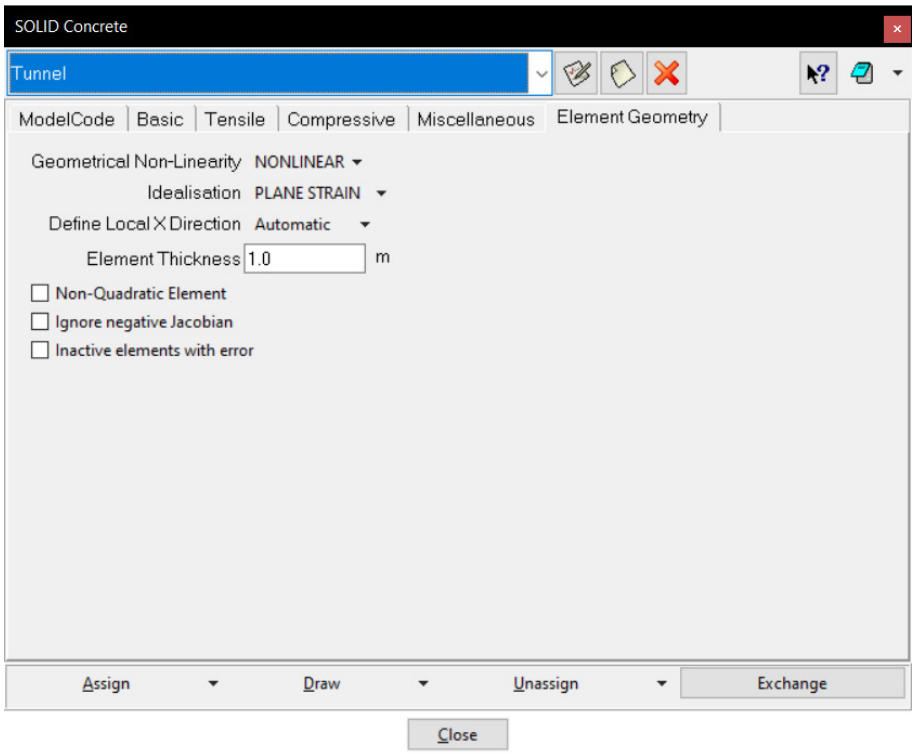

Figure 203: Finite element material specifications concrete (no fire)

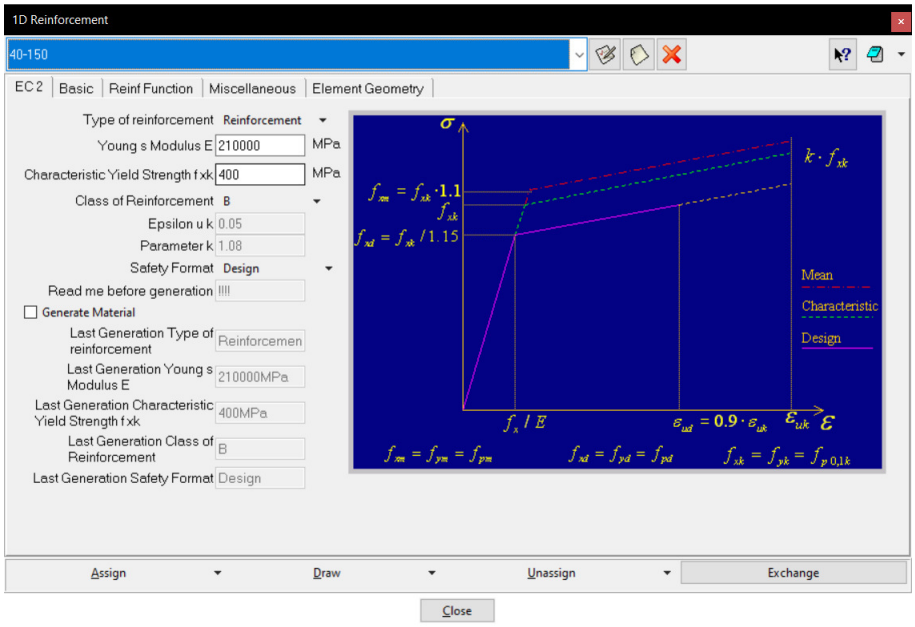

Figure 204: Finite element material specifications reinforcement (no fire)

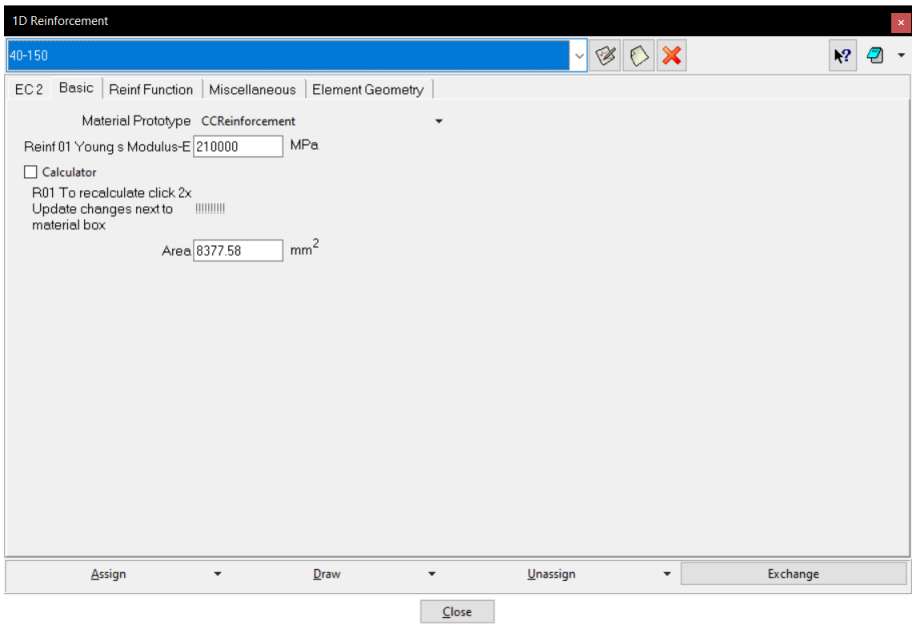

Figure 205: Finite element material specifications reinforcement (no fire)

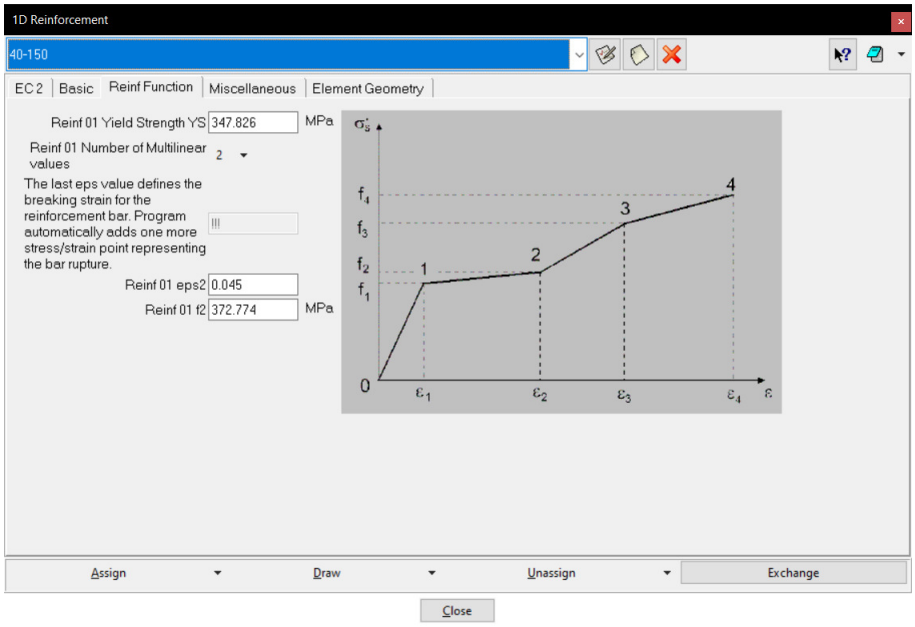

Figure 206: Finite element material specifications reinforcement (no fire)

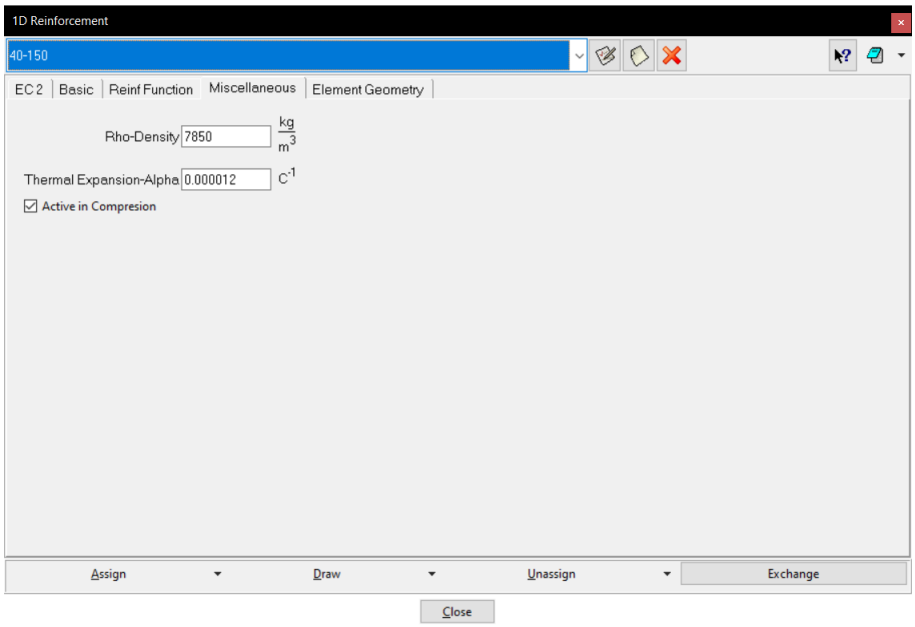

Figure 207: Finite element material specifications reinforcement (no fire)

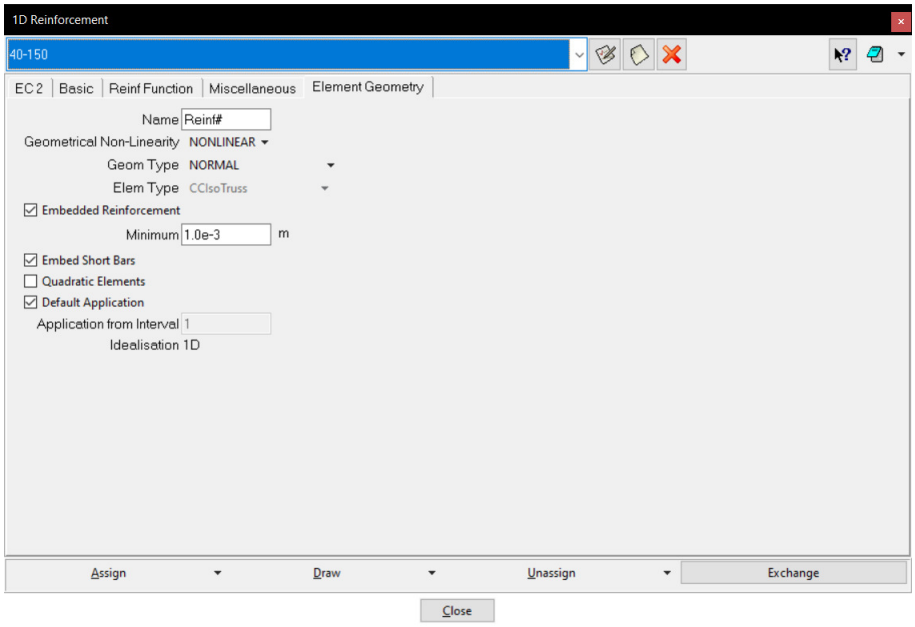

Figure 208: Finite element material specifications reinforcement (no fire)

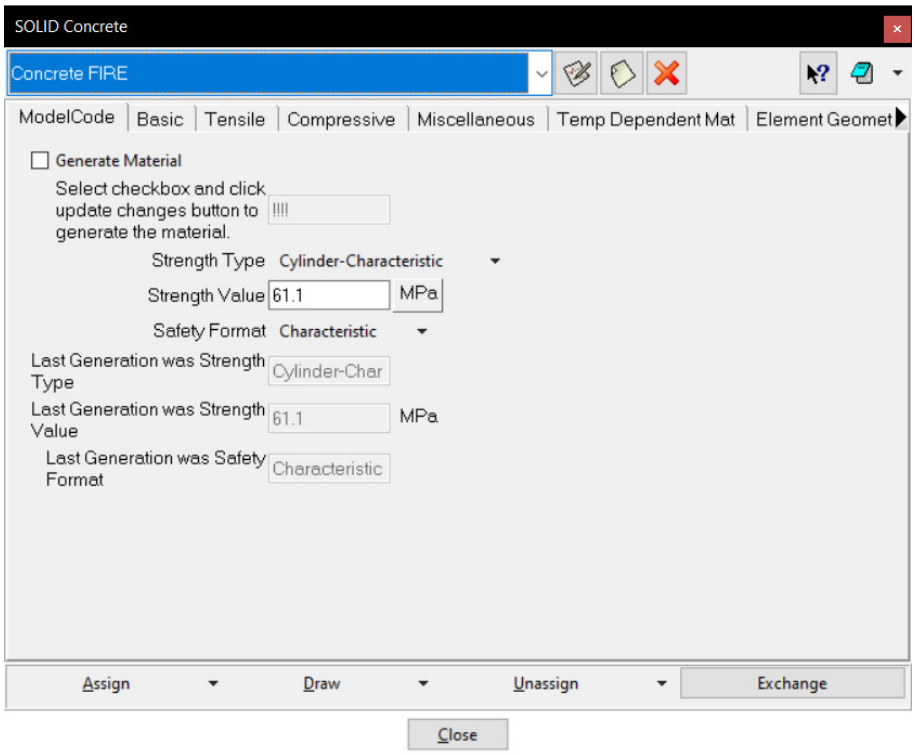

Figure 209: Finite element material specifications concrete (fire)

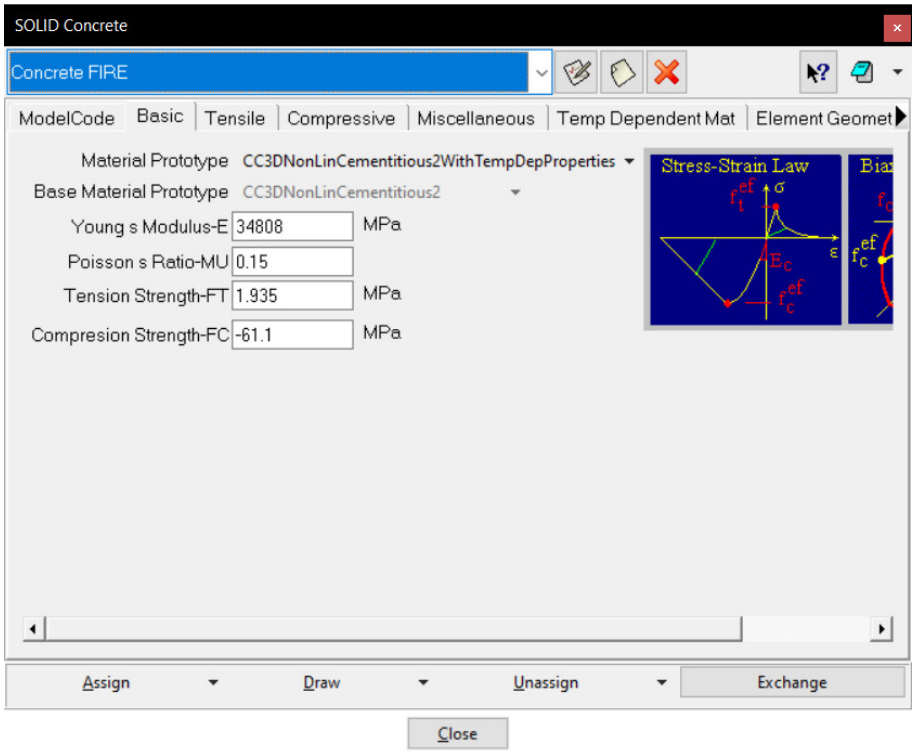

Figure 210: Finite element material specifications concrete (fire)

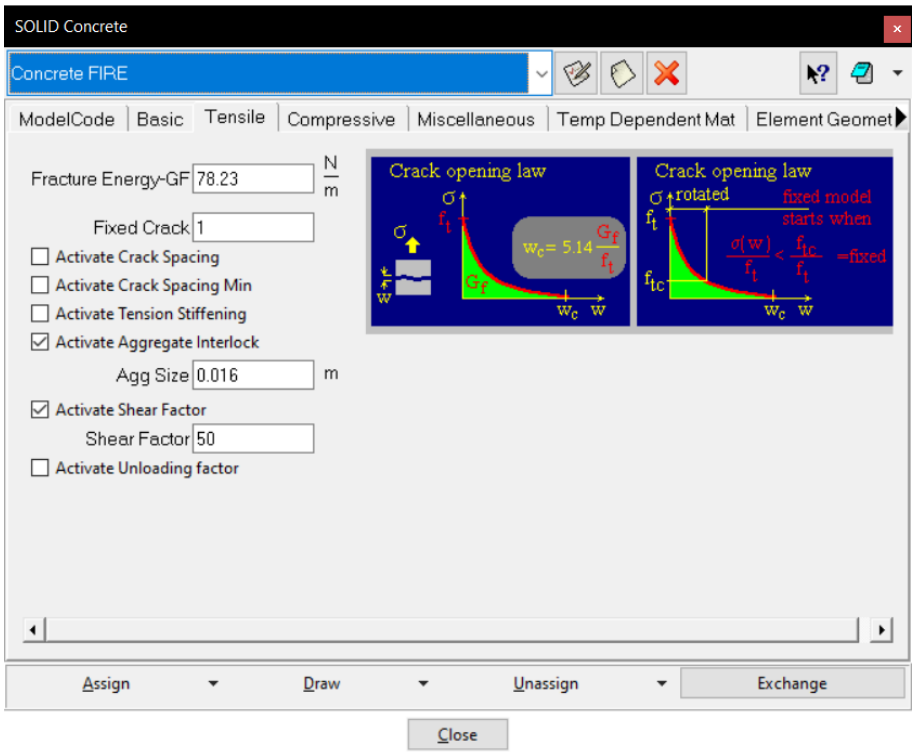

Figure 211: Finite element material specifications concrete (fire)

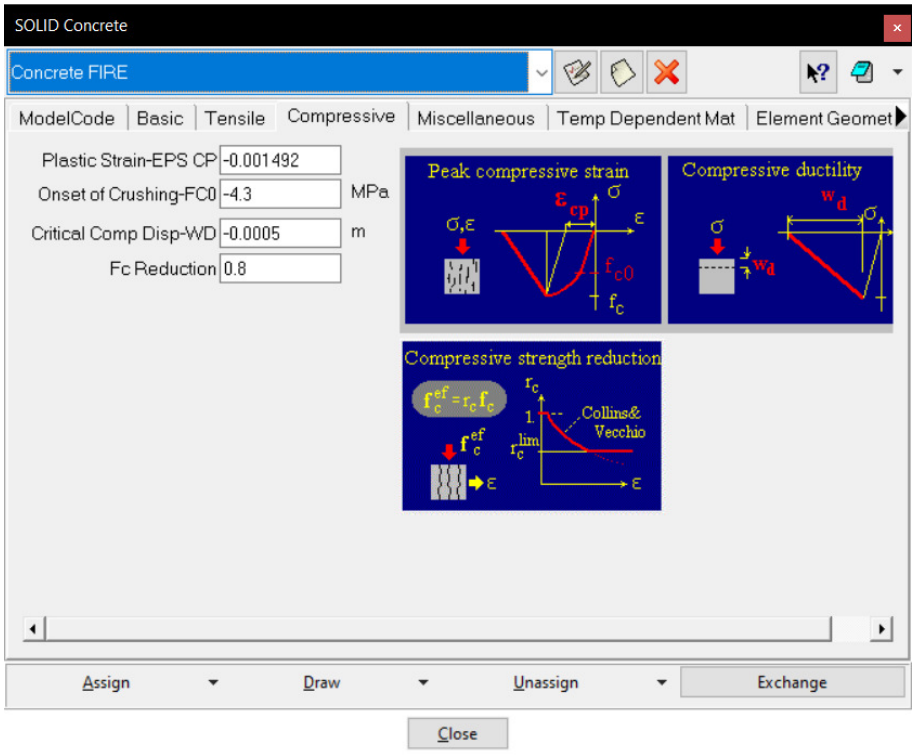

Figure 212: Finite element material specifications concrete (fire)

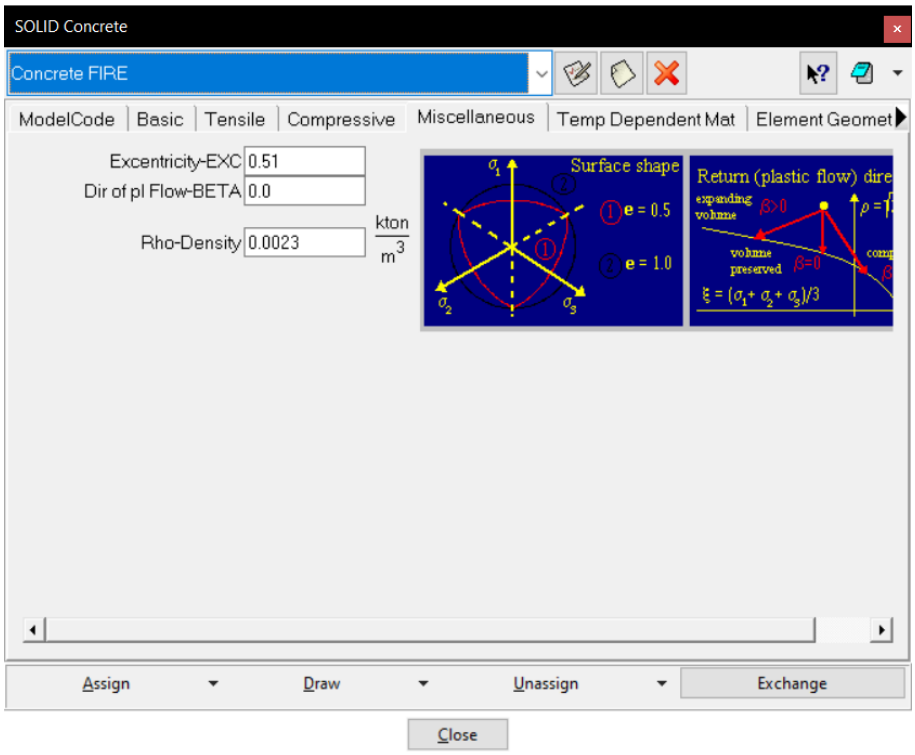

Figure 213: Finite element material specifications concrete (fire)

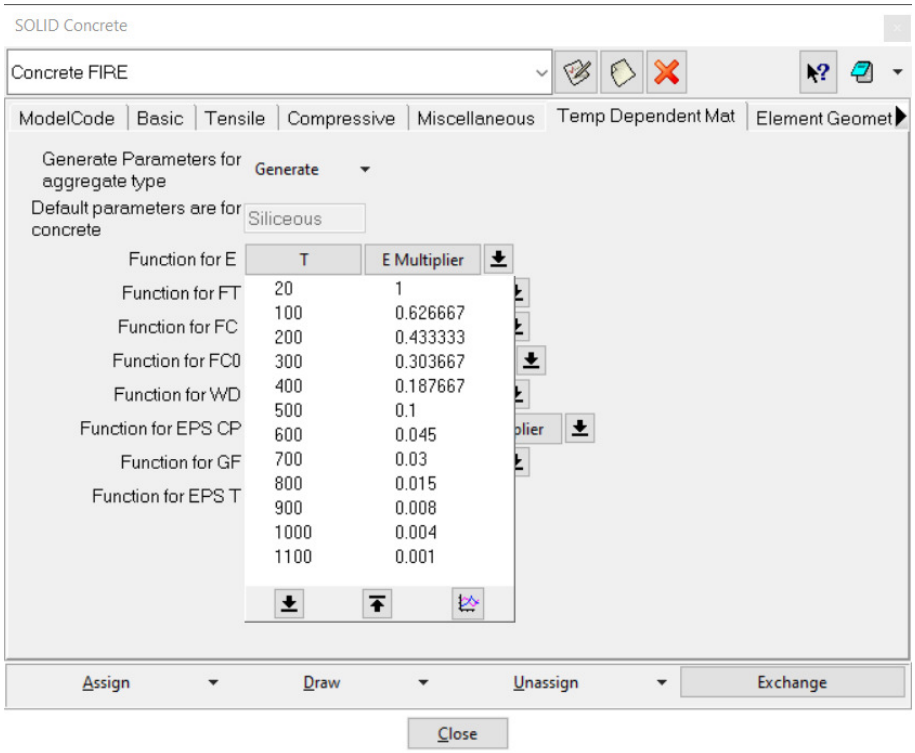

Figure 214: Finite element material specifications concrete (fire)

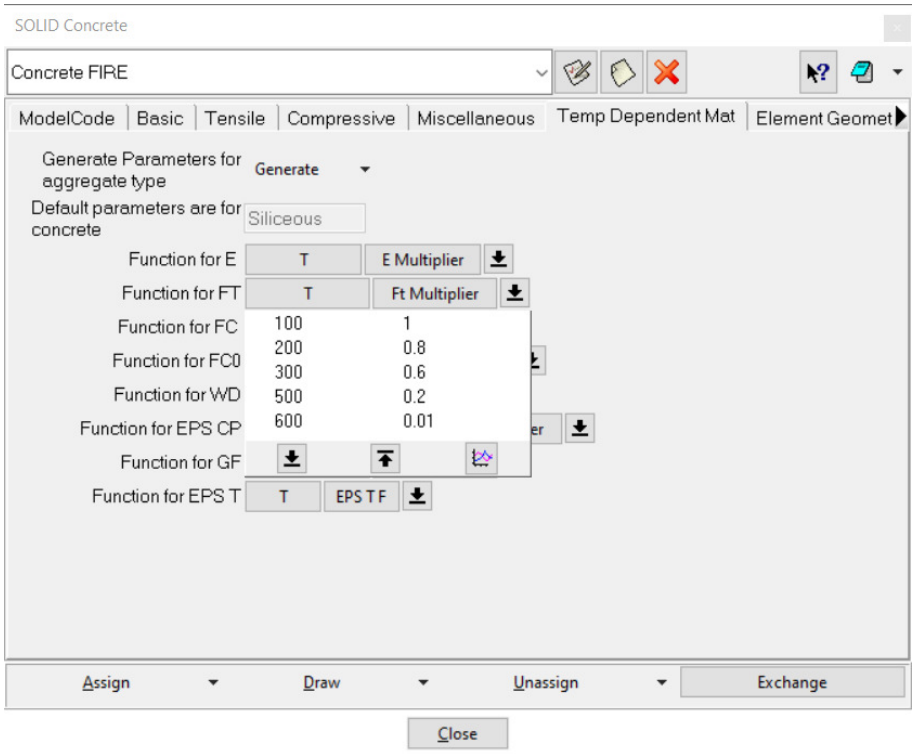

Figure 215: Finite element material specifications concrete (fire)

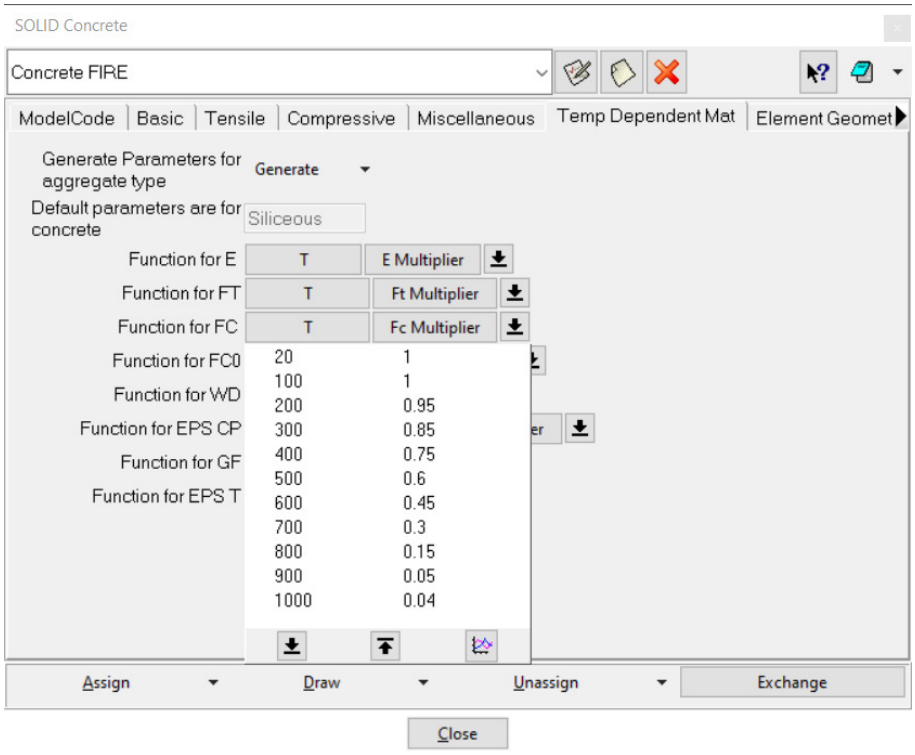

Figure 216: Finite element material specifications concrete (fire)

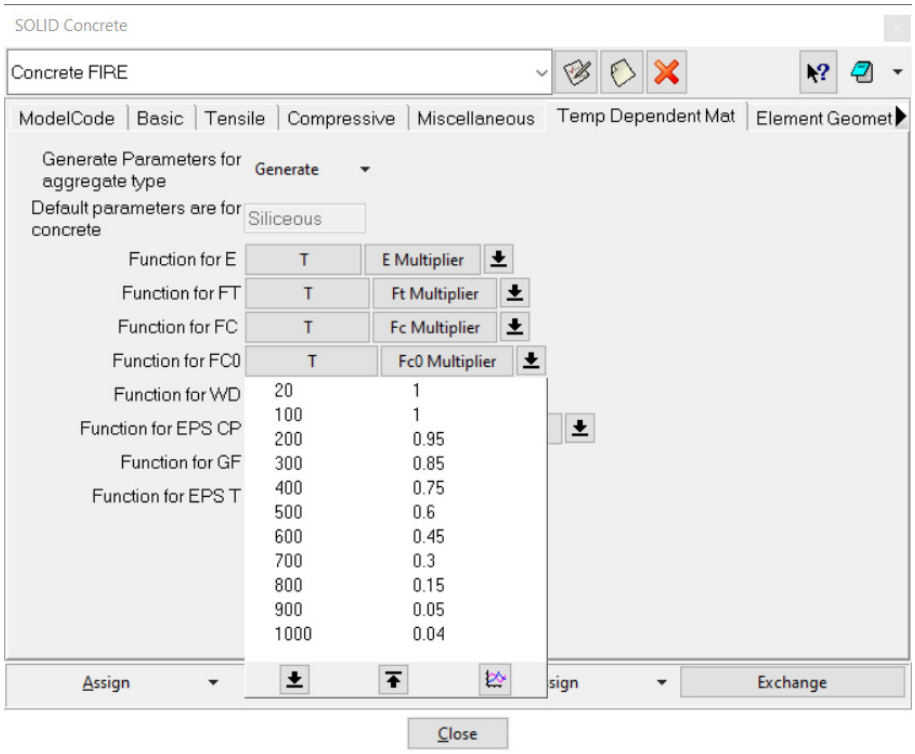

Figure 217: Finite element material specifications concrete (fire)

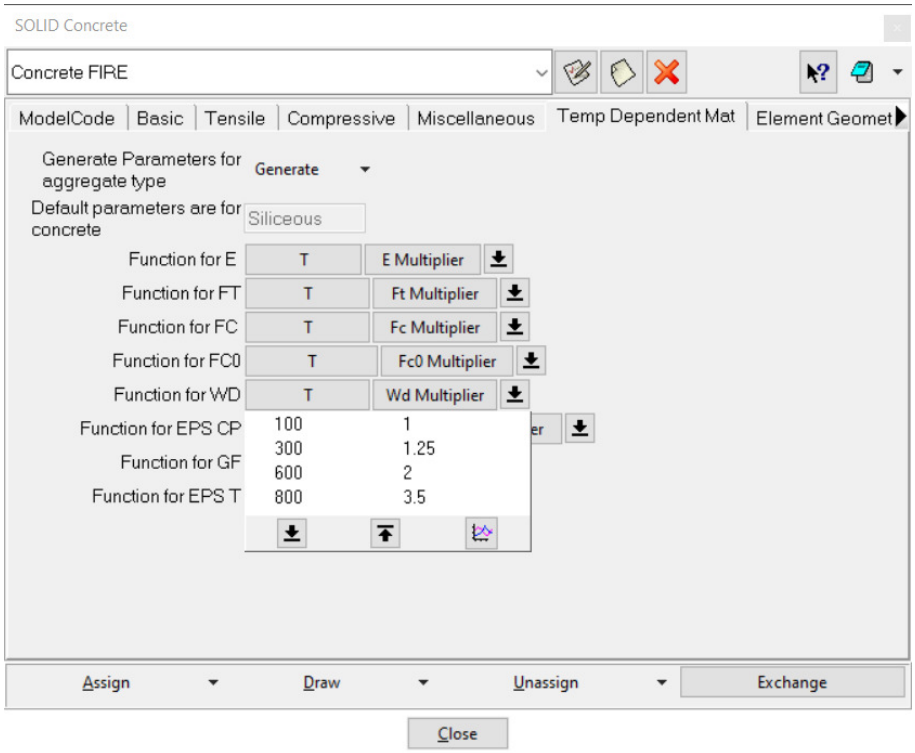

Figure 218: Finite element material specifications concrete (fire)

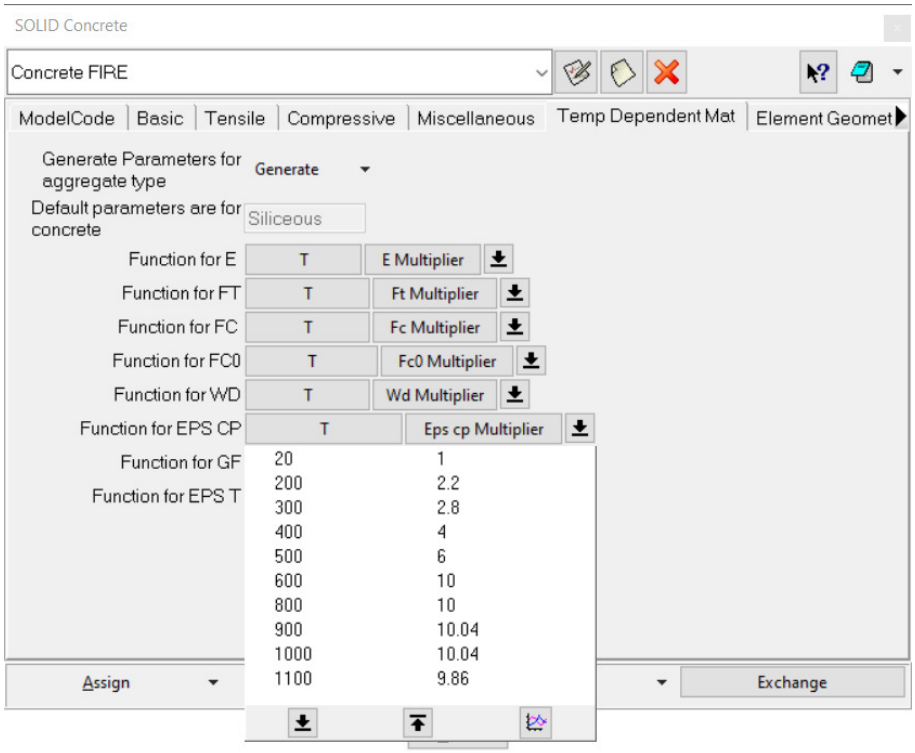

Figure 219: Finite element material specifications concrete (fire)

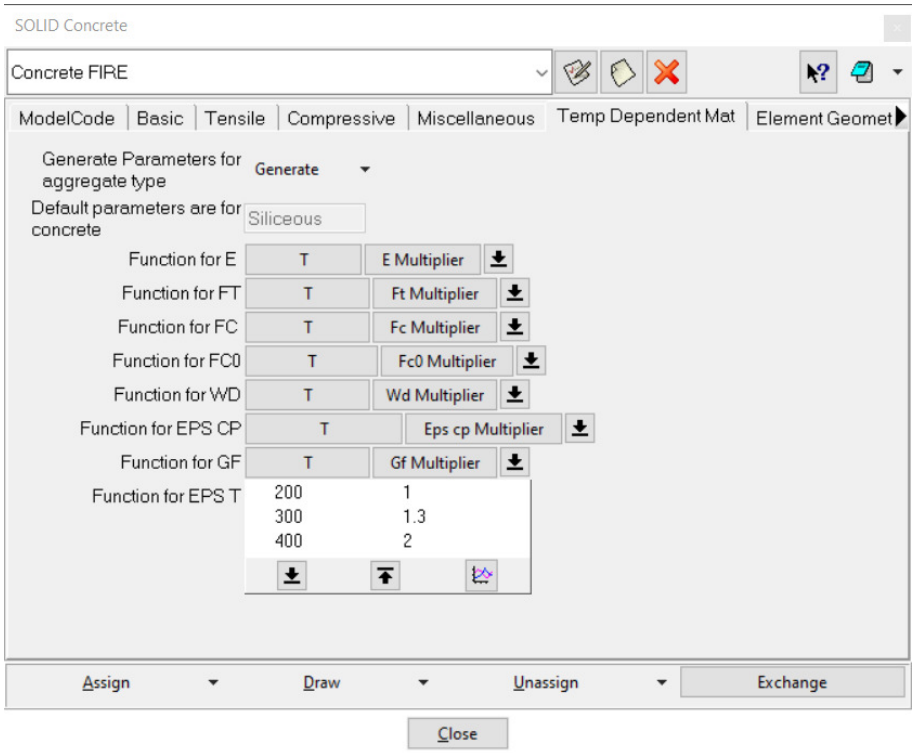

Figure 220: Finite element material specifications concrete (fire)

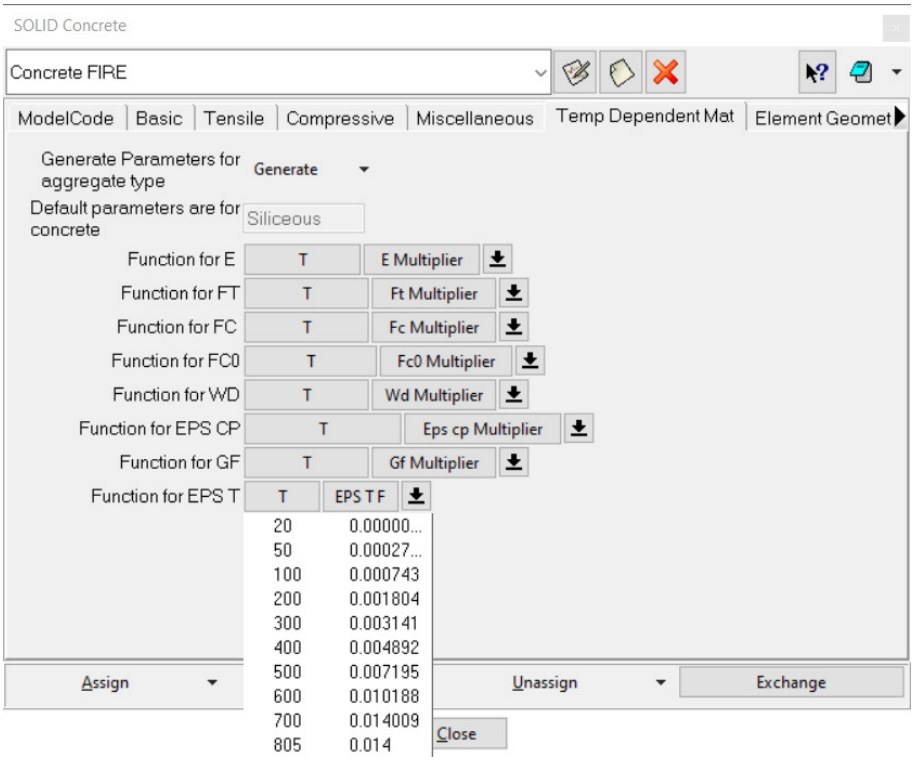

Figure 221: Finite element material specifications concrete (fire)

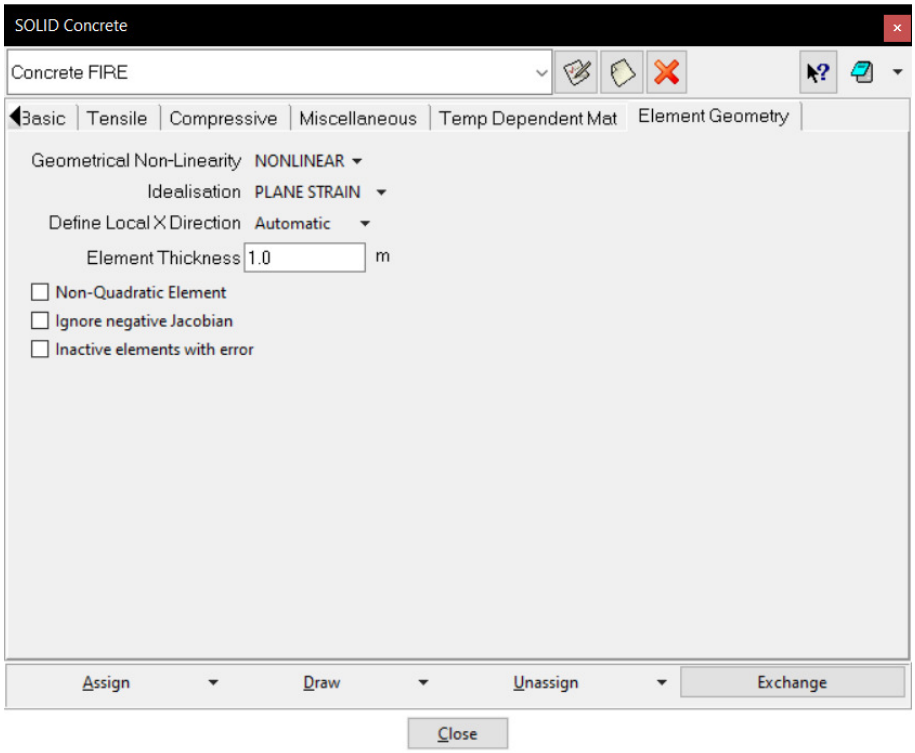

Figure 222: Finite element material specifications concrete (fire)